RÉPUBLIQUE ALGÉRIENNE DÉMOCRATIQUE ET POPULAIRE

MINISTÈRE DE L'ENSEIGNEMENT SUPÉRIEUR ET DE LA RECHERCHE SCIENTIFIQUE

N° d'ordre : ………….
N° de série : ……………

UNIVERSITÉ KASDI MERBAH – OUARGLA

FACULTÉ DES MATHÉMATIQUES ET SCIENCES DE LA MATIÈRE

DÉPARTEMENT DE PHYSIQUE

THÈSE DE DOCTORAT EN SCIENCES

SPECIALITÉ : **PHYSIQUE**

OPTION : **PHYSIQUE DES MATÉRIAUX**

Par : **AYAT ZAHIA**

THÈME

SIMULATION DE PROPRIÉTÉS ÉLECTRONIQUES DANS DES HYDRURES METALLIQUES

Soutenue le 04/07/2019 devant le jury composé de :

Pr.	**Aïadi Kamel Eddine**	**Université Kasdi Merbah**	**Président**
Pr.	**Rhouma Ferhat**	**Université El-Oued**	**Examinateur**
Pr.	**Ouahab Abdelouahab**	**Université Mohamed Khider Biskra**	**Examinateur**
Dr.	**Bouderba Hichem**	**Université Gharddia**	**Examinateur**
Dr.	**Bentouila Omar**	**Université Kasdi Merbah**	**Examinateur**
Pr.	**Daoudi Bahmed**	**Université Gharddia**	**Invité**
Pr.	**Boukraa Aomar**	**Université Kasdi Merbah**	**Rapporteur**

DEMOCRATIC AND POPULAR REPUBLIC OF ALGERIA

MINISTRY OF HIGHER EDUCATION AND SCIENTIFIC RESEARCH

N° d'ordre : …………..
N° de série : ……………

UNIVERSITY OF KASDI MERBAH – OUARGLA

FACULTY OF MATHEMATICS AND MATIER SCIENCES

DEPARTMENT OF PHYSICS

THESIS OF DOCTORATE OF SCIENCES

SPECIALITY: **PHYSICS**

MAJOR : **MATERIALS PHYSICS**

by : **ZAHIA AYAT**

THEME

SIMULATION OF ELECTRONIC PROPERTIES IN METALLIC HYDRIDES

Discussed on 04/07/2019

Acknowledgements

Foremost, I wish to thank my thesis advisor Prof. Aomar Boukraa for all the encouragement and guidance over the past years and for providing me with an excellent chance to work and to complete this doctorate project at the "Laboratoire de Développement des Energies Nouvelles et Renouvelables dans les Zones Arides et Sahariennes (LENREZA)", University of Kasdi Merbah Ouargla.

I would also like to thank all my committee members including Prof. Kamel Eddine Aïadi, Prof. Ferhat Rhouma, Prof. Abdelouahab Ouahab, Dr. Hichem Bouderba, Dr. Omar Bentouila, and Prof. Bahmed Daoudi for their time and patience.

At this point I want to thank Prof. Peter Vajda, Prof. Peter Hreze, Prof. Abdelhafid Kellou, Prof. Mohamed Tayeb Meftah, Dr. Saadi Berri, Dr. Youcef Bouhadda, Dr. Kamel Benyallou, and many others for their scientific support, help and advice. Without them, this work would not have been possible.

Thanks to all my friends inside and outside the Kasdi Merbah University, all my colleagues, and all university workers, especially teachers. I would like to thank everyone who has guided and accompanied my way during the last years.

Finally, I would like to thank my parents, my sisters, my brothers, and my family not only for supporting me during my whole life but most of all for providing me the freedom and encouragement to realize my own ideas.

Thanks to all of you, Zahia Ayat

CONTENTS

Chaper I
Hydrides and metallic hydrides

Chaper II Overview on the theoretical framework 32

Chapter III Pure rare-earths R (R = Gd and Tb): structural, electronic, and magnetic properties 57

Chapter IV

Rare-earth dihydrides RH_2 (R = Gd, and Tb): structural, thermodynamic, and electronic properties

93

LIST OF FIGURES

LIST OF TABLES

General introduction

The environmental awareness in society has increased significantly over the last years and both climate and energy issues have become very important and engaging political topics. The major questions that are being discussed deal with how we can reduce the emission of greenhouse gases into the atmosphere and, in the long run, how we can reduce our dependence on fossil fuels which are the most widely used energy source today [1]. The fact that the fossil fuel supplies are depleting while the future energy demands are steadily increasing makes the research and development of clean energy systems that involve renewable energy more important and of bigger interest than ever before [2].

Today, many scientists and engineers, companies, governmental and non-governmental agencies and even finance institutions are convinced that hydrogen's physical and chemical advantages will make it an important synthetic fuel in the future.

Hydrogen is a clean energy carrier. It can be obtained in a sustainable way by means of electrolysis of water, with electricity produced from sources like sunlight, wind or hydraulic power. Hydrogen can be stored and then used in a stationary or mobile application. In the latter case it can be utilized in combination with an internal combustion engine or a fuel cell.

Hydrogen storage is the main issue that needs to be solved before the technology can be implemented into key areas such as transport. However, neither storage of hydrogen as a compressed gas nor as a cryogenic liquid appears suitable and economical for most types of potential applications. In this respect hydrogen storage in the form of a metal hydride is a promising alternative with many attractive features [3, 4]. Over the past few decades, a major challenge which still persists is to identify optimal candidates for such hydrogen storage among intermetallic compounds. Rare-earth (R) alloys seem promising, owing to a high hydrogen capacity per volume unit and an ability to absorb hydrogen under moderate conditions of temperature and pressure [5], where the interstitial hydrogen atoms strongly modify the electronic structure and add interesting features [6]. The hydrogen absorption properties of these alloys are very much dependent on the constituents, and metal-hydrogen bonding interactions play a major role in the stability of the hydrides.

The name *rare earth* has its origins in the history of the discovery of these elements. They are never found as free metals in the Earth's crust and pure minerals of individual rare earths do not exist. They are found as oxides which have proved to be particularly difficult to separate from each other, especially to 18th and 19th century chemists. The early Greeks defined *earths* as materials that could not be changed further by sources of heat, and these oxides seemed to fit that definition. The *rare* part of their name refers to the difficulty in obtaining the pure elements, and not to their relative abundance in the Earth's crust; all of the rare–earth elements are actually more abundant than silver, and some are more abundant than lead. This also explains why the names of some of the rare–earth elements sound similar to each other — what was originally thought to be the earth of a single element was often found subsequently to be a mixture of two or more earths, requiring the hasty invention of more names derived from the original.

In the case of rare-earth hydrides, many research studies, both experimental and theoretical, have been performed to investigate their interesting physical and chemical properties [6, 7]. General reviews of the properties of hydrogenated rare-earths have been recently given by Vajda [8, 9] and Schöllhammer et al. [10].

Rare earth dihydrides keep the fluorite CaF_2-type structure, where the hydrogen atoms occupy only the tetrahedral (T) sites [11] to give the pure (stoichiometric) dihydride RH_2. By adding more hydrogen to the compound, octahedral (O) interstitial sites accommodate additional x-hydrogen to give the superstoichiometric dihydride RH_{2+x}.

In rare earth superstoichiometric dihydride systems RH_{2+x}, it may be observed that the repulsion between the x octahedral hydrogen (H_{oct}) atoms may lead to their eventual ordering. For low enough temperatures and high enough concentrations of excess hydrogen ($x \geq 0.10$), the order appeared to be long range, whereas the arrangement appeared to be short range ordered at small x values ($x < 0.10$) [12]. The lattice parameters of GdH_{2+x} have been determined by X-ray diffraction (XRD) by Chiheb et al. [13] together with TbH_{2+x}, DyH_{2+x} and YH_{2+x} materials, but without suggesting any type of structure. They observed that the unit cell parameter of GdH_{2+x} decreases with increasing hydrogen content, a behavior similar to the one observed for LaH_{2+x}, NdH_{2+x}, CeH_{2+x} and PrH_{2+x} [14–16].

The selection of proper alloy compositions has to this point been somewhat speculative in nature based upon empirical experimentation. With the use of computational methods, material properties can be evaluated and optimized before the material is processed allowing an optimized structure to be realized quickly. This saves enormous time and efforts compared to experimentally assessing properties due to multiple changes in composition and structure.

The theory of electrons has been a great challenge to physicists since the discovery of the electron in 1896 by Lorentz and Zeeman and also by Thomson in 1897. There was no big progress until the establishment of quantum mechanics in the 1920s. In the 1930s, band theory for independent electrons was gradually elaborated, leading to the classification of materials into insulators, semiconductors, and metals, according to the number of electrons and filling of bands. Furthermore, in the 1930s, several methods were proposed which are still in use today, including the Hartree-Fock method, the augmented plane wave (APW) method (further developed in the 1950s), the orthogonalized plane wave (OPW) method, and the effective potential method (a forerunner of the pseudopotential method). Band structure calculations for high-symmetry simple metals (e.g. Na and Cu) and ionic solids (e.g. NaCl) were done in the 1930s and 1940s. Accurate band calculations for more difficult materials such as semiconductors were done in the early 1950s. Rapid developments in electronic structure calculations were made after the rise of density functional theory (DFT) in the 1960s, based on the Hohenberg-Kohn theorem which states that all properties of these many-body systems are completely determined by the ground state electronic charge density. Electronic structure calculations based on DFT were very limited owing to the unavailability of powerful computers from the 1960s to the early 1980s. The basic idea for DFT is that you do not need to know the motion of every interacting particle in a system, but only the density of valence electrons as a function of position is needed [17]. This theory is convenient because it is much simpler than solving the whole many body Hamiltonian, leading thus to much shorter computational times. With the rapid advancement in computer technology, especially after the new millennium, a single personal computer is able to carry out such calculations for small and medium systems (typically less than 100 atoms in one unit cell). In 2001, Shimojo *et al* [18] were able to study a system of 110,592 atoms using DFT. Other applications included the study of sizeable biological molecules such as DNA [19] or the study of carbon nano-tubes [20]. Hence, due to the merit of Pierre C. Hohenberg, Walter Kohn, Lu Jeu Sham and many others, we nowadays have a very successful way to tackle this many-body problem in most cases.

Other methods for electronic structure calculations include quantum Monte Carlo, the GW method, as well as some generalizations of DFT known as density functional perturbation theory (DFPT), time-dependent density functional theory (TD-DFT) which is an extension of DFT to treat time-dependent problems and excited states [21], etc. The field of electronic structure calculations is rapidly maturing in basic theory, new algorithms, computational methods and computational power.

Modern DFT calculations for solids are determined by several technical choices: (i) The choice of a basis set to expand the Kohn-Sham eigenfunctions which is essentially between plane waves and localized basis functions. (ii) The interactions between the ionic core and the valence electrons can be described either by a full-potential approach or by a pseudopotential. (iii) The method adopted for the determination of the eigenstates of the Kohn-Sham Hamiltonian. (iv) The description of the electron-electron interactions by choosing an appropriate exchange-correlation functional within the hierarchy of functionals proposed within DFT [22]. In those cases where DFT alone does not provide an adequate solution (strong electronic correlations, excited eigenstates, ...), post-DFT corrections such as many-body perturbation theory [23, 24] or dynamical mean field theory [25, 26] may be used to ameliorate the DFT predictions.

DFT does not solve all problems. Examples are strongly correlated materials (*d*- and *f*-electron systems with narrow bands), excited states in semiconductors and insulators, and dispersion forces in rare-gas solids or molecular crystals.

In DFT, the orbital-dependence of the exchange correlation energy is rather weak. In many cases, this is appropriate, but in systems with narrow *d*- or *f*-bands and localized orbitals, DFT fails to account for the strong Coulomb repulsion between electrons occupying these narrow bands, which lead to an enhanced exchange splitting between occupied and empty eigenstates. The DFT+U method attempts to cure this shortcoming by adding a Hubbard-type Coulomb repulsion to the DFT Hamiltonian.

The DFT+U method is a semi-empirical approach, because the Hubbard parameter *U* is an adjustable parameter. However, is has been shown that if the Hubbard correction is applied to spin-polarized GGA calculations, good agreement for lattice parameters, magnetic moments, band gap and exchange splittings can be achieved with a single value of *U*. If, as often reported in the literature, the DFT+U is applied on the basis of non-spin polarized LDA or GGA results, a much larger value of *U* is required to reproduce the experimentally observed exchange splitting, spoiling the agreement for the lattice parameters and other volume-dependent quantities. To some extent, the DFT+U approach has been superseded by hybrid-functional calculations - however, it has still the advantage of a much lower computational effort.

WIEN2k is one of the fastest and reliable simulation codes among all computational schemes. All the computational work presented on our lanthanide intermetallic compounds has been performed by using this code which embeds the framework of density functional theory.

This thesis is organized as follows.

In Chapter I we give a brief description of the key concepts of hydrogen storage, pure rare earths (in bulk) and their hydrides.

In Chapter II, we review the many-body problem of electrons and discuss density functional theory (DFT) with different approximations for the exchange correlation energy; we also review the WIEN2k code.

Ab initio calculations of the properties of molecules and solids have become a common tool of solid state physics and quantum chemistry. Nevertheless open problems remain, the description of the 4*f* states of rare-earth (*R*) elements being one of them. The 4*f*-states were sometimes treated as valence states [27-29] and at other times as core states [27, 30, and 31]. For that, Chapter III is divided in two sections: in the first one, spin polarization is not taken into account and *4f*-states are treated as core electrons; we used LDA and GGA parameterizations of the exchange-correlation functional to calculate the structural and electronic properties of the bulk rare earth R (R = Gd and Tb). In the second section, *4f*-states are treated as valence electrons with spin polarization, a problem solved by means of LSDA and GGA; in addition, local Coulomb repulsions U are treated statically as in the LSDA+U and GGA+U approaches to obtain structural, electronic and magnetic properties of the bulk rare earths R (R = Gd and Tb) .

Chapter IV contains the results of calculations of the equilibrium, electronic and thermodynamic properties of the rare earth dihydrides RH_2 (R = Gd and Tb) computed using the WIEN2k program in both GGA and LDA approximations without taking the spin-polarization into consideration, and with *4f*-states treated as core electrons.

The lattice structure of the terbium–deuterium system was investigated by André et al. [32] and Huang et al. [33] by neutron diffraction spectroscopy. These studies reported that the stoichiometric $TbD_{2.25}$ orders in a DO_{22} configuration (Ni_3Mo-type), where one (*042*) plane is totally occupied by octahedral D-atoms followed by three empty planes. In Chapter V, a first-principles study was carried out to investigate the structural and electronic properties of $LaH_{2.25}$ and $GdH_{2.25}$ in the same tetragonal unit cell with GGA and LDA approximation without spin polarization and with *4f*-states treated as core electrons.

In 1998, Ellner *et al.* [34] determined the unit cell parameters of superstoichiometric gadolinium dihydride $GdH_{2.25}$ by powder diffraction assuming a CaF_2 structure. The same structure was used by Ao et al. (2012) to study the CeH_x superstoichiometric dihydrides (x=2, 2.25, 2.5, 2.75, 1) [35] and by Ao et al. [36] to study the PuH_x superstoichiometric dihydrides (x=2, 2.25, 2.5, 2.75, 1). There are very few simulation works reported for GdH_x (x=1, 2, 3), the last of which was done by Sudha Priyanga *et al.* [37] who investigated the structural, electronic, elastic and magnetic properties of the gadolinium hydride system. In the same year (2015), the same authors studied the structural, electronic, elastic and magnetic properties of the cerium and praseodymium hydrogen systems RH_x (R = Ce, Pr with x = 2, 3) by using first principles calculations [38]. Therefore, in the first section of Chapter VI, we present complete results of a detailed electronic structure calculation of the superstoichiometric $GdH_{2.25}$ without investigating the magnetic properties (with *4f*-states treated as core electrons), which is based on *ab initio* calculations at 0 K within density functional theory (DFT), using a full-potential linear augmented plane-wave (FP-LAPW) method as implemented in the WIEN2k code. In the second section of this Chapter VI, we investigate the electronic structure and the equilibrium properties of one of the less studied superstoichiometric $TbH_{2.25}$. Applying two calculation methods of the density functional theory i.e. the general gradient approximation (GGA) and the local density approximation (LDA) without spin-polarization, with *4f*-states treated as core electrons, we investigate the relaxed and the unrelaxed states. Finally we present a summary of this thesis and an outlook.

References

[1] International Energy Agency (IEA). *Key World Energy Statistics*. 2009.

[2] European Commission, Directorate-General for Research. *Hydrogen Energy and Fuel Cells: A Vision of Our Future*. 2003.

[3] F. Schüth, B. Bogdanovic and M. Felderhoff. *Chem. Commun.* **20**, 2249 (2004).

[4] M. H. Mintz; Z. Gavra; G. Kimmel and Z. Hadari. *J. Less-Common Met.* **74**, 263 (1980).

[5] M. Gupta and J. P. Burger, *Phys. Rev. B* **22**, 6074 (1980).

[6] Y. Fukai. *The Metal—Hydrogen System*. 1993.

[7] J. M. Marchetti, H. L. Corso, J. L. Gervasoni. *Int. J. Hydrogen Energy*. **30**, 627 (2005).

[8] P. Vajda. *Hydrogen in Rare Earth Metals*. 1995.

[9] P. Vajda. *Rare Earth (and Actinide) Dihydrides: Structural, Electronic and Magnetic Properties*. 2013.

[10] G. Schöllhammer, F. Karsai, and P. Herzig. *Fluorite-Type Rare Earth Hydrides Studied from First Principles*. 2013.

[11] P. Vajda. *Phys B.* **289–290**, 435 (2000).

[12] T. J. Udovic, J. J. Rush, and I. S. Anderson. *J. Alloys Compd.* **231**, 138 (1995).

[13] M. Chiheb, J. N. Daou, P. Vajda. *Z. Phys. Chem.* **179**, 255 (1993).

[14] C. E. Holley, R. N. R. Mulford, F. H. Ellinger, W. C. Koehler, W. H. Zachariasen. *J. Phys. Chem.* **59**, 1226 (1955).

[15] H. Müller, P. Knappe, O. Greis. *Z. Phys. Chem. Neue Folge*. **114**, 45 (1979).

[16] P. Knappe, H. Müller. *Z. Anorg. Allg. Chem.* **487**, 63 (1982).

[17] P. Hohenberg and W. Kohn. *Phys. Rev.* **136**, 864 (1964).

[18] F. Shimojo, R. K. Kalia, A. Nakano, and P. Vashishta. *Comput. Phys. Commun.* **140**, 303 (2001).

[19] M. Elstner, P. Hobza, T. Fraueheim, S. Suhai, and E. Kaxiras. *J. Chem. Phys.* **114**, 5149 (2001).

[20] J. Zhao, A. Buldum, J. Han, and J. P. Lu. *Nanotechnology* **13**, 195 (2002).

[21] M. A. Marques and E. K. U. Gross. *Time-dependent density functional theory*. 2003.

[22] J. P. Perdew and K. Schmidt. *In Density Functional Theory and its Applications to Materials*. 2001.

[23] L. Hedin and S. Lundqvist. *In Solid State Physics*. 1969.

[24] M. S. Hybertsen, S. G. Louie. *Phys. Rev. B* **34**, 5390 (1986).

[25] A. George, G.Kotliar, W. Krauth, M. J. Rozenberg. *Rev. Mod. Phys.* **68**, 13 (1996).

[26] K.Held, O. K.Andersen, M. Feldbacher, A. Yamasaki, Y. F. Yang. *J. Phys. Condens. Matter* **7**, 064203 (2008).

[27] L. Peters, I. Di Marco, P. Thunström, M. I. Katsnelson, A. Kirilyuk, and O. Eriksson. *Phys. Rev. B* **89**, 205109 (2014).

[28] M. Dolg, H. Stoll, H. Preuss. *J. Chem. Phys.* **90**, 173 (1989).

[29] X. Cao, M. Dolg. *J. Chem. Phys.* **115**, 7348 (2001).

[30] M. Dolg, H. Stoll, A. Savin, H. Preuss. Theor. *Chim. Acta.* **75**,173 (1989).

[31] M. Hülsen, A. Weigand, M. Dolg. *Theor. Chem. Acc.* **122**, 23 (2009).

[32] G. André, O. Blaschko, W. Schwarz, J. N. Daou, and P. Vajda. *Phys Rev B*. **46**, 8644 (1992).

[33] Q. Huang, T. J. Udovic, J. J. Rush, and J. Schefer. *J. Alloys Compd.* **231**, 95 (1995).

[34] M. Ellner, H. Reule, E. J. Mittemeijer. *J. Alloys Compd.* **279**, 179 (1998).

[35] B. Y. Ao, X. L. Wang, P. Shi, P. H. Chen, X. Q. Ye, X. C. Lai, J. J. Ai and T. Gao. *Int. J. Hydrogen Energy* **33**, 5108 (2012).

[36] B. Y. Ao, P. Shi, Y. Guo, T. Gao. *Chin. Phys. B* **3**, 037103 (2013).

[37] P. G. Sudha, R. Rajeswarapalanichamy, and K. Iyakutti. *Int. J. Hydrogen Energy* **31**, 415 (2015).

[38] P. G. Sudha, R. Rajeswarapalanichamy, and K. Iyakutti. *J. Rare Earths* **30**, 289 (2015).

CHAPTER I

Hydrides and metallic hydrides

*Energy can be stored in different forms: as mechanical energy (for example, potential energy or rotation energy of a flywheel), as electric or magnetic energy (capacitors and coils, respectively), as chemical energy of reactants and fuels (batteries, petrol or hydrogen), or as nuclear fuel (uranium or deuterium) (**Fig. I-1**).*

Hydrogen is expected to play an important role in a future energy economy based on environmentally clean sources and carriers. As a fuel of choice it is light weight, contains a high energy density and its combustion emits no harmful chemical by-products. Moreover, hydrogen is considered as a green energy, because it can be generated from renewable sources and is non-polluting [1-3]. Since the 1970s, hydrogen has been considered as a possible energy carrier for the storage of renewable energy. Hydrogen storage is one of the key technologies that should be developed to utilize hydrogen as a clean energy source. There are at least fifty metallic elements in the periodic table that can store hydrogen.

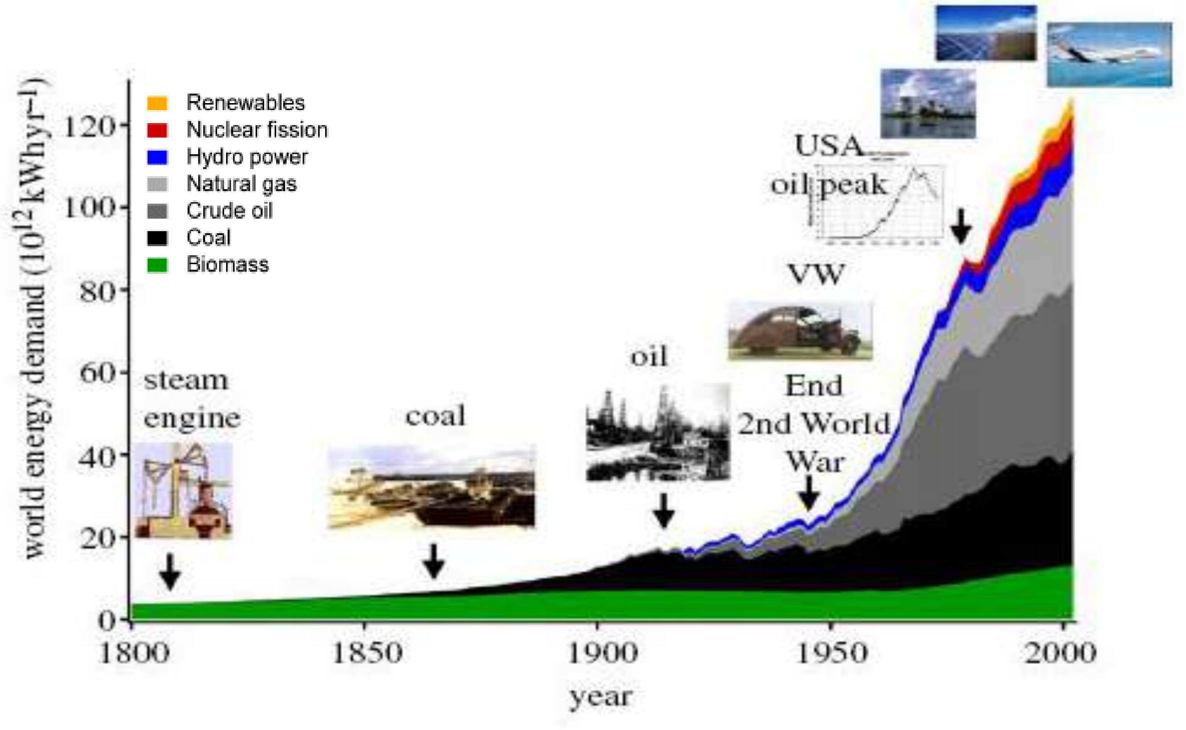

Fig. I-1 Energy demand according to the energy carriers over the last 200 years [4].

I-I <u>Hydrogen</u>

The hydrogen atom is most attractive because its electron (for charge neutrality) is accompanied by only one proton. Hydrogen thus has the best ratio of valence electrons to protons (and neutrons) of all the periodic table, and the energy gain per electron is very high.

Hydrogen is not an energy “source”, that is to say, it is not a primary energy (like natural gas or crude oil), existing freely in nature. It is an energy carrier—a secondary form of energy that has to be manufactured (like electricity, which doesn’t exist freely in usable form either). Hydrogen can be generated from many primary sources—an advantage in itself, since it reduces the chances of creating a hydrogen cartel [5].

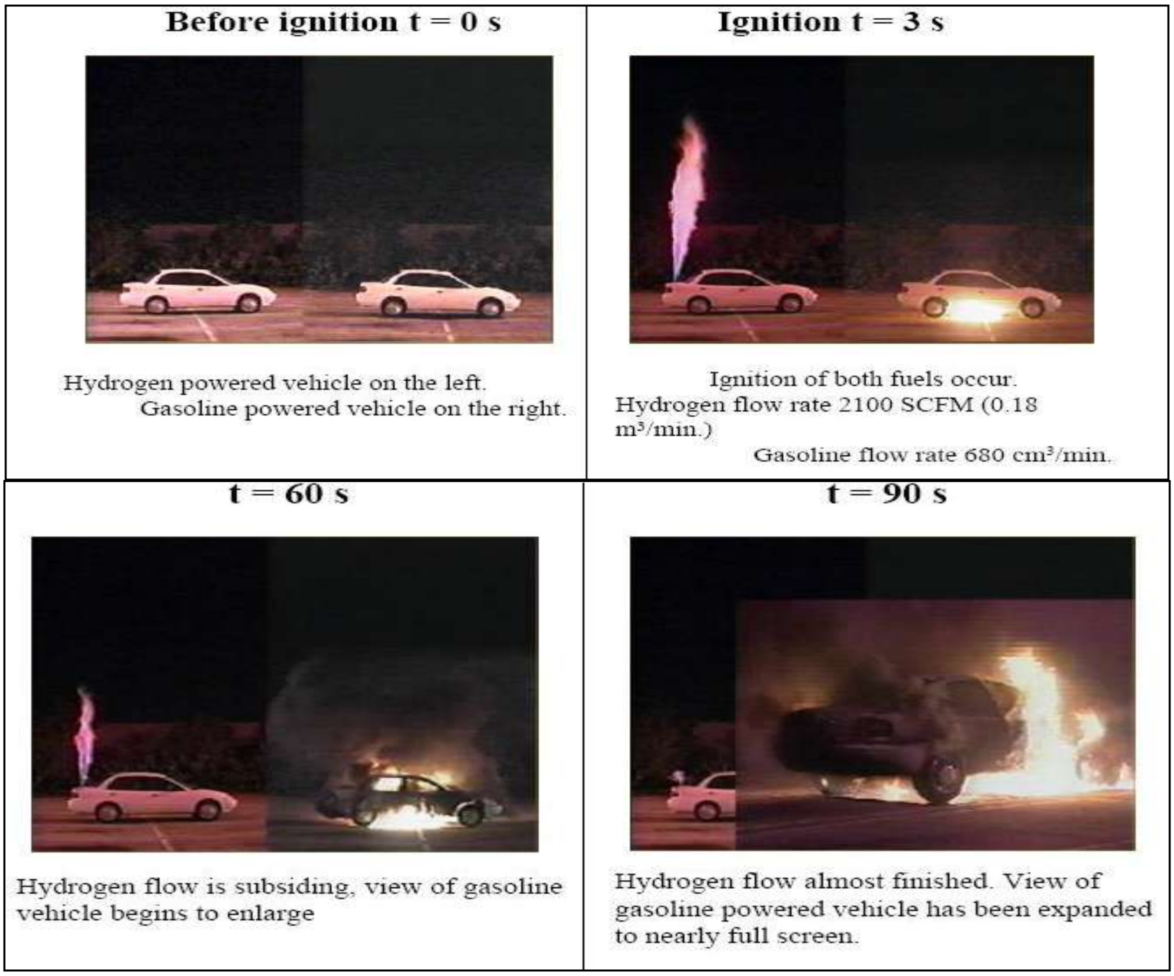

Before ignition t = 0 s

Hydrogen powered vehicle on the left.
Gasoline powered vehicle on the right.

Ignition t = 3 s

Ignition of both fuels occur.
Hydrogen flow rate 2100 SCFM (0.18 m^3/min.)
Gasoline flow rate 680 cm^3/min.

t = 60 s

Hydrogen flow is subsiding, view of gasoline vehicle begins to enlarge

t = 90 s

Hydrogen flow almost finished. View of gasoline powered vehicle has been expanded to nearly full screen.

Fig. I-2 Fuel leak simulation [6].

I-I-1 Hydrogen safety

- Hydrogen is a much safer fuel than is generally believed. It can be used as safely as other gaseous and liquid fuels [7].

- In case of an accident, hydrogen has several very advantageous properties in comparison to conventional fuels. Hydrogen disperses very quickly into the surrounding atmosphere, whereas liquid fuels spread on level surfaces and burn much longer. In addition, hydrogen is non-toxic, hence wrecking of a hydrogen tanker does not cause an environmental catastrophe.
- Although hydrogen is very flammable, quick dispersion makes it very rare for hydrogen to reach combustible concentration outdoors or in well-ventilated indoor spaces (**Fig. I-2**).
- A common misconception is that hydrogen caused the *Hindenburg* disaster. In reality, the *Hindenburg* catastrophe shows that the air ship caught fire because of a highly flammable skin material and not because of the hydrogen gas it contained.

I-I-2 Hydrogen production

Hydrogen is the most abundant element on Earth, but less than 1% is present as molecular hydrogen gas H_2. The overwhelming majority is chemically bound as H_2O in water and some is bound to liquid or gaseous hydrocarbons.

Once produced, hydrogen is a clean synthetic fuel: when burnt with oxygen, the only exhaust gas is water vapor. Whether hydrogen can be considered a clean form of energy on a global scale depends on the primary energy that is used to split water [8].

The clean way to produce hydrogen from water is to use sunlight in combination with photovoltaic cells and water electrolysis.

Other forms of primary energy and other water-splitting processes are also used: the hydrogen consumed today as a chemical raw material (about 5×10^{10} kg per year worldwide) is to a large extent produced using fossil fuels by means of the reaction of hydrocarbon chains ($–CH_2–$) with H_2O at high temperatures, producing H_2 and CO_2. Direct thermal dissociation of H_2O requires temperatures higher than 2000°C (> 900°C with a Pt/Ru catalyst). The chemical energy per mass of hydrogen (142 M J kg^{-1}) is at least three times larger than that of other chemical fuels, for example, the equivalent value for liquid hydrocarbons is 47 M J kg^{-1} [2].

I-I-3 Hydrogen storage

Presently hydrogen can be stored in three forms; gaseous, liquid or as a solid combined with a metal hydride. The most suitable storage method is dependent upon safety aspects, environmental issues, economic criteria and the end-use of hydrogen. These storage methods will be briefly described here.

I-I-3-1 Gaseous storage

The most commonly used and simplest method is to store hydrogen in its natural form as a gas. Storage of gaseous hydrogen is primarily limited by volume considerations as a result of hydrogen's low density, as even at high-pressure, very large volumes are required resulting in high material costs. Today gaseous hydrogen is stored predominantly in steel cylinders at a pressure of 150-200 bar and at an ambient temperature of approximately 25°C [9]. Significant amounts of hydrogen can also be stored within high-pressure storage tanks that can be situated above ground or underground which is similar to the storage of natural gas. The construction material properties in above ground storage impose limitations on the quantity of gaseous hydrogen that can be stored and storage can be accomplished at an increased pressure in an underground pressure tank or underwater tank.

Gaseous hydrogen can be stored in high-pressure, low-weight carbon-fibre composite tanks operating at pressures of between 350 and 700 bar [10]. The advantage of the carbon-fibre composite tank is its low weight. The cost of high-pressure compressed gas tanks is essentially dictated by the cost of the carbon fibers used for lightweight structural reinforcement. Efforts are under way to identify lower-cost carbon fibers that can meet the required high pressure and safety specifications for these tanks. However, lower-cost carbon fibers must still be capable of meeting tank thickness constraints in order to satisfy volumetric capacity targets. Thus, lowering costs without compromising weight and volume is a key challenge. Advances in compression technologies are also required to improve efficiencies and reduce the cost of producing high-pressure gas hydrogen [11]. In general, the carbon fiber cost represents 40-80% of the total tank cost, depending on whether low or high-performance fibers are used.

I-I-3-2 Liquid storage

Liquid hydrogen tanks can store more hydrogen in a given volume than compressed gas tanks. The density of liquid hydrogen is 0.070 kg/l, compared to 0.030 kg/l for 690 bar (10^4 psi) gas tanks [12]. Hydrogen stored in a liquid form is substantially more compressed than in gaseous form and superficially it appears an appealing means of energy storage but there are various contributory negative factors. Primarily, the liquefaction requires a large expenditure of energy (from 25% to 45% of the stored energy is required to liquefy the H_2) and secondly, through the use of insulation, liquid hydrogen must be continually kept at a low temperature of 20 K (-253°C) [13]. There are risks associated with this constant low temperature, due to the high expansion ratio of liquid hydrogen to gaseous hydrogen. If there was a warming of liquid hydrogen extremely high pressures could accumulate and result in damage or an explosion. Therefore Hydrogen boil-off must be minimized or eliminated because of cost, efficiency, range considerations, and safety when vehicles are parked in confined spaces.

Liquid hydrogen must be stored in cryogenic tanks, which is a well-established technique. There are three ways that heat transfer occurs from the external air to the liquid hydrogen: conduction, convection and radiation. Heat transfer increases with external surface area therefore the majority of cryogenic tanks are spherical or cylindrical to minimize the surface area. Most liquid hydrogen storage tanks are also double walled tanks that are insulated with an evacuated layer of Perlite insulation.

I-I-3-3 Metal hydride storage

Another means of hydrogen storage is that of metal hydride storage, this method being a relatively new method. The metal-hydrogen bond offers the advantage of a very high volumetric hydrogen density under moderate pressures [14], which is up to 60% higher than that of liquid hydrogen [15]. The process is nearly reversible and can be expressed by the following equation [16].

$$M + \frac{x}{2}H_2 \underset{\text{Desorption}}{\overset{\text{Absorption}}{\leftrightarrows}} MH_x \pm Q \qquad \text{[I-1]}$$

Where M and H represent metal and hydrogen atoms, respectively. Note that x is the non-stoichiometric coefficient and Q is the heat of formation. The sorption process is exothermic, i.e. the heat of formation is negative, when hydrogen is absorbed in and endothermic when hydrogen is desorbed from the alloy.

Metal hydrides were first discovered in 1866 by Thomas Graham [17]. The first metal hydride discovered was palladium hydride (PdH_x) [17, 18]. Although, there are at least fifty metallic elements in the periodic table that can store hydrogen as shown in **Fig. I-3** (as adopted from Ref. [19]), only a handful of them are suitable for storage at moderate temperatures and pressures. They have been established as excellent media for on-board or stationary hydrogen storage. The sole reason behind the superiority of metal hydrides as storage media over competing/existing technology is their ability to store large amounts of hydrogen at densities greater than cryogenically stored liquid hydrogen.

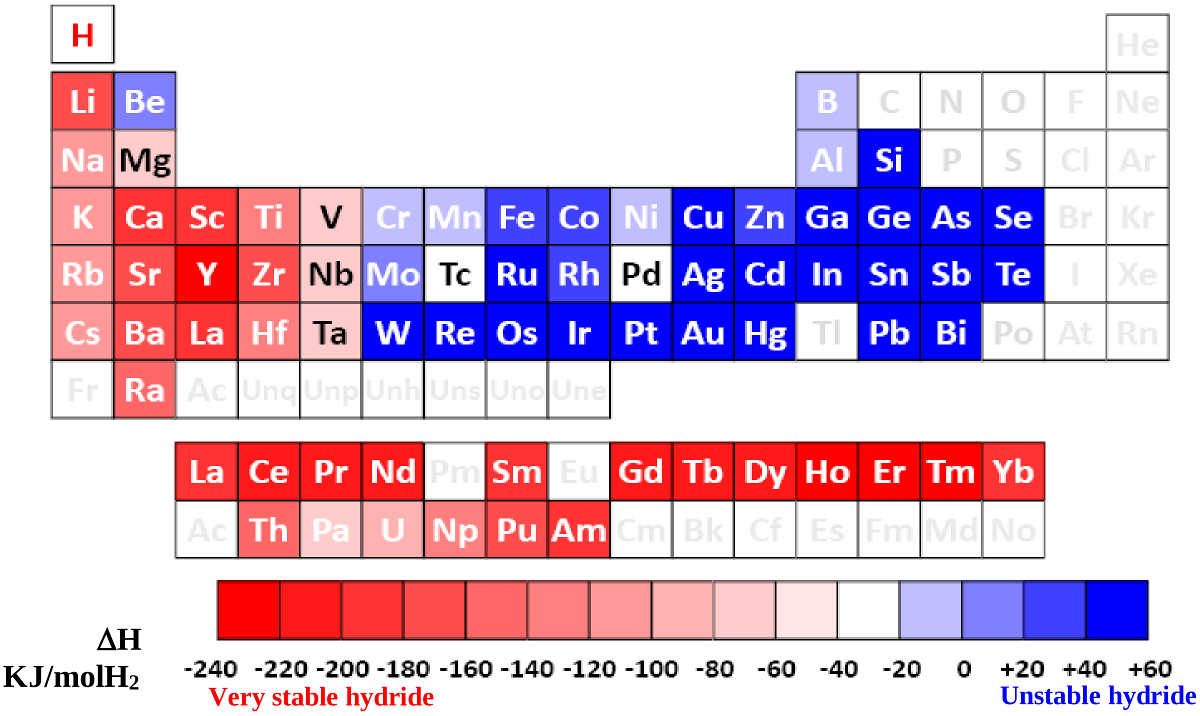

Fig. I-3 Stability of hydrides of pure elements. The higher the enthalpy of formation of the hydride, the more stable the hydride. [19].

The hydrogen absorption mechanism in metals and alloys is schematically illustrated in **Fig. I-4**. Initially molecular hydrogen is physically adsorbed onto the surface of the material by van der Waals forces, as seen on the shaded area in the figure. The metallic surface catalyzes the dissociation of hydrogen molecules which in turn diffuse into the material in an atomic state. Hydride formation is commonly described as a two step process:

(i) At low concentrations (low pressures) the hydrogen is dissolved in the crystal as a solid solution (α-phase). In this state the atoms occupy interstitial positions randomly which result in a slight expansion of the original host lattice. The expansion is locally somewhat larger over a certain volume from each hydrogen atom and makes the nearest vacant sites more favorable for other hydrogen atoms to occupy.

(ii) As the hydrogen pressure, and consequently concentration, increases the interaction between hydrogen and metal atoms becomes more important and a more ordered phase starts to grow (β-phase). The formation of β-phases generally increases the host lattice substantially and the metal atoms often undergo major rearrangements which in some cases also may lead to stabilization of new crystal structures. However, the β-phase does not necessarily appear in every hydrogen accommodating material. Its existence depends on each unique system, i.e. the combination and arrangement of its component elements [20, 21].

The two-phase region ends at a critical temperature T_C, above which the transition from α- to β-phase is continuous.

The crystal structure also plays a critical role for the absorption properties. Stability of hydrides has been correlated with crystallographic factors such as the size of the interstices in the host lattice which must be 0.4 Å or larger [22], the distance between hydrogen atoms in stable hydrides is always more than 2.1 Å and they preferentially occupy the interstitial sites closest to the hydride forming element [23]. The nature of the chemical bond in these compounds is not very clear, but seems to be a crossover between metallic and ionic bonding. These compounds resemble their respective metals, since they exhibit high electronic (metallic) conductivity and usually have a dull metallic appearance. That is why they are commonly referred to as metallic hydrides.

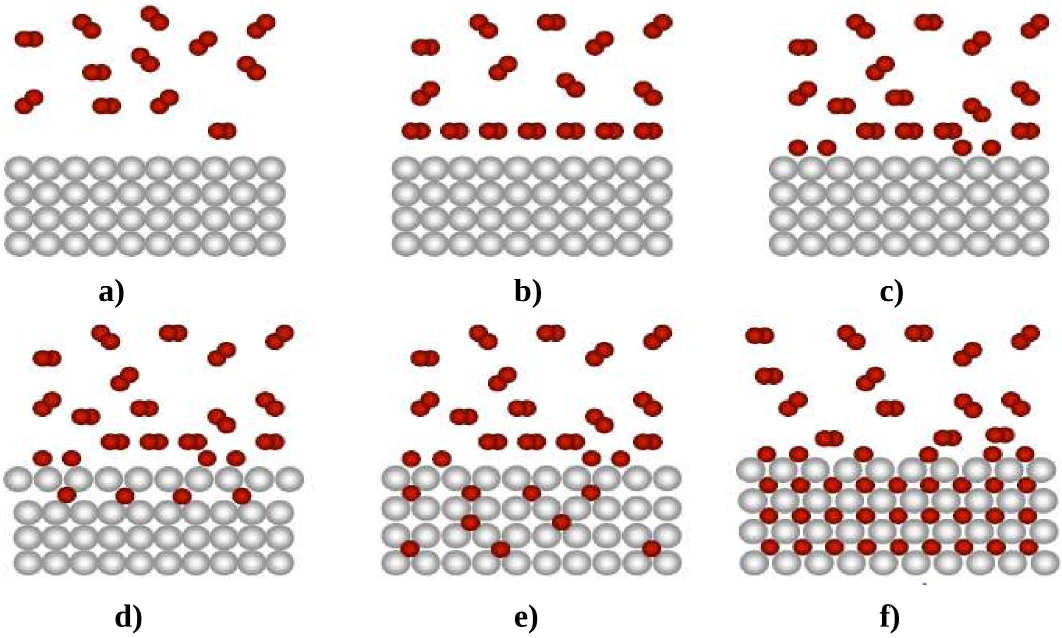

Fig. I-4 Reaction of a H_2 molecule with a storage material: **a**) H_2 molecule approaching the metal surface (hydrogen and metal). **b**) Interaction of the H_2 molecule by Van der Waals forces (Physisorption). **c**) Chemisorbed hydrogen after dissociation (Chemisorption). **d**) Occupation of subsurface sites and diffusion into bulk lattice sites. **e**) Solid solution (α -phase). **f**) Hydride (β -phase).

With the transition metals, the rare earths (lanthanides) and the actinides hydrogen can form stable compounds as well (see **Fig. I-3**). Many of these compounds, (MH_n), show large deviations from ideal stoichiometry (n = 1, 2, 3) and can exist as multiphase systems. The lattice structure is that of a typical metal with hydrogen atoms on the interstitial sites, and for this reason they are also called interstitial hydrides. This type of structure is limited to the compositions MH, MH_2, and MH_3, with the hydrogen atoms fitting into octahedral or tetrahedral holes in the metal lattice, or a combination of the two. Hydrogen is located in the form of atoms, never molecules, on interstitial sites of the host metal lattice. The lattice expands during hydrogen sorption [24], often losing some of its high symmetry [2].

The applications of metal hydrides can be broadly classified into seven distinct categories, which are: 1) thermal systems, 2) energy systems, 3) actuation and sensing, 4) processing, 5) semiconductors, 6) biomimetic and biomedical systems, and 7) nuclear applications in addition to hydrogen storage [25].

I-II The rare-earth hydrides

The rare-earth hydrides have received tremendous attention due to their potential application for hydrogen storage technology [26, 27], where they have an ability to absorb and store hydrogen under moderate conditions of temperature and pressure [28].

The study of hydrided pure rare earths constitutes the fundamental tool in order to understand the basics of the hydriding process, and a good starting point to extrapolate results to alloys.

I-II-1 General characteristics of the rare-earth elements

The rare earth elements (REs) represent a group of 17 chemical elements formed by 15 lanthanides (La-Lu), yttrium (Y), and scandium (Sc). All these elements have similar physical and chemical properties, providing superb characteristics for a variety of modern applications, from batteries in hybrid cars and phosphors for illuminated screens on electronic devices to permanent magnets used in computer hard drives and wind turbines.

Depending on the application, they are used independently or as a mixture, or as an addition to other chemical compounds and/or metal alloys. Sometimes these elements are referred to as ‘vitamins’ because of their exclusive properties and the fact that only minor quantities are needed to boost the performance of the final products. Despite the name ‘rare earth’, these elements are not particularly rare in their total crustal abundance, which exceeds such widely used elements as copper, zinc, nickel, and lead [29]. However, REs are scarce as a mineable resource. The limited availability of rare earth ores reflects a number of factors including the geological controls that affect not only their distribution but underlie technical mining and processing constraints.

These elements are split into two subgroups, the light rare earth elements (LREs) from lanthanum to europium and the heavy rare earth elements (HREs), which include the rest of lanthanide elements along with yttrium. Two elements are excluded from LRE/HRE classification: scandium, due to its unique properties and different occurrence (much smaller ionic radius) [30], and light lanthanide Promethium (Pm), due to its radioactivity.

Rare earth elements are comparatively more abundant in the earth's crust than other commonly exploited elements but not in sufficient concentrations to make them easily exploitable.

I-II-1-1 Discovery and early history

Rare earth elements became known to the world with the discovery of the black mineral "Ytterbite" (renamed to Gadolinite in 1800) by Lieutenant Carl Axel Arrhenius in 1787, at a quarry in the village of Ytterby, Sweden [31]. All the naturally occurring rare earths and all but one of all the rare earth elements had been discovered by the turn of the century and the discovery of the remaining one rare earth had to wait until the discovery of nuclear reactions. Rare earths are always found in varieties of minerals viz. silicates, halides, carbonates, phosphates, etc. but never found as pure metals [32, 33].

I-II-1-2 Production

In the 1950s, South Africa, India, and Brazil had rare earth mines in operation. Further, from the 1960s to the 1980s, Mountain Pass in California became the largest global producer for the same up to 2002 when it closed. Thereafter, China began large scale production and exported rare earths at a cheaper rate (**Fig. I-5**).

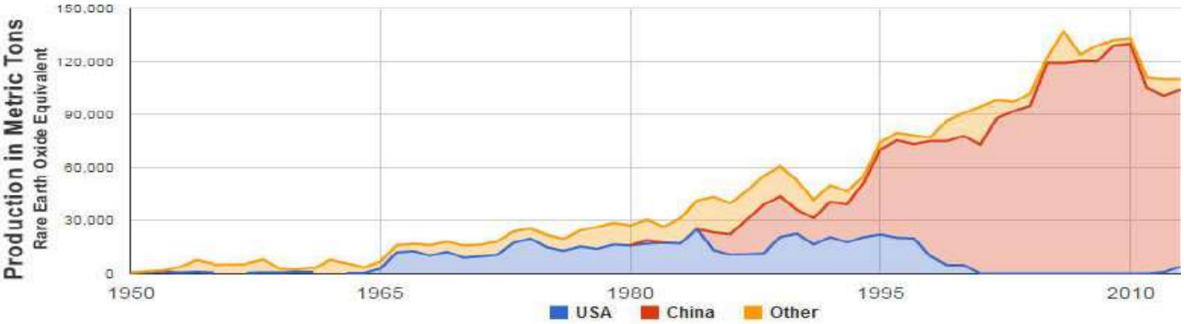

Fig. I-5 This chart shows a history of rare earth element production, in metric tons (1 ton = 10^3 kg) of rare earth oxide equivalent, between 1950 and 2013 [34].

Currently, it is the worldwide producer of rare earth elements producing ~97% of the total world supply. But their incessantly increasing needs has compelled the Chinese government to drastically limit the export of rare earths to 35 × 10^6 kg (35,000 tons) while the yearly demand of other countries is estimated to have reached 80,000 tons in 2015, thus, threatening with a rare earth supply shortage [32, 35].

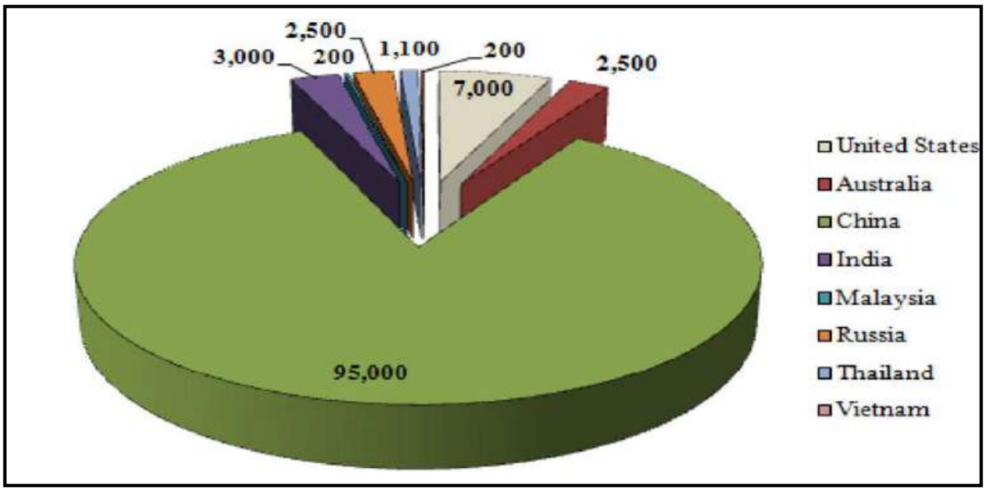

Fig. I-6 Global mine production of rare earth metals in different countries [36].

According to the U.S. Mineral Commodity Summaries of 2015 [36], the global mine production of rare earth metals (**Fig. I-6**) is 110×10^6 kg (110,000 metric tons) while the total reserves are estimated at 130×10^9 kg (130,000,000 metric tons). This restriction of supply is being met by the development of many new mining projects or reopening of old mines. Worldwide exploration for economically exploitable rare earth deposits as well as development of indigenous resources and technologies to meet the future requirements for rare earth metals is being encouraged.

I-II-1-3 Electronic configurations

Spanning the lanthanide series, their *4f* shell is gradually filled. The electronic configuration of an isolated rare earth atom is usually [Xe] $6s^2$ $5d^0$ $4f^n$, where n depends on the atomic number. There are a few exceptions to this, namely Lanthanum, Gadolinium and Lutetium, who have one 5*d* electron and therefore one 4*f* electron less than expected [37]. For isolated atoms, the energy levels are truly discrete and filling the 4*f* shell is straightforward. However, when the atoms form a crystal, the orbitals start to hybridize with other orbitals, and the energy levels broaden into bands. For the crystalline phase of the lanthanides, one cannot any longer speak of the *6s* energy level, instead the 6*s*, 6*p* and 5*d* orbitals hybridize and the energy levels broaden to form the [6*s* 6*p* 5*d*]-band. The 4*f* energy levels and this [*spd*]-band overlap and the consequence is that, for most lanthanides, one of the 4*f* electrons of the isolated atom, gets promoted to the [*spd*]-band in the crystalline phase. The reason for this is that the Coulomb energy to pay for adding an *f* electron is much higher than the kinetic energy to pay for adding a delocalized [*spd*] electron. The outer electronic configuration of the lanthanides in the crystalline phase is therefore approximately $[6s6p5d]^{3} f^{n-1}$, where (n−1) denotes that there is one 4*f* electron less than in the bare atom. Moreover, to these electronic configurations there are a few exceptions. Europium and Ytterbium have only *2* instead of *3* electrons in the [*spd*]-band, since in that way they have an *f*-shell which is empty, half-filled or full.

Table I-1 Structural and electronic properties of the rare earths [39].

Element		*A*	*Electronic configuration*		*Crystal structure*	*Lattice parameters*		
			Atomic	*Solid*		*a (Å)*	*c (Å)*	*c/a*
Scandium	Sc	45	$3d^1 4s^2$		hcp	3.309	5.268	1.592
Yttrium	Y	89	$4d^1 5s^2$		hcp	3.648	5.732	1.571
Lanthanum	La	139	$5d^1 6s^2$	$[spd]^3$	dhcp	3.774	12.171	3.225
Cerium	Ce	140	$4f^2 5d^0 6s^2$	$4f^1[spd]^3$	fcc	5.161	-	-
Praseodymium	Pr	141	$4f^3 5d^0 6s^2$	$4f^2[spd]^3$	dhcp	3.672	11.833	3.222
Neodymium	Nd	144	$4f^4 5d^0 6s^2$	$4f^3[spd]^3$	dhcp	3.658	11.797	3.225
Promethium	Pm	145	$4f^5 5d^0 6s^2$	$4f^4[spd]^3$	dhcp	3.65	11.65	3.19
Samarium	Sm	150	$4f^6 5d^0 6s^2$	$4f^5[spd]^3$	rhom	3.629	26.207	7.222
Europium	Eu	152	$4f^7 5d^0 6s^2$	$4f^7[spd]^2$	bcc	4.583	-	-
Gadolinium	Gd	157	$4f^7 5d^1 6s^2$	$4f^7[spd]^3$	hcp	3.634	5.781	1.591
Terbium	Tb	159	$4f^9 5d^0 6s^2$	$4f^8[spd]^3$	hcp	3.606	5.697	1.580
Dysprosium	Dy	163	$4f^{10} 5d^0 6s^2$	$4f^9[spd]^3$	hcp	3.592	5.650	1.573
Holmium	Ho	165	$4f^{11} 5d^0 6s^2$	$4f^{10}[spd]^3$	hcp	3.578	5.618	1.570
Erbium	Er	167	$4f^{12} 5d^0 6s^2$	$4f^{11}[spd]^3$	hcp	3.559	5.585	1.569
Thulium	Tm	169	$4f^{13} 5d^0 6s^2$	$4f^{12}[spd]^3$	hcp	3.538	5.554	1.570
Ytterbium	Yb	173	$4f^{14} 5d^0 6s^2$	$4f^{14}[spd]^2$	fcc	5.485	-	-
Lutetium	Lu	175	$4f^{14} 5d^1 6s^2$	$4f^{14}[spd]^3$	hcp	3.505	5.549	1.583

The reason for this is that the Coulomb energy to pay when adding an *f* electron to obtain a half-filled of full shell is very small. These exceptions are called divalent elements, since they only have *2* electrons in the [*spd*] band. The other elements are called, as expected, trivalent. Thus, the number of the *5d* electrons is higher in light rare-earth compounds and that increases the cohesion. Concurrently, the number of the *6s* electrons decreases to maintain the trivalence. The valence state of the metallic elements is determined theoretically from the difference of the total energies calculated for the divalent and trivalent configurations [38]. In the following **Table I-2**, the outer electronic configuration of the rare earths is given for both atomic and the crystalline phases, as well as their crystal structures and lattice constants. The metals Gd, Tb, Dy, Ho, Er, Tm and Lu (as given in **Table I-2**) all have the hexagonal close-packed structure (hcp). Lanthanum, praseodymium and neodymium also have a hexagonal structure. Cerium, although it is face-centered cubic at room temperature, transforms to the hexagonal structure if the temperature is lowered to 263.15 K (-10°C) [18]. The *c/a* ratio of the rare-earth metals exhibiting the hexagonal structure is about *3.23* as compared to *1.58* for heavier metals having the hexagonal close-packed structural. Samarium has a unique rhombohedral structure which can also be indexed in the hexagonal system to give a *c/a* ratio of *7.25*. The structures of europium and ytterbium would be expected to differ from those of the other rare-earth metals in view of the unusual stability of their $4f^7$ and $4f^{14}$ electronic configurations as discussed previously.

I-II-1-4 Magnetic structure

The *4f* electrons determine the magnetic behavior of the rare earth metals. In the completed *4f* subshell, the magnetic effects of different electrons cancel each other out, but in the incomplete *4f* subshell, they do not. The exchange interactions between *4f* electrons are indirect, mediated by *5d*, *6s* electrons.

Some of the magnetic structures exhibited by the heavy rare–earth metals are shown schematically as a function of temperature in **Fig. I-7**. Whilst not presenting the subtlety of he spin alignments in some of the more exotic magnetic structures, it does show some of the diversity of the magnetic phases displayed by some of the metals in the rare–earth series.

The magnetic moments of the rare–earth metals are dominated by the spin contribution from the highly localized *4f* electrons, and are thus good examples of local–moment ferromagnets. As the *4f* electron shell can accommodate *14* electrons, a half–filled shell has seven electrons with parallel spins (according to Hunds' rule, the empirical rule in atomic physics that states that in general parallel spins are a lower–energy configuration than anti-parallel spins). Thus, the *4f* electrons contribute *7* μ_β to the total magnetic moment of Gd (~ *7.6* μ_B) [39], and similarly large contributions to the total moments for the other magnetic rare–earth metals. In contrast to the situation with itinerant ferromagnets (based on the magnetic transition metals), the valence electrons contribute a small fraction of the overall magnetic moment per atom — in the case of Gd, the *5d 6s* valence electrons contribute *0.6* μ_B, less than 10% of the total moment [39].

The magnetic structures of the rare–earth metals and many rare–earth–based compounds are well understood as the result of many decades of experimental study and the development of the local spin–density approximation in calculations of the valence electronic structures of solids.

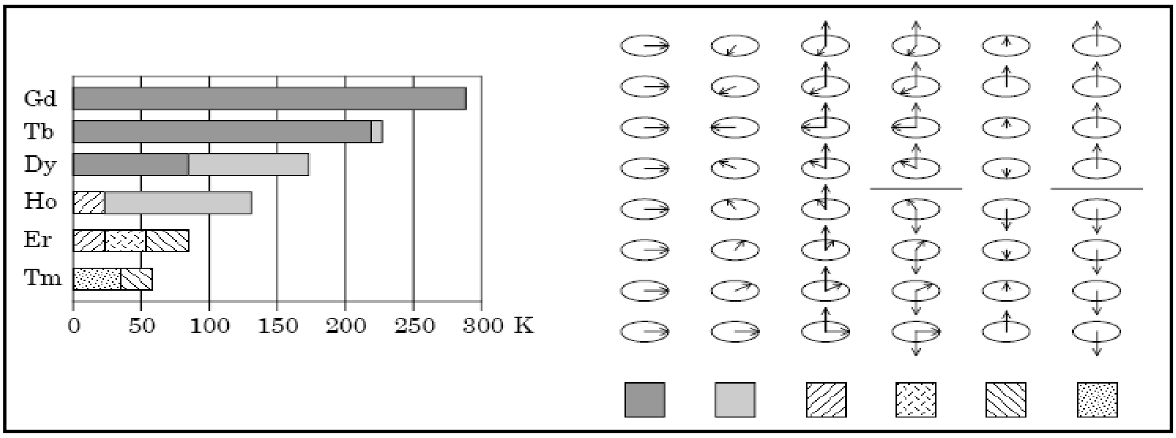

Fig. I-7 Some of the magnetic phases of the heavy rare-earth metals. For each magnetic phase, the arrows represent the changing magnitudes and directions of the components of magnetic moments relative to the basal planes (circles) from one atomic plane to the next. [39].

The existence of ferromagnetism at room temperature in gadolinium was reported and confirmed by Klemm and Bommer (1937) [40]. Much of the detailed studies on the magnetic behavior of the rare earth elements were carried out by the Ames group (Iowa, USA) in the 1950s.

Elucidation of the magnetic behavior of the rare earth metals, as has been the case with their many other properties, was greatly dependent on the availability of rare earth metals in high levels of purity and in special forms such as large single crystals [41].

For the heavy rare earth ions, spin-orbit coupling is much stronger than for *3d* transition metals, due to the larger charge of the nucleus and the smaller mean radius of the valence orbitals. According to the Pauli Exclusion Principle, two electrons cannot have identical quantum numbers, thus the orbitals are gradually filled starting from the one with lowest energy. The effect of the Coulomb repulsion and the spin-orbit coupling on the energy of the orbitals are described by Hund’s rules. These rules for a partially filled subshell are the following: (1) the value of the sum of the electron spins on the subshell is maximal ($S = \Sigma s_i$), (2) the value of the sum of the orbital angular momentum is maximal ($L = \Sigma l_i$) and (3) if the subshell is less than half full the total angular momentum is $J = |L - S|$, if the subshell is more than half full then $J = L + S$. The third rule is the result of the spin-orbit coupling. Roughly speaking, L is always parallel to J, but S is antiparallel in the first half of the series and parallel in the second half.

Table I-2: Hund's rules ground-states and magnetic moments of the rare earth [42].

Element		***m_l***										***Moments μ_J***
		-3	**-2**	**-1**	**0**	**1**	**2**	**3**	***S***	***L***	***J***	***(μ_B)***
La	f^0								0	0	0	0
Ce	f^1	↑							$\frac{1}{2}$	3	$\frac{5}{2}$	2.535
Pr	f^2	↑	↑						1	5	4	3.578
Nd	f^3	↑	↑	↑					$\frac{3}{2}$	6	$\frac{9}{2}$	3.618
Pm	f^4	↑	↑	↑	↑				2	6	4	2.683
Sm	f^5	↑	↑	↑	↑	↑			$\frac{5}{2}$	5	$\frac{5}{2}$	0.845
Eu	f^7	↑	↑	↑	↑	↑	↑	↑	$\frac{7}{2}$	0	$\frac{7}{2}$	7.937
Gd	f^7	↑	↑	↑	↑	↑	↑	↑	$\frac{7}{2}$	0	$\frac{7}{2}$	7.937
Tb	f^8	↑↓	↑	↑	↑	↑	↑	↑	3	3	6	9.721
Dy	f^9	↑↓	↑↓	↑	↑	↑	↑	↑	$\frac{5}{2}$	5	$\frac{15}{2}$	10.646
Ho	f^{10}	↑↓	↑↓	↑↓	↑	↑	↑	↑	2	6	8	10.607
Er	f^{11}	↑↓	↑↓	↑↓	↑↓	↑	↑	↑	$\frac{3}{2}$	6	$\frac{15}{2}$	9.581
Tm	f^{12}	↑↓	↑↓	↑↓	↑↓	↑↓	↑	↑	1	5	6	7.561
Yb	f^{14}	↑↓	↑↓	↑↓	↑↓	↑↓	↑↓	↑↓	0	0	0	0
Lu	f^{14}	↑↓	↑↓	↑↓	↑↓	↑↓	↑↓	↑↓	0	0	0	0

The moments associated to the spin and orbital angular moments combine to give a total moment associated to the total angular momentum vector. The spin moment is:

$$\mu_S = -\frac{g_S\ \mu_S}{\hbar}\ S, \qquad [I\text{-}1]$$

with the *gyromagnetic* factor of the electronic spin $g_S \approx 2$ and the Bohr magneton μ_B. The magnitude of this moment is $\mu_S = g_s\mu_B\sqrt{S(S+1)} \approx 2\mu_B\sqrt{S(S+1)}$, where we used the property that the eigenvalue of S^2 is $\hbar^2 S(S+1)$. The magnitude of the orbital moment is:

$$\mu_L = \mu_B\sqrt{L(L+1)} \qquad [I\text{-}2]$$

which is also directed opposite to L. Note that the *gyromagnetic* factor for the orbital moment is $g_L = 1$, which is why it does not appear in Eq. [I-2].

The coupled moment as a function of the total angular momentum J can be written in a similar form

$$\mu_J = g_J \mu_B \sqrt{J(J+1)} \qquad \text{[I-3]}$$

where the Landé factor g_J has a more complicated form, due to the factor two in the spin moment that is not present in the orbital moment. The Landé factor is:

$$g_J = 1 + \frac{J(J+1) + S(S+1) - L(L+1)}{2J(J+1)} \qquad \text{[I-4]}$$

As a summary, the Hund’s rules ground state and the corresponding magnetic moments are listed in **Table I-3** for all rare earths. The (↑) and (↓) arrows indicate the *ms* occupation of the *ml* orbitals.

I-II-2 General characteristics of the rare-earth hydrides

Prior to 1950, the rare earth hydrides were usually referred to as solid solutions [43]. Shortly thereafter, several authors [44-46] applied the term “interstitial compounds” to these hydrides.

Since that year, considerable evidence has been obtained for the existence of hydride phases of definite composition. These phases do not, in general, exhibit the whole number stoichiometry usually associated with chemical compounds. In addition, phases whose compositions can be varied over wide ranges exist for several of the rare earth metal-hydrogen systems.

The hydrides of lanthanides have been the subject of many investigations due to the fact that their physical properties can be tuned by changing the hydrogen concentration.

The rare earths absorb hydrogen easily (exothermally) under favorable pressure and temperature (P, T) conditions and exhibit for these principally trivalent metals a phase diagram of the type presented in **Fig. I-8**. This phase diagram is characterized by broad existence ranges around the stoichiometric compositions: the hcp α-phase solid solution of the parent metal, the cubic β-phase dihydrides and hcp γ-phase trihydrides [47]. As shown in **Fig. I-8**, at low concentrations, hydrogen in R metals can be described as a lattice gas. The metal lattice expands in proportion to the hydroge and metallic properties (α-RH_x phase).

At higher concentrations, stable dihydride (β-$RH_{2\pm x}$) and trihydride (γ-$RH_{3\pm x}$) phases are formed, the dihydride being a better metal than the elemental rare earth. This has been explained tentatively within the so-called hydridic model, where the electrons contributed by the hydrogen atoms form - together with the rare earth conduction electrons - deep lying bands below the Fermi level.

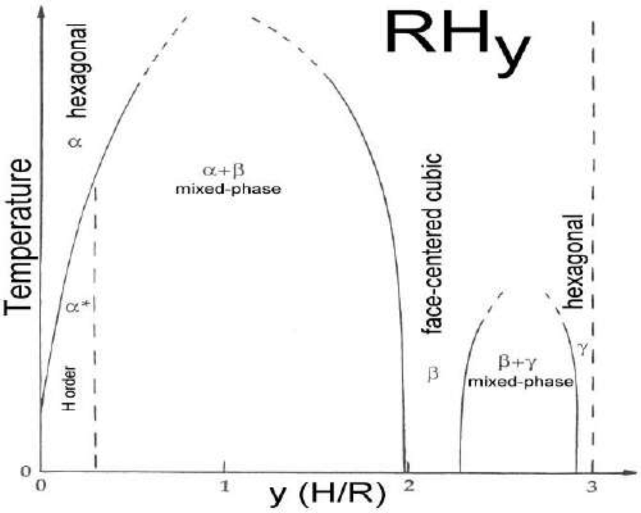

Fig. I-8 Typical phase diagram of a trivalent R-H system.

The hydrogen atom incorporated in a hydride occupies an interstice surrounded by metal atoms in one of the following two modes: a tetrahedral structure (**Fig. I-9-a**) or an octahedral structure (**Fig. I-9-b**) (in either case, the apices of the structure are occupied by metal atoms).

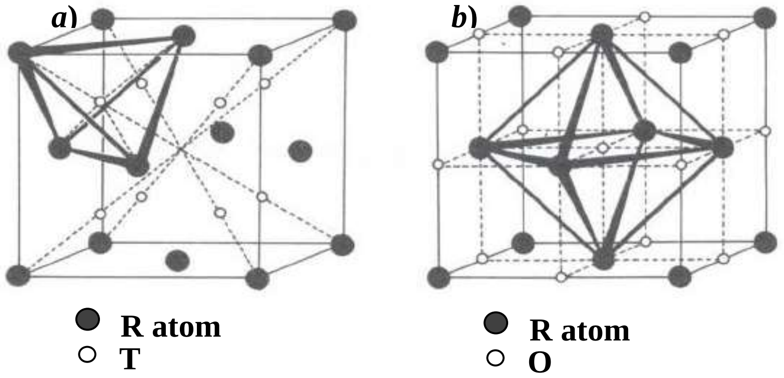

Fig. I-9 The (*a*) tetrahedral (T) and (*b*) octahedral (O) vacancies in fcc lattices.

From **Table I-4**, all rare earth dihydrides have a cubic structure, except for EuH_2 and YbH_2, which are isostructural with CaH_2 (orthorhombic structure) [49], although for RH_{2+x} with $\sim 0.25 < x \leq 0.5$ (**Fig. I-10**), the hydride ions are distorted from their ideal tetrahedral/octahedral positions and form an ordered superlattice [48]. The trihydrides of the light rare earth metals lanthanum and cerium are cubic (no γ phase) and the trihydrides of the heavier rare earth metals, like GdH_3 and TbH_3, usually have hexagonal/trigonal structures [50-52]. This hexagonal structure starts to form at high values of x in RH_{2+x} (**Fig. I-8**) (mixed phase) for the latter rare earth metals, but can only be obtained as a single phase at higher hydrogen contents, i.e. $x \approx 1$ [53].

The composition ranges for these rare earth di- and trihydrides are listed in **Table I-4**, where one can note that the lower existence limit for the trihydrides seems to be close to $x = 1$

for most rare earths, a fact confirmed by neutron diffraction studies on trihydrides in several R metal cases [54-56].

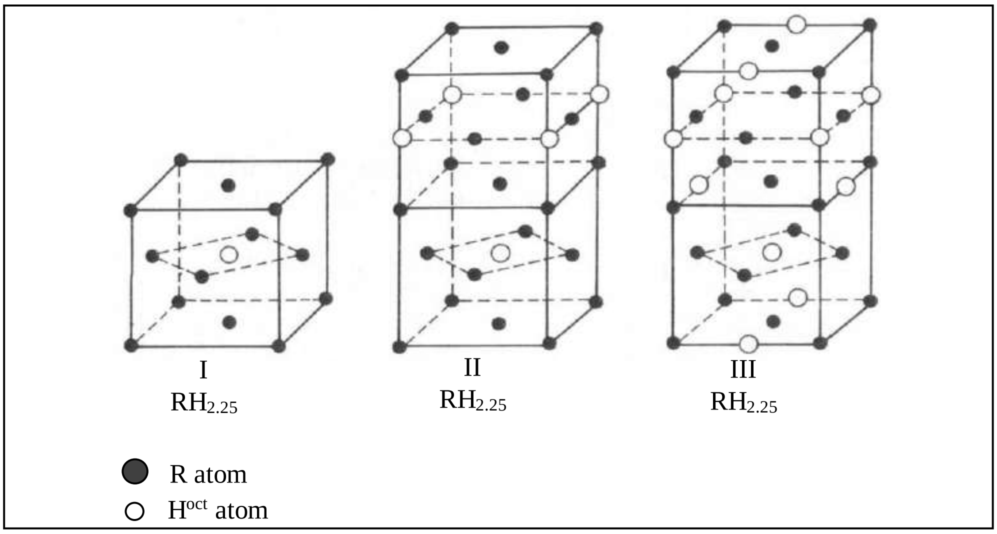

Fig. I-10 Superstructures of $RH_{2.25}$ and $RH_{2.50}$ [48].

Vajda in Ref. [57] deduced some general observations:

- An overall trend of decreasing lattice parameter with increasing atomic number; this is the well-known phenomenon of the "lanthanide contraction" where the gradual filling of the *4f*-shell (with a net break at half filled Gd) leads to a reduced nuclear repulsion and smaller ionic radius.
- When adding octahedral hydrogen atoms, x, into the stoichiometric dihydride RH_2, giving RH_{2+x}, one observes another decrease of the lattice parameter, which seems at first somewhat surprising, in view of the presence of additional interstitial impurity material. The reason for this is mainly electronic and related to the rather ionic nature of the H_{oct} interaction with the metal lattice. This effect as well as the trend for a decreasing extension of the pure β-phase (decreasing x_{max}) have been attributed by Renaudin et al. [58] to an increasing competition between the energy gain due to R-H bond shortening and the energy loss due to repulsive H-H interactions.

The magnetism of the rare-earth elements is characterized by their open *4f*-shell electrons, which can give rise to large magnetic moments and to a multitude of fascinating phenomena caused by the competition between magnetic anisotropy and RKKY (Ruderman-Kittel-Kasuya-Yosida) interactions on the one hand and the hydrogen sublattice (via the crystal field) on the other. Thus, the peculiar quasi-unidimensional chains of H–H pairs formed along the *c*-axis in the α-phase of some of the hcp rare earths (α^*-RH_x) affect different types of magnetic ordering in very different ways. This is demonstrated through the interactions with the conical ferromagnetism of Er on the one hand and the *c*-axis-oriented 3-4 ferromagnetism of Tm on the other, as well as with their *c*-axis-modulated sinusoidal magnetism. In the case of the β-RH_{2+x} phase, the excess *x*-hydrogen occupying the octahedral sites of the CaF_2-type dihydride lattice often order in a tetragonal sublattice of DO_{22} symmetry corresponding to stoichiometric $RH_{2.25}$. This strongly modifies the various commensurate and incommensurate magnetic structures present, sometimes leading to their complete vanishing or to the appearance of short-range order [59].

Table I-3 Crystal structures of rare earth metals, adapted from Ref [60].

Metal hydride	*Structure*	*Existence range (H/M)*	*Reference*
LaH_2	Cubic		[61,62]
CeH_2	Cubic		[61,62]
PrH_2	Cubic		[61,62]
NdH_2	Cubic	2-2.61 (2.87)	[52] ([64])
NdH_3	Hexagonal/Trigonal	~3	[52, 64]
SmH_2	Cubic	1.93-2.40	[64]
SmH_3	Hexagonal/Trigonal	2.59-3	[60, 65]
EuH_2	Orthorhombic		[49, 66]
GdH_2	Cubic	1.82-2.3	[67]
GdH_3	Hexagonal/Trigonal	2.85-3	[50]
TbH_2	Cubic	1.90-2.25	[68]
TbH_3	Hexagonal	2.81-3	[65]
DyH_2	Cubic	1.94-2.23	[69]
DyH_3	Hexagonal	2.86-3	[65]
HoH_2	Cubic	1.95-2.12	[64]
HoH_3	Hexagonal/Trigonal	2.95-3	[63]
ErH_2	Cubic	1.95-2.10	[64]
ErH_3	Hexagonal	2.82-3	[65]
TmH_2	Cubic	1.99-2.06	[64]
TmH_3	Hexagonal	2.76-3	[65]
YbH_2	Orthorhombic		[49]
YbH_{2+x}	Cubic	2-2.55	[70]
LuH_2	Cubic	1.85-2.03	[64]
LuH_3	Hexagonal	2.78-3	[65]
ScH_2	Cubic		[66]
YH_2	Cubic	1.91-2.08	[64]
YH_3	Hexagonal	2.77-3	[65]

The research on hydrides of the rare earth elements has attracted much attention due to their interesting chemical, optical, electrical, and magnetic properties [71–74]. However, most of studies have focused on loose powders [75] and thin films [76–80], with much less attention being given to bulk polycrystalline hydrides materials. This is due to the difficulties encountered in the production of pure bulk polycrystalline materials, because of the high reactivity of rare earth metals and hydrogen-induced stress making bulk samples disintegrate into powders. Besides, in the synthesis process, the high temperatures required to density powders may produce hydrogen desorption that leads to the destruction of the original microstructures and phases because of the semiconductor–metal transition in these systems. The properties of bulk samples of hydrogenated rare-earths have been reviewed by Vajda [47].

I-II-2-1 Gadolinium

Gadolinium (Gd) is one of the most attractive rare-earth (R) metals, because of its good electrical conductivity and large magnetic moment [81-85]. Commercial pure Gd metal is generally prepared by fusion electrolysis of its fluorides, with further refinement by Electron Beam Melting (EBM) in an inert atmosphere or by distillation in vacuum to obtain the cast metal. Upon distillation, the metallic impurities can be easily removed by evaporation, and their concentrations can be reduced to several mass ppm (parts per million) [86, 87]. However, it is of great difficulty to remove the non-metallic impurities, especially oxygen and nitrogen [88, 89], because of their strong affinity with Gd. Moreover, the reduced metals are vulnerable to contamination by gas traces in these processes. Therefore, commercial gadolinium often solidifies a large amount of non-metal impurities, dramatically undermining its physical and chemical properties.

Additionally, Gadolinium (Gd) has an hcp crystallographic structure and the simplest magnetic structure of the rare earths because the $4f^7$ electrons have an isotropic $L = 0$ ground state, $8S^{7/2}$. The magnetic structure of bulk Gd has been extensively studied by neutron diffraction experiments [90] and by torque magnetometry [91] as reviewed by Jensen and Mackintosh [92]. It is ferromagnetic with a Curie temperature of 290 K and the residual magnetic anisotropy causes the moment to align preferentially along the *c*-axis just below T_C. At lower temperature, the magnetic moments rotate towards the basal plane, reaching a maximum tilt angle of 60° at 180 K before decreasing to just below 30° at 4.2 K.

Arons and Schweizer [93] have studied the magnetic properties of GdD_{2+x} samples by susceptibility measurements and neutron diffraction. $GdD_{1.93}$ is face centered cubic and antiferromagnetic with a Néel temperature of 20 K although for x=0, a helical structure with a modulation wavevector along the *[111]* direction is observed. According to gadolinium–hydrogen system depending on the hydrogen concentration, three phases can be acquired: (1) a metallic α phase ($x<1$) having an hcp structure; (2) a metallic β phase ($1 < x < 2$) with an fcc structure; (3) an hcp insulating γ phase ($2<x<3$).

I-II-2-2 Terbium

Terbium (Tb) is one of the heavy rare earth metals that has a hexagonal structure. The character of the terbium hydride could be changed from metallic in the solid solution, through even more metallic in a dihydride, to insulating or semimetallic in a trihydride [94].

The substoichiometry of the pure dihydride depended more on the metallurgical state of the specimen than on thermodynamics. Detailed neutron scattering studies on this system [95] have shown that the octahedral D-atoms were ordering for $0.1 < x < 0.25$ in a DO_{22} (space group *I4/mmm*) structure (Ni_3Mo-type) such that every occupied (*420*)-plane was followed by three empty ones (**Fig. I-11**) corresponding to a stoichiometric composition of $TbD_{2.25}$. Similar ordering manifestations were observed in most other β-RH_{2+x} systems.

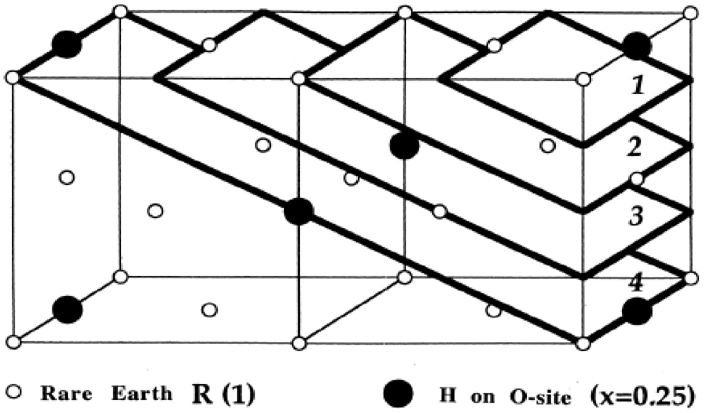

Fig. I-11 Octahedral H-superlattice in β-$RH_{2.25}$ systems (the H-atoms on the T-sites are omitted, for clarity). The x-hydrogen form a Ni_3Mo-type structure (DO_{22}) giving a $RH_{2.25}$ stoichiometry [95].

The magnetic structure of terbium dideuteride has been described in three papers [96-98] in terms of three different (inconsistent) models.

Neutron diffraction [99, 100] has shown that pure $TbD_{2.00}$ exhibits two overlapping antiferromagnetic (AF) configurations (**Fig. I-12**).

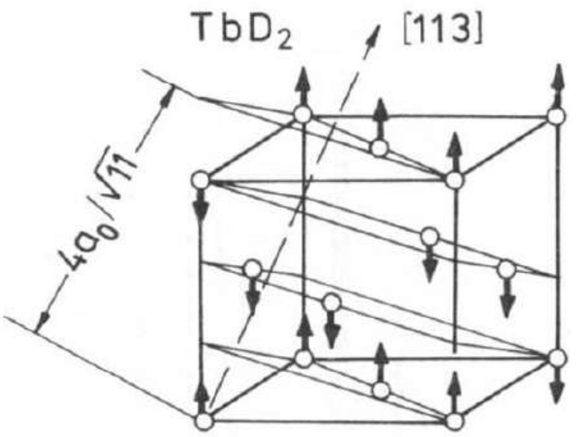

Fig. I-12 Proposed magnetic structures for TbD_2 [99].

One, Below T=16 K, commensurate with the lattice (with a magnetic unit cell four times bigger than the chemical unit cell) and modulated with a propagation vector $k_c = \frac{1}{4}[113]$; the other, between 15 and 19 K (also called 'intermediate' structure), is incommensurate, with a slightly *T*-dependent propagation vector $k_{ic} = \frac{1}{8}[116]$.

I-III Summary

This chapter has given an introduction to the potential applications for hydrogen storage and an overview of the different technologies available for storing hydrogen. Metallic and intermetallic hydrides can be used as hydrogen storage materials as they have several advantages. Rare-earth (R) alloys seem promising, owing to a high hydrogen capacity per volume unit and an ability to absorb hydrogen under moderate conditions of temperature and pressure, where the interstitial hydrogen atoms strongly modify the electronic structure and add interesting features. The hydrogen absorption properties of these alloys are very much dependent on the constituents, and metal-hydrogen bonding interactions play a major role in the stability of the hydrides.

Reference

[1] A. Izanlou and M. K. Aydinol. *Int. J. Hydrogen Energy* **35**, 1681 (2010).
[2] L. Schlapbach and A. Züttel. *Nature* **414**, 353 (2001).
[3] M. Bououdina, D. Grant, and G. Walker. *Int. J. Hydrogen Energy* **31**, 177 (2006).
[4] A. Züttel, A. Remhof, A. Borgschulte, and O. Friedrichs. *Phil. Trans. R. Soc. A* **368**, 3329 (2010).
[5] P. Hoffmann. *Tomorrow's Energy: Hydrogen, Fuel Cells, and the Prospects for a Cleaner Planet*. 2012.
[6] M. R. Swain. *Fuel Leak Simulation*. 2001.
[7] European Commission, Directorate-General for Research. *Hydrogen Energy and Fuel Cells: A Vision of Our Future*. 2003.
[8] C. J. Winter and J. Nitsch. *Hydrogen as an Energy Carrier: Technologies, Systems, Economy*. 1988.
[9] "Hydrogen Storage/ University of Strathclyde." [Online]. Available: http://www.esru.strath.ac.uk/EandE/Web_sites/99-00/hybrid_PV_FC/hydrogenstorage.html. [Accessed: 20-Jul-2017].
[10] T. Riis, E. F. Hagen, P. J. S. Vie, Ø. Ulleberg. *Hydrogen Production and Storage - R&D Priorities and Gaps*. 2006.
[11] M. Kutz. *Environmentally Conscious Alternative Energy Production*. 2007.
[12] *Hydrogen Storage*. 2013. https://wiki.uiowa.edu/display/greenergy/Hydrogen+Storage.

[13] Organisation for Economic Co-operation and Development (OECD)/International Energy Agency (IEA). *Prospects for Hydrogen and Fuel Cells*. 2005. https://doi.org/10.1787/9789264109582-en.

[14] S. S. Murthy. *J. Heat. Transf.* **134**, 31020 (2012).

[15] J. J. Reilly and G. D. Sandrock. *Sci. Am.* **242**, 5118 (1980).

[16] A. W. C. Van den Berg and C. O. Areán. *Chem. Commu.* **6**, 668 (2008).

[17] Jr. R. C. Bowman and G. Sandrock. *Metal hydrides for Energy storage and conversion applications. In: Proceedings of GLOBAL 2000 atoms for prosperity*. 2003.

[18] W. M. Mueller, J. P. Blackledge, and G. G. Libowitz. *Metal hydrides*. 1968.

[19] B. MASSICOT. *Étude du système Fe–Ti–V et de ses applications au stockage de l'hydrogène*. Thesis. Paris XII University; France. 2009.

[20] G. K. Shenoy, B. D. Dunlap, P. J. Viccaro, and D. Niarchos. *Hyperfine interact.* **9**, 531 (1981).

[21] S. Rundqvist, R. Tellgren, Y. Andersson. *J. Less-Comm. Met.* **101**, 145 (1984).

[22] C. E. Lundin, F. E. Lynch, and C. B. Magee. *J. Less-Common Met.* **56**, 19 (1977).

[23] A. C. Switendick. *Z. Phys. Chem. N. F.* **117**, 89 (1979).

[24] Y. Fukai. *Z. Phys. Chem.* **164**,165 (1989).

[25] M. M. H. Bhuiya, A. Kumar, K. J. Kim. *Int. J. Hydrogen Energy* **40**, 2231 (2015).

[26] J. N. Huiberts, R. Griessen, H. H. Rector, R. J. Wijngaarden, J. P. Dekker, D. G. de Groot, and N. J. Koeman. *Nature* **380**, 231 (1996).

[27] P. J. Kelly, J. P. Dekker, and R. Stumpf. *Phys. Rev. Lett.* **78**, 1315 (1997).

[28] M. Gupta and J. P. Burger. *Phys. Rev. B* **22**, 6074 (1980).

[29] C. K. Gupta and N. Krishnamurthy. *Extractive Metallurgy of Rare Earths*. 2005.

[30] M. K. Jha, A. Kumari, R. Panda, J. R. Kumar, K. Yoo, and J. Y. Lee. *Hydrometallurgy* **161**, 77 (2016).

[31] K. A. Jr. Gschneidner, J. Cappellen. *Two hundred Years of Rare Earths: 1787–1987*. 1987.

[32] A. Jordens, Y. P. Cheng, and K. E. Waters. *Miner. Eng.* **41**, 97 (2013).

[33] A. Kumari, R. Panda, M. K. Jha, J. R. Kumar, and J. Y. Lee. *Miner. Eng.* **79**, 102 (2015).

[34] *M.* King Hobart. *REE-Rare Earth Elements and their Uses*. 2017. https://geology.com/articles/rare-earth-elements/.

[35] M. Panayotova and V. Panayotov. *Min. Miner. Process.* **55**, 142 (2012).

[36] U. S. Geological Survey. *Mineral Commodity Summaries 2015*. 2015. http://dx.doi.org/10.3133/70140094.

[37] Neil W. Ashcroft and N. David Mermin. *Solid state physics*. 1976.

[38] A. Delin, L. Fast, B. Johansson, J. M. Wills, and O. Eriksson. *Phys. Rev. Lett.* **79**, 4637 (1997).

[39] S. D. Barrett and S. S. Dhesi. *The Structure of Rare-earth Metal Surfaces*. 2001.

[40] W. Klemm and H. Bommer. *Z. Anorg. Chem.* **231**, 138 (1937).

[41] Jr. K. A. Gschneidner and A. H. Daane. *Handbook on the Physics and Chemistry of Rare Earths*. (1988).

[42] I. L. M. Locht. *Cohesive and Spectroscopic properties of the Lanthanides within the Hubbard I Approximation*. 2015.

[43] D. P. Smith. *Hydrogen in Metals*. 1948.

[44] H. J. Emeleus and J. S. Anderson. *Modern Aspects of Inorganic Chemistry*. 1952.

[45] T. Moeller. *Inorganic Chemistry*. 1952.

[46] D. T. Hurd. *An Introduction to the Chemistry of the Hy*drides. 1952.

[47] P. Vajda. *Hydrogen in rare earth metals*. 1995.

[48] A. G. Khachaturyan. *Phys. Status Solidi b* **60**, 9 (1973).

[49] W. L. Korst and J. C. Warf. *Inorg. Chem.* **5**, 1719 (1966).

[50] M. Ellner, H. Reule, and E. J. Mittemeijer. *J. Alloy. Compd.* **309**, 127 (2000).

[51] H. Kohlmann, F. Werner, K. Yvon, G. Hilscher, M. Reissner, and G.J. Cuello. *Chem.* **13**, 4178 (2007).

[52] G. Renaudin, P. Fischer, and K. Yvon. *J. Alloys Compd.* **313**, L10 (2000).

[53] R. Dronskowski, S. Kikkawa, A. Stein. *Handbook of Solid State Chemistry*. 2017.

[54] T. J. Udovic, Q. Huang, and J. J. Rush. *Hydrogen in Semicon-ductors and Metals*. 1998.

[55] T. J. Udovic, J. J. Rush, Q. Huang, and I. S. Anderson. *J. Alloys Compd.* **253**, 241 (1997).

[56] T. J. Udovic, Q. Huang, R. W. Erwin, B. Hjörvarsson, and R. C. C. Ward. *Phys. Rev. B* **61**, 12701 (2000).

[57] P. Vajda. *Rare earth (and actinide) dihydrides: structural, electronic and magnetic properties*. 2013.

[58] G. Renaudin, P. Fischer, and K. Yvon. *J. Alloys Compd.* **330-332**, 175 (2002).

[59] P. Vajda. *Phys B.* **289–290**, 435 (2000).

[60] G. G. Libowitz. *The solid state chemistry of binary metal hydrides*. 1965.

[61] T. J. Udovic, Q. Huang, and J. J. Rush. *J. Solid State Chem.* **122**, 151 (1996).

[62] C. E. Holley, R. N. R. Mulford, F. H. Ellinger, W. C. Koehier, and W. H. Zachariasen. *J. Phys. Chem.* **59**, 1226 (1955).

[63] F. C. Perkins, and C. E. Lundin, *The holmium-hydrogen system. J. Electrochem. Soc.* **115**, 21 (1968).

[64] T. J. Udovic, Q. Huang, and J. J. Rush. *J. Alloys Compd.* **356**, 41 (2003).

[65] A. Pebler and W. E. Wallace. *Chem.* **66**, 148 (1962).

[66] K. I. Hardcastle and J. C. Warf. *Inorg. Chem.* **5**, 1728 (1966).

[67] G. G. Libowitz and J. G. Pack. *J. Phys. Chem.* **73**, 2352 (1969).

[68] Q. Huang, T. J. Udovic, J. J. Rush, J. Schefer, and I. S. Anderson. *J. Alloys Compd.* **231**, 95 (1995).

[69] T. J. Udovic, Q. Huang, J. W. Lynn, R. W. Erwin, and J. J. Rush. *Phys. Rev. B* **59**, 11852 (1999).

[70] J. C. Warf and K. I. Hardcastle. *Inorg. Chem.* **5**, 1736 (1966).

[71] P. Tessier. *Hydrogen storage in metastable FeTi*. Thesis. McGill University; Canada. 1995.

[72] E. Shalaan, H. Schmitt, and K-H Ehses. *Thin Solid Films* **489**, 330 (2005).

[73] I. Tereshina, S. Nikitin, W. Suski, J. Stepien-Damm, W. Iwasieczko, H. Drulis, and K. Skokov. *J. Alloys. Compd.* **404–406**, 172 (2005).

[74] I. Aruna, B. R. Mehta, L. K. Malhotra, and S. M. Shivaprasad. *Adv. Funct. Mater.* **15**, 131 (2005).

[75] T. Palewski, N. V. Tristan, H. Drulisb, and J. Cwik. *J. Alloys. Comp.* **404–406**, 584 (2005).

[76] K. V. Rottkay, M. Rubin, F. Michalak, R. Armitage, T. Richardson, J. Slack, and P. A. Duinel. *Electrochim. Acta.* **44**, 3093 (1999).

[77] P. Vajda and O. J. Zogal. *J. Alloys Compd.* **330–332**, 381 (2002).

[78] M. Brill, J. Bloch, and M. H. Mintz. *J. Alloys Compd.* **330–332**, 492 (2002).

[79] P. Tessier, D. Fruchart, and D. Givord. *J. Alloys Compd.* **330–332**, 369 (2002).

[80] E. Nowicka, R. Nowakowski, and R. Dus. *Appl. Surf. Sci.* **254**, 4346 (2002).

[81] P. P. Murmu, J. Kennedy, B. J. Ruck, G. V. M. Williams, A. Markwitz, S. Rubanov, and A. A. Suvorova. *J. Mater. Sci.* **47**, 1119 (2012).

[82] A. Svalov, L. Lokamani, R. Schäfer, V. Vas’kovskiy, and G. Kurlyandskaya. *J. Alloys Compd.* **615**, 366 (2014).

[83] M. Daszkiewicz, Yu. O. Pashynska, O. V. Marchuk, L. D. Gulay, and D. Kaczorowski. *J. Alloys Compd.* **616**, 243 (2014).

[84] H. Q. Liu, X. B. Zhao, F. Liu, Y. Song, Q. Sun, T. J. Zhu, and F. P. Wang. *J. Mater. Sci.* **43**, 6933 (2008).

[85] S. Thakur, R. Rai, and A. Tiwari. *Solid State Commun.* **197**, 1 (2014).

[86] Z. Zhang, Z. Wang, D. Chen, R. Miao, Q. Zhu, X. Zhang, L. Zhou, and Z. Li. *Vacuum.* **102**, 67 (2014).

[87] K. Mimura, T. Sato, and M. Isshiki. *J. Mater. Sci*. **43**, 2721 (2008).

[88] K. Kamihira, R. Hasegawa, and O. Ogawa. *Mater. Trans.* **34**, 243 (1993).

[89] Y. Waseda and M. Isshiki. *Purification Process and Characterization of Ultra High Purity Metals*. 2002.

[90] J. W. Cable and E. O. Wollan. *Phys. Rev.* **165**, 733 (1968).

[91] W. D. Corner and B. K. Tanner. *J. Phys. C: Solid State Phys.* **9**, 627 (1976).

[92] J. Jensen and A. R. Mackintosh. *Rare Earth Magnetism: Structure and Excitations.* 1991.

[93] R. R. Arons and J. Schweizer. *J. Appl. Phys.* **53**, 2645 (1982).

[94] B. Stalinski. *Bull. Acad. Pol. Sci. Class.* **III 5**, 1001 (1957).

[95] G. André, O. Blaschko, W. Schwarz, J. N. Daou, and P. Vajda. *Phys. Rev. B* **46**, 8644 (1992).

[96] D. E. Cox, G. Shirane, W. J. Takei and W. E. Wallace. *J. Appl. Phys.* **34**, 1352 (1963).

[97] H. Shaked, Jr. J. Faber, M. H. Mueller, and D. G. Westlake. *Phys. Rev. B* **16**, 340 (1977).

[98] W. Schafer and G. Will. *J. Magn. Magn. Mater.* **14**, 315 (1979).

[99] H. Shaked, D. G. Westlike, Jr. J. Faber, and M. H. Mueller. *Phys. Rev. B* **30**, 328(1984).

[100] P. Vajda, J. N. Daou, and G. André, *Phys. Rev. B* **48**, 6116(1993).

CHAPITER II

Overview on the theoretical framework

The study at the quantum level of the electronic, magnetic and other properties of a periodic crystal is one of the traditional subjects of solid state physics. At present, a lot of theoretical schemes have been proposed to interpret experimental measurements, to predict new effects and to design new materials from first principle (or ab initio). A calculation is said to be ab initio if it starts from the basic equations of motion (Schrödinger or Dirac equation) without the use of any empirical parameters. Density-functional theory (DFT) is the method of choice for the ab initio description (i.e., based on the fundamental equations of quantum mechanics) of the ground-state properties of atoms, molecules, and periodic solids. In this chapter an introduction to DFT calculations and the basic concepts behind it will be given.

II-I The Born-Oppenheimer approximation (or adiabatic approximation)

The Hamiltonian of a many-body condensed-matter system with *N* electrons and *M* nuclei can be written as [1]:

$$\hat{H}=\frac{-\hbar^2}{2}\sum_i\frac{\nabla^2_{\vec{R}_i}}{M_i}-\frac{\hbar^2}{2}\sum_i\frac{\nabla^2_{\vec{r}_i}}{m_e}-\frac{1}{4\pi\varepsilon_0}\sum_{i,j}\frac{e^2Z_i}{|\vec{R}_i-\vec{r}_j|}+\frac{1}{8\pi\varepsilon_0}\sum_{i\neq j}\frac{e^2}{|\vec{r}_i-\vec{r}_j|}+\frac{1}{8\pi\varepsilon_0}\sum_{i\neq j}\frac{e^2Z_iZ_j}{|\vec{R}_i-\vec{R}_j|} \qquad \text{[II-1]}$$

The mass of the nucleus at $\vec{R}_i$ is M_i with atomic number Z_i, the electrons have mass m_e and are at $\vec{r}_i$. $\hbar = h/2\pi$ where h is the Plank constant.

The Hamiltonian in Eq. [II-1] is composed of five terms: the two first terms are the kinetic energy of the M nuclei and the N electrons, respectively. The Coulomb attraction between the electrons and nuclei is represented by term three, and the fourth and fifth terms describe respectively the interelectron and internuclear repulsion energies.

In solid state physics, amongst other fields, one usually uses the Born-Oppenheimer approximation (or adiabatic approximation) (1927) [2], which is based on the observation that the masses of nuclei and electrons are orders of magnitude different. The nuclei are much heavier and therefore much slower than the electrons. One can hence ‘freeze’ them at fixed positions and assume the electrons to be in instantaneous equilibrium with them. In other words, only the electrons are kept as players in the many body problems. The kinetic energy of the nuclei can be neglected and the Coulomb repulsion between the nuclei can be considered constant. The Coulomb attraction that the nuclei exert on the electrons can now be described as a static external potential experienced by the electrons.

The Hamiltonian for the electronic degrees of freedom becomes

$$\hat{H} = \frac{-\hbar^2}{2m_e}\sum_i \nabla_i^2 + \sum_i V_{ext}(\vec{r}_i) + \frac{1}{2}\sum_{i \neq j} \frac{e^2}{|\vec{r}_i - \vec{r}_j|} \qquad \text{[II-2]}$$

where the indices *i* and *j* run over the different electrons.

One can rewrite the Hamiltonian as

$$\hat{H} = \hat{T} + \hat{V}_{ext} + \hat{V} \qquad \text{[II-3]}$$

The first term ($\hat{T}$) is the kinetic energy of the electrons. The second term ($\hat{V}_{ext}$) is the external potential that the electrons experience due to the nuclei (at their fixed positions). The last term ($\hat{V}$) is the Coulomb repulsion between the electrons.

It is precisely this last term which makes this problem still incredibly difficult to solve: all electrons interact with all electrons. Although this is still manageable for systems with a small amount of electrons, diagonalizing the Hamiltonian becomes quickly a problem when approaching macroscopic solids. However, that is precisely what one would like to do, since the eigenvalues of this Hamiltonian give the energy of the system and the eigenfunctions give the electron many-body wave functions.

II-II The Hartree-Fock Approximation

The earliest attempt to solve the Schrödinger equation of atomic systems was led by D. R. Hartree (1928) [3, 4]. He assumed that in a system of N electrons surrounding a fixed nucleus, each electron experiences a field due to the mean field (potential) of other ($N-1$) electrons and the nucleus. Hartree approximated the effect of many body interactions by the potential which arises from the (N−1) electrons distributed according to their own wavefunctions ψ_i and solved the corresponding Schrödinger equation for the single electron orbitals $\psi_i(N)$ of these wavefunctions represent the occupied states of the atom and $|\psi_i|^2$ gives the magnitude of charge density of the *i*-th electron. The total charge density (ρ) of the atomic system will be given by summing the orbital densities over the occupied orbitals.

Unlike the orbitals ψ_i, the electron density ρ of an atomic or molecular system is an observable quantity, for example, in X-ray scattering experiments, (ρ) is related to the spatial distribution of the electrons [5, 6]. Such an interpretation of (ρ) is natural and according to *E.* Schrödinger, electron density is the distribution of negative charge in real space [7, 8].

Let $\Psi_H(\vec{r})$ (which can be derived from the trial function) be a many-electron wave function for non-interacting electrons called Hartree wave function and given by:

$$\Psi_H(\vec{r}_i)=\psi_1(\vec{r}_1)\,\psi_2(\vec{r}_2)\ldots\psi_N(\vec{r}_N) \qquad \text{[II-4]}$$

with the index *i* running over all electrons and each $\psi_i(\vec{r}_i)$ satisfies a one-electron Schrödinger equation with potential arising from average field of the other electrons ("self-consistent field"). On using a variational argument, one arrives at the single-electron Hartree equation

$$\left[\frac{-\hbar^2}{2m_e}\vec{\nabla}_r^2+\frac{e^2}{4\pi\varepsilon_0}\int\frac{\rho(\vec{r}')}{|\vec{r}-\vec{r}'|}d\vec{r}'+\hat{V}_{ext}\right]\psi_i(\vec{r})=\varepsilon_i\psi_i(\vec{r}) \qquad \text{[II-5]}$$

where ε_i are Lagrange multipliers introduced to take into account the normalization of the single-electron wave functions ψ_i. The Hartree potential is defined as

$$V_H^i(\vec{r})=\frac{e^2}{4\pi\varepsilon_0}\int\frac{\rho(\vec{r}')}{|\vec{r}-\vec{r}'|}d\vec{r}' \qquad \text{[II-6]}$$

Where $\vec{r}$ and $\vec{r}'$ are the electron positions.

In the Hartree-Fock scheme, the simplest, yet physically sound approximation to the complicated many-electron wave function is utilized. It consists of approximating the *N*-electron wave function by an *antisymmetrized* product of *N* one-electron wave functions $\psi_i(x_i)$ [9]. For simplicity, we shall neglect the spin of electrons and keep only the spatial degrees of freedom. For an arbitrary number of electrons, forming combinations of orbitals such as these can be achieved using the determinant of a matrix, the so-called **Slater determinant**:

$$\Psi=\frac{1}{\sqrt{N!}}\begin{vmatrix}\psi_1(x_1) & \psi_2(x_1) & \cdots & \psi_N(x_1)\\ \psi_1(x_2) & \psi_2(x_2) & \cdots & \psi_N(x_2)\\ \vdots & \vdots & \ddots & \vdots\\ \psi_1(x_N) & \psi_2(x_N) & \cdots & \psi_N(x_N)\end{vmatrix} \qquad \text{[II-7]}$$

with $\{\psi_i\}$ a set of orthonormal functions and $\frac{1}{\sqrt{N!}}$ is a normalization constant.

The Hartree-Fock approximation to the wavefunction is equivalent to a mean-field solution of Schrödinger's equation in which each electron moves within an average field due to the presence of all other electrons.

In 1930, Hartree-Fock [10, 11] proposed a single-electron equation which can be written as:

$$\left[-\frac{\hbar^2\nabla_r^2}{2m}+V_{ext}(\vec{r})+V_H^i(\vec{r})+V_x(\vec{r})\right]\psi_i(\vec{r})=\varepsilon_i\psi_i(\vec{r}) \qquad \text{[II-8]}$$

Where $V_{ext}(\vec{r})$ is the potential due to the nuclei and $V_x(\vec{r})$ is the exchange potential.

The central idea of the Hartree-Fock approach is that the energy obtained by any (normalized) trial wave function, different from the actual ground state wave function, is always an upper bound, i.e. higher than the actual ground state energy. If the trial function happens to be the desired ground state wave function, the energies are [12]

$$E_{trial}\geq E_0 \qquad \text{[II-9]}$$

The Hartree-Fock scheme performs very well for atoms and molecules, and is therefore used a lot in quantum chemistry.

An excellent source for an in-depth discussion of many aspects of the HF approximation and more sophisticated techniques related to it is the book by Szabo and Ostlund (on 1982) [13].

II-III Outline of the Thomas–Fermi model

The Thomas-Fermi model, created independently by Llewellyn H. Thomas (**Fig. II-1**) [14] and E. Fermi (**Fig. II-2**) [15] around 1926, is a quantum mechanical theory for the electronic structure of a many-body system. In this method, they used the electron density $\rho(\vec{r})$ as the basic variable instead of the wavefunction. The idea of the model is that, given a large atom with many electrons, one can approximately model it by a simple nonlinear problem for a specified charge

Fig. II-1 : Llewellyn Hilleth Thomas (1903–1992)

Fig. II-2 : Enrico Fermi (1901–1954).

density. In other words, this statistical model can be used to approximate the distribution of electrons in an atom. Based on the uniform electron gas, they proposed the following functional for the kinetic energy:

$$T_{TF}\left[\rho(\vec{r})\right]=\frac{3}{10}\left(3\pi^{2}\right)^{2/3}\int\rho^{5/3}(\vec{r})d\vec{r} \qquad \text{[II-10]}$$

The Thomas-Fermi model is defined by the energy functional for the ground state energy of the system for a certain amount of electrons in the atom with a particular charge. The energy of an atom is obtained using the classical expression for the nuclear-electron attractive potential and the electron-electron repulsive potential:

$$E_{TF}\left[\rho(\vec{r})\right]=\frac{3}{10}\left(3\pi^{2}\right)^{2/3}\int\rho^{5/3}(\vec{r})d\vec{r}-Z\int\frac{\rho(\vec{r})}{\vec{r}}d\vec{r}+\frac{e}{2}\iint\frac{\rho(\vec{r})\rho(\vec{r}\,')}{|\vec{r}-\vec{r}\,'|}d\vec{r}\,d\vec{r}\,' \qquad \text{[II-11]}$$

The approximations used in the Thomas-Fermi-type approach are so crude that the theory suffers from many problems. The most serious one is that the theory fails to describe bonding between atoms, thus molecules and solids cannot be formed in this theory [16]. Although it is not good enough to describe electrons in matter, its concept to use electron density as the basic variable illustrates the way DFT works, which means that the Thomas–Fermi theory and its extensions were the predecessors of modern density functional theory (DFT).

II-IV Density functional theory

The quantum many body problem obtained after the first level approximation (Born-Oppenheimer) is much simpler than the original one, but still far too difficult to solve (because everything interacts). A historically very important method is the Hartree-Fock (HF) method, described in many condensed matter textbooks. It performs very well for atoms and molecules, and is therefore used a lot in quantum chemistry. For solids it is less accurate, however. We will not treat HF, but explain a more modern and probably also more powerful method: Density Functional Theory (DFT). Although its history goes back to the early thirties of the 20*th* century, it is Pierre C. Hohenberg and Walter Kohn who came with a brilliant idea (in 1964) [17]. Roughly speaking, they stated that if you have the ground-state density of the particles in space and the interaction between the particles, you have in principle access to any property of the system. For this achievement, Walter Kohn (1923-2016) was awarded the Chemistry Noble Prize in 1998 for “his development of the density functional theory” [18].

It is usually called a first principles method or an *ab initio* method, because it allows people to determine many properties of a condensed matter system by just giving some basic structural information without any adjustable parameter.

It provides an alternative way to investigate condensed matter systems, other than the traditional experimental method and pure theoretical method based on quantum theory. It is becoming a useful tool used by both experimentalists and theorists to understand the characteristic properties of materials and to make specific predictions of experimentally observable phenomena for real materials and to design new materials.

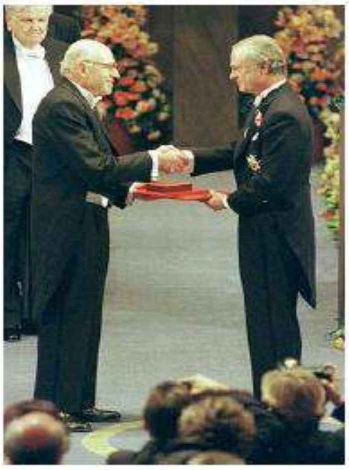

Fig. II-3 Walter Kohn receiving his Noble Prize from His Majesty the King at the Stockholm Concert Hall.

Electronic structure calculations based on density functional theory has become more and more popular in condensed matter physics, quantum chemistry and material science.

Density functional theory is by far the most widely used approach for electronic structure calculations nowadays. **Fig. II-4** shows the number of publications where the phrase “density functional theory” appears in the title or abstract (taken from the ISI Web of Science) [19]. The graph speaks for itself.

There are a number of reviews and books [20-23] that proved to be good references for learning the fundamentals of DFT and electronic structure calculations.

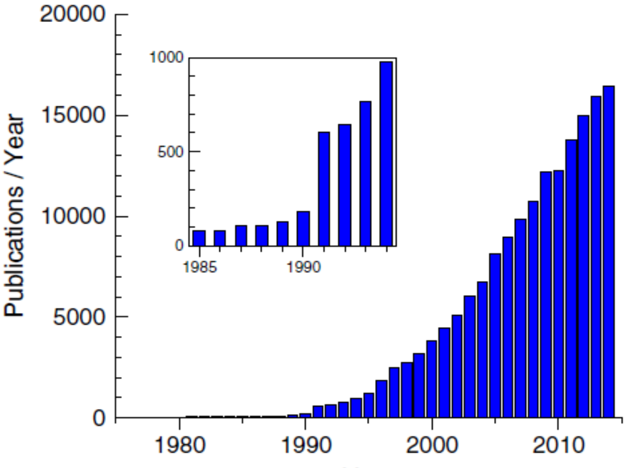

Fig. II-4 Number of publications per year (1975–2014) on topics (“density functional” or “DFT”). The number of publications depends on the precise search criteria, but the overall picture is unchanged [19].

II-IV-1 The Hohenberg-Kohn Theorems

The Hohenberg-Kohn theorems [17] shift the attention from the wave function, depending on the position vectors of all electrons simultaneously, to the density, which depends only on one position vector. The traditional formulation of the two theorems of Hohenberg and Kohn is as follows (by considering a non-magnetic system with spin degeneracy):

Theorem 1 *For any system of interacting particles (atom, molecule, solid) in an external potential* $V_{ext}(\vec{r})$*, the potential* $V_{ext}(\vec{r})$ *is determined uniquely, except for a constant, by the ground-state particle density* $\rho_0(\vec{r})$.

Corollary 1 *Since the Hamiltonian is thus fully determined, except for a constant shift of the energy, it follows that the many-body wave functions for all states (ground and excited) are determined. Therefore all properties of the system are completely determined given only the ground-state density* $\rho_0(\vec{r})$.

Theorem 2 *A universal functional of the energy E[n] in terms of the density* $\rho_0(\vec{r})$ *can be defined, valid for any external potential* $V_{ext}(\vec{r})$*. For any particular* $V_{ext}(\vec{r})$*, the exact ground-state energy of the system is the global minimum value of this functional, and the density* $\rho(\vec{r})$ *that minimizes the functional is the exact ground-state density* $\rho_0(\vec{r})$ *[24, 25].*

Corollary 2 *The functional E[ρ] alone is sufficient to determine the exact ground-state energy and density. In general, excited states of the electrons must be determined by other means.*

The first Hohenberg–Kohn theorem is a uniqueness theorem which establishes a one-to-one mapping between the electron density and the external potential, i. e. the first Hohenberg-Kohn theorem closes the circle: from the ground-state density the external potential is uniquely defined (except for a constant shift) as illustrated in the right scheme outside:

$$\begin{tikzcd}
V_{ext}(\vec{r}) \arrow[d] & & \rho_0(\{\vec{r}\}) \arrow[ll, "\text{Hohenberg-Kohn}"'] \\
\hat{\mathrm{H}} \arrow[r] & \Psi_i(\{\vec{r}\}) \arrow[r] & \Psi_0(\{\vec{r}\}) \arrow[u]
\end{tikzcd}$$

Starting from the external potential $V_{ext}(\vec{r})$ the route to obtain the density is known from quantum mechanics: constructing the Hamiltionian $\hat{\mathrm{H}}$, solving the Schrödinger equation and obtaining the wave functions $\Psi_i(\vec{r})$, including the ground-state $\Psi_0(\vec{r})$, which gives the ground-state density $\rho_0(\vec{r})$.

While the first Hohenberg-Kohn theorem claims that it is possible to find $V_{ext}(\vec{r})$ from $\rho_0(\vec{r})$, the second gives a clue how to find it.

The second Hohenberg-Kohn theorem affirms the existence of a universal energy functional $E_{tot}[\rho]$. The total electronic energy functional $E_{tot}[\rho]$ can be written in the following form [17, 26]:

$$E_{tot}[\rho]=\int V_{ext}(\vec{r})\rho(\vec{r})d\vec{r}+F_{HK}[\rho] \qquad \text{[II-12]}$$

Where $F_{HK}[\rho]$ is the Hohenberg-Kohn density functional. The exact ground state density of a system in a particular external potential $V_{ext}(\vec{r})$ is the density that minimizes $E_{tot}[\rho]$. The charge density (ρ) is the main variable in DFT. The functional $F_{HK}[\rho]$ is independent of the external potential $V_{ext}(\vec{r})$ and is applicable to any arbitrary system. However, the form of the functional $F_{HK}[\rho]$ is unknown *a priori*.

The Hohenberg-Kohn functional can be divided into three terms [17, 27]:

$$F_{HK}[\rho]=T_0[\rho]+V_H[\rho]+V_{xc}[\rho] \qquad \text{[II-13]}$$

Where $T_0[\rho]$ is the kinetic energy of a non-interacting electron gas (auxiliary system), $V_H[\rho]$, is the Hartree potential, which describes the Coulomb interaction of each electron in the system with the total electron density (ρ). This means that this term also contains the interaction of each electron with itself because each electron contributes to the total electron density. $V_{xc}[\rho]$ is the exchange-correlation potential which accounts for self-interactions within the electron gas.

II-IV-2 The Kohn-Sham (KS) formulations

The most widely used programs today are based on the Kohn-Sham's formalism to the original density functional theory, which was published in1965 and which makes DFT calculations possible with even a single personal computer. In fact, this method is so widely used that many researchers simply say DFT when they really mean Kohn-Sham DFT (KS-DFT) [28].

Interacting problem *Non-interacting problem*

$$\begin{tikzcd}
V_{ext}(\vec{r}) \arrow[d] & & \rho_0(\{\vec{r}\}) \arrow[ll, "\text{Hohenberg-Kohn}"'] \arrow[r, leftrightarrow, "\text{Kohn}", "\text{Sham}"'] & V_{ext}(\vec{r}) \arrow[d] & & \rho_0(\{\vec{r}\}) \arrow[ll, "\text{Hohenberg-Kohn}"'] \\
\hat{H} \arrow[r] & \Psi_i(\{\vec{r}\}) \arrow[r] & \Psi_0(\{\vec{r}\}) \arrow[u] & \hat{H} \arrow[r] & \Psi_i(\{\vec{r}\}) \arrow[r] & \Psi_0(\{\vec{r}\}) \arrow[u]
\end{tikzcd}$$

Combining the Hohenberg-Kohn theorems and the Kohn-Sham's formalism, which are presented in the scheme below, has proven to be remarkably successful. In fact, shifting the attention from the wave functions to the ground-state density makes it easier to find useful approximations.

The theorem of Kohn and Sham [29] can now be formulated as follows:

$$\hat{H}_{KS}\Phi_i = \xi_i\Phi_i \qquad [II-14]$$

$\Phi_i(\vec{r})$: single-particle wave function,

ξ_i : single-particle energy.

The idea of The KS equations was to replace the original (interacting) many-body problem with an auxiliary independent particle system, specifically, it maps the original interacting system with real potential onto a fictitious non-interacting system whereby the electrons move within an effective Kohn-Sham single-particle potential. The many-body effects are approximated by a so-called exchange-correlation functional in the effective Kohn-Sham single-particle potential. For the auxiliary independent-particle system, the auxiliary Hamiltonian is

$$\hat{H}_{KS} = \hat{T}_0 + \hat{V}_H + \hat{V}_{xc} + \hat{V}_{ext} = \frac{-\hbar^2}{2m_e}\vec{\nabla}_i^2 + \frac{e^2}{4\pi\varepsilon_0}\int\frac{\rho(\vec{r}')}{|\vec{r}-\vec{r}'|}\, d\vec{r}' + \frac{\delta E_{xc}[\rho]}{\delta\rho} + \hat{V}_{ext} \qquad [II-15]$$

Where $\hat{T}_0$ denotes the kinetic energy operator of an electron, $\hat{V}_H$ is the Hartree potential operator of an electron, $\hat{V}_{xc}$ is the exchange-correlation potential operator and E_{xc} the so-called exchange-correlation energy which is defined by [30, 31]:

$$E_{xc}[\rho] = F_{HK}[\rho] - T_0[\rho] - V_H[\rho] \qquad [II-16]$$

From the ground-state density, the auxiliary potential $\hat{V}_{KS}(\vec{r})$ can, in principle, be constructed with the Hohenberg-Kohn theorems for a non-interacting system, and it is defined with the following expression:

$$\hat{V}_{KS}(\vec{r}) = \hat{V}_H + \hat{V}_{xc} + \hat{V}_{ext} \qquad [II-17]$$

Kohn and Sham presented the following self-consistent equation to reach the minimization of the total energy of a many-electron system

$$\left[\frac{-\hbar^2}{2m_e}\vec{\nabla}_i^2 + \hat{V}_{KS}(\vec{r})\right]\Phi_i(\vec{r}) = \xi_i\Phi_i(\vec{r}) \qquad [II-18]$$

The exact ground-state density $\rho(\vec{r})$ of an *N*-electron system is

$$\rho(\vec{r}) = \sum_{occ}\Phi_i^*(\vec{r})\Phi_i(\vec{r}) = \sum_{i=1}^{N}|\Phi_i(\vec{r})|^2 \qquad [II-19]$$

The KS equations [29] must be solved consistently because the effective KS potential (V_{KS}) and the electron density $\rho(\vec{r})$ are closely related. This is usually done numerically through some self-consistent iteration as shown in **Fig. II-5**. The process starts with an initial electron density, usually a superposition of atomic electron densities, then the effective KS potential (V_{KS}) is calculated and the KS equation is solved with single particle eigenvalues and wavefunctions, a new electron density is then calculated from the wavefunctions. After this, a self-consistency condition is checked. This condition can be the change of total energy or electron density from the previous iteration or total force acting on atoms is less than some chosen small quantity, or a combination of these individual conditions. If self-consistency is not achieved, the calculated electron density will be mixed with electron density from previous iterations to obtain a new electron density. A new iteration will start with the new electron density. This process continues until self-consistency is reached. Afterwards, various quantities can be calculated including total energy, forces, stress, eigenvalues, electron density of states, band structure, etc..

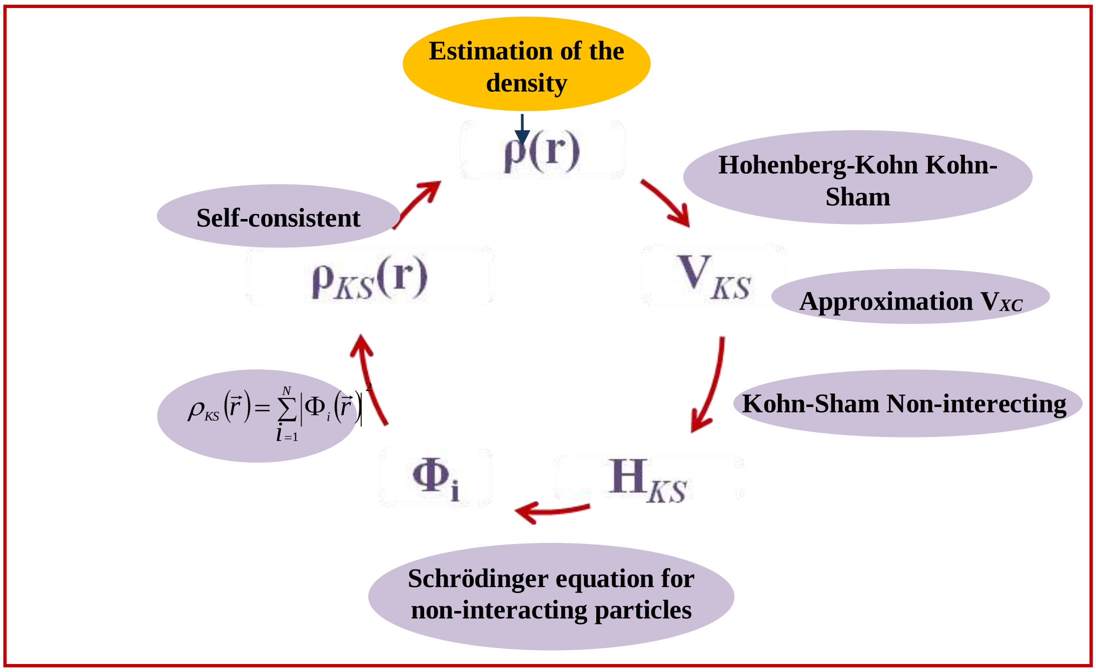

Fig. II-5 : Schematic of the DFT cycle : solving the Kohn-Sham equations self-consistently.

By using independent-particle methods, the KS equations provide a way to obtain the exact density and energy of the ground state of a condensed matter system.

$$\underbrace{\left(\frac{-\hbar^2}{2m_e}\vec{\nabla}_m^2+\frac{e^2}{4\pi\varepsilon_0}\int\frac{\rho(\vec{r}')}{|\vec{r}-\vec{r}'|}d\vec{r}'+\hat{V}_\alpha+\hat{V}_{ext}\right)}_{\hat{H}_{Sp}}\Phi_m(\vec{r})=\xi_m\Phi_m(\vec{r}) \qquad [II-20]$$

where:

$\hat{H}_{SP}$: the single-particle hamiltonian.

- ✓ For the Hartree-Fock approximations :

$\hat{V}_{\alpha}$: the exchange operator,

$\Phi_m(\vec{r})$: true one-electron (or single-particle) orbitals. Exchange is treated exactly, but correlation effects are not included at all.

- ✓ For the DFT in the LDA approximation (also LSDA, GGA):

$\hat{V}_{\alpha}$: the exchange-correlation operator,

$\Phi_m(\vec{r})$: mathematical single-particle orbitals. Exchange and correlation are treated but both approximately.

The similarity between the Hartree-Fock and Kohn-Sham equations means that the same mathematical techniques can be used to solve them. Both sets of equations have to be solved self-consistently. In order to solve the equations, we need to find the expansion coefficients $C_{m\alpha}$ in order to express Φ_m in a given basis set $\{\Phi_{\alpha}(\vec{r})\}$:

$$\Phi_m = \sum C_{m\alpha}\Phi_{\alpha}(\vec{r}) \qquad [II-21]$$

The expansion coefficients $C_{m\alpha}$ are, via the Rayleigh-Ritz principle [32], determined from the secular equation:

$$(H_{KS} - \xi_m S)C_m = 0 \qquad [II-22]$$

H_{KS} : Kohn-Sham Hamiltonian,
S : Overlap matrix.

II-IV-3 The exchange-correlation functionals

The results so far are exact, provided that the functional form of $E_{xc}[\rho]$ is known. The problem of determining the exact functional form of the universal Hohenberg-Kohn density functional is treated by the following approximations.

II-IV-3-1 Local density approximation LDA

In the *local density approximation* (LDA) [20, 24, 29, and 33], the contribution to the exchange-correlation energy from each infinitesimal volume in space, $d\vec{r}$, is taken to be the value it would have if the whole of space were filled with a homogeneous electron gas with the same density as is found in $d\vec{r}$, i.e.

$$E_{xc}^{LDA}[\rho(\vec{r})] = \int \rho(\vec{r})\, \xi_{xc}(\rho(\vec{r}))d\vec{r} \qquad \text{[II-23]}$$

where ξ_{xc} is the exchange-correlation energy per electron (particle) in a homogeneous (uniform) electron gas of density $\rho(\vec{r})$ [34]. This energy per particle is weighted with the probability $\rho(\vec{r})$ that there is an electron at this position.

The exchange-correlation energy for the homogeneous electron gas has been calculated by Ceperley [35] and Alder [24] using Monte Carlo methods. In these methods, an electron gas containing virtually an infinite number of electrons is subjected to a positive background charge distribution in an infinite volume which leads to a constant electron density everywhere.

The quantity $\xi_{xc}(\rho(\vec{r}))$ can be further split into exchange and correlation contributions,

$$\xi_{xc}(\rho(\vec{r})) = \xi_x(\rho(\vec{r})) + \xi_c(\rho(\vec{r})) \qquad \text{[II-24]}$$

The exchange part, ξ_x, which represents the exchange energy of an electron in a uniform electron gas of a particular density, was originally derived by Slater and Dirac [36, 37] in the late 1920's as:

$$\xi_x = -\frac{3}{4}\left(\frac{3\rho(\vec{r})}{\pi}\right)^{1/3} \qquad \text{[II-25]}$$

II-IV-3-2 Generalized gradient approximations GGA

An intuitive first step to improve the LDA functional is to make the exchange-correlation contribution of every infinitesimal volume not only dependent on the local density in that volume, but also on the density in the neighboring volumes. In other words, the *gradient* of the density will play a role. The first attempts to include the gradients did not work very well, and especially for large gradients the expansions performed poorly. But later on, more elaborate ways of taking the gradient of the density ($\nabla\rho(\vec{r})$) into account (for the non-homogeneity of the true electron density) were developed and so-called *Generalized Gradient Approximation* (GGA) [38].

Unlike LDA, there is no unique way to express $\xi_{xc}(\rho(\vec{r}))$ in GGA and several GGA functionals exist [2]. Furthermore, many GGA functionals are fitted to a set of experimental parameters, which deprives these functionals from their first-principles status. Thus, the exchange-correlation energy is given in the following form:

$$E_{xc}^{GGA}[\rho(\vec{r})] = \int \rho(\vec{r})\, \xi_{xc}\left(\rho(\vec{r}), |\nabla\rho(\vec{r})|\right) d\vec{r} \qquad \text{[II-26]}$$

In practice, $\xi_{xc}(\rho(\vec{r}))$ is usually split into its exchange and correlation contributions

$$\xi_{xc}(\rho(\vec{r})) = \xi_x(\rho(\vec{r})) + \xi_c(\rho(\vec{r})) \qquad \text{[II-27]}$$

The first one is based on a GGA exchange functional developed by Becke [39], which is abbreviated simply as B88 (or often just as B)

$$\xi_x^{B88} = \xi_x^{LDA}\left[1 - \frac{\beta x^2}{2^{1/3} A_x \left(1 + 6\beta x \sinh^{-1}(x)\right)}\right] \qquad \text{[II-28]}$$

where

$$x = \frac{2^{1/3}|\nabla\rho|}{\rho^{4/3}} \quad , \; A_x = \frac{3}{4}\left(\frac{3}{\pi}\right)^{1/3}$$

This functional has only one adjustable empirical parameter *β*. The value of *β = 0.0042* was determined based on the best fit to the energies of six noble gas atoms (He through Rn) using *HF* orbitals, for that it is described as a semi-empirical functional.

The correlation part of $\xi_{xc}(\rho(\vec{r}))$ developed by Lee et al. [40], which is abbreviated simply as LYP

$$\xi_c^{LYP} = -\frac{a}{1 + d\rho^{-1/3}}\left\{\rho + b\rho^{-2/3}\left[C_F \rho^{5/3} - 2t_w + \frac{1}{9}\left(t_w + \frac{1}{2}\nabla^2\rho\right)\right] e^{-c\rho^{-1/3}}\right\} \qquad \text{[II-29]}$$

where

$$t_w = \frac{1}{8}\left(\frac{|\nabla\rho|^2}{\rho} - \nabla^2\rho\right) \quad , \; C_F = \frac{3}{10}\left(3\pi^2\right)^{2/3}$$

$$a = 0.04918 \;,\; b = 0.132 \;,\; c = 0.2533 \;,\; d = 0.349$$

Perdew, Burke, and Ernzerhof (PBE) [38] presented a simplified construction of a simplified GGA for exchange and correlation in which all parameters are fundamental constants, which may be described as an *ab-initio* (non-empirical) functional.

The GGA form for the exchange energy is simply

$$\zeta_x^{PBE} = \int \rho(\vec{r})\, \xi_x^{LDA}(\rho(\vec{r}))\, F_x(s)\, d\vec{r} \qquad \text{[II-30]}$$

where $\rho(\vec{r})$ is the electron density, $s = |\nabla\rho| / \left[2(3\pi)^{1/3}\rho^{4/3}\right]$ is the dimensionless reduced gradient, $\xi_x^{LDA}(\rho(\vec{r})) = -3/[4(3/\pi)^{1/3}\rho^{1/3}]$ is the exchange energy density per particle for a uniform electron gas (UEG), and $F_x(s)$ is the exchange enhancement factor. The enhancement factor for the PBE [38] is

$$F_x(s) = 1 + k - k/\left(1 + (\mu s^2)/k\right)$$

The parameters μ and k are set to *0.21951* and *0.804* respectively.

In the GGA framework, the correlation energy (for a spin-unpolarized system) can be written as [41]

$$\zeta_c^{PBE} = \int \rho(\vec{r})\, \left\{\xi_c^{LDA}(\rho(\vec{r})) + \beta_c t^2 + \ldots\right\} d\vec{r} \qquad \text{[II-31]}$$

Where $\xi_c^{LDA}(\rho(\vec{r}))$ is the correlation energy density per particle for a uniform electron gas (UEG), β_c is a coefficient, and $t = |\nabla\rho| / \left[4(3\pi)^{1/6}\rho^{7/6}\right]$ is the appropriate reduced density gradient for correlation. The value of β_c for the slowly varying high-density limit was obtained by Ma and Brueckner [42]

$$\beta_c^{PBE} = \lim_{n\to\infty}\beta_c = \beta_{MB} = 0.066725 \qquad \text{[II-32]}$$

A somewhat different approach to obtain GGA's has been used by Langreth and Mehl [43], Perdew [44], and Perdew and Wang [45, 46].

II-IV-3-3 Hybrid Functionals

Improvements in the development of better XC functionals mostly came from investigations of properties of the hypothetical *exact XC* functional [12]. Better XC functionals that are classified as *meta*-GGA [47] and *hyper*-GGA [48] functional approximately model the *exact behavior*.

On the other hand, in DFT, the orbital-dependence of the exchange correlation energy is rather weak. In many cases, this is appropriate, but in systems with narrow *3d*- bands (transition metal oxides) or *4f*-bands (rare earth compounds) and localized orbitals, DFT fails to account for the strong Coulomb repulsion between electrons occupying these narrow bands, which lead to an enhanced exchange splitting between occupied and empty eigenstates.

The DFT+U method, originally proposed by Hubbard and Anderson [49], attempts to cure this defect by adding a Hubbard-type Coulomb repulsion to the DFT total energy Hamiltonian [50-54], while the rest of valence electrons are treated at the level of “standard” approximate DFT functionals.

The effect of the added U is to first split the “correlated” orbitals and then to shift the occupied orbitals in the direction of lower energy and the unoccupied orbitals in the direction of higher energy. The obtained distance in energy (which is the total shift) has roughly the value of U [55].

In addition, the DFT+U method is a semi-empirical approach because the Hubbard parameter U, the free parameter, is not known and needs to be evaluated. This can be done by a comparison of calculated properties with experimental measurements or by constrained DFT calculations.

In its general form, DFT+U may be thought of as the net contribution from (1) the standard DFT calculation (E^{DFT}) within the LDA or GGA approximation, (2) the Hubbard term (E^{U}) that explicitly models the Coulomb energy associated with the localized atomic orbitals of interest (e.g., *3d* and *4f* electrons) which contains electron-electron interactions as modeled in the Hubbard Hamiltonian, and (3) removal of a double counting term (E^{dc}) that corresponds to a mean field description of these interactions obtained in the homogeneous electron gas limit with a standard DFT functional,

$$E^{DFT+U}\left[\rho,\left\{n_{lm}^{a\sigma}\right\}\right]=E^{DFT}\left[\rho\right]+E^{U}\left[\left\{n_{lm}^{a\sigma}\right\}\right]-E^{dc}\left[\left\{n_{lm}^{a\sigma}\right\}\right] \qquad \text{[II-33]}$$

where ρ is the electronic density, and $n_{lm}^{a\sigma}$ are the atomic-orbital occupations for the atom a (*lm* magnetic quantum numbers, σ is a spin index) experiencing the”Hubbard” term.

The electron-electron Coulomb interaction energy E^{U} is given a more general expression borrowed from the HF method [56]:

$$E^{U}\left[\left\{n_{lm}^{a\sigma}\right\}\right]=\frac{1}{2}\sum_{a\sigma\{lm\}}\left\{U_{ll'mm'}^{a}\,n_{lm}^{a\sigma}\,n_{l'm'}^{a-\sigma}+\left(U_{ll'mm'}^{a}-U_{ll'm'm}^{a}\right)n_{lm}^{a\sigma}\,n_{l'm'}^{a\sigma}\right\} \qquad \text{[II-34]}$$

where U is a Coulomb parameter [57]. As in the case of semi-empirical schemes such as the Hubbard model, the electron-electron repulsion operator is replaced by an operator representing screened electron-electron repulsion between electrons in the given shell.

- Most commonly, the double counting term E_{dc} is obtained as:

$$E_{dc}\left[\left\{n_{lm}^{a\sigma}\right\}\right]=\frac{1}{2}\sum_{al}U_{al}\,N_{al}\,(N_{al}-1)-\frac{1}{2}\sum_{al}J_{al}\sum_{\sigma}N_{al\sigma}\,(N_{al\sigma}-1) \qquad \text{[II-35]}$$

J is exchange parameter [57], N_{al} is the total occupancy for a given site and $N_{al\sigma}$ is the total occupancy for a given site and spin σ

$$N_{al}=\sum_{\sigma m}n_{lm}^{a\sigma} \qquad \text{[II-36]}$$

$$N_{al\sigma}=\sum_{m}n_{lm}^{a\sigma} \qquad \text{[II-37]}$$

And U_{al} is the effective electron-electron repulsion interaction parameter that may be calculated [58-62] or, more commonly, tuned [63-65] and is specific to each atom and subshell.

- After all simplifications, Eq. [II-33] can be rewritten as follows [56]:

$$E^{DFT+U}\left[\rho,\left\{n_{lm}^{a\sigma}\right\}\right]=\frac{1}{2}\sum_{a\sigma}\sum_{lm}U^{a}_{lmlm}\left(n_{ll}^{a\sigma}\,\delta_{lm}-n_{lm}^{a\sigma}\,n_{ml}^{a\sigma}\right) \qquad \text{[II-38]}$$

Using the definition of the atomic orbital occupations given in Eq. [II-36] and Eq. [II-37], it is instructive to derive the Hubbard contribution to the KS potential. From the energy functional in Eq. [II-38] it is easy to obtain [66]:

$$V_{alm}(r)\equiv V_{eff}(r)-U_{al}^{eff}\left(n_{lm}^{a\sigma}-\frac{1}{2}\right) \qquad \text{[II-39]}$$

$$V_{eff}=V_{LDA}=V_{ext}+\frac{e^{2}}{4\pi\varepsilon_{0}}\int\frac{\rho(\vec{r}')}{|\vec{r}-\vec{r}'|}d\vec{r}'+\frac{\delta\mathrm{E}_{xc}[\rho]}{\delta\rho} \qquad \text{[II-40]}$$

U_{al}^{eff} is a key approximation often used in modern DFT+U practice, defined as:

$$U_{al}^{eff}=U_{al}-J_{al} \qquad \text{[II-41]}$$

Eq. [II-39] shows that the Hubbard potential is repulsive for less than half-filled orbitals ($n_{lm}^{a\sigma}<1/2$), and attractive for the others. That is, at its heart, as first proposed by Hubbard and Anderson, the U discourages pairing of electrons, while the J encourages it [67].

II-IV-4 The basis set

In order to solve the Kohn-Sham equations, Eq. [II-18], numerically, one needs to calculate matrix elements of the Hamilton operator for a given basis set. While the choice of plane waves as basis functions is very appealing, describing the rapid oscillations of the wave function close to the nucleus in a plane wave basis set is inefficient.

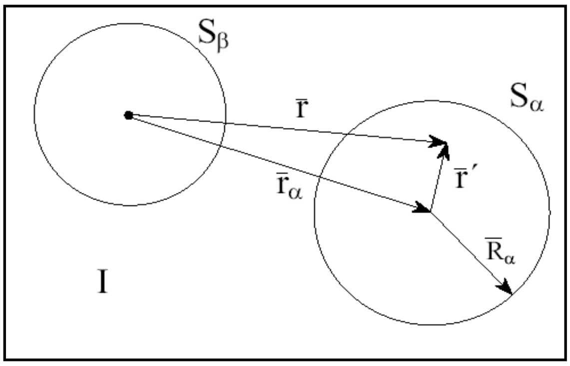

Fig.II-6 Division of a unit cell in muffin tin regions and an interstitial region, for a case with two atoms [66].

This problem can be solved by dividing the unit cell into non overlapping atomic spheres “α” (centered at the atomic sites), the so-called muffin-tin spheres, and an interstitial region “I” (**Fig. II-6**) [66].

Different basis sets are used in these respective regions. The idea behind this lies in the fact that the inner region of an atom (the core) is shielded from outer regions and electrons behave as they would in a free atom, and therefore, could be described by atomic like functions.

While in the outer region away from the core (where most chemistry happens), electrons are free, and plane waves provide a good description of their wavefunctions.

II-IV-4-1 Augmented plane wave basis set (APW)

Right from the beginning it has to be said that the APW-method itself is of no practical use any more today. But for didactical reasons it is advantageous to discuss APW first, before going to its successors, LAPW and APW+lo.

The augmented plane wave (APW) approach, originally proposed by Slater [68, 69], uses a mixed basis set for I and MT regions (**Fig. II-6**). In the interstitial region, plane waves are used to represent the wave functions, while inside the MT-spheres the wave functions are expanded in terms of the solutions of the scalar relativistic Dirac equation, which is solved for a set of energy parameters and for the spherically symmetric component of the potential. The basis functions are labeled by the interstitial plane wave indices. Inside the MT-spheres the plane waves are replaced by a linear combination of the radial solutions of the scalar relativistic Dirac equation in such a way that the basis function is continuous at the MT-sphere boundary. Hence, the APW basis functions are:

$$\Phi_{\vec{K}}^{\vec{k}}(\vec{r},\mathrm{E})=\begin{cases}\dfrac{1}{\sqrt{\Omega}}e^{i\left(\vec{k}+\vec{K}\right)\vec{r}} & \vec{r}\in I\\ \sum\limits_{l,m}A_{lm}^{\alpha,\vec{k}+\vec{K}}u_l^{\alpha}\left(r',E_l^{\alpha}\right)Y_{lm}\left(\hat{r}'\right) & \vec{r}\in S_{\alpha}\end{cases}\qquad\text{[II-42]}$$

where we denoted the radial solutions of the scalar relativistic Dirac equation for atom α by u_l^α, $\vec{r}' = \vec{r} - \vec{r}_\alpha$ (see **Fig. II-6**) is the position vector with respect to the center of atom α. The coefficients $A_{lm}^{\alpha,\vec{k}+\vec{K}}$ are determined from the requirement that the wavefunctions have to be continuous at the boundary of the muffin-tin spheres. The $Y_{lm}(\hat{r})$ are spherical harmonics. Note that Ω is the volume of the unit cell.

Each plane wave is augmented by an atomic-like function in every atomic sphere and therefore called augmented plane wave method (APW). However, an energy-independent APW basis set like in Eq. [II-41] does not provide sufficient variational freedom. The use of an energy-dependent APW-basis set is possible but entails a nonlinear energy dependence of the Hamiltonian operator, which dramatically increases the complexity of the eigenvalue problem.

II-IV-4-2 linearized augmented plane wave basis set (LAPW)

In 1975, Andersen proposed [70] to linearize the non-linear eigenvalue problem in APW by using linear combinations of both the radial functions u_l^α and their derivatives $\dot{u}_l^\alpha$ with respect to energy (which may be computed from eigenvalues and corresponding partial charges (see e.g. Ref. [71])) in such a way that the basis function and its first derivative are continuous at the MT-sphere boundary. The resulting basis functions are called *linearized* augmented plane waves (LAPW) and are given by

$$\Phi_{\vec{K}}^{\vec{k}}(\vec{r}) = \begin{cases} \dfrac{1}{\sqrt{\Omega}} e^{i\left(\vec{k}+\vec{K}\right)\vec{r}} & \vec{r} \in I \\ \sum\limits_{l,m} \left[A_{lm}^{\alpha,\vec{k}+\vec{K}} u_l^\alpha\left(r', E_l^\alpha\right) + B_{lm}^{\alpha,\vec{k}+\vec{K}} \dot{u}_l^\alpha\left(r', E_l^\alpha\right) \right] Y_{lm}(\hat{r}') & \vec{r} \in S_\alpha \end{cases} \qquad \text{[II-43]}$$

The coefficients $B_{lm}^{\alpha,\vec{k}+\vec{K}}$ and $A_{lm}^{\alpha,\vec{k}+\vec{K}}$ are functions of $\vec{K}$ and chosen in such a way that this basis function matches (in value and slope) with each plane wave (PW) of the corresponding basis function for the interstitial region. More details can be found on this method in the literature [66, 34].

II-IV-4-3 linearized augmented plane wave with Local Orbitals basis set (LAPW+LO)

States that leak out of the muffin tin sphere are called *valence states*. Valence states participate in chemical bonds, and these states are treated by LAPW. In order to describe semi-core states, the LAPW basis set may be supplemented with local orbitals (LOs) [72]. In contrast to the LAPW basis functions defined in Eq. [II-43], a local orbital is zero everywhere in space with the exception of the interior of the MT sphere of that atom, hence its name *local* orbital (LO). A local orbital is defined as:

$$\Phi_{\alpha,LO}^{lm}(\vec{r})=\begin{cases}0 & \vec{r}\notin S_{\alpha}\\ \left[A_{lm}^{\alpha,LO}u_{l}^{\alpha}\left(r',E_{1,l}^{\alpha}\right)+B_{lm}^{\alpha,LO}\dot{u}_{l}^{\alpha}\left(r',E_{1,l}^{\alpha}\right)+C_{lm}^{\alpha,LO}u_{l}^{\alpha}\left(r',E_{2,l}^{\alpha}\right)\right]Y_{lm}(\hat{r}') & \vec{r}\in S_{\alpha}\end{cases} \qquad \text{[II-44]}$$

The coefficients $A_{lm}^{\alpha,LO}$, $B_{lm}^{\alpha,LO}$ and $C_{lm}^{\alpha,LO}$ are determined with the boundary condition such that LO vanishes in value and slope at the muffin-tin radius (zero in interstitial region and in MT sphere of other atom). The inclusion of LO's makes the computation of matrix elements somewhat more difficult but one has a better model and saves computational time, since no semi-core states need to be calculated in separate LAPW run.

The problem with the APW method was the energy dependence of the basis set. This energy dependence could be removed in the LAPW+LO method, at the cost of a somewhat larger basis set size (due to LAPW itself, and due to adding local orbitals.).

II-IV-4-4 The `pure' APW+lo basis set

Sjöstedt, Nordström and Singh (2000) [73] have shown that the standard LAPW method with the additional constraint on the plane waves (PWs) matching in value and slope the solution inside the sphere is not the most efficient way to linearize Slater's APW method. It can be made much more efficient when one uses the standard APW basis, but with $u_{l}^{\alpha}\left(r',E_{l}^{\alpha}\right)$ at a fixed energy E_{l}^{α} in order to keep the linear eigenvalue problem. One then adds a new local orbital (which is abbreviated to lo) to have enough variational flexibility in the radial basis functions. The resulting basis set is called APW+lo [74], whose basis set contains two kinds of functions. The first kind is APW's, with a set of fixed energies $E_{1,l}^{\alpha}$:

$$\Phi_{\vec{K}}^{\vec{k}}(\vec{r},E)=\begin{cases}\dfrac{1}{\sqrt{\Omega}}e^{i(\vec{k}+\vec{K})\vec{r}} & \vec{r}\in I\\ \sum\limits_{l,m}A_{lm}^{\alpha,\vec{k}+\vec{K}}u_{l}^{\alpha}\left(r',E_{1,l}^{\alpha}\right)Y_{lm}(\hat{r}') & \vec{r}\in S_{\alpha}\end{cases} \qquad \text{[II-45]}$$

The second kind is defined as:

$$\Phi_{\alpha,lo}^{lm}(\vec{r})=\begin{cases}0 & \vec{r}\notin S_{\alpha}\\ \left[A_{lm}^{\alpha,lo}u_{l}^{\alpha}\left(r',E_{1,l}^{\alpha}\right)+B_{lm}^{\alpha,lo}\dot{u}_{l}^{\alpha}\left(r',E_{1,l}^{\alpha}\right)\right]Y_{lm}(\hat{r}') & \vec{r}\in S_{\alpha}\end{cases} \qquad \text{[II-46]}$$

This new lo (denoted with lower case to distinguish it from the LO given in Eq. [II-44]) looks almost like the old "LAPW"-basis set, but here $A_{lm}^{\alpha,lo}$ and $B_{lm}^{\alpha,lo}$ do not depend on $\vec{K}$ and are determined by the requirement that "lo" is zero (in value and not in slope) at the sphere boundary and normalized. Though these basis functions have "kinks" at the sphere boundary due to discontinuity in their derivatives (slope), the total wavefunction is smooth and differentiable.

II-IV-4-5 Full-Potential Linearized Augmented Plane wave Method (FP-LAPW)

In the past, in the majority of applications of APW and LAPW methods, inside the muffin-tins, the potential is approximated to be spherically symmetric, and in many implementations the interstitial potential is set constant (**Fig. II-7**). The restrictions to the potential are commonly called shape-approximations. The potential in the unit cell $V(r)$ was typically approximated by

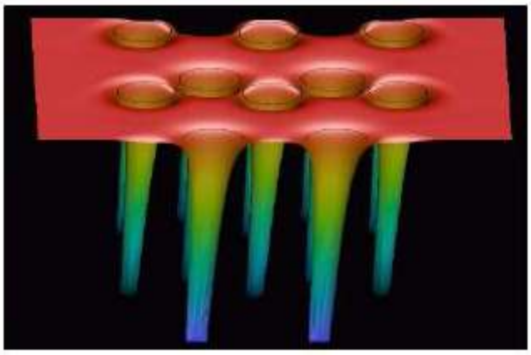

Fig. II-7 Muffin tin approximation.

$$V(r)=\begin{cases} V_K^0 = const. & \vec{r}\in I \\ V_{LM}^0(r) & \vec{r}\in S_\alpha \end{cases} \qquad [II-47]$$

In the full-potential LAPW method (FP-LAPW) [75, 76] there are no shape approximations in the interstitial region and inside the muffin-tin spheres (**Fig. II-8**). The potential and charge density are expanded (a) into lattice harmonics (inside each atomic sphere) and (b) as a Fourier series (in interstitial region) and thus they are completely general.

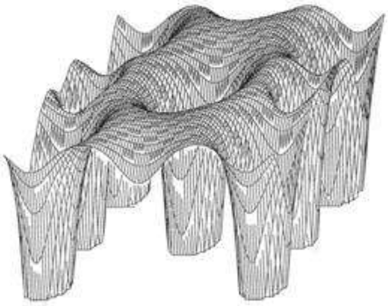

Fig. II-8 Full potential.

$$V(r)=\begin{cases} \sum_K V_K e^{i\vec{K}\bullet\vec{r}} & \vec{r}\in I \\ \sum_{LM} V_{LM}\, Y_{lm}(\hat{r}) & \vec{r}\in S_\alpha \end{cases} \qquad [II-48]$$

The charge density, $\rho(r)$, is represented in the same way as the potential:

$$\rho(r)=\begin{cases}\sum_{K}\rho_K e^{i\vec{K}\bullet\vec{r}} & \vec{r}\in I\\ \sum_{LM}\rho_{LM}Y_{lm}(\hat{r}) & \vec{r}\in S_\alpha\end{cases} \qquad [II-49]$$

A local coordinate system for each atomic sphere is defined according to the point group symmetry of the corresponding atom to have the smallest number of " lm " values in the lattice harmonics expansion. In order to relate local and global coordinate systems of the unit cell, a rotation matrix is used.

II-IV-5 Calculation code used

Some of the widely used codes:

- VASP (http://cms.mpi.univie.ac.at/vasp/)
  - Commercial, Plane-Wave Basis, Pseudopotentials
- PWSCF (http://www.quantum-espresso.org/)
  - Free, Plane-Wave Basis, Pseudopotentials
- CASTEP (http://ccpforge.cse.rl.ac.uk/gf/project/castep/)
  - Free in UK, licensed elsewhere, Plane-Wave Basis, Pseudopotentials
- ABINIT (http://www.abinit.org/)
  - Free, Plane-Wave basis, Pseudopotentials
- SIESTA (http://www.uam.es/depatamentos/ciencas/fismateriac/siesta)
  - Free, LCAO basis set, Pseudopotentials
- WIEN2k (http://www.wien2k.at/)
  - Commercial (modest license fee), all-electron, augmented wave method.

In this work we used the WIEN2k program package [77]. The major steps in the development during the last four decades were described in detail in a review [78] and previous articles [71, 79 and 80].

The computer code WIEN2k is used to study crystal properties on the atomic scale by employing the linearized-augmented-plane-wave (LAPW) method within density functional theory (DFT), the most precise schemes for solving the KS equations. The advantage of first-principle (*ab initio*) methods lies in the fact that they can be carried out without knowing any experimental data.

WIEN2k is written in FORTRAN 90 and requires a Unix/Linux operating system since the programs are linked together via C-shell scripts.

II-IV-5-1 General remarks on WIEN2k

- Each “case”runs in his own directory: ***./case***
- The “master input” is called: ***case.struct***
- Initialize a calculation: ***init_lapw***
- Run scf-cycle: ***run_lapw (runsp_lapw)***
- The “master output” is called: ***case.scf***
- One can run WIEN2k using any web browser and the *w2web* interface, but also at the command line of an xterm.

II-IV-5-2 Some applications of WIEN2k

i) Band structure and density of states (DOS) calculations

The energy band structure and corresponding density of states are essential quantities that determine the electronic structure of a system. Their inspection provides information about conduction properties (metal, insulator or semiconductor) and gives insight into the chemical bonding. By looking at site decomposed partial densities of states one can find a hint for the strength of interactions between the orbitals of the constituting atoms. The band structure is also useful in connection with photoelectron spectra.

ii) Electron densities

The electron density is the key quantity in DFT. By taking its Fourier transform the static structure factors can be determined easily, and it can be compared with experimental X-ray diffraction data.

iii) Total energy and phase transitions

The relative stability of different phases can be computed by the total energy. With the knowledge of total energy, the relative stability of different phases can be computed by keeping as many parameters constant as possible in order to have a cancellation of systematic errors. In such cases it is possible to keep many parameters constant as possible in order to have a cancellation of systematic errors. These parameters for example, the atomic size of spheres, the plane-wave cut-off, the k-mesh, the DFT functional the treatment of relativity, etc. Because the energy differences are small, so a consistent treatment of the systems to be compared will help to minimize these computational effects.

iv) Forces and structural optimization

In cases where the atoms occupy general positions that are not fixed by the crystal symmetry, the knowledge of the forces acting on atoms helps in optimizing the structure parameters. Forces can be computed in WIEN2K and are crucial for such optimizations.

v) Spectra

The photoelectron spectra, X-ray emission and absorption spectra can be calculated using partial densities of states and the transition probabilities between a valence and a core state. Such spectra provide useful information on local binding situations of the atom, whose core state is involved. Optical spectra and related quantities e.g. energy dependence of real and imaginary parts of the dielectric constant can be calculated from the electronic response which is further used to determine absorption coefficient, refractive index, electron energy loss spectrum and reflectivity by using the Kramers-Kroening relation [82].

II-V Summary

To conclude, in this chapter we have presented a brief overview of Density functional theory (DFT). DFT is a quantum mechanical modelling method used in Physics and Chemistry to investigate the electronic structure of many-body systems, in particular atoms, molecules, and the condensed phases. An analytical solution of the many-electron Schrdinger equation is not available, and a numerical solution, while perfectly possible in theory, is effectively impossible in practice for more than a handful of electrons due to the finite speed and memory of computers. An approach to lower computational cost of molecular calculations can therefore be the use of a less complex base variable. The foundation for such an approach has been provided by Hohenberg and Kohn in 1964 when they proofed that the electron density, a variable only depending on 3 spatial variables, in principle contains all information about the ground state properties of a system. This also marked the birth of density functional theory (DFT).

DFT has become very popular in recent years. This is justified based on the pragmatic observation that it is less computationally intensive than other methods with similar accuracy.

References

[1] K. Burke. *The ABC of DFT*. 2009. http://dft.uci.edu/materials/bookABCDFT/gamma/g1.pdf.

[2] M. Born and R. Oppenheimer. *Ann. Phys.* **389**, 457 (1927).

[3] J. C. Slater, *The Calculation of Molecular Orbitals*. 1979.

[4] D. R. Hartree. *The Calculation of Atomic Structures*. 1957.

[5] N .H. March. *Theory of Inhomogeneous Electron Gas*. 1963.

[6] F. L. Hirschfeld. *Accurate Molecular Structures: Their Determination and Importance*. 1992.

[7] E. Schrödinger. *Ann. Phys.* **386**, 109 (1926).

[8] R. F. W. Bader. *J. Mol. Struct. (THEOCHEM)* **943**, 2-18 (2010).

[9] E. Kaxiras. *Atomic and electronic structure of solids*. 2003.

[10] D. R. Hartree. *Proc. Cam. Phil. Soc.* **24**, 89 (1928).

[11] V. Z. Fock. *Z. Phys.* **61**, 209 (1930).

[12] P. A. M. Dirac. *Math. Proc. Cam. Phil. Soc.* **35**, 416-418 (1939).

[13] A. Szabo and N. S. Ostlund. *Modern Quantum Chemistry: Introduction to Advanced Electronic Structure Theory*. 1982.

[14] L. H. Thomas. *Proc. Camb. Phil. Soc.* **23**, 542 (1926).

[15] E. Fermi. Rend. *Accad. Naz. Lincei* **6**, 602 (1927).

[16] E. Teller. *Rev. Mod. Phys.* **34**, 627 (1962).

[17] P. Hohenberg and W. Kohn. *Phys. Rev.*, **136**, B864, (1964).

[18] The Nobel Fundation, «The Nobel Prize of Chemistry 1998», 1998.

[19] R. O. Jones. *Mod. Phys.* **87**, 897 (2015).

[20] R. G. Parr and W. Yang. *Density Functional Theory of Atoms and Molecules*. 1989.

[21] G. Baskaran. *Electron Correlation in the Solid State*. N. H. March. 1999.

[22] J. Callaway and N. H. March. *Solid State Phys.* **38**, 135 (1984)

[23] R. M. Martin. *Electronic structure: basic theory and practical methods*. 2004.

[24] W. Koch, M. C. Holthausen. *A Chemist's Guide to Density Functional Theory*. 2001.

[25] R. D. Morgan. *Springer Handbook of Atomic, Molecular, and Optical Physics*. 2006.

[26] W. Kohn. *Rev. Mod. Phys.* **71**, 1253 (1998).

[27] Y. A. Wang and E. A. Carter. *Orbital free kinetic-energy density functional theory*. 2000.

[28] H. S. Yu, S. L. Li, and D. G. Truhlar. *J. Chem. Phys.* **145**, 130901 (2016).

[29] W. Kohn and L. J. Sham. *Phys. Rev.* **140**, A1133 (1965).

[30] M. Levy. *Proc. Natl. Acad. Sci.* **76**, 6062 (1979).

[31] R. M. Dreizler and E. K. U. Gross. *Density Functional Theory: An Approach to the Quantum Many-Body Problem*. 1990.

[32] P. W. Atkins. *Molecular Quantum Mechanics*. 1983.

[33] W. Kohn and P. Vashishta. *Theory of Inhomogeneous Electron Gas*. 1963.

[34] D. J. Singh and L. Nordrtröm. *Plane waves, pseudopotentials and the LAPW method*. 1994.

[35] D. M. Ceperley and B. J. Alder. *Phys. Rev. Lett.*, **45**, 566 (1980).

[36] J. C. Slater. *Phys. Rev.* **81**, 385 (1951).

[37] P. A. M. Dirac. *Proc. Camb. Phil. Soc.* **26**, 376 (1930).

[38] J. P. Perdew, K. Burke, and M. Ernzerhof. *Phys. Rev. Lett.* **77**, 3865(1996).

[39] A. Becke. *Phys. Rev. A* **38**, 3098 (1988).

[40] C. T. Lee, W. T. Yang, and R. G. Parr. *Phys. Rev. B* **37**, 785 (1988).

[41] Y. Zhao and D. G. Truhlar. *J. Chem. Phys.* **128**, 184109 (2008)

[42] S. K. Ma and K. A. Brueckner. *Phys. Rev.* **165**, 18 (1968).

[43] D. C. Langreth and. J. Mehl. *Phys. Rev. B* **28**:1809, 1983.

[44] J. P. Perdew. *Phys. Rev. B* **33**, 8822 (1986).

[45] J. P. Perdew. *Physica B*, **172**, 1 (1991).

[46] J. P. Perdew. *Electronic Structure of Solids*. 1991.

[47] J. Tao, J. P. Perdew, V. N. Staroverv, and G. E. Scuseria. *Phys. Rev. Lett.* **91**, 146401 (2003).

[48] J. P. Perdew, V. N. Staroverov, J. Tao, and G. E. Scuseria. *Phys. Rev. A* **78**, 052513 (2008).

[49] H. J. Kulik. *J. Chem. Phys.* **142**, 240901 (2015).

[50] J. Hubbard. *Proc. Roy. Soc. Lond. A* **276**, 238 (1963).

[51] J. Hubbard. *Proc. Roy. Soc. Lond. A* **277**, 237 (1964).

[52] J. Hubbard. *Proc. Roy. Soc. Lond. A* **281**, 401 (1964).

[53] J. Hubbard. *Proc. Roy. Soc. Lond. A* **285**, 542 (1965).

[54] J. Hubbard. *Proc. Roy. Soc. Lond. A* **296**, 82 (1967).

[55] V. I. Anisimov, J. Zaanen, and O. K. Anderen. *Phys. Rev. B* **44**, 943 (1991).

[56] D. D. O'Regan, N. D. M. Hine, M. C. Payne, and A. A. Mostofi. *Phys. Rev. B* **85**, 085107 (2012).

[57] V. I. Anisimov and O. Gunnarsson. *Phys. Rev. B* **43**, 7570 (1991).

[58] H. J. Kulik and N. Marzari. *J. Chem. Phys.* **133**, 114103 (2010).

[59] N. J. Mosey and E. A. Carter. *Phys. Rev. B* **76**, 155123 (2007).

[60] M. Cococcioni and S. de Gironcoli. *Phys. Rev. B* **71**, 035105 (2005).

[61] H. J. Kulik, M. Cococcioni, D. A. Scherlis, and N. Marzari. *Phys. Rev. Lett.* **97**, 103001 (2006).

[62] H. J. Kulik, and N. Marzari. *J. Chem. Phys.* **135**, 194105 (2011).

[63] L. Wang, T. Maxisch, and G. Ceder. *Phys. Rev. B* **73**, 195107 (2006).

[64] C. Loschen, J. Carrasco, K. Neyman, and F. Illas. *Phys. Rev. B* **75**, 035115 (2007).

[65] M. Huang and S. Fabris, *J. Phys. Chem. C* **112**, 8643 (2008).

[66] S. Cottenier. *Density Functional Theory and the family of (L)APW methods: a step-by-step introduction*. 2013.

[67] B. Himmetoglu, A. Floris, S. Gironcoli, and M. Cococcioni. *Int. J. Quantum Chem.* **114**, 14 (2014).

[68] J. C. Slater. *Phys. Rev.* **51**, 846, (1937).

[69] T. L. Loucks. *Augmented Plane Wave Method*. 1967.

[70] O. K. Andersen. *Phys. Rev. B* **12**, 3060 (1975).

[71] S. Blügel and G. Bihlmayer. *Full-Potential Linearized Augmented Plane wave Method*. 2006.

[72] D. J. Singh. *Phys. Rev. B* **43**, 6388 (1991).

[73] E. Sjöstedt, L. Nordström, and D. J. Singh. *Solid State Commun.* **114**, 15 (2000).

[74] G. K. H. Madsen, P. Blaha, K. Schwarz, E. Sjörstedt, and L. Nordström. *Phys. Rev. B* **64**, 195134 (2001).

[75] D. R. Hamann. *Phys. Rev. Lett.,* **212**, 662 (1979).

[76] E. Wimmer, H. Krakauer, M. Weinert, and A. J. Freeman. *Phys. Rev. B*, **24**, 864 (1981).

[77] P. Blaha, K. Schwarz, G. Madsen, D. Kvasnicka, and J. Luitz, *Wien2k, an Augmented Plane Wave Plus Local Orbitals Program for Calculating Crystal Properties*. Techn. Universität, Vienna, Austria, 2001, ISBN 3-9501031-1-2. http://www.wien2k.at.

[78] K. Schwarz, P. Blaha, and S. B. Trickey. *Mol. Phys.* **108**, 3147 (2010).

[79] K. Schwarz and P. Blaha. *Comput. Mater. Sci.* **28**, 259 (2003).

[80] K. Schwarz, P. Blaha, and G. K. H. Madsen. *Comput. Phys. Commun.* **147**, 71 (2002).

CHAPITER III

Pure rare-earths R (R = Gd and Tb): structural, electronic, and magnetic properties

The heavy rare earth elements share a common outer electronic configuration, differing only in the number of inner 4f electrons they have . Based on the wealth of experimental information available for the rare-earths [1], it is by now established that the 4f shell has localized electron states, where band-dispersion effects are negligible.

Since there are f electrons in the metal atoms, nonmagnetic (NM), and ferromagnetic (FM) states are all considered to obtain the ground-state properties of the rare earth compounds.

In this Chapter, we have also focused our investigation on the structural, electronic and magnetic properties of rare earth gadolinium (Gd) and terbium (Tb), which have been investigated extensively using first-principles calculations and where f electrons are considered. A theoretical treatment of f electrons is sometimes arduous [2]. For that the 4f electrons are treated independently as core electrons in the former case (nonmagnetic) and as valence electrons in the latter case (ferromagnetic).

III-I Non spin-polarized study

III-I-1 Computational methods

Our calculations are based on density functional theory (DFT) [3, 4]. The full potential linearized augmented plane wave (FP-LAPW) method as implemented in the WIEN2k package [5], which solves the Kohn-Sham equations self-consistently, was used for the calculations. The cutoff in the charge density Fourier expansion, G_{max}, was taken to be 20 $Ry^{1/2}$, where 1 Ry = 13.60570 eV.

Rare earths can be problematic for DFT calculations. We note that one can expect the existence of finite localized magnetic moments on the *4f* electrons. This magnetic aspect has not been considered in our calculations in this section. It is known, indeed, that, in rare earths, the *4f* electrons, being very close to the core, are expected to be chemically inert. This leads us to consider *4f* electrons as atom-core electrons, i.e. they cannot hybridize with the other *s*, *p*, and *d* valence electrons anymore and are perfectly localized [6]. For these reasons, the contribution of the *4f* electrons are removed from the valence bands, and are treated as those of core electrons.

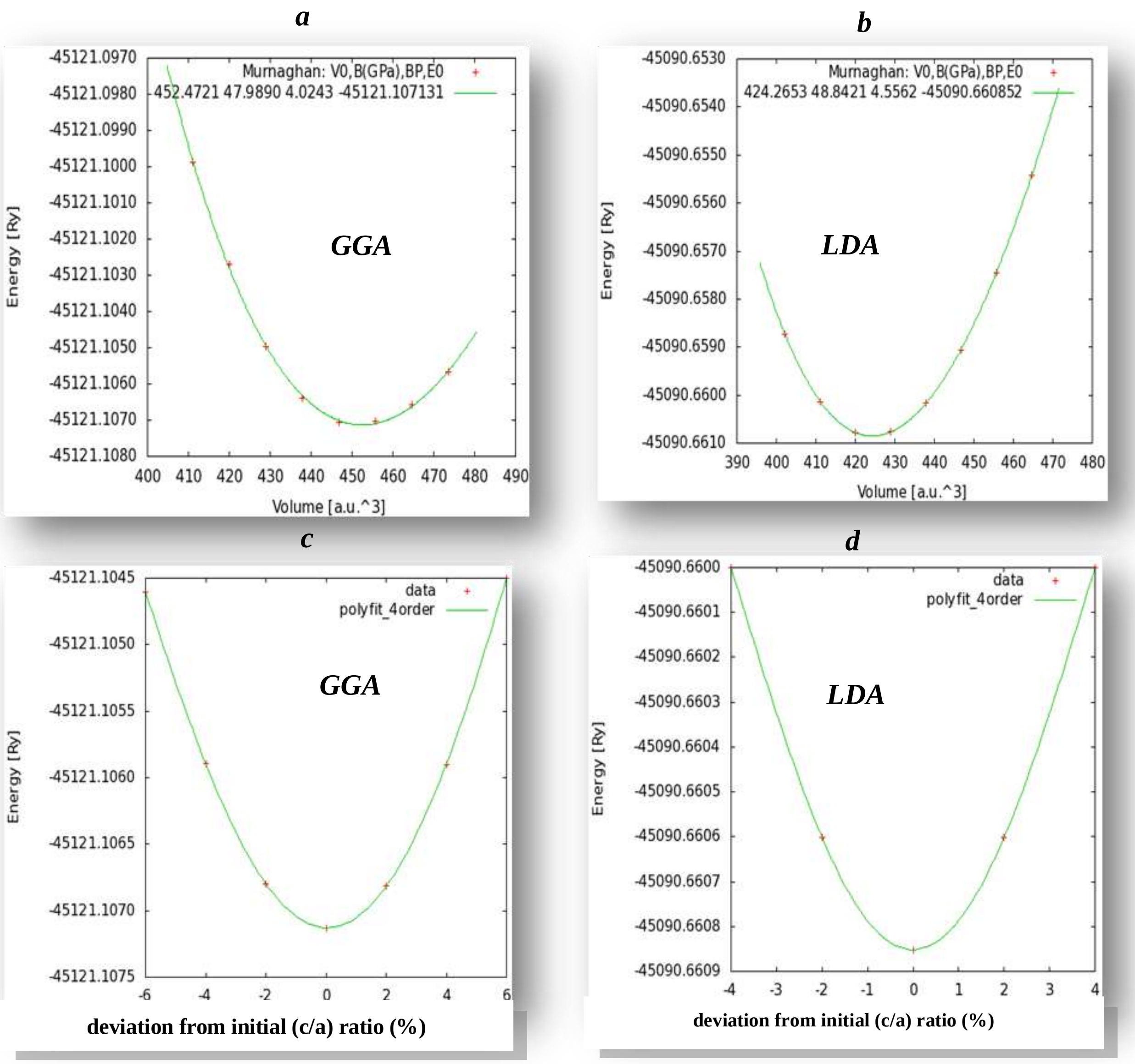

Fig. III-1 Calculated total energy curves for Gd as a function of volume in both GGA (a) and LDA (b), and as function of deviation from initial (c/a) ratio (%) in both GGA (c) and LDA (d) approximations.

We used an energy of -8 Ry to separate core and valence states, while the Gd ($5s^25p^65d^16s^2$) and Tb ($5s^25p^65d^16s^2$) orbitals were treated as valence states (we did not treat the *f* orbitals of Gd and Tb as valence electrons but as core electrons). Exchange and correlation effects were treated within the density functional with the generalized-gradient approximation of Perdew, Burke and Ernzerhof (GGA96) [7] and the local density approximation (LDA) [8]. The calculations were based on an optimized number of k-points of 1000, without considering the spin polarization. The self-consistent calculations are considered to be converged only when the calculated energy changes by less than 0.1 mRy.

III-I-2 Results and discussion

III-I-2-1 Structural properties

To calculate the ground state properties of R (R = Gd, and Tb) compounds, the total energies are calculated for different volumes around the equilibrium cell volume (V_0) and the (c/a) ratios for both LDA and GGA approximations. The plot of calculated total energies versus reduced and enlarged volume for the Gd and Tb are given in **Figs. III-1 and III-2** respectively.

Table III-1 Equilibrium lattice parameters a_0, c_0 (in Å), bulk modulus B_0 (in GPa), pressure derivative B_0', total energy (Ry) and cohesion energy E_{coh} (eV) for Gd compared to experimental data and other works.

	a_0	***c_0***	***c_0/a_0***	***B_0***	***B_0'***	***Total energy***	***E_{coh}***	***Reference***
LDA	3.5739	5.6838	1,5904	48.842	4.5562	-45090.660852	-10.0307	Present work
	3.4785	5.5799	1.604	37.9				[9]
GGA	3.6513	5.8070	1.5904	47.9890	4.0243	-45121.107131	-8.7921	Present work
	3.6402	5.8258	1.600	36.7				[9]
Exp.	3.634	5.781	1.591					[10]
	3.595	5.785						[11]

The calculated total energy is fitted to Murnaghan's equation of state [12] to determine the ground state properties such as the equilibrium lattice constant (a_0 and c_0), the bulk modulus (B_0), and its pressure derivative (B_0'), total energy and cohesion energy. The calculated equilibrium parameters found using LDA and GGA-PBE approximations are given in **Tables III-1** and **III-2** for Gd and Tb respectively, which also contains experimental and theoretical data for comparison. It is worth noting that the value of (E_0) using the LDA approximation is less than its value is using the GGA approximation.

We should emphasize that our calculated *a*-lattice constants, *c*-lattice constants and the (*c/a*) ratio show agreement with the experimental data and the previous theoretical results. However, it may be noted here that the LDA calculations for lattice parameters are underestimated by comparison to experimental results and GGA calculations are overestimated. Conversely for the bulk modulus, it is the GGA value which is lower than that of the LDA by *1.75%* for Gd and by *19.87%* for Tb as a result of the over-binding characteristic of LDA.

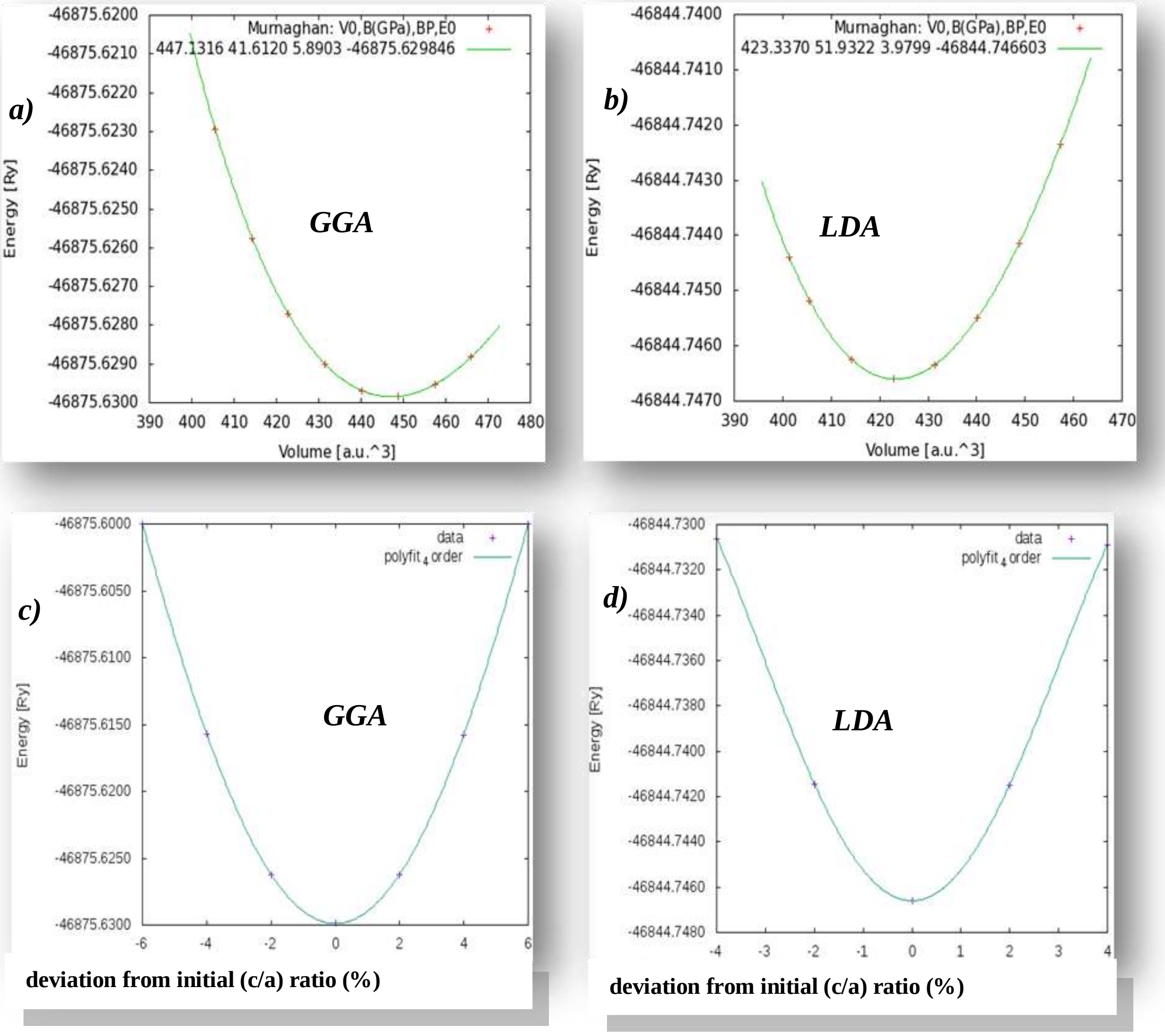

Fig. III-2 Calculated total energy curves for Tb as a function of volume in both GGA (a) and LDA (b), and as function of deviation from initial (c/a) ratio (%) in both GGA (c) and LDA (d) approximations.

Hence, GGA overestimates the lattice parameter whereas it underestimates bulk modulus (B_0) in comparison with LDA. These results are consistent with the general trends of the LDA and GGA approximations [9, 13 and 14].

Table III-2 Equilibrium lattice parameters a_0, c_0 (in Å), bulk modulus B_0 (in GPa), pressure derivative B_0', total energy (Ry) and cohesion energy E_{coh} (eV) for Tb compared to experimental data and other works.

	a₀	***c₀***	***c₀/a₀***	***B₀***	***B₀'***	***Total energy***	***E*coh**	***Reference***
LDA	3.5782	5.6576	1.5811	51.9322	3.9799	-46844.746603	-9.9121	Present work
	3.3669	5.4632	1.623	40.5				[9]
GGA	3.6440	5.7616	1.5811	41.6120	5.8903	-46875.629846	-8.7017	Present work
	3.5851	5.7809	1.612	27.5				[9]
Exp.	3.606	5.697	1.580					[10]

The cohesive energy, E_{coh}, of a solid is defined as the minimum energy required for separating it into its constituent (neutral) atoms (or molecules, if we are dealing with a molecular solid) under conditions of temperature T → 0 K and pressure P = 1 atm:

$$E_{coh}(R) = E_R^{bulk} - E_R^{atom}, \qquad \text{[III-1]}$$

where E_R^{bulk} is the total energy of the compound at the equilibrium lattice constant and E_R^{atom} is the atomic energies of the pure constituent atoms which is calculated using the same GGA /LDA framework. The cohesive energy values of Gd and Tb are also displayed in **Tables III-1** and **III-2**. From the latter, it is observed that the absolute values of cohesive energy of both compounds calculated by LDA are higher than those calculated by GGA due to the above-mentioned over-binding effect.

III-I-2-2 Electronic properties

Band structures, densities of states, and partial electron densities have been employed in order to get a better understanding of the chemical bonding in these rare earth compounds.

The calculated electronic band structures along the high symmetry directions in the Brillouin zone and corresponding total density of states for Gd and Tb with GGA and LDA approximations are shown in **Figs. III-3** and **III-4** respectively, from these figures, the R has a metallic character because of the absence of gap at the Fermi level in both GGA and LDA approximations.

As we can see from **Figs. III-3** and **III-4**, the calculated band structures of R with LDA are similar to those with GGA, but there are some differences as the valence bands calculated by LDA are slightly larger than those calculated by GGA approximation for both compounds.

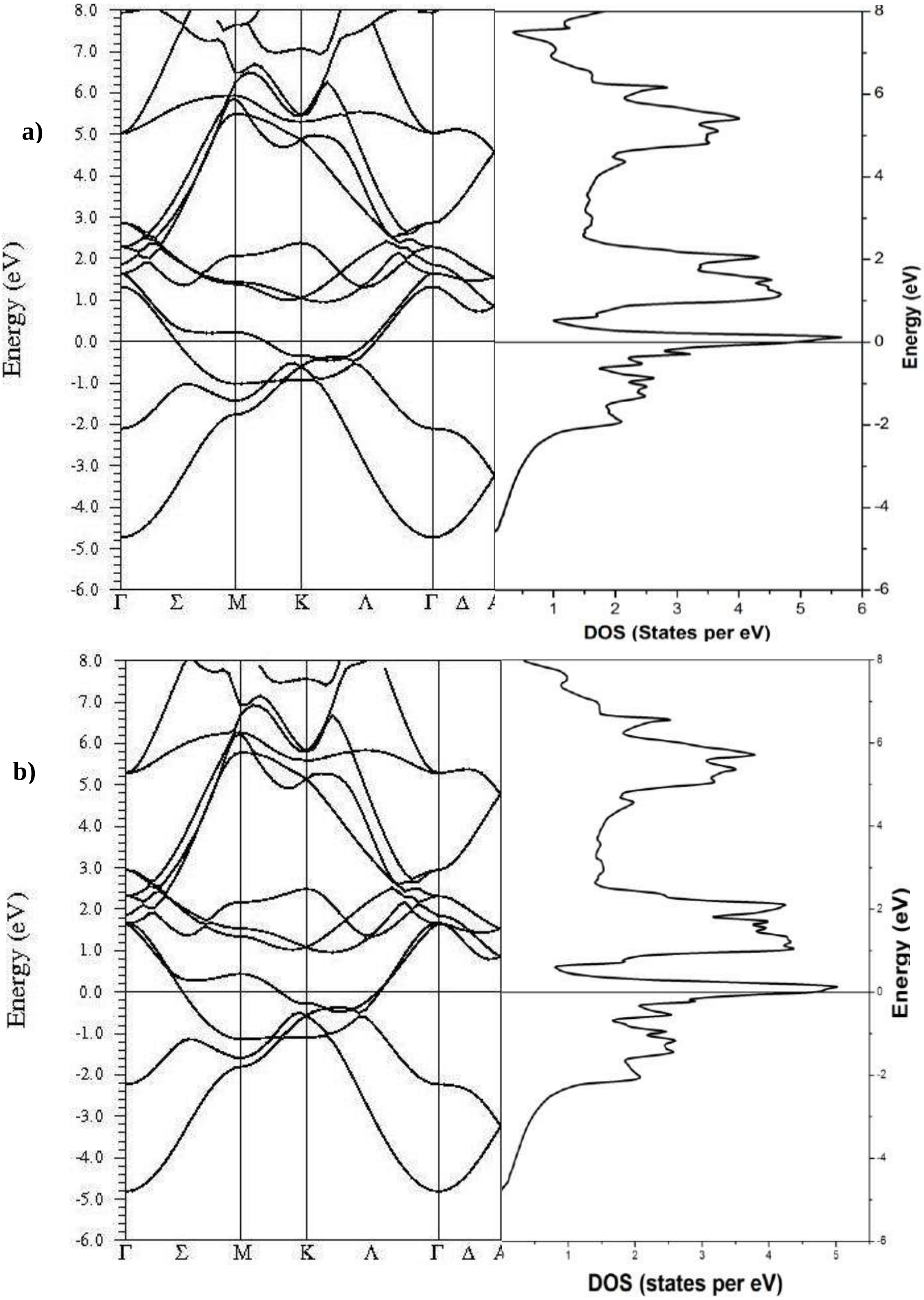

Fig. III-3 Density of states (right panel) and electronic band structure along high-symmetry directions (left panel) of Gd in: **a**) GGA and **b**) LDA; the Fermi energy is at 0 eV.

The total DOS of R (R=Gd, Tb) has similar features in both GGA and LDA (see **Figs. III-3** and **III-4**) especially at the Fermi level. However, these figures show small but non negligible differences as the peaks in the GGA are slightly sharper and narrower than those of LDA. Also in LDA, the total DOS moves a little towards lower energies and the Fermi energy increases compared to GGA.

The total electronic DOS along with the partial electronic DOS reveal all important features of band structures.

The *l*-projected density of states (DOS) plots (**Figs. III-5** and **III-6**) provides an even clearer picture of the elemental contributions to the electronic structure of R (R=Gd, Tb). Generally speaking, under crystal field effects (hcp symmetry) the orbital *d* consists of: *d-z2*, (*d-xy*, *d-x2y2*), and (*d-xz*, *d-yz*) states, and the orbital *p* consists of: *p-z* and (*p-x*, *p-y*).

As one can see, those top valence states right below the Fermi level are predominantly R-*5d* states. The R-*p* states, however, also make a noticeable contribution where the contribution of *s* states is negligible. This suggests that *d* states of rare-earth atoms play dominant roles in the metallic nature of the two compounds. Note here that in our calculation all *d-z2*, *dx2y2+Dxy*, and *dxz+Dyz* states participate at Fermi energy in addition of participates of the hybridization with *p-z* and *px+ py* states.

Table III-3 Fermi energy and density of states at the Fermi level for Gd.

	Fermi energy (Ry)	***N(E_F) (states/Ry)***
Gd (GGA)	0.40705	66.80
Gd (LDA)	0.42586	63.83

Table III-4 Fermi energy and density of states at the Fermi level for Tb.

	Fermi energy (Ry)	***N(E_F) (states/Ry)***
Tb (GGA)	0.34204	63.45
Tb (LDA)	0.34763	62.04

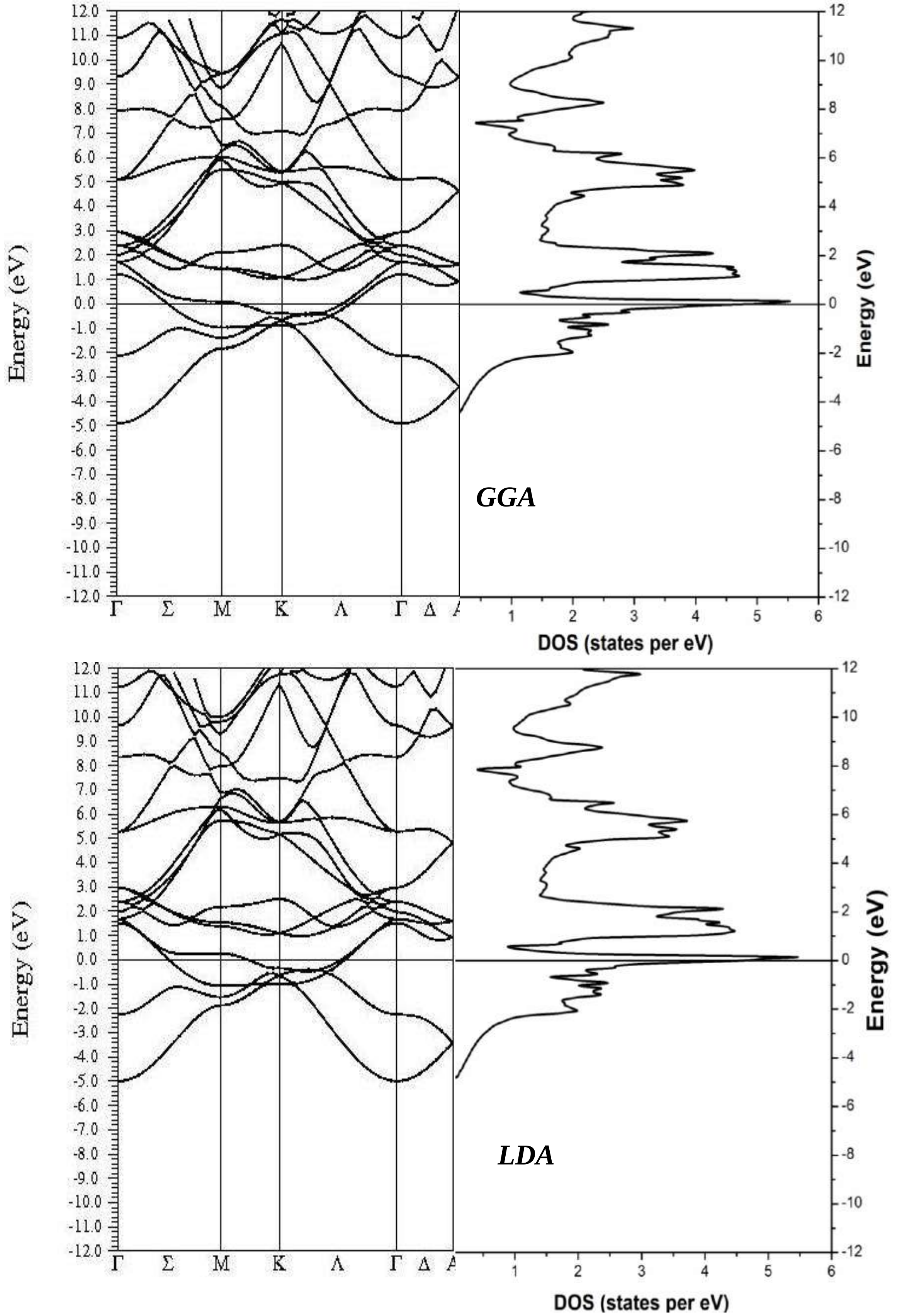

Fig. III-4 Density of states (right panel) and electronic band structure along high-symmetry directions (left panel) of Tb in the GGA and LDA, the Fermi energy being at 0 eV.

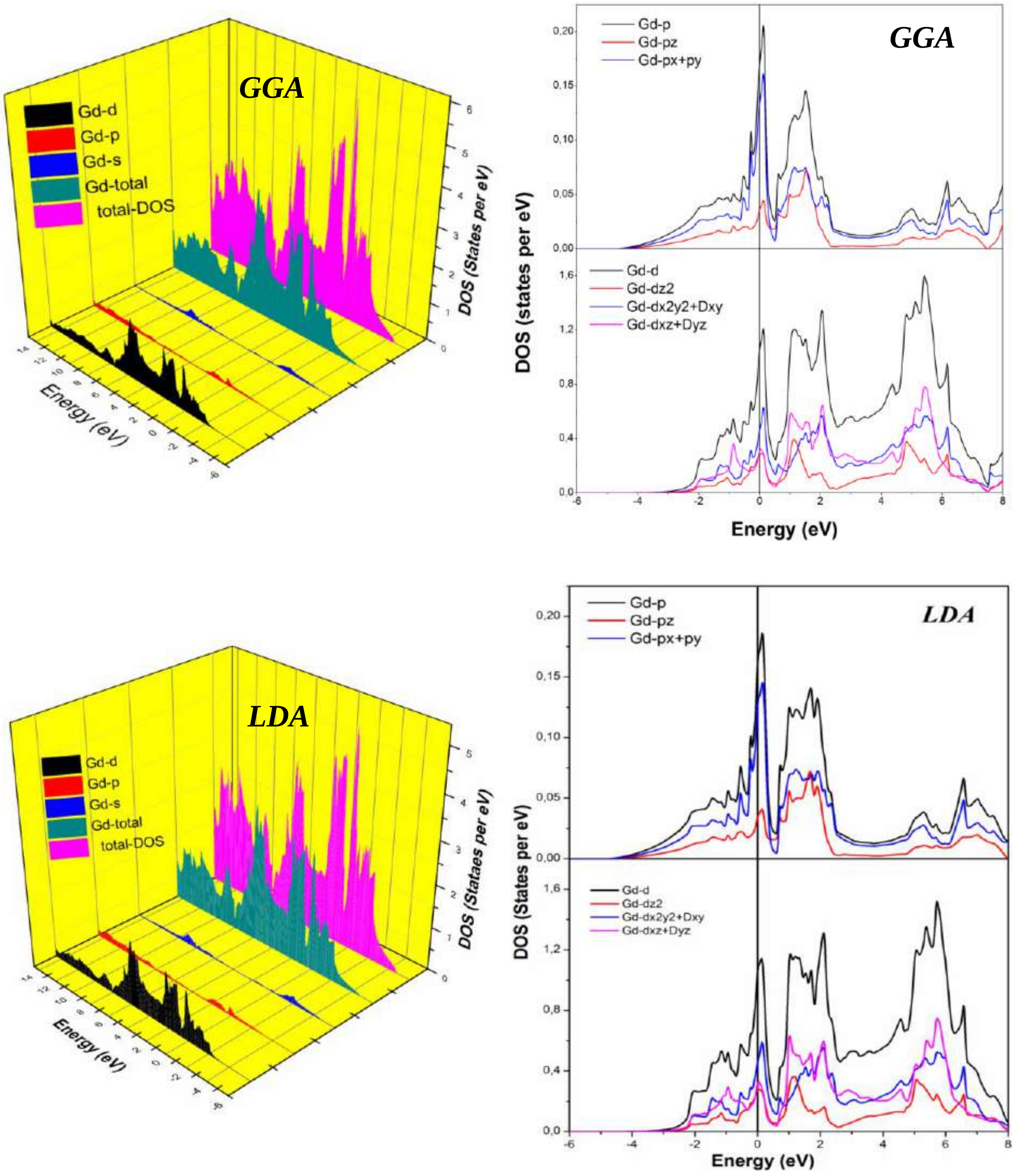

Fig. III-5: The calculated total and partial density of states for Gd in the GGA and in the LDA, the Fermi energy being at 0 eV.

According to the data in **Tables III-3** and **III-4**, the density of states on the Fermi level $N(E_F)$ is not negligible and is smaller in LDA than in GGA because the latter causes an under-binding effect of the crystal (the crystal structure is more compact in LDA). In addition, it can be remarked that when the equilibrium lattice parameter decreases, the Fermi energy increases in both compounds.

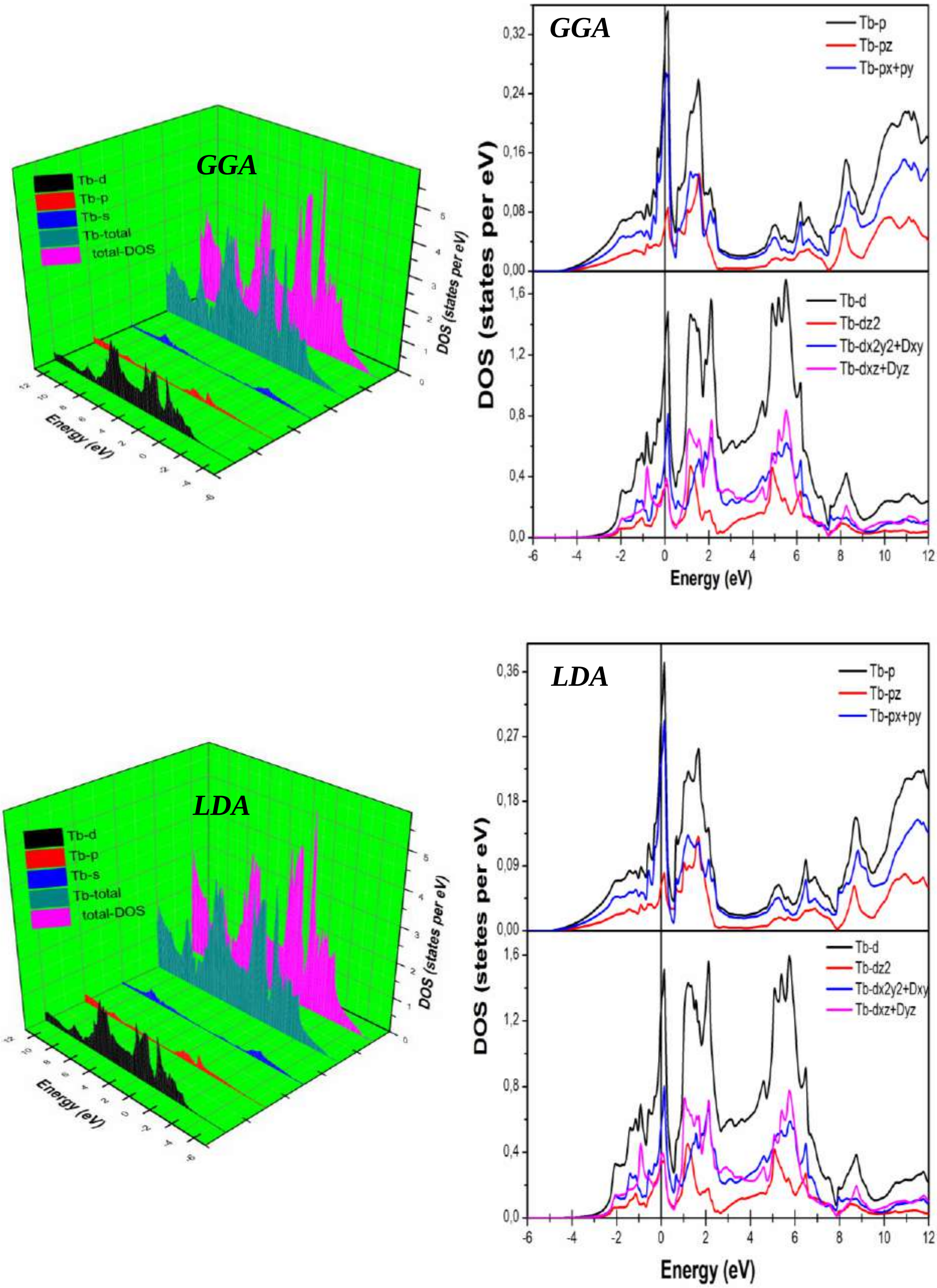

Fig. III-6: The calculated total and partial density of states for Tb in the GGA and LDA, the Fermi energy being at 0 eV.

III-II Spin polarized study

In this subsection we will analyze the influence of the polarization of spins. All LDA and GGA calculations reported above are done without spin polarized coupling. However, for the magnetic properties to which the *4f*-electron contribution is crucial, magnetic coupling effects must be included. Note that the magnetic ground states of these compounds R (R=Gd, and Tb) are of a ferromagnetic type [15].

III-II-1 Spin polarized GGA and LSDA

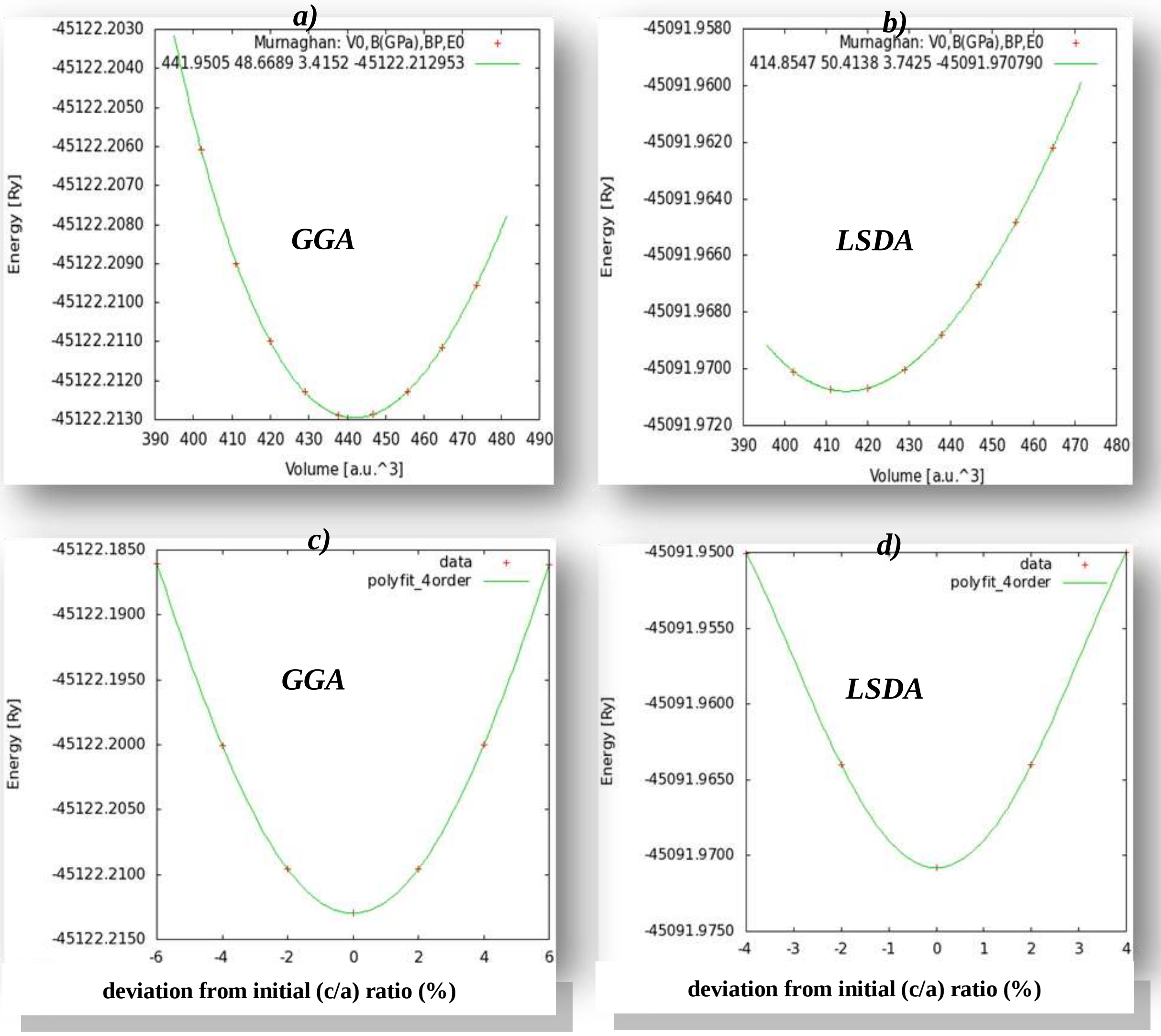

Fig. III-7 Calculated total energy curves (spin polarized calculation) for Gd as a function of volume in both GGA (a) and LSDA (b), and as function of deviation from initial (c/a) ratio (%) in both GGA (c) and LSDA (d) approximations.

III-II-1-1 Computational details

The presence of *f*-state electrons in these compounds inducing high electron correlations in these materials lead us to study these systems using spin local density approximation (LSDA) [16] and the PBE GGA exchange-correlation functional for the ferromagnetic state within a hexagonal structure, where the space group is *P 63/mmc* (*No. 194*).

The Kohn-Sham equations of the LSDA and GGA were also solved using the full potential linearized augmented plane-wave (FLAPW) method [17, 18] as implemented in the WIEN2k [6] code. It would be nice to describe the states ($4f^7\ 5s^2 5p^6 5d^1\ 6s^2$) of Gd and ($4f^8\ 5s^2 5p^6 5d^1\ 6s^2$) of Tb as the valence states. The cutoff energy, which defines the separation of valence and core states, was chosen as -8 Ry. Taking a convergence energy of 10^{-4}Ry, the number of k-point parameters were optimized to 1000 k-points.

II-II-1-2 Structural properties

The calculated lattice constants (a_0, c_0), bulk modulus (B_0), the pressure derivative of bulk modulus (B_0'), for Gd and Tb using spin polarized GGA and LSDA, are obtained according to Murnaghan's equation of state [12] and by fitting the total energy to volume points. We also present the E−V relationship of the R (R=Gd, and Tb) in **Figs. III-7** and **III-8**. The cohesive energies of this compound are calculated from the difference between the total atomic energies of Gd and Tb atoms and the minimum energy of bulk Gd and Tb.

Table III-5 Equilibrium lattice parameters a_0 and c_0 (in Å), bulk modulus B_0 (in GPa), pressure derivative B_0', total energy (Ry), and cohesive energy E_{coh} (eV) for Gd obtained with GGA and LSDA calculations, compared to experimental data and other works.

	a_0	c_0	c/a	B_0	B_0'	*Total energy*	E_{coh}	*Reference*
LSDA	3.5472	5.6414	1.5904	50.4138	3.7425	-45091.970790	-8.022	Present work
	3.62	5.80						[19]
GGA	3.6228	5.7617	1.5904	48.6689	3.4152	-45122.212953	-6.8809	Present work
	3.502	5.727		49	4.01			[20]
Exp.	3.595	5.785						[11]

The calculated ground state properties for Gd and Tb are listed in **Tables III-5** and **III-6** respectively and are compared with the experimental and other available theoretical data. The cohesive energies of these compounds are also displayed in these Tables.

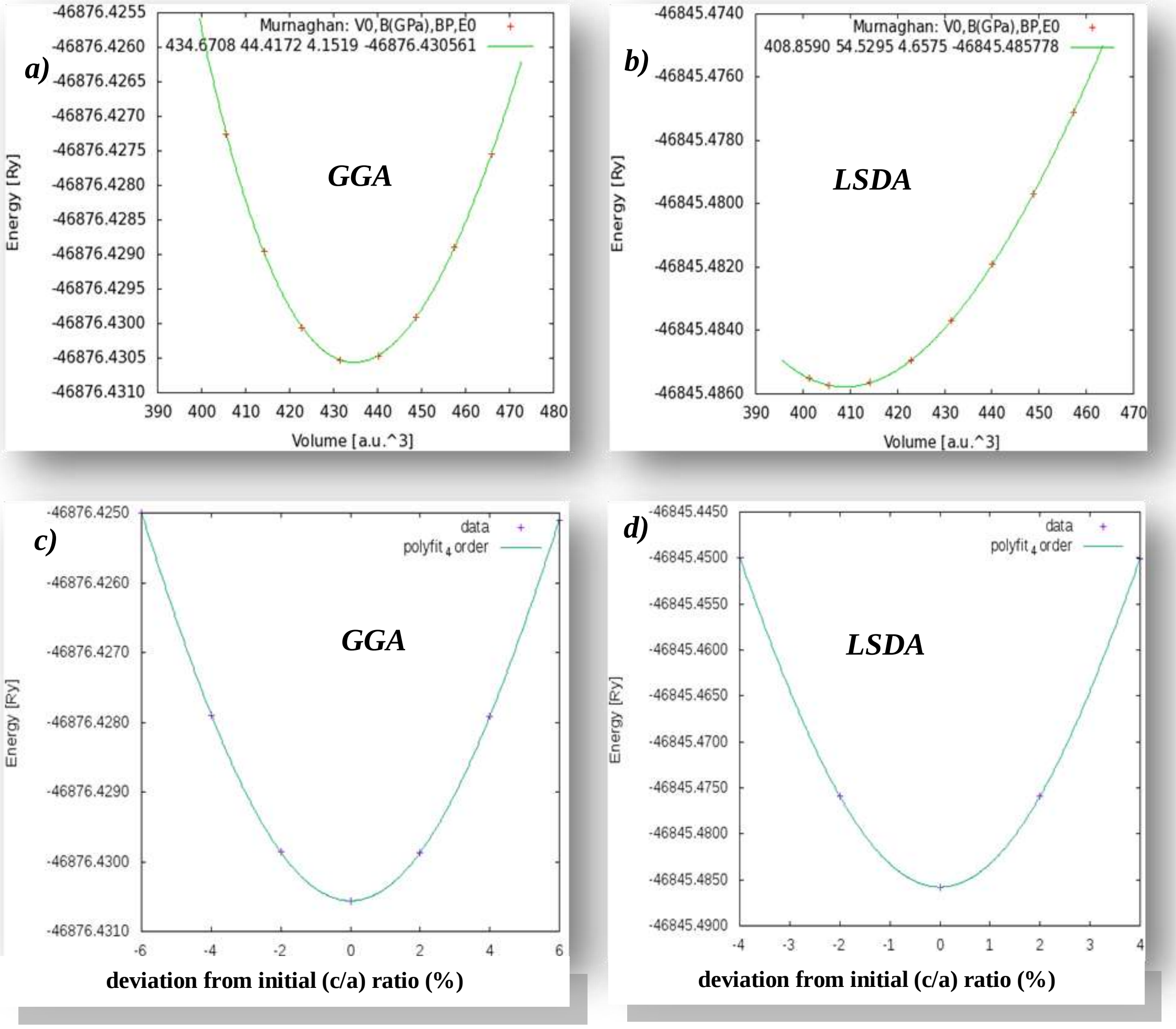

Fig. III-8 Calculated total energy curves (spin polarized calculation) for Tb as a function of volume in both GGA (a) and LSDA (b), and as function of deviation from initial (c/a) ratio (%) in both GGA (c) and LSDA (d) approximations.

From **Tables III-5** and **III-6**, it is found that the present calculations are in agreement with the experimental and other theoretical results. The calculated values of (c/a) are slightly less than the ideal value of $\sqrt{8/3}$.

For lattice parameters the results of GGA method, however, are closer to the experimental results than the results obtained from LSDA approximation. It is also worth noting that the values within the LSDA method are underestimated, while the values within

GGA approximation are overestimated. In contrast, the value of the bulk modulus in LSDA is larger than that in GGA for both compounds. In addition from **Table III-6** (for Gd), bulk modulus and its first-order derivative show good agreement with available literature values.

Table III-6 Equilibrium lattice parameters a_0 and c_0 (in Å), bulk modulus B_0 (in GPa), pressure derivative B_0', total energy (Ry), and cohesive energy E_{coh} (eV) for Tb obtained with GGA and LSDA calculations, compared to experimental data and other works.

	a₀	***c₀***	***c/a***	***B₀***	***B₀'***	***Total energy***	***Ecoh***	***Reference***
LSDA	3.5369	5.5923	1.5811	54.5295	4.6575	-46845.485778	-7.4401	Present work
GGA	3.6099	5.7076	1.5432	44.4172	4.1519	-46876.430561	-8.7017	
Exp.	3.606	5.697	1.580					[10]

The obtained ground state from optimization curves is used to calculate self-consistently electronic and magnetic properties (densities of states, band structure, and magnetic moment) of the considered rare earths within the two approximations with a comparative context.

III-II-1-3 Electronic properties

The calculated spin-polarized band structures at the theoretical equilibrium lattice constant along high-symmetry directions of the first Brillouin zone with GGA and LSDA approximations of Gd and Tb compounds are shown in **Figs. III-9** and **III-10** respectively.

In the GGA and LSDA (see **Figs. III-9** and **III-10**), both valence bands and conduction bands cross the Fermi level and lead to its partial filling, thus both GGA and LSDA predict a metallic behavior for R (R=Gd, and Tb).

Generally speaking, in compounds, the charge distribution due to anions surrounding the metal ion induces a static electric field, named ligand-field, or crystal field, which produces a splitting of the energy levels occupied by localized electrons. The angular part of the crystal field parameters reflects the influence of the spatial arrangement of the anions. The rare-earth *5d* electron interacts strongly with the surrounding anions, making the *4f–5d* excitation energy depend on the bonds. Owing to the crystal field, the energy difference between *d* orbitals varies; it increases with oxidation number. Inversely, the energies of the *4f* orbitals are barely sensitive to the crystal field and the 4*f* orbital moments are not quenched by it. With regard to *4f* energy levels in rare-earth ions, their crystal field splitting is generally not taken into account because it is much smaller than the splitting due to the spin–orbit interaction (*J*), which is strong in many of the rare-earth compounds. Indeed, partly filled *4f* orbital behave like localized magnetic moments [21].

GGA

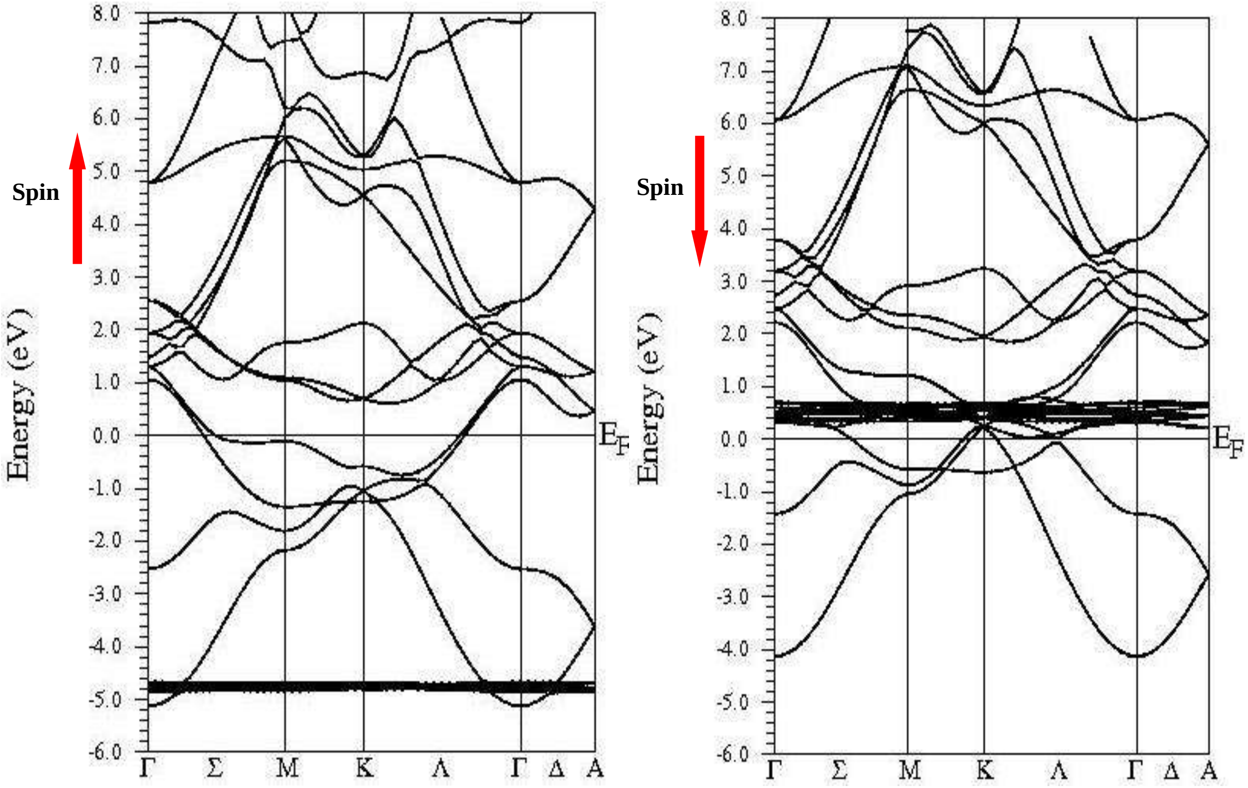

LSDA

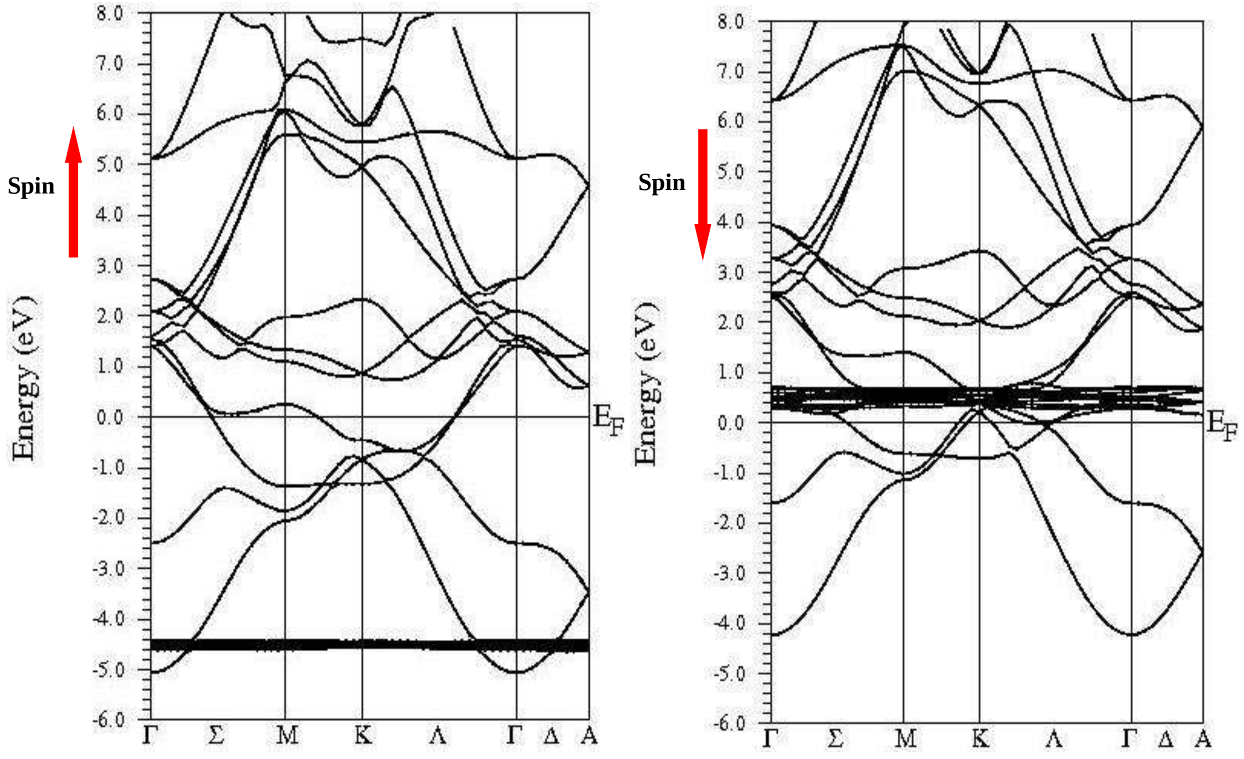

Fig.III-9 Spin dependent band structures for Gd in both spin polarized GGA and LSDA approximations, the Fermi energy being at 0 eV.

GGA

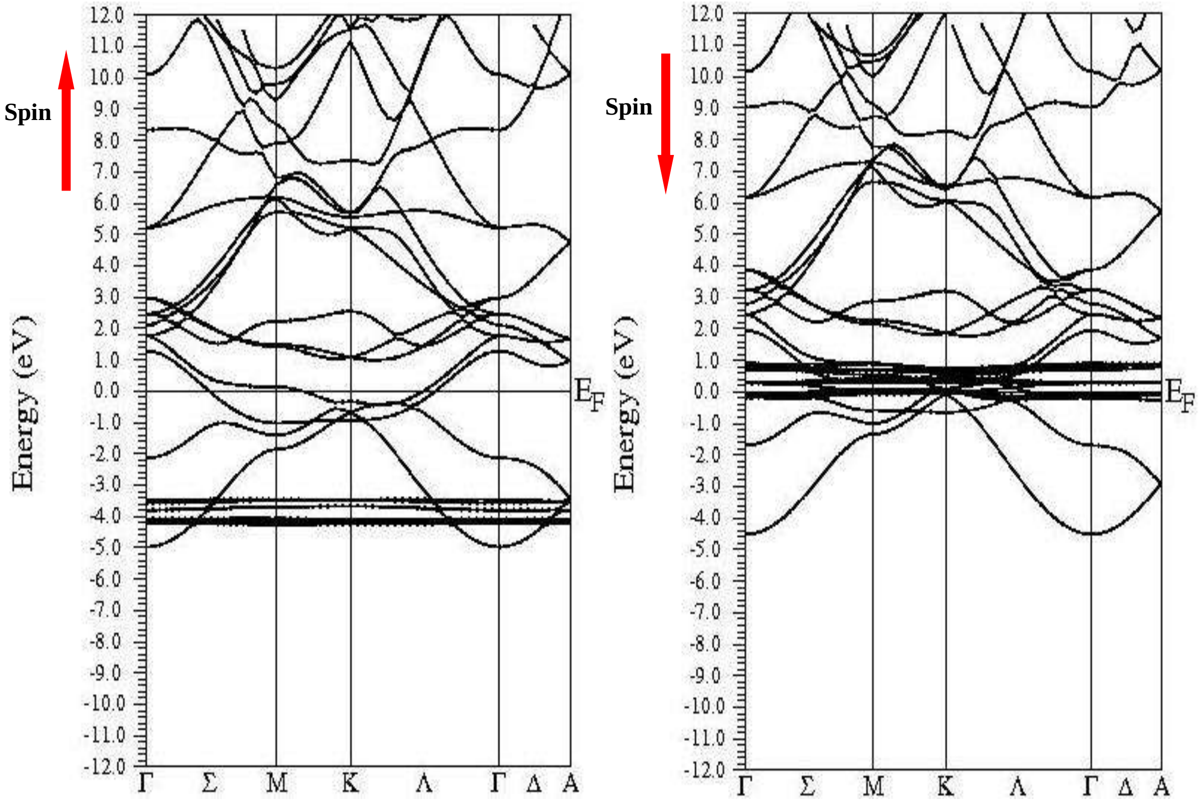

LSDA

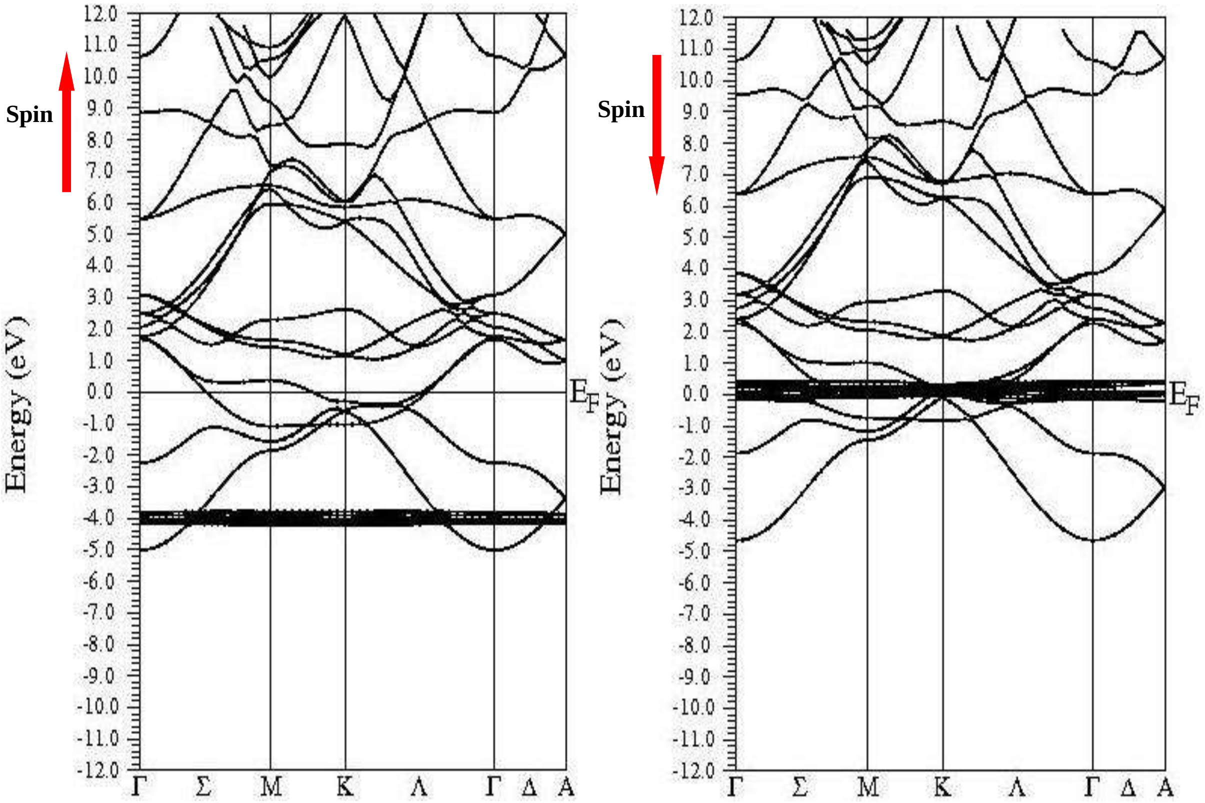

Fig. III-10 Spin dependent band structures for Tb in both spin polarized GGA and LSDA approximations, the Fermi energy being at 0 eV.

Comparing the band structures of spin up states to that of spin down states for R (R=Gd, and Tb) (**Figs. III-9** and **III-10**) in both approximations, we found that the band structures of spin up states shift towards bonding states at lower energies compared to that of spin down states. It is known that the 4*f* bands are generally very narrow, and significantly different from the bands dominated by *s*, *p* and *d* states. Therefore there exist strong on-site Coulomb repulsions between the highly localized *f* electrons [22, 23]. From **Figs. III-9** and **III-10**, we see that the 4*f* bands in the band structures of spin up states are positioned above the bottom of the valence band while in the band structures of spin down states are positioned in the bottom of the conduction band. As we can see from **Figs. III-9** and **III-10**, the band structures of R (R=Gd and Tb) in GGA are similar to those in LSDA. The major differences arise from the valence band of the majority spin (spin up) channel, where in **Fig. III-9** (for Gd), along the Γ-M direction, the number of bands below E_F are *5* in GGA while in LSDA they are *4* bands, and in **Fig. III-10** (for Tb) the occupied *4f* bands are split further due to spin–orbit coupling (as illustrated above), leading to better agreement with experiments [24] where the *4f* bands in GGA are wider than those in LSDA.

The spin polarized total and partial density of states DOSs for R (R=Gd, and Tb) in the GGA and LSDA are calculated to explain the origin of the electronic bands and reveal the contribution of different orbitals in the band structures. The total and partial densities of states, in which the spin-up and spin-down are indicated, are shown in **Figs. III-11** and **III-12** for Gd and **Fig. III-13** for Tb. The Fermi level set as 0 eV. From these figures it is seen that the metallic behavior in the majority spin (spin up) channel is dominated by only the *d*-states of the R (R=Gd, and Tb), whereas, in the minority spin (spin down) channel, it is mainly due to the contribution from R-*d* and *f* state electrons at the Fermi level. However, due to the highly localized character of the *4f*-electrons, it is very unlikely that density of states can have a finite R-*4f* contribution at Fermi level and cross E_F due to the underestimate of Coulomb repulsion of the *4f* electrons in the both GGA and LSDA approximation. Further, the peaks in both the majority and minority spin channel of GGA are sharper when compared to the LSDA.

We note also that the R-*s* and *p* states are located below the Fermi level in both majority and minority spin states; it is found that, in these rare earths, all components (*D-z2*, *Dx2y2+Dxy*, and *Dxz+Dyz*) of the *d* orbital contribute to the Fermi level in both channels.

From the plot of total and partial density of states for the gadolinium (Gd) (**Figs. III-11** and **III-12**) calculated with GGA and LSDA approximations, it can be observed clearly in both approximations two sharp peaks in the *4f*-projected density of states, one corresponding to the majority spin (spin up) channel and the other to the minority spin (spin down) channel.

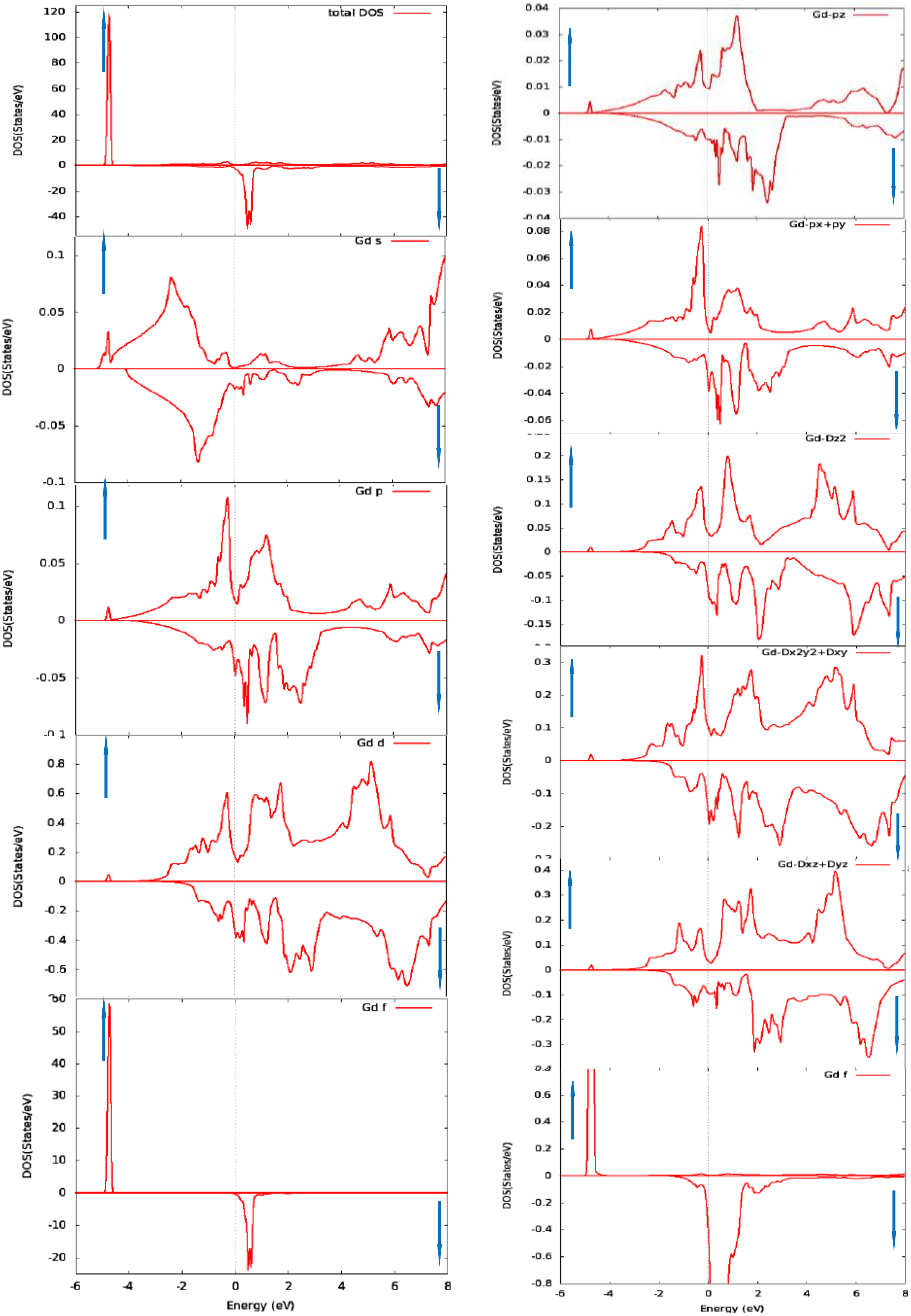

Fig. III-11 Spin dependent total and partial density of states for Gd in GGA approximation (spin polarized study), the Fermi energy being at 0 eV.

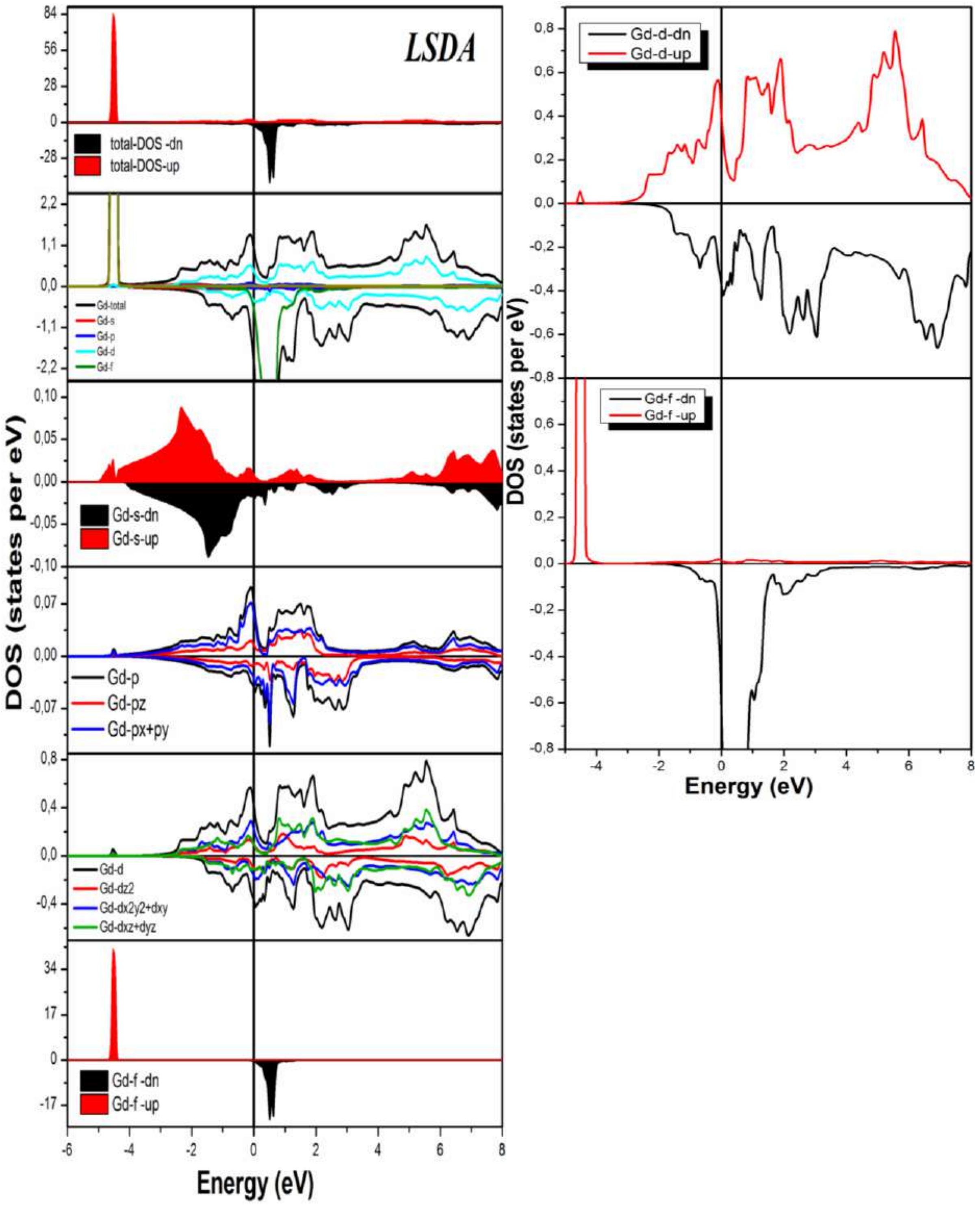

Fig. III-12 Spin dependent total and partial density of states for Gd in LSDA approximation, the Fermi energy being at 0 eV.

It is found that in the majority spin (spin up) channel, the occupied Gd *4f* states are inserted below the Fermi level around *-4.7452 eV* with GGA and around *-4.5324 eV* with LSDA, while in the minority spin (spin down) channel the unoccupied Gd *4f* states are about *0.5067 eV* with GGA and about *0.5018 eV* with LSDA above the Fermi level. Besides, one can immediately notice that the *s*, *p* and *d* states around the Fermi level of GGA shift slightly towards bonding states at lower energies compared to those of LSDA for both the majority and minority spin channel.

It is noted that the total and partial density of states for terbium (Tb) calculated with LSDA are basically the same as those obtained with the GGA (**Fig. III-13**), even though the splitting and the sharpening of Tb-*4f* peaks are noticeably different. The Tb-*4f* peaks in the GGA are sharper and more split than that in the LSDA. In the case of spin up states (see **Fig. III-13**), the bottom of the valence band is occupied by the Tb-*4f* states in the range ~ *-4.33358* to *-3.40839 eV* with GGA and in the range ~ *-4.27372* to *-3.70227 eV* with LSDA. At ~ *-2.15665 eV* with GGA and at ~ *-2.23285 eV* with LSDA, the contribution of Tb-*d* state takes place. In the case of spin down states, the Tb-*d* peak appears at ~ *-1.66685 eV* with GGA and at ~ *-1.82467 eV* with LSDA, and the occupied Tb-*4f* states form a very narrow peak at about *0.55117 eV* with GGA and at about *0.70900 eV* with LSDA below the Fermi level (because it is partially filled). While the unoccupied Tb-*d* and Tb-*f* states are situated above the Fermi level (conduction band).

Table III-7 Fermi energy and density of states at the Fermi level for Gd.

	Fermi energy (Ry)	***N(E$_F$) (states/Ry/spin)***	
		Spin down	***Spin up***
Gd (GGA)	0.41876	28.89	10.12
Gd (LSDA)	0.43112	37.19	24.21

In **Tables III-7** and **III-8**, we report the Fermi energy and density of states at the Fermi level for Gd and Tb in both approximations respectively (values are found in *case.outputtdn* and *case.outputtup* files (case is Gd or Tb)).

Table III-8 Fermi energy and density of states at the Fermi level for Tb.

	Fermi energy (Ry)	***N(E$_F$) (states/Ry/spin)***	
		Spin down	***Spin up***
Tb (GGA)	0.34451	184.94	30.18
Tb (LSDA)	0.35011	185.64	26.88

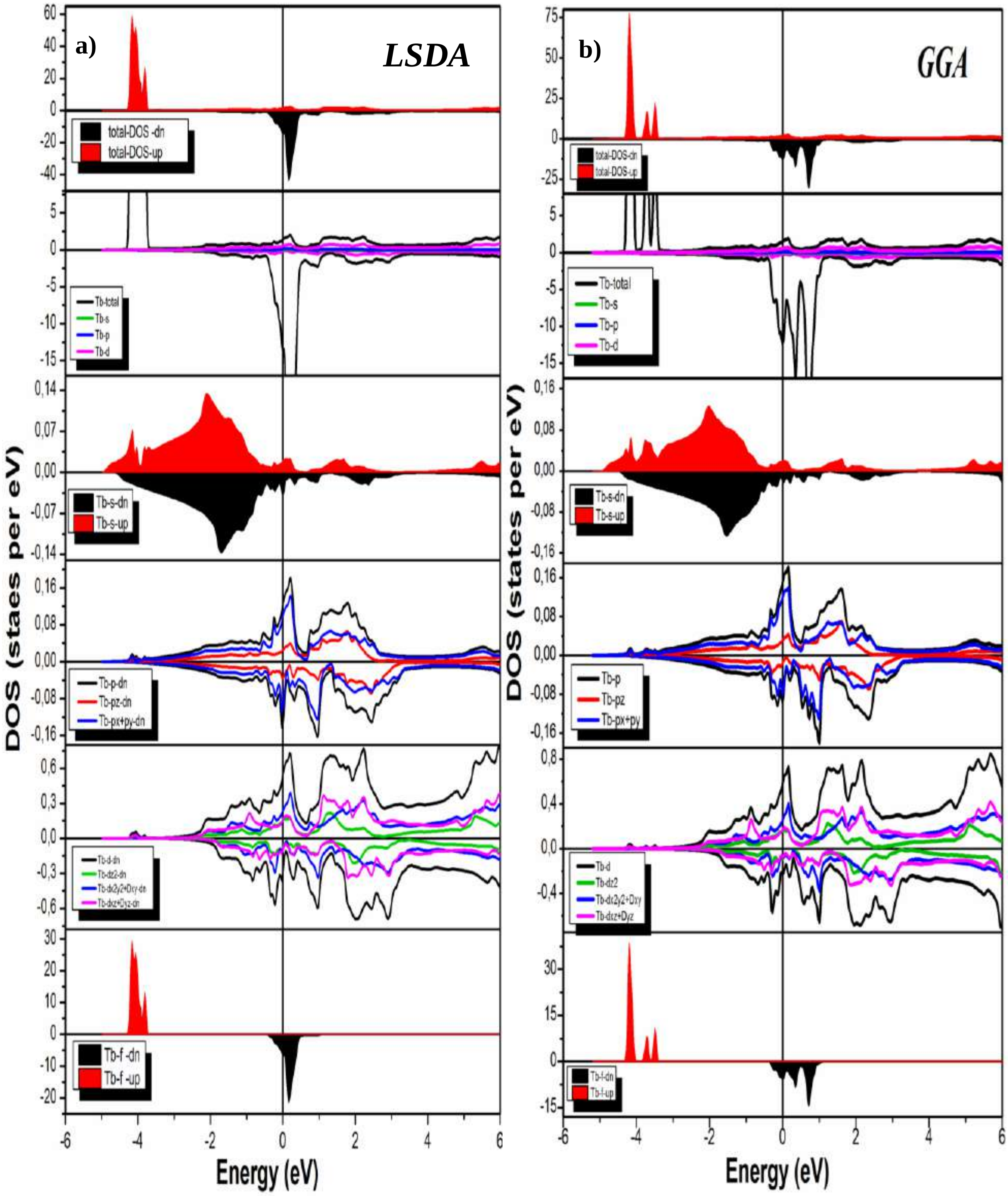

Fig. III-13 Spin dependent total and partial density of states for Tb in: **a**) LSDA and **b**) GGA approximations, the Fermi energy being at 0 eV.

As seen in **Tables III-7** and **III-8**, our density of states results at the Fermi level in the spin down states are higher than those in the spin up states within both approximations. The Fermi energy results in LSDA are higher than those in GGA.

III-II-1-4 Magnetic properties

The rare earth materials have high magnetic moments and form a wide range of magnetic structures.

Owing to its half-filled *4f* shell, the gadolinium ion has orbital angular momentum L=0. Hence the effects of spin orbit coupling can be neglected in our calculations of gadolinium. For the terbium, however, the coupling of spin and orbital moments is important in obtaining estimates of their magnetic moments and magnetic ordering temperatures. Nonetheless, the type of magnetic order and magnetic ordering vector are determined by the *s*, *p*, and *d* conduction electrons, which are little affected by spin-orbit (*J*) coupling which all the heavy rare earths have in common.

Table III-9 Calculated total and partial magnetic moment (in μB (Bohr Magneton)) of the Gd in the ferromagnetic configuration (FM) for hexagonal structure, obtained with GGA and LSDA calculations, and compared to others.

	Magnetic moment in interstitial	***Magnetic moment in Gd atom***	***Spin Magnetic Moment in cell μ_{tot}***	***Reference***
LSDA	0.59647	7.27662	15.14972	Present work
GGA	0.73652	7.32661	15.38974	Present work
Others		8.0		[20]
		7.44		[25]
		7.41		[26]
Exp.		7.63		[27]

The calculated magnetic moments, using GGA and LSDA, of the Gd and Tb, are reported in **Tables III-9** and **III-10** respectively. From these Tables, it can be remarked that the magnetic moment of the Gd and Tb atoms calculated by LSDA is a little smaller in comparison with that calculated by GGA. This small difference may be due to the difference in the lattice parameter values.

Our results for the magnetic moment of the Gd atom (**Table III-9**) calculated by GGA and LSDA show reasonable agreement with the experimental data of *7.63* μB [27] and with the theoretical value $\mu_{eff}^{th} = g\mu_B\sqrt{J(J+1)}$ of *7.94* μB [28] and also the results of previous studies [20, 25, 26].

It is clear from **Table III-10** that our calculated magnetic moment of Tb is *5.8601* μ_B with LSDA and *5.9516* μ_B with GGA, the latter being closer to the experimentally measured value [29].

Table III-10 Calculated total and partial magnetic moment (in μ_B (Bohr Magneton)) of the Tb in the ferromagnetic configuration (FM) for hexagonal structure, obtained with GGA and LSDA calculations, and compared to experiment.

	Magnetic moment in interstitial	***Magnetic moment in Tb atom***	***Spin Magnetic Moment in cell μ_{tot}***	***Reference***
LSDA	0.0167	5.8601	11.7369	Present work
GGA	0.1251	5.9516	12.0284	Present work
		5.83		[30]
Exp.		6.5		[29]

III-II-2 GGA+U and LDA+U study

III-II-2-1 Computational details

The total energy calculations are performed using the full potential linearized augmented plane wave (FP-LAPW) method [17, 18] as implemented in the Wien2k code [4]. The valence electron configurations are $4f^7\ 5s^2\ 5p^6\ 5d^1\ 6s^2$ for Gd and $4f^8\ 5s^2\ 5p^6\ 5d^1\ 6s^2$ for Tb atoms. It is well known that the conventional DFT calculations cannot describe the correct ground states energy levels for the systems containing open *3d* (transition elements), *4f* (rare earths) or *5f* (actinides) shells because of the strong onsite Coulomb interactions in the shells. Hence, a DFT with a Hubbard parameter *U* (DFT+*U*) method can be used for the transition elements, rare earths [31–33] and actinides [34]. We applied the Hubbard parameter *U* correction to R (R=Gd, and Tb) *4f* electrons in order to take account of their strong correlation effects [35, 36]. Although the chemical inertness of the *4f* shell can be achieved in this way, by pushing occupied states to low energies and unoccupied states well above the Fermi level. The exchange correlation effects are treated using the GGA+U [37] and LSDA+U [38].

In our DFT+U calculations, we use $U= 7.07\ eV$ (Coulomb parameter) and $J= 0.95\ eV$ (exchange parameter) for Gd [39], and U=7.0 eV and $J= 0.9$ eV for Tb [40] (and put these values in the *case.inorb* file) in order to study the structural, electronic and magnetic properties of these materials. The self-consistent procedure was performed with 1000 k points in the irreducible part of the Brillouin zone; self-consistency was achieved with a tolerance in the total energy of 0.1 mRy.

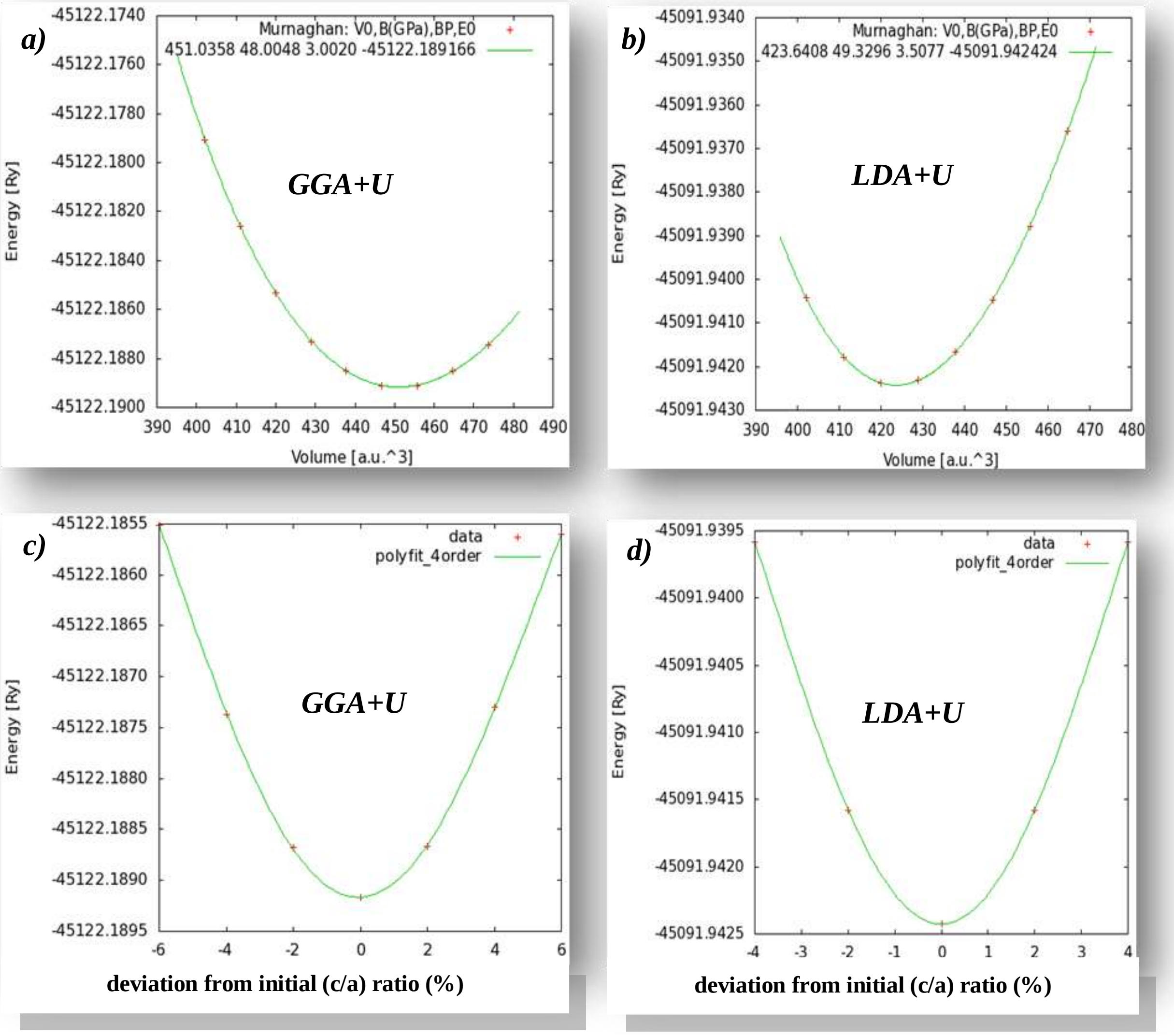

Fig. III-14 Calculated total energy curves for Gd as a function of volume in both GGA+U (a) and LSDA+U (b), and as a function of deviation from initial (c/a) ratio (%) in both GGA+U (c) and LSDA+U (d) approximations.

III-II-2-2 Structural properties

The volume corresponding to the minimum energy is the equilibrium volume (V_0). These data are then fitted to Murnaghnan's equation of state [12] to determine the bulk modulus (B_0) and its first derivative (B_0'). **Figs. III-14** and **III-15** show the variation of total energy with cell volume for both compound Gd and Tb, respectively. The results obtained are summarized in **Tables III-11** and **III-12**, together with the experimental and other available theoretical values. The cohesive energies of these compounds displayed also in these Tables are calculated from the difference between the total atomic energies of R (R= Gd, and Tb) atoms and the minimum energy of bulk compound.

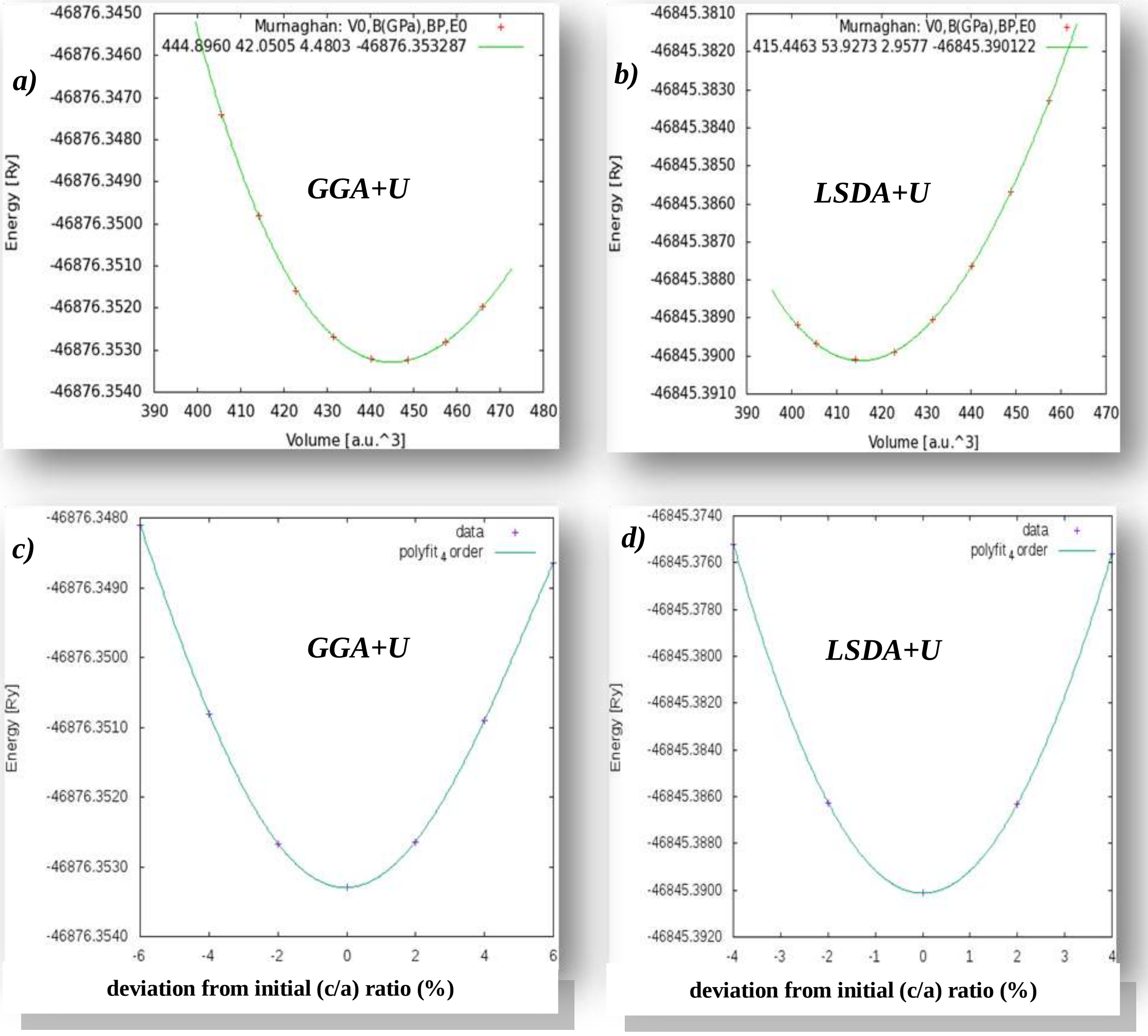

Fig. III-15 Calculated total energy curves for Tb as a function of volume in both GGA+U (a) and LSDA+ U (b), and as a function of deviation from initial (c/a) ratio (%) in both GGA+U (c) and LSDA+U (d) approximations.

From the data in **Tables III-11** and **III-12** of Gd and Tb respectively, we observe that LSDA+U underestimate and GGA+U overestimate the lattice parameter (a_0 and c_0) with respect to the experimental value, in agreement with the general behavior of these methods [42]. A small difference can also be seen in the magnitude of the energy, which means that it is sensitive to the approximations used in the calculation.

As concerns bulk modulus (B_0), the result from GGA+U is lower than that from LSDA+U, for both Gd and Tb, which results from the overbinding characteristic of LSDA+U approximation. Furthermore, (B_0) of standard DFT is higher than that of DFT+U for both systems.

Table III-11 Equilibrium lattice parameters a_0 and c_0 (in Å), bulk modulus B_0 (in GPa), pressure derivative B_0', and total energy (Ry), and cohesive energy E_{coh} (eV) for Gd obtained with GGA+U and LSDA+U calculations, compared to experimental data and other works.

	a₀	***c₀***	***c/a***	***B₀***	***B₀'***	***Total energy***	***E_coh***	***Reference***
LSDA+U	3.5721	5.6810	1.59038	49.3296	3.5077	-45091.942424	-9.3154	Present work
GGA+U	3.6475	5.8009	1.59037	48.0048	3.0020	-45122.189166	-8.1126	
	3.599	5.776		40	3.98			[19]
Exp.	3.634	5.781	1.591					[10]
	3.595	5.785						[11]

Table III-12 Equilibrium lattice constant a_0 and c_0 (in Å), bulk modulus B_0 (in GPa), pressure derivative B_0', and total energy (Ry) and cohesion energy E_{coh} (eV) for Tb obtained with GGA+U and LSDA+U calculations, compared to experimental data and other works.

	a₀	***c₀***	***c/a***	***B₀***	***B₀'***	***Total energy***	***E_coh***	***Reference***
LSDA+U	3.5558	5.6222	1.5811	53.9273	2.9577	-46845.390122	-11.2868	Present work
GGA+U	3.6379	5.7520	1.5811	42.0505	4.4803	-46876.353287	-10.4172	
Exp.	3.606	5.697	1.580					[10]

It is little surprise that the calculated cohesive energies with GGA+U are smaller than those calculated with LSDA+U (by *19.784%* for Gd and *14.509%* for Tb). This is because the increase of the lattice parameter goes along with a decrease of the cohesion of the crystal.

The obtained ground state properties are used to calculate self-consistently electronic and magnetic properties of the compound.

III-II-2-3 Electronic structure

In order to understand the electronic structure of R (R=Gd, and Tb), the spin dependent band structure of the Gd and Tb is computed using GGA+U and LSDA+U exchange correlation and depicted in **Figs. III-16** and **III-17** respectively. It is found that both the minority and the majority spin channel exhibit metallic behavior because several bands cross the Fermi level. The fact is further confirmed by the atomic site projected densities of states (PDOS) profiles in **Figs. III-18** and **III-19** for Gd and **Fig. III-20** for Tb, which show a finite number of electrons at the Fermi level.

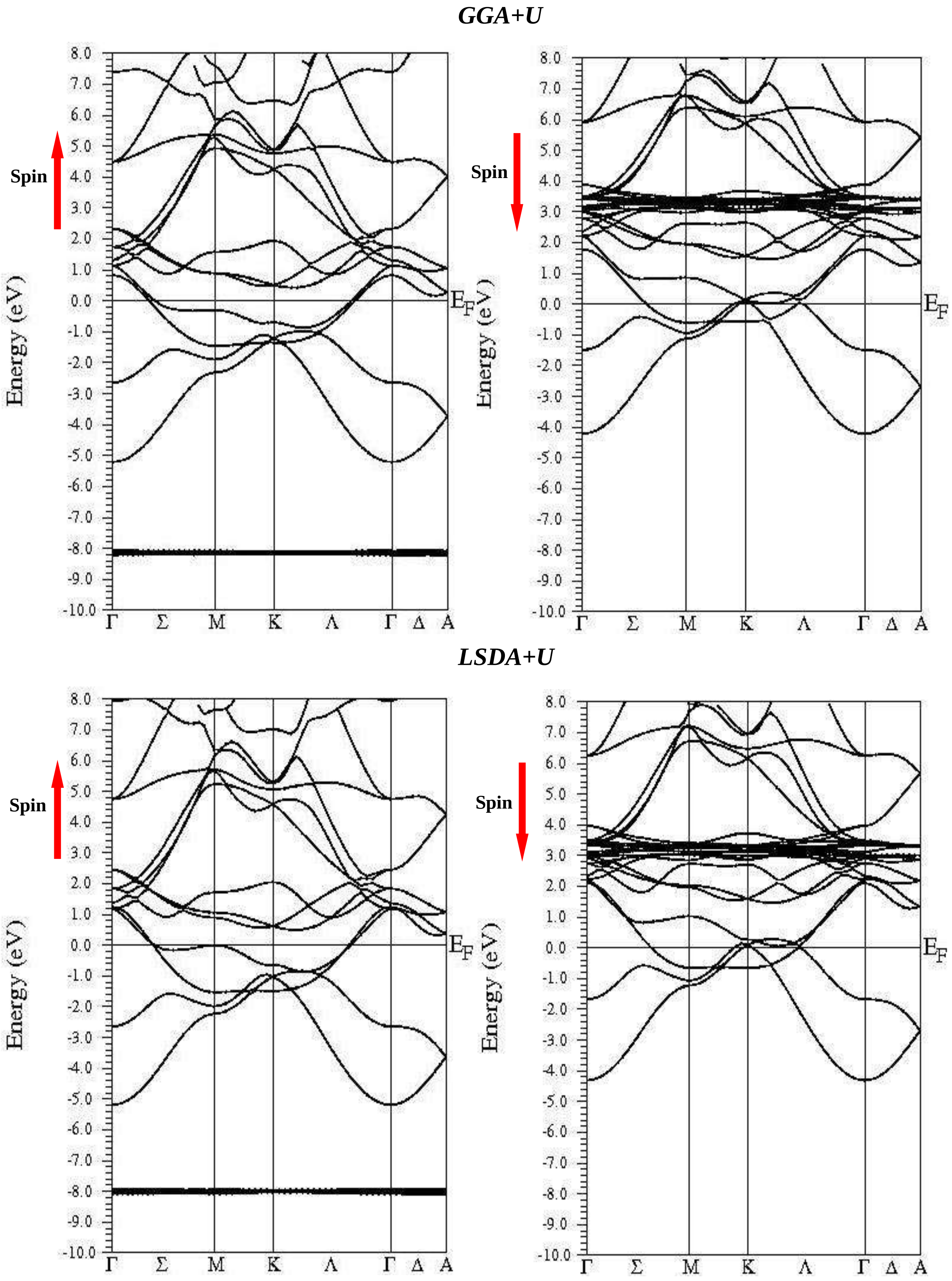

Fig. III-16 Calculated band structures for Gd in both approximations GGA+U and LSDA+U.

GGA+U

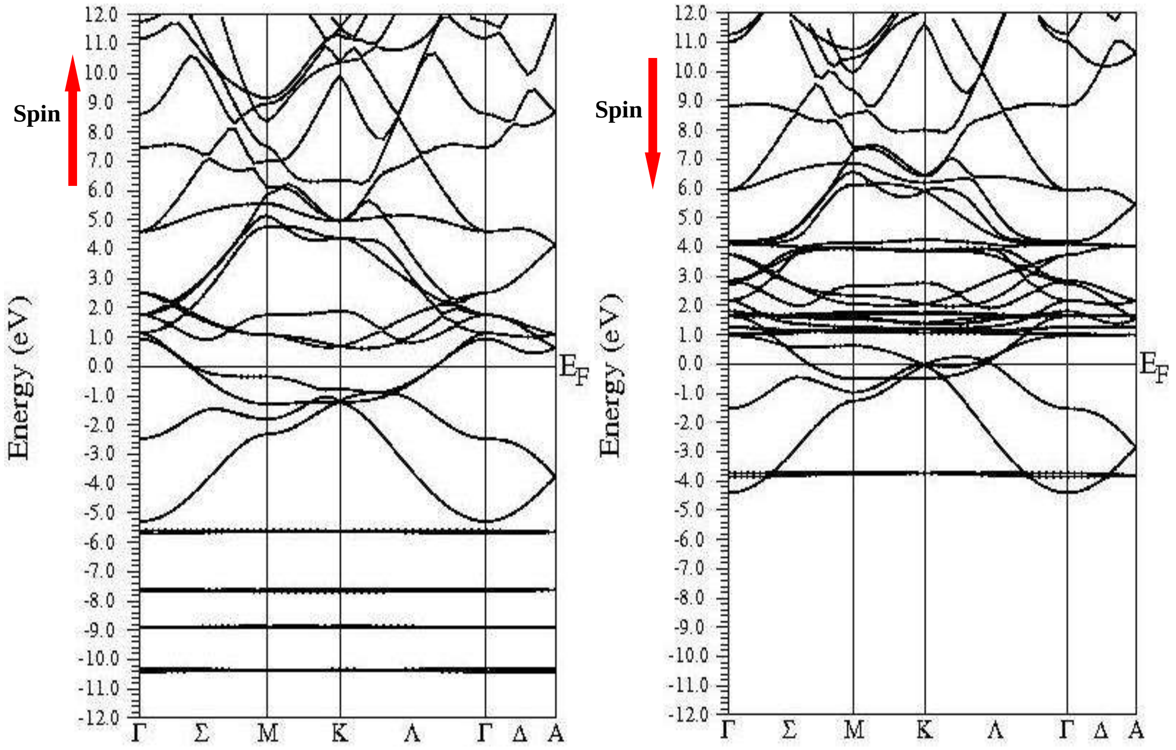

LDA+U

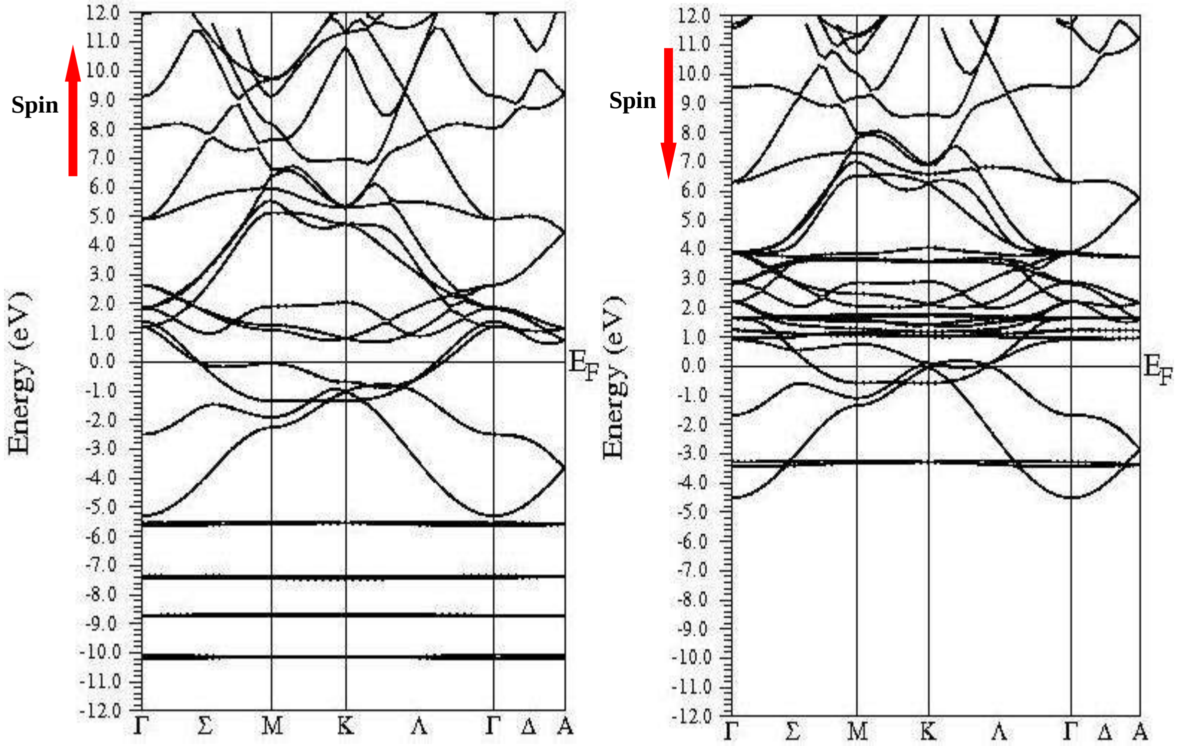

Fig. III-17 Calculated band structures for Tb in GGA+U and LSDA+U approximations, the Fermi energy being at 0 eV.

From **Tables III-13** and **III-14**, it is also observed that the density of states at the Fermi level ($N(E_F)$) is not negligible for both minority spin (spin down) electrons and majority spin (spin up) electrons within both approximations. We note that the Fermi energy in LSDA+U is higher than that in GGA+U for both compounds.

Table III-13 Fermi energy and density of states at the Fermi level for Gd obtained with GGA+U and LSDA+U calculations.

	Fermi energy (Ry)	*N(E_F) (states/Ry/spin)*	
		Spin down	*Spin up*
Gd (GGA+U)	0.41637	15.55	10.43
Gd (LSDA+U)	0.42950	16.56	7.13

Table III-14 Fermi energy and density of states at the Fermi level for Tb obtained with GGA+U and LSDA+U calculations.

	Fermi energy(Ry)	*N(E_F) (states/Ry/spin)*	
		Spin down	*Spin up*
Tb (GGA+U)	0.34349	12.44	8.98
Tb (LSDA+U)	0.34978	13.47	8.00

For R (R=Gd, and Tb), the LSDA+U and GGA+U energy band structures illustrated in **Figs. III-16** and **III-17** are qualitatively similar. Indeed, the crossings of bands with the Fermi level are nearly the same in the two approximations, where the values of the Fermi energy are *0.41637 Ry* for Gd and *0.34349 Ry* for Tb in GGA+U and a higher *0.42950 Ry* and *0.34978 Ry* for Tb in LSDA+U for Gd (**Tables III-13** and **III-14**).

When we focus our attention to the M point (**Figs. III-16** and **III-17**), we clearly see that the width of the valence band in LSDA+U is slightly higher than that in GGA+U in both compounds, as a consequence of the reduced lattice parameter. Indeed, from **Figs. III-16** and **III-17**, it is seen that the *4f* bands are very narrow, significantly different from the bands dominated by *s*, *p* and d states. Therefore, it can be concluded that there exist a strong on site Coulomb repulsions between the highly localized *f* electrons. The spin–orbit term may be ignored since the *4f* shells are exactly half occupied for Gd, whereas with non-zero total orbital angular momentum, the spin–orbit term (*J*) may be significant for Tb where the occupied *4f* bands are split further due to spin–orbit coupling, hence **Fig. III-17** presents the theoretical band structure of Tb that takes into account both the Hubbard *U* term and the spin–orbit interaction.

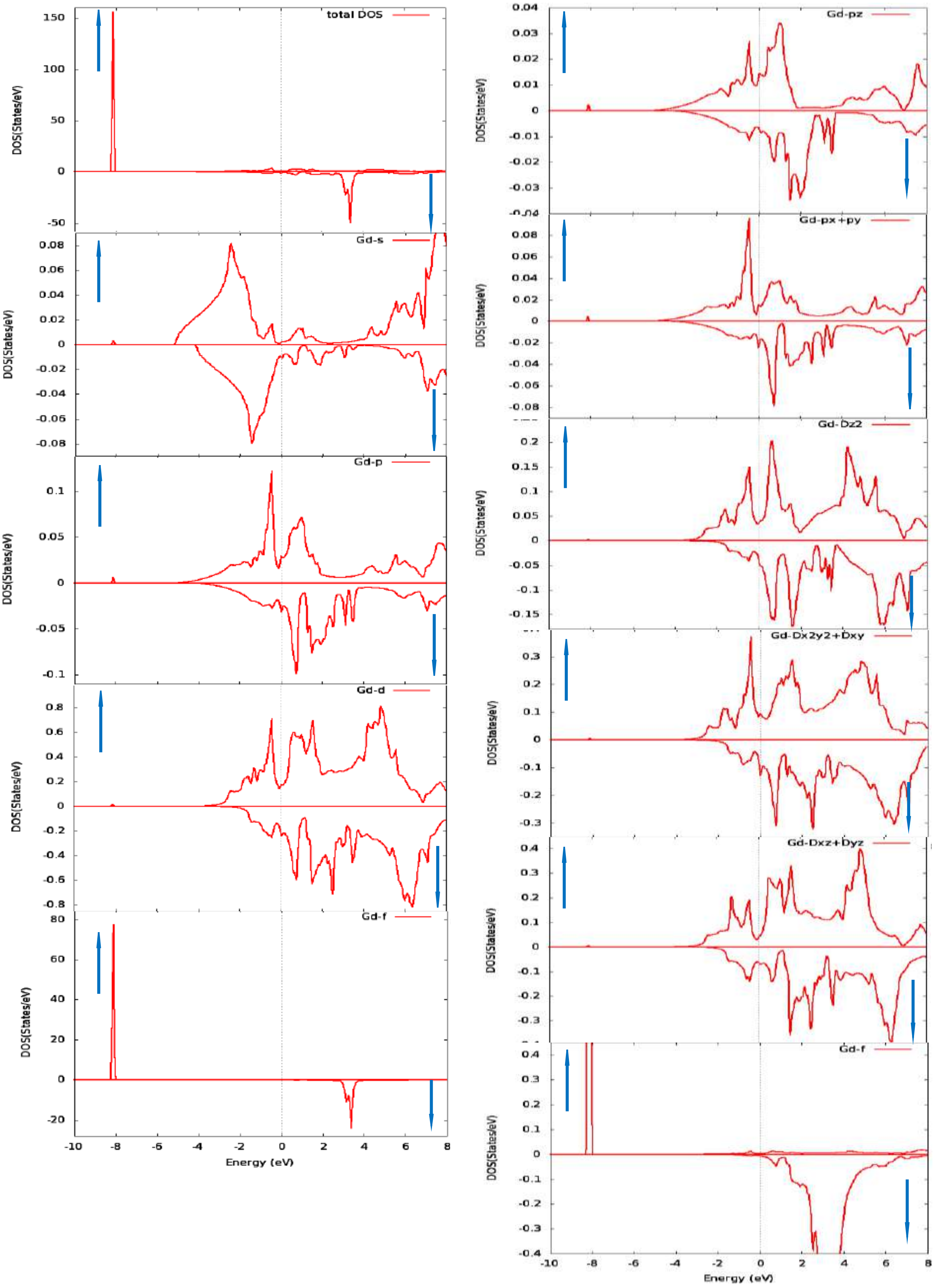

Fig. III-18 Spin dependent total and partial density of states for Gd in GGA+U approximation, the Fermi energy being at 0 eV.

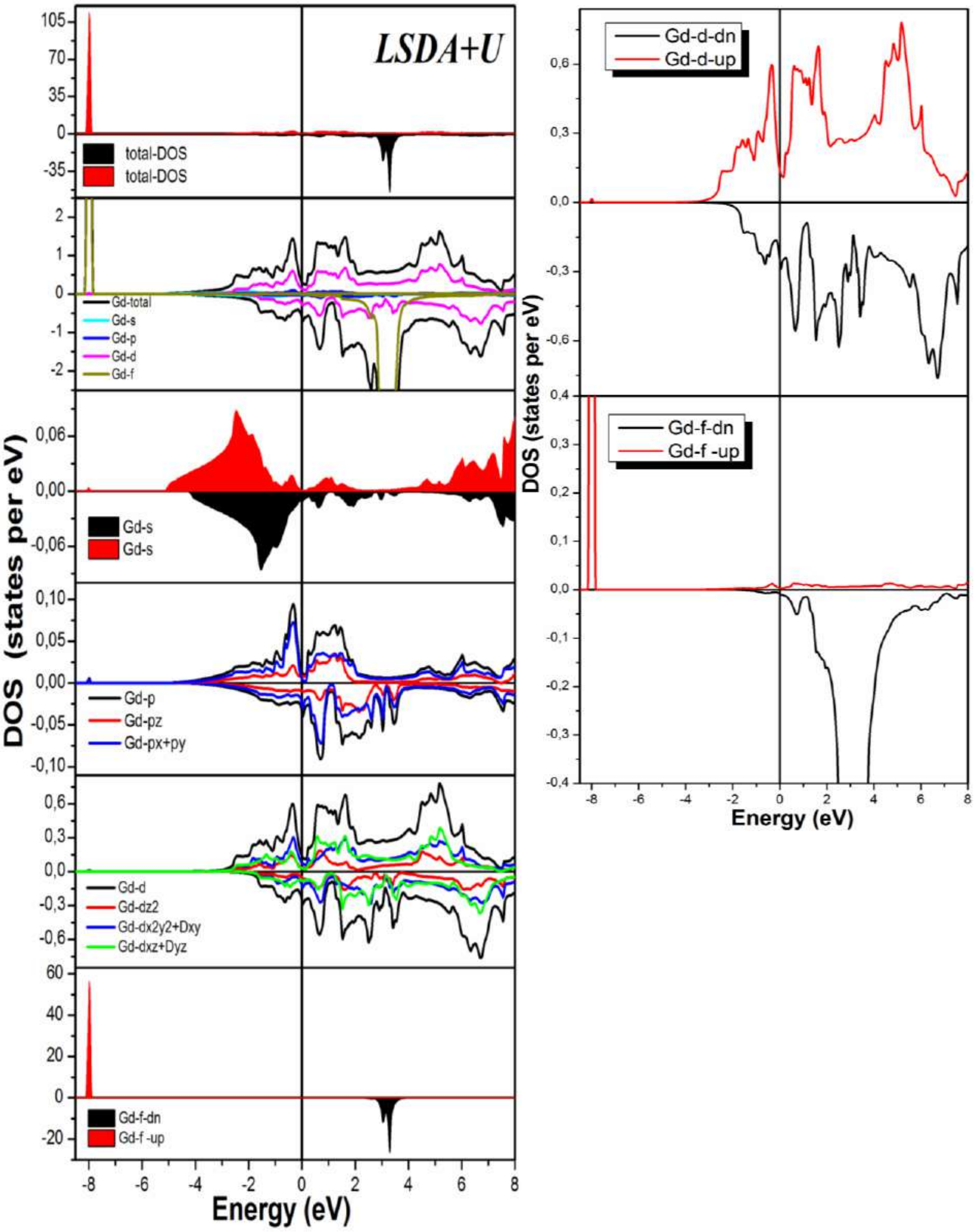

Fig. III-19 Spin dependent total and partial density of states for Gd in LSDA+U approximation, the Fermi energy being at 0 eV.

The *l*-projected density of states (DOS) plot provides an even clearer picture of the elemental contributions to the electronic structure of Gd and Tb. **Figs. III-18** and **III-19** for Gd and **Fig. III-20** for Tb show the spin dependant total density of states and the projected density of states calculated with GGA+U and LSDA+U for the Gd and Tb respectively. The valence band (VB) and conduction band (CB) around the Fermi level are primarily dominated by R-*5d* electrons in both spin (up and down), where all *D-z2*, *Dx2y2+Dxy*, and *Dxz+Dyz* electrons participate. The width of valence band in spin up states is slightly larger than that in spin down.

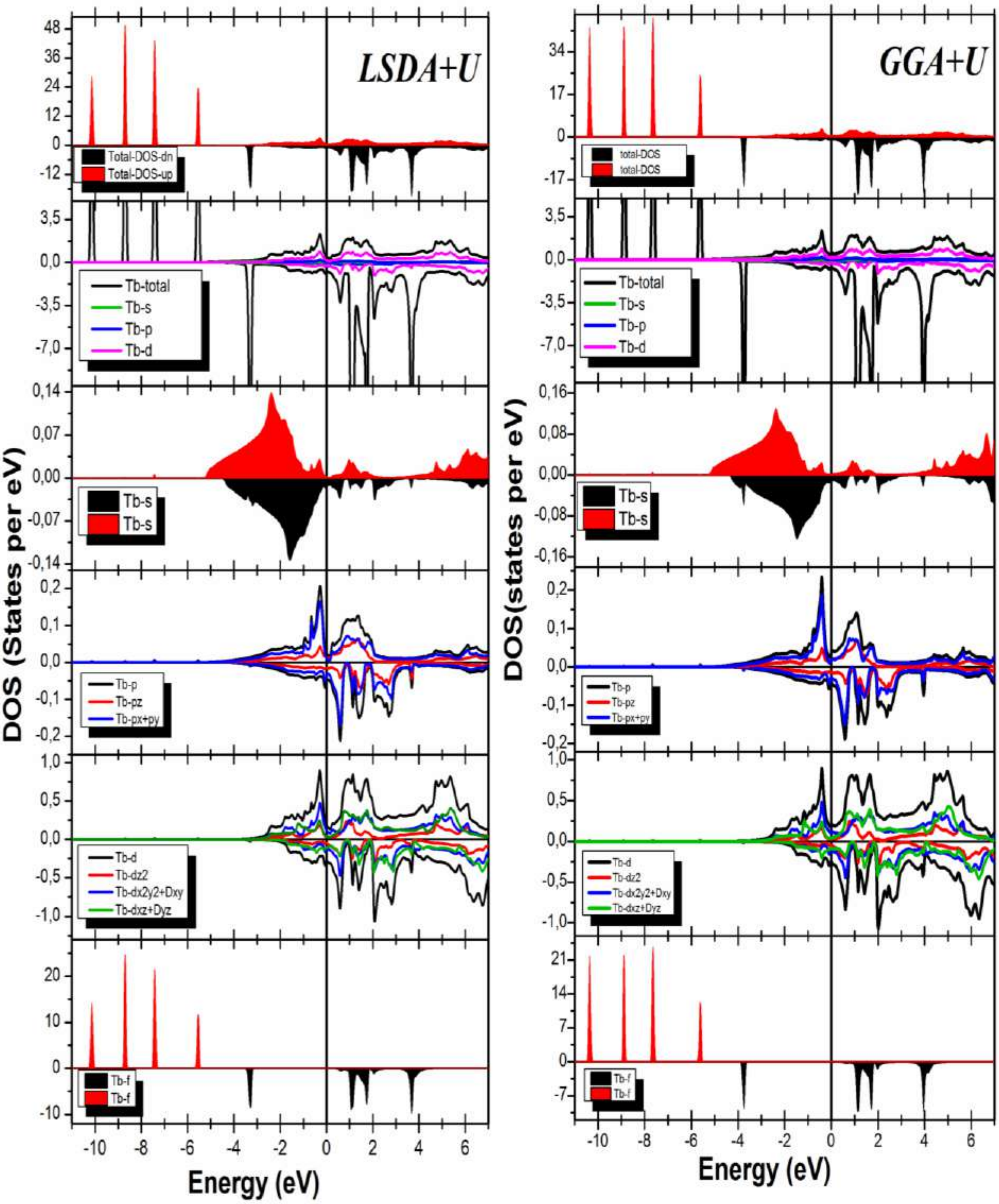

Fig. III-20 Spin dependent total and partial density of states for Tb in LSDA+U and in GGA+U approximations. Spin up (↑) and down (↓) states are plotted separately above and below the thin horizontal zero line. The Fermi energy is at 0 eV.

For Gd (see **Figs. III-18** and **III-19**), it is seen that in the valence band the 4*f* occupied states manifest themselves with a sharp peak (majority spin channel) at *-8.11409 eV* with GGA+U and at *-7.99341 eV* with LSDA+U below the Fermi energy, while the empty 4*f* states (minority spin channel) are well separated and can be found near *3.39642 eV* with GGA+U and near *3.29941 eV* with LSDA+U above E_F.

From **Fig. III-20** for both approximations, we observe instead different peaks of the *4f*-projected density of states well below and well above the Fermi level. In spin up states, the *4f* levels are narrower than those in the spin down states.

For both spin directions in this compound (**Fig. III-20**), just below the Fermi level, the peaks are formed due to Tb-*d* state electrons and also Tb-*p* state electrons which make a non-negligible contribution.

III-II-2-4 Magnetic properties

The rare-earth metals have similar crystal structures, which arise from the electronic structure of the valence shells as the localized 4*f* shell is being filled [42-45]. In spite of this, their magnetic structures vary significantly [21]. This is directly related to the mechanism of the exchange interaction in these materials where the spin-polarized 4*f* wave functions of each atom do not overlap but are responsible for a large magnetic moment. In contrast, the *s*, *p*, and *d* electrons are delocalized and form bands.

The calculated total and atom-resolved magnetic moments, using GGA+U and LSDA+U, of Gd and Tb, are summarized in **Tables III-15** and **III-16** respectively.

Table III-15 Calculated total and partial magnetic moment (in μ_B (Bohr Magneton)) of the Gd in the ferromagnetic configuration (FM) for hexagonal structure, obtained with GGA+U and LSDA+U calculations and compared to others.

	Magnetic moment in interstitial	*Magnetic moment in Gd atom*	*Spin Magnetic Moment in cell μ_{tot}*	*Reference*
LSDA+U	0.68839	7.41937	15.52714	Present work
GGA+U	0.77176	7.41404	15.59985	Present work
Others		7.92		[20]
Exp.		7.63		[27]
Theo.		7.94		[28]

The present study shows that the total magnetic moment of the studied compounds originate from the exchange-splitting of the *4f* states of the rare-earth, where it is equal to *7.41* μ_B with GGA+U and to *7.42* μ_B with LSDA+U for Gd atom and equal to *6.52* μ_B with GGA+U and to *6.54* μ_B with LSDA+U for Tb atom. The results obtained with the LSDA+U method are slightly in better agreement with the experimental data compared to those calculated by the GGA+U method. The magnetic moments of the Gd and Tb atoms (**Tables III-15** and **III-16**) are in agreement with the available data [46].

Table III-16 Calculated total and partial magnetic moment (in μ_B (Bohr Magneton)) of the Tb in the ferromagnetic configuration (FM) for hexagonal structure, obtained with GGA+U and LSDA+U calculations and compared to others.

	Magnetic moment in interstitial	***Magnetic moment in Tb atom***	***Spin Magnetic Moment in cell*** μ_{tot}	***Reference***
LSDA+U	0.36365	6.53567	13.43500	Present work
GGA+U	0.44671	6.52331	13.49334	Present work
Exp.		6.5		[29]
Theo.		9.72		[47]

III-III <u>Summary</u>

The results of the calculations presented in this chapter show that in the pure rare earths R (R = Gd, and Tb) the LDA leads to an overbinding— smaller lattice constants and larger cohesive energies and bulk moduli—while the GGA results show a significant underbinding in both spin polarized and non-spin polarized studies. On the other hand, the GGA calculated lattice constants agree well with available experimental data. The absolute values of cohesive energy of the R (R = Gd, and Tb) calculated by LDA and by LSDA/LSDA+U in the spin polarization calculation are higher than those calculated by GGA and by GGA/GGA+U in the spin polarization calculation due to the overbinding effect.

The calculations of band structures and densities of states clearly show that the pure R (R = Gd, Tb) in both spin polarized and non-spin polarized studies exhibit metallic behavior. In addition the calculated magnetic moment of the R (R = Gd, and Tb) show reasonable agreement with previous results in the literature.

References

[1] K. A. Gschneidner and L. Eyring. *Handbook on the Physics and Chemistry of Rare Earths*. 1978.

[2] Y. Wang and M. Y. Chou. *Phys. Rev. B* **51**, 7500 (1995).

[3] P. Hohenberg and W. Kohn. *Phys. Rev. B*, **136**, 864 (1964).

[4] W. Kohn and L. J. Sham, *Phys. Rev. A* **140**, 1131(1965).

[5] P. Blaha, K. Schwarz, G. Madsen, D. Kvasnicka, and J. Luitz, *Wien2k, an Augmented Plane Wave Plus Local Orbitals Program for Calculating Crystal Properties*, Techn. Universität, Vienna, Austria, 2001, ISBN 3-9501031-1-2.

[6] P. Vajeeston, R. Vidya, P. Ravindran, H. Fjellvåg, A. Kjekshus, and A. Skjecltorp. *Phys. Rev. B* **65**, 075101 (2002).

[7] J. P. Perdew, K. Burke, and M. Ernzerhof. *Phys. Rev. Lett.* **77**, 3865 (1996).

[8] J. P. Perdew and Y. Wang. *Phys. Rev.* **45**, 13244 (1992).

[9] A. H. Reshak and J. Morteza. *J. Alloys Compd.* **555**, 362 (2013).

[10] B. J. Beaudry and K. A. Gschneidner. *Preparation and basic properties of the rare earth metals*. 1978.

[11] J. Banister, S. Legvold, and F. H. Spedding. *Phys. Rev.* **94**, 1140 (1954).

[12] F. D. Murnaghan. *Proc. Natl. Acad. Sci.* **30**, 244 (1944).

[13] A. Bouhemadou, R. Khenata, M. Kharoubi, T. Seddik, A. H. Reshak, and Y. Al-Douri. *Comp. Mater. Sci.* **45**, 474 (2009).

[14] D. Heciri, L. Beldi, S. Drablia, H. Meradji, N. E. Derradji, H. Belkhir, and B. Bouhafs. *Comput. Mater. Sci.* **38**, 609 (2007).

[15] W. C. Koehle. *J. Appl. Phys.* **36**, 1078 (1965).

[16] U. von Barth and L. Hedin. *J. Phys. C* **5**, 1629 (1972).

[17] J. C. Slater. *Adv. Quant. Chem.* **1**, 5564 (1964).

[18] D. J. Singh and L. Nordrtröm. *Plane waves, pseudopotentials and the LAPW method*. 1994

[19] M. Petersen, J. Hafner, and M. Marsman. *J. Phys. Condens. Matter* **18**, 7021 (2006).

[20] G. Sudha Priyanga, R. Rajeswarapalanichamy, and K. Iyakutti. *Int. J. Hydrogen Energy* **31**, 415 (2015).

[21] J. Jensen and A. R. Mackintosh. *Rare Earth Magnetism*. 1991.

[22] P. W. Anderson. *Phys. Rev.* **115**, 2 (1959).

[23] P. W. Anderson. *Rev. Mod. Phys.* **50**, 191 (1978).

[24] C-G Duan, T. Komesu, H-K Jeong, J. Choi, C. N. Borca, W. G. Yin, J. Liu, W. N. Mei, P. A. Dowben, A. G. Petukhov, B. D. Schultz, and C. J. Palmstrøm. *Surf. Rev. Lett.* **11**, 531 (2004).

[25] I. Turek, J. Kudrnovsky´, G. Bihlmayer, and S. Blügel. *J. Phys. Condens. Matter* **15**, 277 (2003).

[26] P. Kurz, G. Bihlmayer, and S. Blügel. *J. Phys. Condens. Matter* **14**, 6353 (2002).

[27] I. D. Hughes, M. Däne, A. Ernst, W. Hergert, M. Lüders, J. Poulter, J. B. Staunton, A. Svane, Z. Szotek, and W. M. Temmerman. *Nature* **446**, 650 (2007).

[28] S. Blundell. *Magnetism in Condensed Matter*. 2001.

[29] K. Tezuka, Y. Hinatsu, Y. Shimojo, and Y. Morii. *J. Phys. Condens. Matter* **10**, 11703 (1998).

[30] M. Chunlan, Y. Ling, and Y. Zhongqin. *J. Phys. Condens. Matter* **17**, 7963 (2005).

[31] V. I. Anisimov, F. Aryasetiawan, and A. I. Lichtenstein. *J. Phys. Condens Matter*, **9**, 767 (1997).

[32] D. A. Andersson, S. I. Simak, B. Johansson, I. A. Abrikosov, and N. V. Skorodumova. *Phys. Rev. B* **75**, 035109 (2007).

[33] B. Amadon, F. Jollet, and M. Torrent. *Phys. Rev. B* **77**, 155104 (2008).

[34] P. Soderlind, G. Kotliar, K. Haule, P. M. Oppeneer, and D. Guillaumont. *MRS Bull.* **35**, 883 (2010).

[35] D. D. O. Regan, M. C. Payne, and A. A. Mostofi. *Phys. Rev. B* **83**, 245124 (2011).

[36] J. Feng, B. Xiao, C. L. Wan, Z. X. Qu, Z. C. Huang, and J. C. Chen. *Acta Mater*. **59**, 1742 (2011).

[37] C. Loschen, J. Carrasco, K. M. Neyman, and F. Illas. *Phys. Rev. B* **75**, 035115 (2007).

[38] V. I. Anisimov, J. Zaanen, and O. K. Andersen. *Phys. Rev. B* **44**, 943 (1991).

[39] S. Berri. *J. Magn. Magn. Mater.* **385**, 124 (2015).

[40] V. I. Anisimov, F. Aryasetiawan, and A. I. Lichtenstein. *J. Phys. Condens. Matter* **9**, 767 (1997).

[41] P. Haas, F. Tran, and P. Blaha. *Phys. Rev. B* **79**, 085104 (2009).

[42] B. Johansson and A. Rosengren. *Phys. Rev. B* **11**, 2836 (1975).

[43] J. C. Duthie and D. G. Pettifor. *Phys. Rev. Lett.* **38**, 564 (1977).

[44] H. L. Skriver. *Phys. Rev. B* **31**, 1909 (1985).

[45] A. Delin, L. Fast, B. Johansson, J. M. Wills, and O. Eriksson. *Phys. Rev. Lett.* **79**, 4637 (1997).

[46] S. D. Barrett and S. S. Dhesi. *The Structure of Rare-earth Metal Surfaces*. 2001.

[47] C. Kittel. *Introduction to Solid State Physics*. 2005.

CHAPITER IV

Rare-earth dihydrides RH_2 (R = Gd and Tb): structural, electronic, and thermodynamic properties

Over the past few decades, a major challenge which still remains is to identify optimal intermetallic candidates for hydrogen storage. Rare earth (R) alloys are seen as promising materials, owing to high hydrogen capacity per volume unit and an ability to absorb hydrogen under moderate conditions of temperature and pressure [1], where the interstitial hydrogen atoms strongly modify the electronic structure and add interesting features [2]. Dihydrides are obtained from an exothermic reaction which forms stable compounds crystallizing in the cubic fluorite structure of the CaF_2 type [3]. This crystal structure consists of two sublattices: the fcc sublattice of the R-atoms, and that of the H-atoms occupying ideally all the tetrahedral interstices of the former.

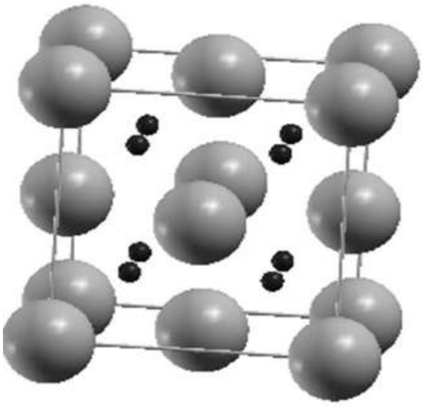

***Fig. IV-1** The compound crystallizes in the CaF_2 fluorite type structure: the large spheres represent rare earth atoms (× 4) and small spheres hydrogen atoms occupying tetrahedral sites (× 8) (figure plotted with XCrysDen [4]).*

The aim of this chapter is to study theoretically the structural, electronic and thermodynamic properties of rare earth dihydrides RH_2 (R = Gd and Tb) using first-principles methods. No magnetic (no spin polarization) calculations are carried out in this chapter.

IV-I Gadolinium dihydride GdH_2

IV-I-1 Computational methods

Our calculations are based on density functional theory (DFT) [5, 6]. In this work, the full potential linearized augmented plane wave (FP-LAPW) method as implemented in the WIEN2k package [7] was used for the calculations, in which the Kohn-Sham equations are solved self-consistently. In this method, electronic wave functions, the charge density and the crystal potential are expanded as spherical harmonics inside the non-overlapping atomic spheres of radius R_{MT}, and as plane waves in the remaining space of the unit cell. The muffin-tin radii (the atomic spheres radii), R_{MT}, selected for Gd and H were 2.25 bohr and 1.8 bohr, respectively. We have chosen the basis set size $R^{min}_{MT}*K_{max} = 9$, where R^{min}_{MT} is the smallest atomic sphere radius inside the cell and K_{max} is a cutoff for the basis function wave vector. The cutoff in the charge density Fourier expansion, G_{max}, was taken to be 20 $Ry^{1/2}$. We also mention that the integrations over the Brillouin zone are performed up to 400 k-points in its irreducible wedge. We used an energy to separate core and valence states equal to -8 Ry. Exchange and correlation effects were treated within the density functional with the generalized-gradient approximation of Perdew, Burke and Ernzerhof (GGA96) [8]. We have taken a value of 5.3022 Å [9] as the actual lattice constant for the calculations. The self-consistent calculations are considered to be converged only when the calculated energy changes by less than 0.1 mRy.

IV-I-2 Results and discussion

The ground-state structural parameters have been obtained by minimizing the total energy with respect to the volume. By fitting this total energy versus volume data to the non-linear Murnaghan equation of state [10], as shown in **Fig. IV-2**, we obtained the lattice constant, the value of the bulk modulus and its pressure derivative at equilibrium. The results are given in **Table IV-1** along with earlier experimental and theoretical findings. Our

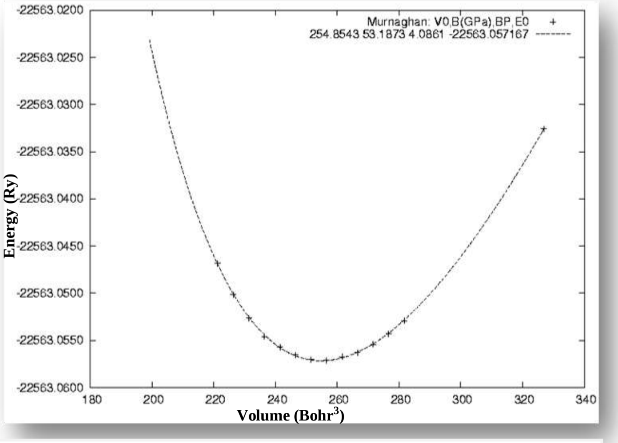

Fig. IV-2 Total-energy of GdH_2 as a function of volume.

calculated structural parameters show very good agreement with the available results [9, 11, and 12].

Table IV-1 Equilibrium lattice constant a_0 (in Å), bulk modulus B_0 (in GPa), pressure derivative B_0', and total energy (Ry) compared to experimental data and other works for GdH_2.

	a₀	***B₀***	***B₀'***	***Total energy***	***Reference***
GGA	5.326	53.1873	4.0861	-22563.057167	Present work [13]
Exp.	5.296 (extrapolated to 0K)				[9]
Experiment and Spin polarized DFT	5.3				[11]
Exp.	5.303				[12]

We calculated the electronic band structures at the equilibrium lattice constant for different high-symmetry points in the Brillouin zone.

The calculated band structure and total DOS of GdH_2 are shown in **Fig. IV-3**, the dashed line indicating the Fermi level. Note that all the 7*f* electrons are found in a single unsplit peak at Fermi level thus missing the strong correlation between *f* electrons. This is not acceptable from the point of view of the electronic distribution. In order to circumvent this problem, DFT calculations going beyond the LDA/GGA scheme level can to some extent improve on the treatment of correlation: methods such as LDA+U, self-interaction correction (SIC) and open core calculations have been cited [14].

In this work, we used the less sophisticated 'open core' approach in which contributions of the *4f* electrons are removed from the valence bands, a procedure equivalent to the LDA+U approximation where U = +∞ for the *f* electrons. These *f* electrons are treated as atomic electrons, i.e. they cannot hybridize with the other valence *s*, *p*, and *d* electrons anymore and are perfectly localized [15].

However, one can expect the existence of finite localized magnetic moments on the *4f* electrons. This magnetic aspect has not been considered in our calculations.

Table IV-2 Fermi energy and density of states at the Fermi level for GdH_2 (our results Ref. [13]).

	Fermi energy (Ry)	***N(E_F) (states/Ry)***
GdH_2	0.52165	13.3759

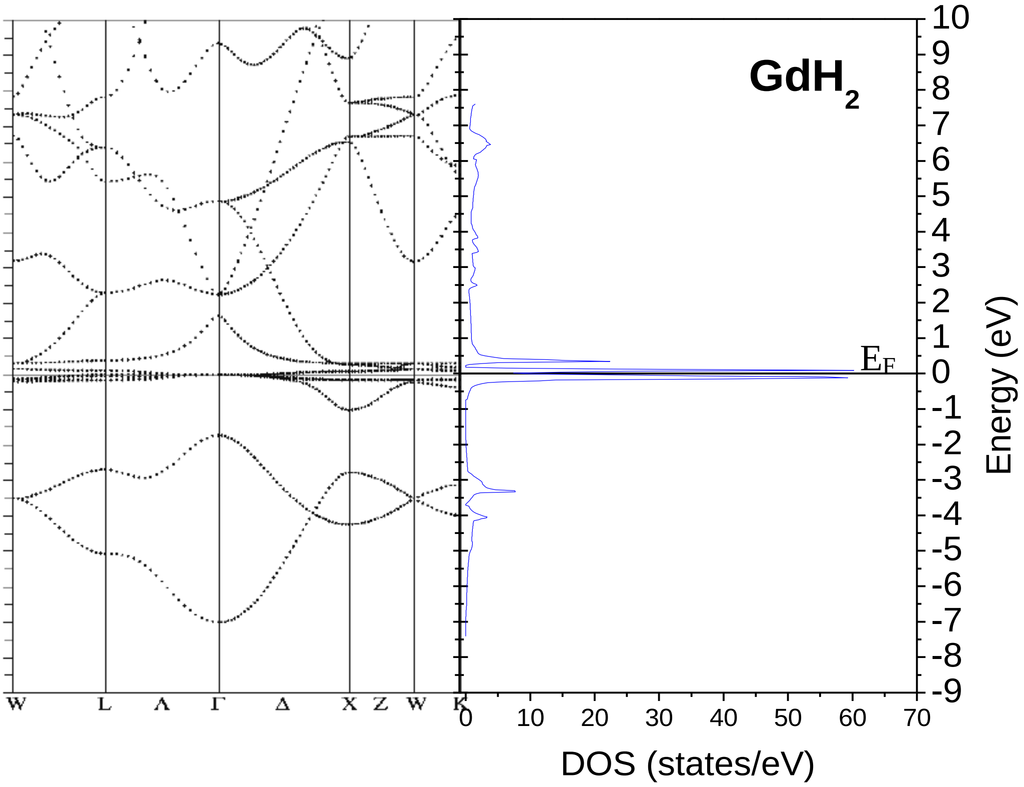

Fig. IV-3 Density of states (right panel) and electronic band structure along high-symmetry directions (left panel) of GdH$_2$, the Fermi energy being at 0 eV.

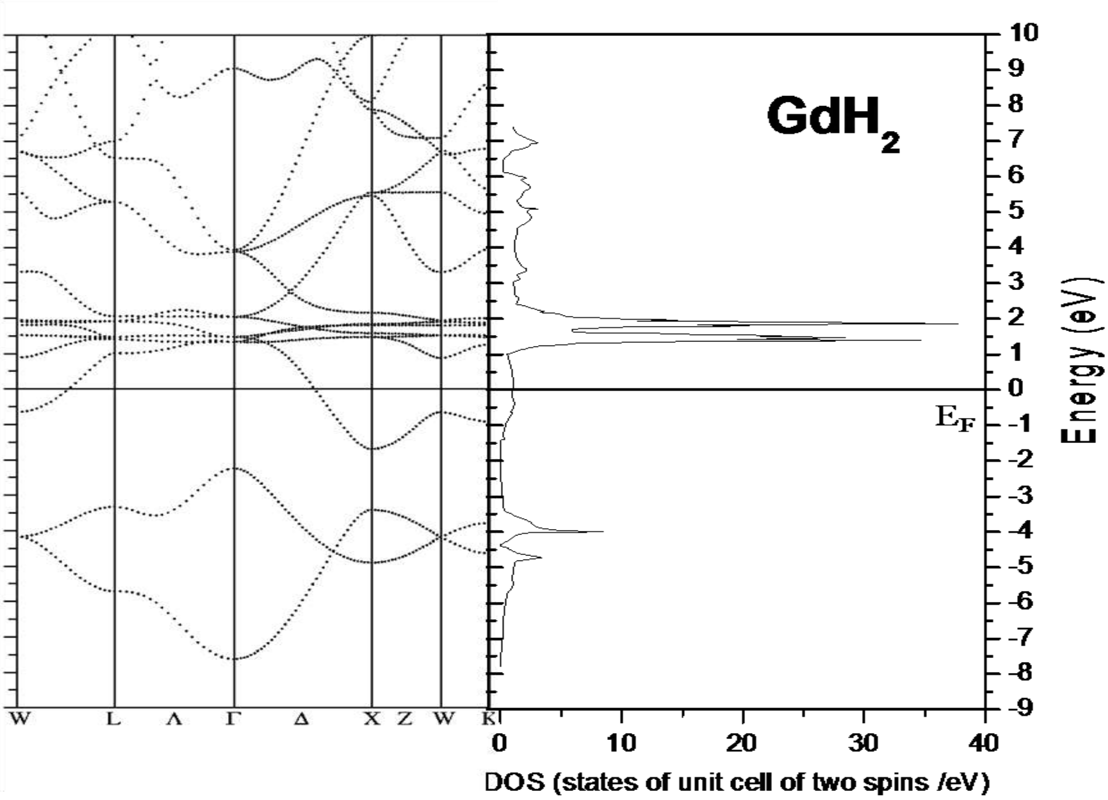

Fig. IV-4 Density of states (right panel) and electronic band structure along high-symmetry directions (left panel) of GdH$_2$ within the 'open core' approach, the Fermi energy being at 0 eV.

After applying the open core procedure, the calculation is iterated until convergence. This establishes the values of the Fermi energy (E_F) and the density of states at the Fermi level $N(E_F)$ (**Table IV-2**).

The band structure and total density of states calculated using the 'open core' treatment of GdH_2 is shown in **Fig. IV-4**. The unit of density of states is *state per eV* and the energy is the electron volt. The energy origin in this figure indicates the Fermi level.

Note that the only difference with the previous calculations is the shifting of the sharp peak due to *4f* electrons above the Fermi energy.

Fig. IV-4 shows qualitative agreement with calculations made by Gupta (1980) [1], Switendick (1971) [16], Misemer et al. (1982) [17] on rare-earth systems and a good agreement with the photoemission experiments by Koitzsch et al. (2004) [11] on this particular GdH_2 system, and particularly with those of Fujimori et al. (1980) [18].

This figure indicates that only two new bands are added below the Fermi energy and above $E=-7.6417eV$. The new bands are a direct consequence of there being two hydrogen atoms in the unit cell and would not appear in structures with only one hydrogen atom in the unit cell, although the presence of the two low-lying metal-hydrogen bands is a feature common to all the fluorite-structure metal dihydrides [19]. These low-lying bands play an important role in the stability of the compound as was confirmed by ultraviolet (UV) photoemission experiments by Weaver et al. [20].

The width of the valence band is *5.3607 eV*, which is much smaller than that of TiH_2; this is due to the small *H-H* separation leading to the large *H-H* interaction in TiH_2. This confirms that the valence band width is principally determined by the *H-H* interaction and therefore sensitive to the *H-H* distance [18].

In Fig. IV-4, two large peaks are found in the DOS of the first two bands, with the first peak centered at $E=-4.7301\ eV$ and the second higher peak at $E=-3.9953\ eV$. These low-lying bands are filled by four of the five valence electrons of this compound, the fifth valence electron filling the bottom of the metal *5d* band [1, 16, 17, and 19]. In the same figure (band structure) more bands cross $E=E_F$ and therefore this compound must show a metallic behavior. This is confirmed by all the profiles of the DOS which show a finite number of electrons at the Fermi level. The latter lies *1.383 eV* above the bottom of the *5d* metal bands.

In order to analyze the atomic interaction between a hydrogen atom and its different neighboring atoms, the total DOS has been decomposed into its partial (*s*, *p*, *d* and *f*) wave components around the H where each Gd site sits in the middle of a cube with eight tetrahedral sites at the corners.

In **Figs. IV-5** and **IV-6**, we show the total DOS decomposition into components according to the value of the angular momentum (*s*: L=0; *p*: L=1; *d*: L=2; *f*: L=3) inside the MT (Muffin Tin) spheres of the Gd and of the hydrogen.

From **Fig. IV-6,** one can clearly see that the two low-lying bands are largely formed by the *s* states of hydrogen. Indeed, the shape of the L=0 component of the DOS inside the hydrogen MT spheres has a structure of two peaks, and this shape is very similar to the total DOS.

Cubic symmetry leads to the degeneracy of states of metallic quintuple states in triple (*d-t2g*) and double (*d-eg*) states [1].

Some *d-t2g* states, and, to a lesser extent, *s* and *p* states of the metal have been significantly affected by the interaction of metal-hydrogen (Me-H) (orbits of the hydrogen *1s*), and are located at lower energies (the lowest point at Γ), where the formation of this band poses the question of this bond's ionicity; a charge-transfer analysis points to an effective charge transfer away from the metal site to the tetrahedral hydrogen sites [17].

As noted above, it was shown that the hybridization is important in the low-lying bands which contain a contribution from the metal in addition to that of hydrogen (**Fig. IV-7**).

Dihydrides cannot literally be considered purely ionic compounds [1],

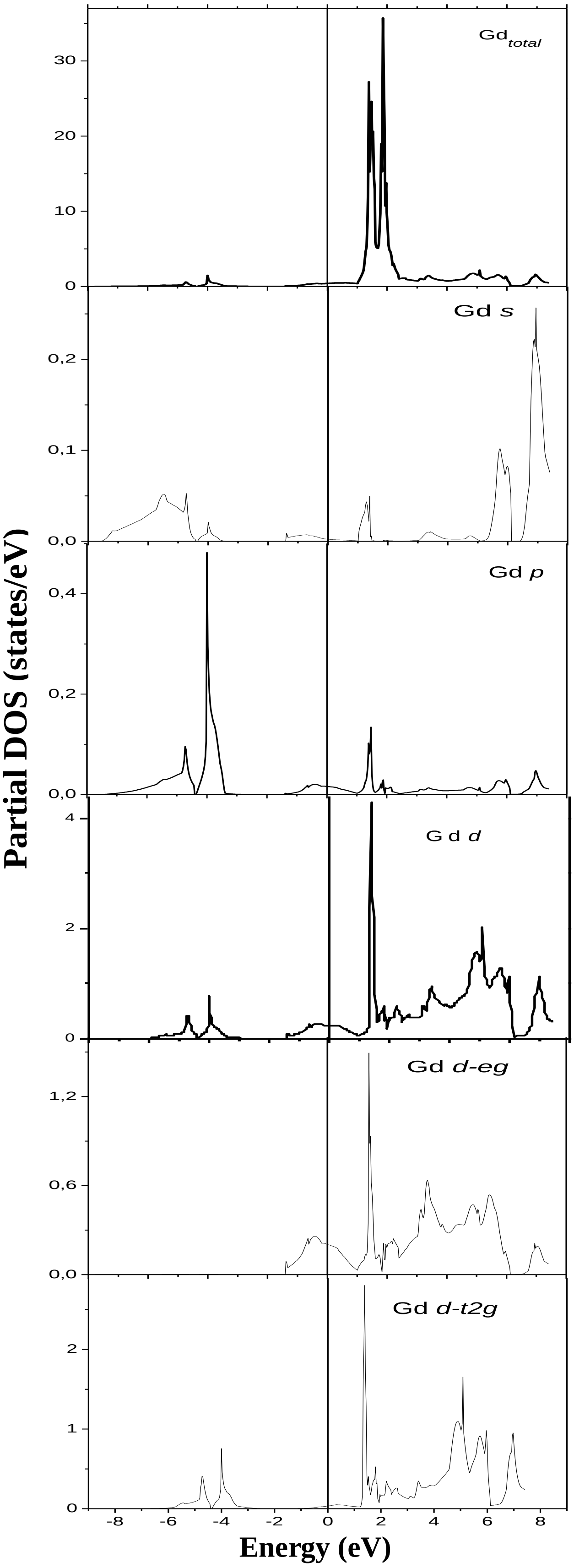

Fig. IV-5 Orbital-projected DOS's for Gd in GdH_2.

even though the results show that hydrogen in tetrahedral sites is negatively charged [3]. The nature of bonding in this compound (and nearly all rare earth dihydrides) must be discussed in terms of interactions between metal *d* states and hydrogen *1s* states [16].

The second electronic band (at Γ and below the *d* bands) is formed by a combination of antibonding orbitals of the two states of the hydrogen *1s* states in the unit cell. **Fig. IV-5** shows the presence of *s* states of the metal on the negative energy side ($E<E_F$) of the first two bands while the metal *p* states give an important contribution to the second peak observed below E_F in the total DOS. On the other hand, the bottom of the conduction band is *d-eg* like; we can see that a moderate contribution of Gd-*p* states is present, against a very small contribution from Gd-*s* states and H-*s* states near the Fermi level.

An unoccupied *4f*-electrons peak is localized in the region of the conduction band some electrons volts above the Fermi level (E_F). This is an artifact due to the 'open core' method used to make the calculation since it is known that the *4f*-electrons are located in the core of atoms and their states should not appear.

Net depopulation of the metal *5d* bands during hydrogenation, which is a common feature to most rare earth dihydrides, plays an important role in the magnetic

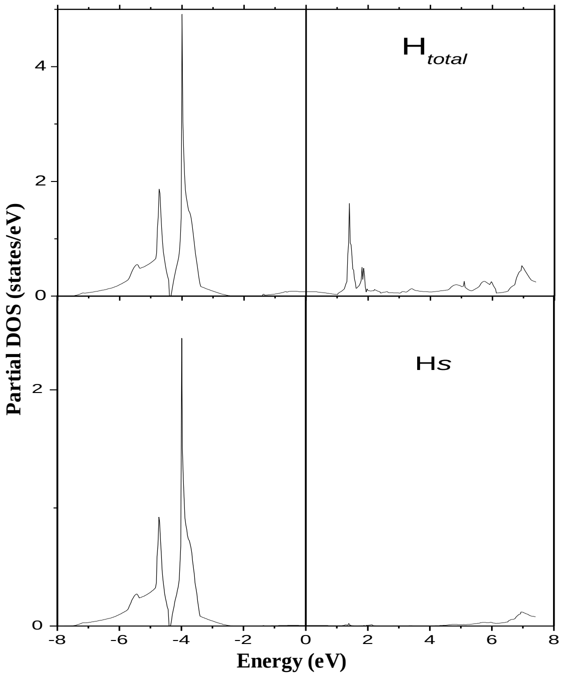

Fig. IV-6 Orbital-projected DOS's for H_2 in GdH_2.

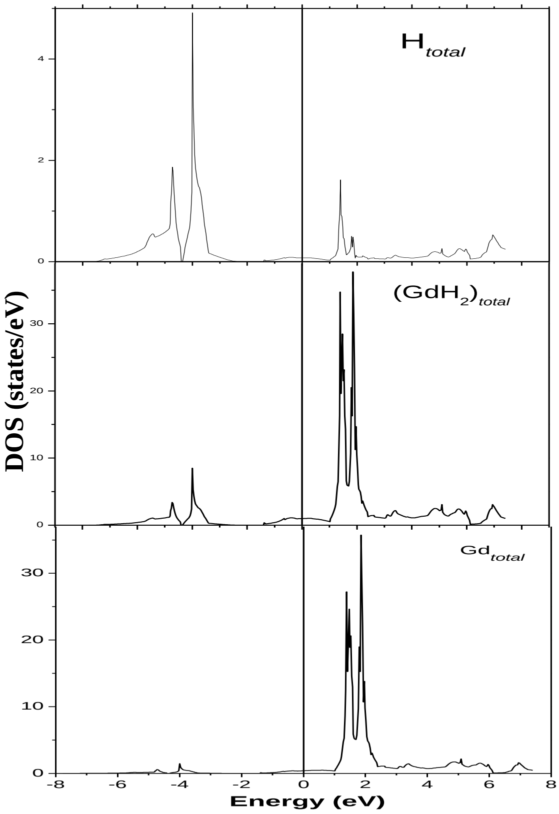

Fig. IV-7 The calculated total and partial density of states for GdH_2.

properties of these compounds.

IV-II Terbium dihydride TbH_2

IV-II-1 Computational method

First principles calculations based on the density functional theory were performed [5, 6] using the full potential linearized augmented plane wave (FP-LAPW) method as implemented in the WIEN2k Package [7]. The cutoff in the charge density Fourier expansion, G_{max}, was taken to be $20\ Ry^{1/2}$, where $1\ Ry = 13.60570\ eV$. We adopted the generalized gradient approximation (GGA) [8] of the Perdew, Burke and Ernzerhof (GGA96) functional and the local density approximation (LDA) [21] to describe the exchange–correlation interactions [22].

Rare earths can be problematic for DFT calculations. We note that one can expect the existence of finite localized magnetic moments on the *4f* electrons. This magnetic aspect has not been considered in our calculations. It is known, indeed, that, in rare earths, the *4f* electrons, being very close to the core, are expected to be chemically inert. This leads us to consider *4f* electrons as atomic electrons, i.e. they cannot hybridize with the other valence *s*, *p*, and *d* electrons anymore and are perfectly localized [23]. For these reasons, the contribution of the *4f* electrons are removed from the valence bands, and are treated as those of core electrons. It is known that in WIEN2k the core states feel only a spherical potential, are not split by crystal fields and do not contribute to it.

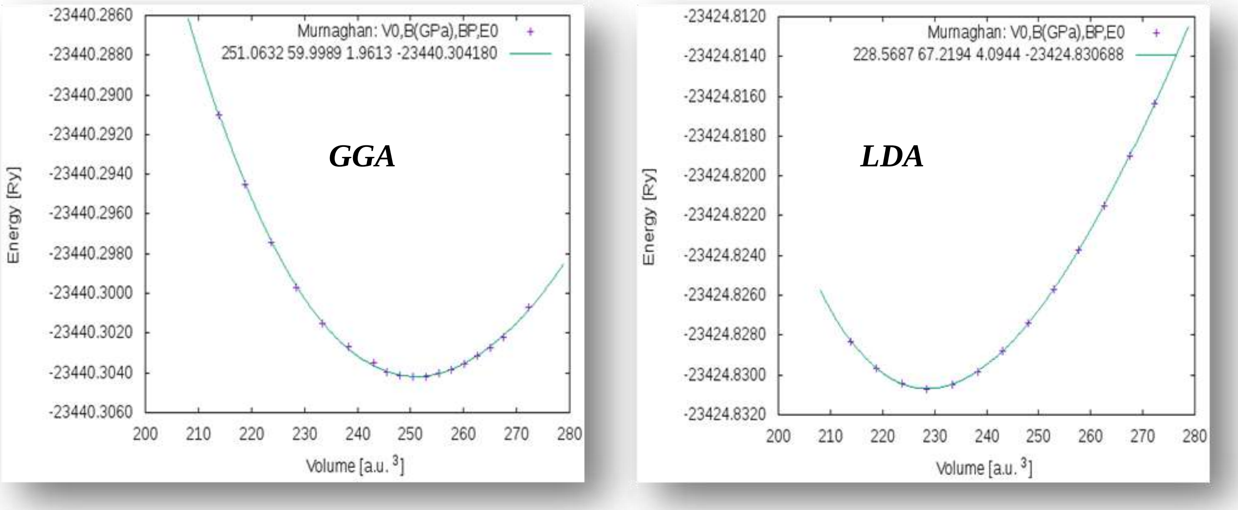

Fig. IV-8 Total energy of TbH_2 as a function of volume in both GGA and LDA approximations.

We used an energy of -8 Ry to separate core and valence states, and the Tb ($5s^2 5p^6 5d^1 6s^2$) and H ($1s^1$) orbitals were treated as valence states (we did not treat the *f* orbitals of Tb as valence electrons but as core electrons). The calculations were based on an optimized number of k-points of 1000, without considering the spin polarization. The calculations were considered converged for changes of the total energy smaller than 10^{-4} Ry between two consecutive iterations.

IV-II-2 Results and discussion

IV-II-2-1 Ground state properties

The bulk modulus describes the resistance of the solid to the uniform volume deformation (i.e. hydrostatic pressure) and it is described by the following equation:

$$B = -V \frac{\partial P}{\partial V} \qquad \text{[IV-1]}$$

Here P is a hydrostatic pressure and V is a unit cell volume. It is possible to calculate bulk modulus by performing series of calculations as a function of the relative volume of the unit cell (ranging from −m% to m%). Such calculations provide the dependence of the total energy on the unit cell volume $E_{tot}(V)$, which can be fit with a Murnaghan equation of state of the form [10, 24]:

$$E_{tot}(V) = E_{tot,0} + \frac{B_0 V}{B_0'}\left(\frac{(V_0/V)^{B_0'}}{B_0' - 1} + 1\right) - \frac{B_0 V_0}{B_0' - 1} \qquad \text{[IV-2]}$$

Here $E_{tot,0}$ and V_0 are equilibrium total energy and volume, respectively, and B_0 is the bulk modulus at the equilibrium (P=0).

We obtained bulk modulus (B), derivative of bulk modulus (B'), equilibrium volume (V_0) and the ground state energy (E_0) of unit cell through volume optimizations as shown in **Fig. IV-8** and listed in **Table IV-3** together with the available data. Calculated E(V) data of TbH_2 were fitted to the non-linear Murnagham equation of state [10].

There is good numerical agreement between experimental and calculated lattice constants. Moreover, our calculated lattice parameter of TbH_2 is smaller than that of GdH_2, which is in agreement with the experimental observation reported by Ref. [25].

It may be noted here that the lattice parameter LDA calculations underestimate experimental results by about 2.04% while GGA calculations overestimate them by about

1.07%. In addition, it can be found from **Table IV-3** that the GGA lattice constant value is 3.18 % larger than that obtained by LDA for TbH_2.

Table IV-3 Equilibrium lattice constant a_0 (in Å), bulk modulus B_0 (in GPa), pressure derivative B_0', and total energy (Ry) for TbH_2 compared to experimental data and other works.

	method	*a_0*	*B_0*	*B_0'*	*Total energy*	*Reference*
TbH_2	GGA	5.2993	59.9989	1.9613	-23440.304180	Present work [25]
	LDA	5.1360	67.2194	4.0944	-23424.830688	Present work
	Exp.	5.2430				[9]
GdH_2	GGA	5.326	53.1873	4.0861	-22563.0572	[13]
	Exp.	5.296				[9]

Furthermore, the bulk modulus of TbH_2 when computed with LDA is higher than that of GGA, which is mainly due to the fact that the cell volume expands while computed with GGA.

All physical properties are related to the total energy. For instance, the equilibrium lattice constant of a crystal is the lattice constant that minimizes the total energy. If the total energy is calculated, any physical property

IV-II-2-2 Electronic properties

Due to the periodicity of the lattice, the band structure is calculated for the first Brillouin zone only. The symmetry of the lattice allows the calculation of all possible non-equivalent bands by selecting a one-dimensional path in this zone, which includes all the important high symmetry points. These points are marked by capital Greek and Latin letters and are shown on the band structure plots.

The electronic band structure calculated in density functional theory is calculated from the electron density by solving Kohn-Sham equations and calculating the energy eigenvalues.

The energy which corresponds to the highest occupied orbital is called *Fermi level* and is usually set to zero. The energy levels just below the Fermi level E_F are called *valence band* as they correspond to the electrons which take part in the bond formation. The unoccupied states above E_F are called *conduction band*. Another possibility for analyzing the electronic structure is to calculate the density of states (DOS), which is the number of electrons occupying the same energy level in the first Brillouin zone.

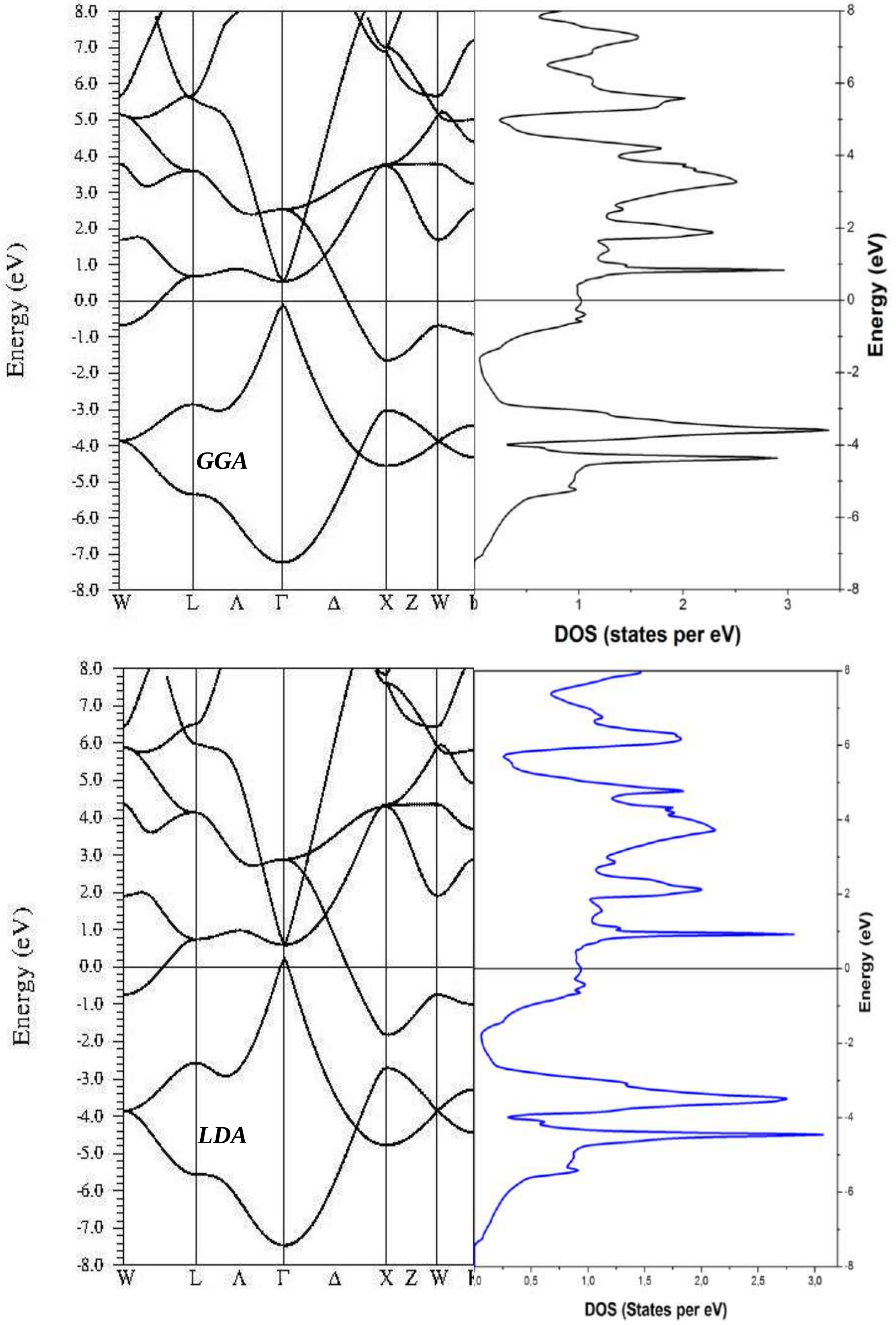

Fig. IV-9 Calculated density of states (right panel) and calculated electronic band structure along high-symmetry directions (left panel) of TbH$_2$ with GGA and LDA, the Fermi energy being at 0 eV.

The calculated band structure and the total density of states for TbH_2 in both GGA and LDA approximations are depicted in **Fig. IV-9**, where E_F is set at 0 eV. It can be clearly seen that this dihydride shows metallic features with a non negligible amount of electrons traversing the Fermi level (see **Table IV-4**). However the calculated density of states at the Fermi level $N(E_F)$ with LDA becomes smaller than that calculated with GGA. The overall band profiles for both approximations are almost similar to each other.

Comparing the GGA-calculated band structure of TbH_2 to that with LDA (**Fig. IV-9**), we find that the LDA-calculated band structure downshifts slightly to lower energies compared to that with GGA, hence the Fermi energy in LDA is slightly larger than that in GGA (**Table IV-4**).

The calculated total DOS of TbH_2 in both GGA and LDA approximations (**Fig. IV-9**) also exhibits a metallic nature due to the presence of some amount of localized DOS across the Fermi energy. Hence, our calculations show that TbH_2 is metallic, in agreement with electrical resistivity measurement interpretations [26].

It can be seen clearly from **Fig. IV-9** that the total DOS in both approximations behave similarly in both the position and shape of the peaks, but with some noticeable changes.

The total density of states describes the distribution of energies for all electrons in the system, while the partial DOS shows the energy distribution of the electrons of a particular atom and its orbital (*s*, *p*, *d*).

Generally speaking, under crystal field effects the orbital *d* consists of: d_{xy}, d_{xz}, d_{yz}, $d_{x^2-y^2}$ and d_{z^2} states. If the material or solid has symmetry (symmetry here refers to the atomic environment's symmetry, not the orbital's), the orbital *d* splits into the two groups e_g and t_{2g}. The d_{z^2} and $d_{x^2-y^2}$ orbitals are collectively called the e_g orbitals, whereas the d_{xy}, d_{xz}, and d_{yz} orbitals are called the t_{2g} orbitals (**Fig. IV-10**).

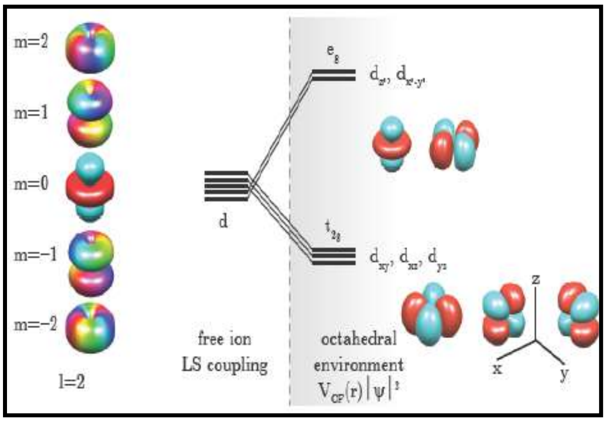

Fig. IV-10 Illustration of the splitting of a free ion's *d* orbitals in an octahedral crystal field. Left side shows the *d* orbitals with different *z* angular momentum component, color is the phase of the complex amplitude. Right side shows the low lying threefold degenerate t_{2g} orbitals and the higher energy twofold degenerate e_g orbitals [27].

The total and partial density of states of TbH_2 calculated in GGA and LDA are shown in **Fig. IV-11**.

Table IV-4: Fermi energy and density of states at the Fermi level for TbH_2.

	Fermi energy (Ry)	*$N(E_F)$ (states/Ry)*
GGA	0.52341	10.30
LDA	0.55723	9.79

The fact is further confirmed by the atomic site projected densities of states (PDOS) profiles in **Fig. IV-11**, which shows a finite number of electrons at the Fermi level, the metal character of TbH_2 mainly comes from the *d* electrons and *p* electrons of the Tb atom, while the *f* electrons of Tb have almost no contribution.

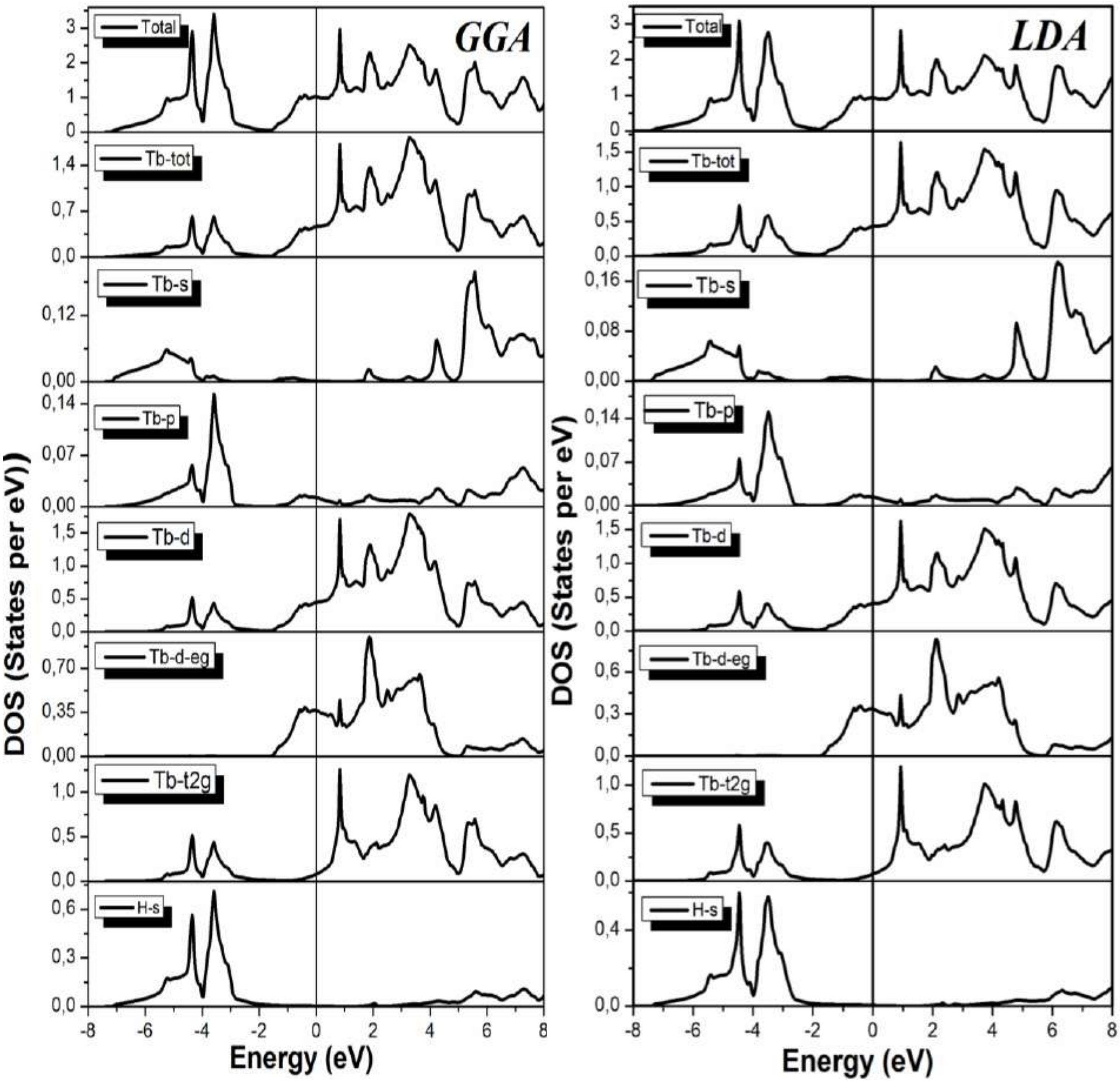

Fig. IV-11 **C**alculated total and partial density of states for TbH_2 in both GGA and LDA approximations, the Fermi energy being at 0 eV.

It can be clearly seen from this figure that the valence band (VB) and conduction band (CB) around the Fermi level are primarily dominated by Tb-*d* electrons, whereas contributions from H-*s* electrons are negligible. In the conduction band, the main contributions are due to the unoccupied states of Tb-*5d*, where the unoccupied bottom of the conduction band is due to the *d-t2g* states peak of Tb and the occupied levels just below E_F are dominated by *d-eg* states of Tb (the Fermi level lies *1.71636 eV* above the bottom of the *5d-eg* metal bands).

The valence band of TbH_2 is formed with Tb-*d* and H-*s* states (as displayed in **Fig. IV-12**) with a non negligible Tb-*p* contribution.

The bottom of the valence band is occupied primarily by the Tb-*d-t2g* and H-*s* states in the range ~ -6 to ~ -2 eV. H-*s* states only contribute to the states of the two lower bands. The main hybridization interactions between Tb-*5d-t2g* and H-*s* orbitals are shown by similarities in the position and shape of the peaks in their respective projected DOS. The presence of the hybridization effects reveals that there are certain covalent bonds in TbH_2.

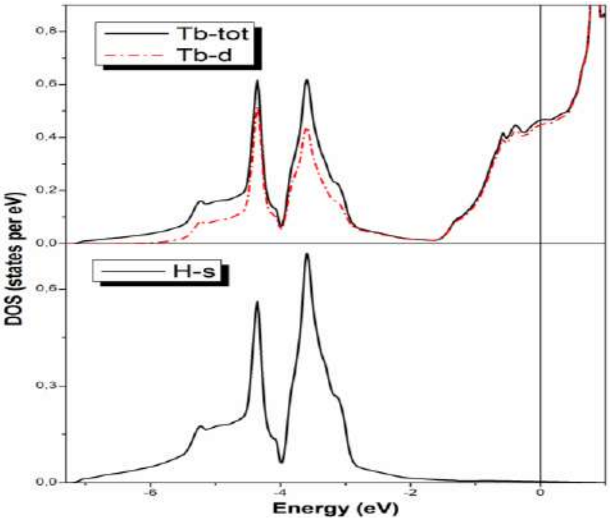

Fig. IV-12 Calculated partial density of states for TbH_2 with GGA, the Fermi energy being at 0 eV.

The interpretation of the chemical bonding is further substantiated by the analysis of the valence-electron-charge density along the representative (110) plane in the fcc CaF_2-type crystal as shown in **Fig. IV-13**. The charge density around Tb and H atoms are all near spherically distributed with a slight deformation towards the directions to their respective nearest-neighboring atoms and there are clear covalent bridges between Tb and H_{tet} atoms. Evidently, considerable charge accumulates in the bonding regions of Tb and H_{tet} atoms, which strengthens the view that TbH_2 has a certain covalent character.

Another point of interest is the existence of a little charge in the interstitial regions away from the bonds which gives a metallic character to this compound, confirming therefore our DOS analysis, and a similar behaviour reported in Ref. [28] (in other rare earth dihydrides).

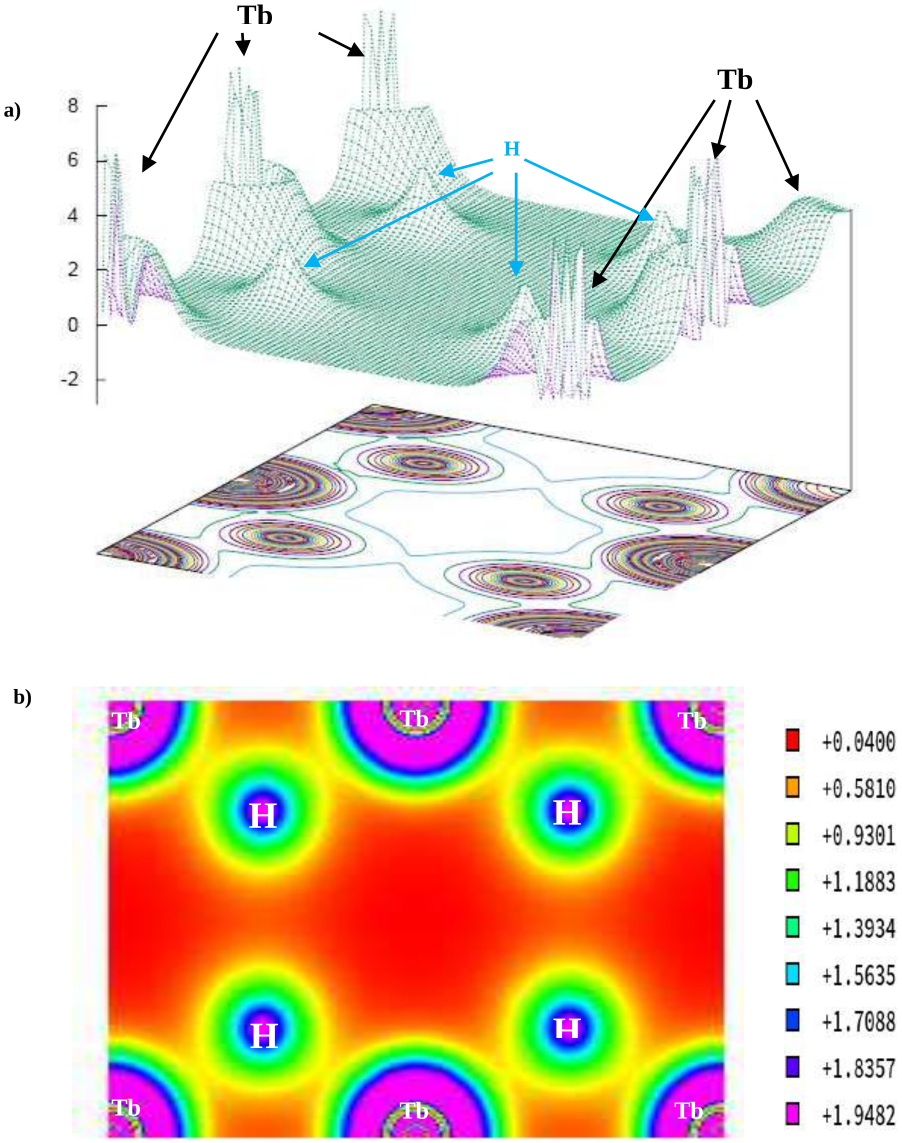

Fig. IV-13 Calculated valence-electron-charge density contour (in electron per Å^3) of TbH_2 in the (110) plane in **(a)** three (large values near the Tb atom are cut out) and **(b)** two dimensions.

IV-III Calculation of the total energy of the H_2 molecule

The total energy of H_2 is obtained by taking a relatively large cubic unit cell, approximately 10x10x10 Angstrom units (i.e. $a=b=c=10$ Å) containing one H_2 molecule in its center as shown in **Fig. IV-14** (plotted using Xcrysden [4]). In this way one simulates the gaseous state of H_2 at ambient conditions.

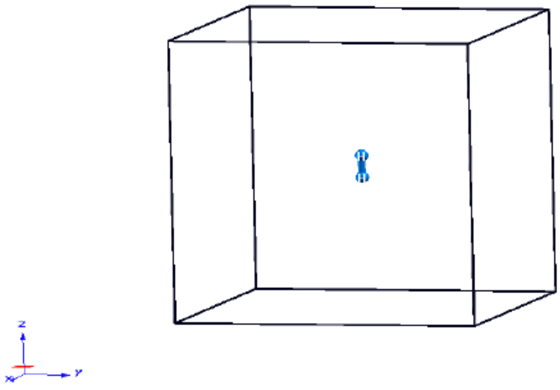

Fig. IV-14 Conventional unit cell for H_2.

The total energy of the hydrogen molecule was calculated using the same code as used previously with an optimized number of k-points of 100. The geometry was instead considered converged, when all atomic force components are smaller than 1. Relaxed positions are reported as displacements (in units of lattice parameters) from ideal positions.

Analysis of the forces shows that the forces (from *case.scf* file) on the hydrogen atoms are zero in the *x* and *y* directions, but nonzero in the *z* direction. The results for H_2 obtained before (unrelaxed state) and after (relaxed state) the geometrical optimization of the internal variables with both GGA and LDA approximations are tabulated in **Table IV-5** together with other available data.

Table IV-5 Unrelaxed and relaxed positions of equivalent atoms for the H_2 molecule in units of lattice parameters (*a, b, c*) for (*x, y, z*) coordinates, respectively, and total energy (Ry) with LDA and GGA approximations.

Method		***Positions***						***Energy***	***Reference***
		x		***y***		***z***			
Unrelaxed	LDA	0.50	0.50	0.50	0.50	0.537	0.463	-2.26925128	Present work
	GGA	0.50	0.50	0.50	0.50	0.537	0.463	-2.32754445	
Relaxed	LDA	0.50	0.50	0.50	0.50	0.53837127	0.46162873	-2.27014894	
	GGA	0.50	0.50	0.50	0.50	0.53755349	0.46244651	-2.32772272	
Others								-2.324803	[29]
								-2.320	[30]
								-2.32806871	[31]

The calculated total energies of the hydrogen molecule are very close to the value obtained by others, for both cases using the initial or relaxed structures. The calculated total energies are slightly overestimated in the GGA than that in the LDA calculations. As expected, the total energies calculated by relaxing the structure are slightly larger than those of the initial unrelaxed structure.

IV-IV Thermodynamic properties

In principle, theoretical evaluation of the hydride stability can be made directly from the total energy of the alloys involved in the hydrogenation reaction.

$$R + H_2 \rightarrow RH_2 \tag{IV-1}$$

We define ΔH_f as the heat of formation for the chemical reaction (IV-1) as follows:

$$\Delta H_f = E_{RH_2} - E_{R(hcp)} - E_{H_2} \qquad [IV\text{-}3]$$

where E_{RH_2}, $E_{R(hcp)}$ and E_{H_2} are the total energies of RH_2, R and H_2, respectively. The E_{H_2} taken in this calculation was calculated previously using GGA and LDA approximations (relaxed state).

To get more insight into the stability of the RH_2, we calculated the cohesive energy $E_{coh}(RH_2)$ (R = Gd, and Tb) and the average binding energy per H atom $E_b(H)$. The cohesive energy $E_{coh}(RH_2)$ and the average binding energy per H atom $E_b(H)$ [32] of RH_2 are expressed as:

$$E_{coh}(RH_2) = E_{RH_2} - E_R^{atom} - 2\,E_H^{atom} \qquad [IV\text{-}4]$$

$$E_b(H) = \frac{1}{2}\left[E_{RH_2} - E_{R(hcp)}\right] - E_{H(atom)} \qquad [IV\text{-}5]$$

Tables IV-6 and **IV-7** include the WIEN2k calculations of ΔH_f, $E_b(H)$ and $E_{coh}(RH_2)$ that are used to understand the stability of RH_2 (R = Gd, and Tb) with the two approximations. From **Table IV-6**, it is observed that, for TbH_2, the LDA calculation gives a much larger formation energy compared to the GGA approximation.

Table IV-6 Calculated cohesive energy E_{coh} (eV), binding energy E_b (eV/atom), and heat of formation (ΔH_f) (kJ/mol H_2) for GdH_2 in GGA methods.

	method	***E_{coh}***	***$E_b(H)$***	***ΔH_f***	***Reference***
GdH_2	GGA	-13.938559292	-4.77125715	-270.5016586	Present work
	other			-196	[33]

Additionally, our calculated value of ΔH_f for RH_2 is in qualitative agreement with Andreasen's results [34] (as it is situated in the experimental interval values for heats of formation of rare earth metal hydrides), also, it is found that the GdH_2 and TbH_2 have negative heats of formation, which suggests that these dihydrides can be easily synthesized at ambient condition.

On the other hand, the cohesive energy and average binding energy per H atom of TbH_2 in the GGA is less than that in the LDA by 8.568% and by 5.543% respectively. This makes the value of cohesive energy and average binding energy per H atom decrease with increasing cell parameter.

Table IV-7 Calculated cohesive energy E_{coh} (eV), binding energy E_b (H) (eV/atom), and heat of formation (ΔH_f) (kJ/mol H_2) for TbH_2 in both GGA and LDA methods.

	method	E_{coh}	$E_b(H)$	ΔH_f	***Reference***
TbH_2	GGA	-13.290380707	-4.469775698	-212.335202917	Present work
	LDA	-14.407427294	-4.725686906	-268.643842203	
	others			-213	[33]

IV-V Summary

In this chapter, we studied the structural, electronic, and thermodynamic properties for stoichiometric dihydrides, viz. β-GdH_2 and β-TbH_2. Calculations performed using an *ab initio* FP-LAPW method as implemented in the WIEN2k code have led to the following conclusions:

- The lattice parameter LDA calculations underestimate experimental results while GGA calculations overestimate them. In addition, the GGA calculated lattice constants agree well with available experimental data.
- The nature of bonding in the rare-earth dihydrides RH_2 (R = Gd, Tb) must be discussed in terms of interaction between metal *d* states and hydrogen 1*s*-states.
- The position and width of the low-lying bands depend quite sensitively on the type of rare earth considered.
- The low-lying bands found in these dihydrides are not composed uniquely of hydrogen *s* states but rather show a strong hybridization with metal *d*- and also metal *s*- and *p*-states.
- The Fermi energy E_F falls at a level where most of the electronic states are rare-earth *5d* conduction states.
- The H*s*-state has no contribution near the Fermi level.
- LDA leads to an overestimation of cohesion and formation heats.
- It is found that the GdH_2 and TbH_2 have negative heats of formation, which suggests that these dihydrides can be easily synthesized at ambient conditions.
- The value of cohesive energy and average binding energy per H atom decrease with increasing cell parameter.

References

[1] M. Gupta and J. P. Burger. *Phys. Rev. B* **22**, 6074 (1980).

[2] Y. Fukai. *The Metal-Hydrogen System*. 1993.

[3] M. Gupta. *Solid State Commun.* **27**, 1355 (1978).

[4] A. Kokalj. *XCrysDen - a new program for displaying crystalline structures and electron densities*, Comp. Mater. Sci. 28 (2003) 155. Code available from http://www.xcrysden.org.

[5] P. Hohenberg and W. Kohn. *Phys. Rev.* **136**, B864 (1964).

[6] W. Kohn and L. J. Sham. *Phys. Rev. A* **140**, A1133 (1965).

[7] P. Blaha, K. Schwarz, G. Madsen, D. Kvasnicka, and J. Luitz. *Wien2k, an Augmented Plane Wave Plus Local Orbitals Program for Calculating Crystal Properties*. Techn. Universität, Vienna, Austria, 2001, ISBN 3-9501031-1-2.

[8] J. P. Perdew, K. Burke, and M. Ernzerhof. *Phys. Rev. Lett.* **77**, 3865 (1996).

[9] M. Chiheb, J. N. Daou, and P. Vajda. *Z. Phys. Chem.* **179**, 271 (1993).

[10] F. D. Murnaghan. *Proc. Natl. Acad. Sci.* **30**, 244 (1944).

[11] C. Koitzsch, J. Hayoz, M. Bovet, F. Clerc, L. Despont, C. Ambrosch-Draxl, and P. Aebi. *Phys. Rev. B* **70**, 165114 (2004).

[12] M. Ellner, H. Reule, and E. J. Mittemeijer. *J. Alloys Compd.* **279**, 179 (1998).

[13] Z. Ayat, B. Daoudi, A. Ouahab, and A. Boukraa. *Metallofiz. Noveishie Tekhnol.* **37**, 593 (2015).

[14] S. Jalali Asadabad, S. Cottenier, H. Akbarzadeh, R. Saki, and M. Rots. *Phys. Rev. B* **66**, 195103 (2002).

[15] P. Vajeeston, P. Ravindran, R. Vidya, A. Kjekshus, H. Fjellvåg, and V. A. Yartys. *Phys. Rev. B* **67**, 014101 (2003).

[16] A. C. Switendick. *Int. J. Quantum Chem.* **5**, 459 (1971).

[17] D. K. Misemer and B. N Harmon. *Phys. Rev. B* **26**, 5634 (1982).

[18] A. Fujimori and N. Tsuda. *Solid state Commun.* **41** (1982) 491.

[19] A. C. Switendick. *Solid State Commun.* **8**, 1463 (1970).

[20] J. H. Weaver. *Bull. Amer. Phys. Soc.* **23**, 295 (1978).

[21] J. P. Perdew and Y. Wang. *Phys. Rev.* **45**, 13244 (1992).

[22] J. P. Perdew, J. A. Chevary, S. H. Vosko, K. A. Jackson, M. R. Pederson, D. J. Singh, and C. Fiolhais. *Phys. Rev. B* **46**, 6671 (1992).

[23] P. Vajeeston, R. Vidya, P. Ravindran, H. Fjellvåg, A. Kjekshus, and A. Skjecltorp. *Phys. Rev. B* **65**, 075101 (2002).

[24] F. Birch. *Phys. Rev.* **71**, 809 (1947).

[25] Z. Ayat, A. Boukraa, B. Daoudi, and A. Ouahab. *Chin. J. Phys.* **55**, 2157 (2017).

[26] P. Vajda. *Hydrogen in rare earth metals*. 1995.

[27] S. Tóth. *Magnetism of 3d Frustrated Magnetic Insulators: α-$CaCr_2O_4$, β-$CaCr_2O_4$ and Sr_2VO_4*. Thesis. Technischen Universität Berlin; Berlin. 2012.

[28] B. Y. Ao, X. L. Wang, P. Shi, P. H. Chen, X. Q. Ye, X. C. Lai, J. J. Ai, and T. Gao. *Int. J. Hydrogen Energy* **33**, 5108 (2012).

[29] Y. Song, Z. X. Guo, and R. Yang. *Phys. Rev. B* **69**, 094205 (2004).

[30] H. Nakamura, D. Nguyen-Manh, and D. G. Pettifor. *J. Alloys Compd.* **281**, 81 (1998).

[31] http://www.blacklightpower.com/theory/bookdownload.shtml.

[32] Y. Wang and M. Y. Chou. *Phys. Rev. B* **49**, 10731 (1994).

[33] G. G. Libowitz and A. J. Maeland. *Handbook on the Physics and Chemistry of Rare Earths*. 1979.

[34] A. Andreasen. *Predicting formation enthalpies of metal hydrides*. 2004.

CHAPITER V

Superstoichiometric rare-earth dihydrides $RH_{2.25}$ (R = La and Gd) with I4/mmm space group: structural and electronic properties

Structural and electronic properties of superstoichiometric $LaH_{2.25}$ and $GdH_{2.25}$ in a tetragonal structure will be presented in this chapter. The calculations are based on ab initio calculations at 0 K within density functional theory (DFT), using a full-potential linear augmented plane-wave (FP-LAPW) method with both GGA and LDA approximations as implemented in the WIEN2k code.

V-I Computational method

Reliability of the scheme of the calculations is crucial for scientific investigations particularly for uncommon quantum many body systems. Microscopic study of a typical solid material, containing approximately 10^{23} atoms per cm^3, is a quantum many-body problem. DFT [1, 2] based first-principles methods are intensively used to investigate microscopically the fundamental properties of solid materials. Here we use the FP-LAPW method embodied in the WIEN2k computational package [3] which is now considered as one of the most accurate DFT approaches. The cutoff in the charge density Fourier expansion, G_{max}, was taken to be 20 $Ry^{1/2}$.

Rare earths can be problematic for DFT calculations. We note that one can expect the existence of finite localized magnetic moments on the *4f* electrons. This magnetic aspect has not been considered in our calculations. It is known, indeed, that, in rare earths, the *4f* electrons, being very close to the core, are expected to be chemically inert. This leads us to consider *4f* electrons as atom-core electrons, i.e. they cannot hybridize with the other *s*, *p*, and *d* valence electrons anymore and are perfectly localized [4]. For these reasons, the contribution of the *4f* electrons are removed from the valence bands, and are treated as those of core electrons.

The core states energy was separated from the valence states, at -8.0 Ry, while the Gd ($5s^2 5p^6 5d^1 6s^2$), La ($5s^2 5p^6 5d^1 6s^2$) and H ($1s^1$) orbitals were treated as valence states (we did not treat the *f* orbitals of Gd as valence electrons but as core electrons). Exchange and correlation effects were treated within the density functional with the generalized-gradient approximation of Perdew, Burke and Ernzerhof (GGA96) [5] and the local density approximation (LDA) [6]. The calculations were based on an optimized number of k-points of 1000, without considering the spin polarization. The self-consistent convergence criteria of total energy calculations of the system are achieved when the total energy is stabilized within 10^{-4} Ry.

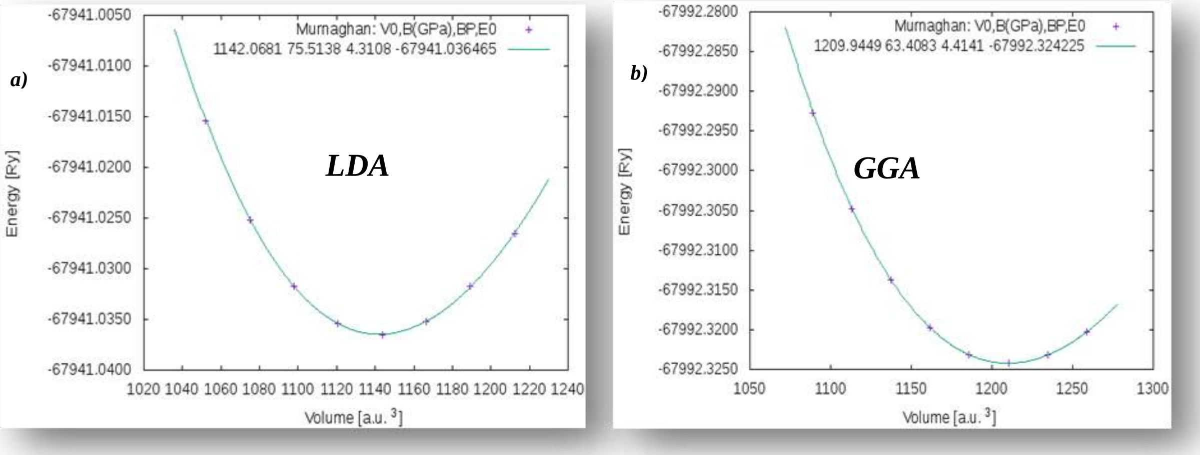

Fig. V-1 Calculated total energy curves for $LaH_{2.25}$ as a function of cell volume in the (a) LDA and (b) GGA approximations.

V-II <u>Results and discussion</u>

V-II-1 Equilibrium properties

For the present investigation, we have used a 1x1x2 supercell of $LaH_{2.25}$ and $GdH_{2.25}$ conventional unit cell for the tetragonal structure, where its space group is *I4/mmm* (*No. 139*). The simulated unit cell is optimized for total energy (E) as a function of volume (V). Then the obtained total energies are inserted into Murnaghan's equation of state [7] to find the ground state structural parameters. We present the E(V) relationship of the $LaH_{2.25}$ and $GdH_{2.25}$ for both LDA and GGA approximations in **Figs. V-1 (*a*)** and **(*b*)** and in **Figs. V-2 (*a*)** and **(*b*)** respectively. We extract the lattice parameter, the value of the bulk modulus, and its first order pressure derivative. The results data are listed in **Table V-1** and **Table V-2** together with previous experimental and theoretical findings. There are no experimental data for the bulk modulus available for this material and there is no direct *ab initio* theoretical information available for $LaH_{2.25}$ and $GdH_{2.25}$ related to the effects of interstitial H atoms on their local atomic environment in this structure.

Table V-1 Calculated equilibrium lattice constant (a_0, c_0) (in Å), bulk modulus B_0 (in GPa), its first order pressure derivative B_0', and total energy (Ry) of $LaH_{2.25}$ for GGA and LDA approximations compared to experimental and theoretical data.

	Method	a_0	c_0	B_0	B_0'	***Total energy***	***Reference***
$LaH_{2.25}$	GGA	5.6202	11.3528	63.4083	4.4141	-67992.324225	Present work
	LDA	5.5131	11.1364	75.5138	4.3108	-67941.036465	
$LaD_{2.25}$	Exp. (at 17 K)	5.6174(1)	11.3054(3)				[8]
$LaH_{2.25}$		5.6082	11.2879				[9]
LaH_2	Exp.	5.6698					[10]
$ErH_{1.95}$	Exp.			67±3	9 fixed		[11]
$ErH_{2.091}$	Exp.			73±4	8 fixed		[11]

Our calculated lattice parameters for $LaH_{2.25}$ and $GdH_{2.25}$ are in excellent agreement with the other theoretical and available experimental data; see **Tables V-1** and **V-2**.

The GGA equilibrium lattice parameter (a_0 and c_0) for $LaH_{2.25}$ and $GdH_{2.25}$, from **Tables V-1** and **V-2**, slightly overestimates the experimental value, while the LDA value is clearly smaller than the experimental one. Conversely for the bulk modulus, it is the GGA value which is lower than that of the LDA as a result of the known over-binding characteristic of LDA. Hence, GGA overestimates lattice parameters whereas it underestimates bulk moduli (B_0) in comparison with LDA, a feature also observed in several similar systems in other simulation works [12].

Moreover, our calculated lattice parameter of $GdH_{2.25}$ in GGA is smaller than that of GdH_2 in both GGA and GGA+U methods reported by Sudha Priyanga et al. [13], which is in agreement with the observed experimental trend as reviewed by Vajda [10].

Furthermore, in GGA, the bulk modulus value of and $GdH_{2.25}$ is larger than that of and GdH_2; this behaviour is similar to that found experimentally in the ErH_{2+x} system (as shown in **Table V-1** and **V-2**) [11] and theoretically by using GGA+U+SO (SO stands for spin-orbit coupling) calculations in the PuH_{2+x} system [17] and by using the GGA method in the ScH_{2+x}, YH_{2+x}, LaH_{2+x} and LuH_{2+x} systems [18]. Moreover, we found that the value of the lattice parameter decreases with increasing excess hydrogen (x) in the GdH_{2+x} system as found by a pseudopotential method plus LDA with a plane-wave basis in the YH_{2+x} system [19], by

LDA+*U* calculations in the CeH_{2+x} system [20], and by GGA+*U*+SO calculations in the PuH_{2+x} system [17].

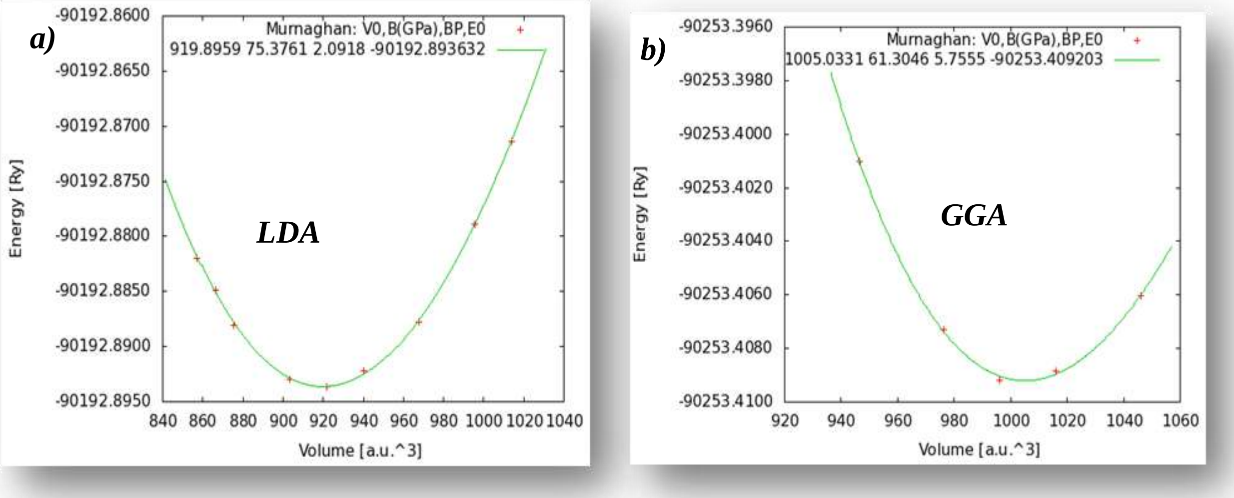

Fig. V-2. Calculated total energy curves for $GdH_{2.25}$ as a function of cell volume in the (a) LDA and (b) GGA approximations.

Table V-2 Calculated equilibrium lattice constant (a_0, c_0) (in Å), bulk modulus B_0 (in GPa), its first order pressure derivative B_0', and total energy (Ry) of $GdH_{2.25}$ for GGA and LDA approximations compared to experimental data.

	Method	a_0	c_0	B_0	B_0'	*Total Energy*	*Reference*
$GdH_{2.25}$	GGA	5.301	10.6025	61.3046	5.7555	-90253.409203	Present work
	LDA	5.147	10.294	75.3761	2.0918	-90192.893632	[14]
	Exp.	5.2926					[15]
GdH_2	GGA	5.326		53.1873	4.0861	-22563.057167	Present work [16]
$ErH_{1.95}$	Exp.			67±3	9 fixed		[11]
$ErH_{2.091}$	Exp.			73±4	8 fixed		[11]

V-II-2 Electronic properties

The calculated electronic band structures at the equilibrium lattice constant for different high-symmetry points in the Brillouin zone and the total density of states DOS of $LaH_{2.25}$ and $GdH_{2.25}$ in GGA and LDA at 0 K are shown in **Figs. V-3** and **V-4** respectively, where the dashed line at zero eV indicates the Fermi energy.

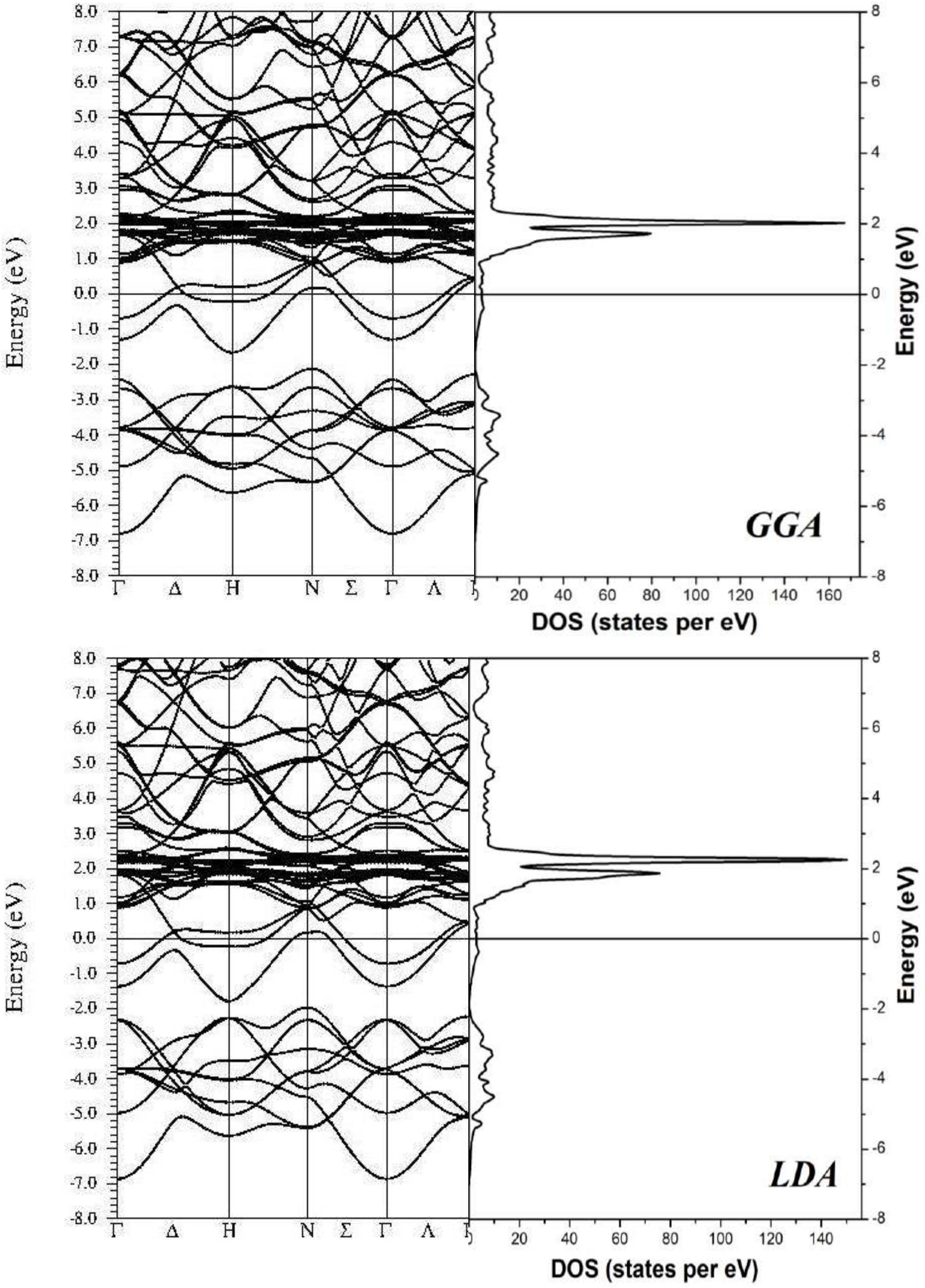

Fig. V-3 Density of states (right panel) and electronic band structure along high-symmetry directions (left panel) of $LaH_{2.25}$ in the GGA and LDA, the Fermi energy being at 0 eV.

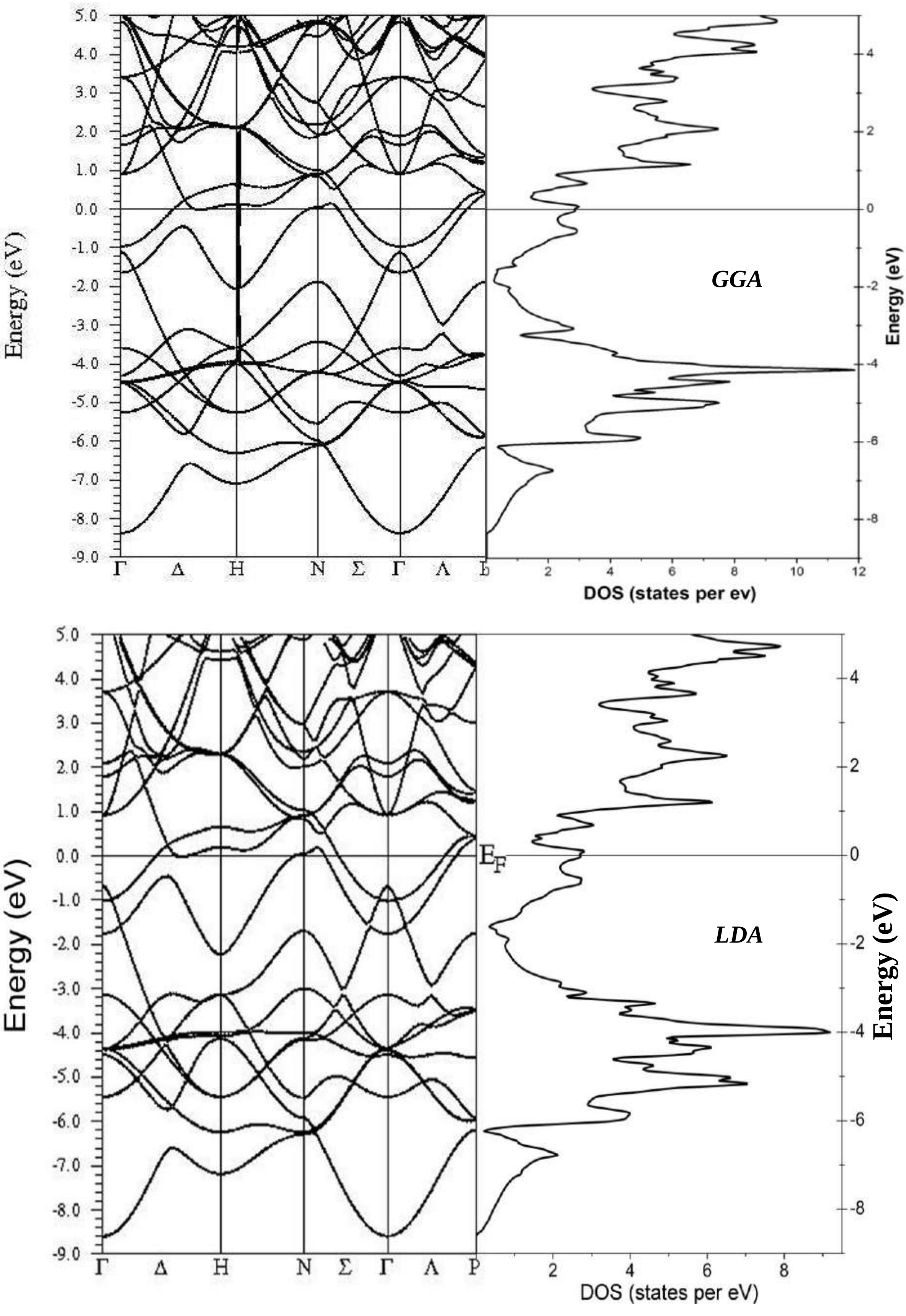

Fig. V-4 Density of states (right panel) and electronic band structure along high-symmetry directions (left panel) of $GdH_{2.25}$ in the GGA and LDA, the Fermi energy being at 0 eV.

Clearly, in both figures, several bands cross the Fermi level (E_F), confirming that $LaH_{2.25}$ and $GdH_{2.25}$ possesses a metallic ground-state (the density of states on the Fermi level $N(E_F)$ is not negligible as seen in **Tables V-3** and **V-4**), in agreement with electrical resistivity measurement interpretations [10].

Table V-3 Calculated Fermi energy and density of states at the Fermi level for $LaH_{2.25}$.

	Fermi energy (Ry)	***$N(E_F)$ (states/Ry)***
LaH_{225} (GGA)	0.57078	40.75
LaH_{225} (LDA)	0.58848	38.64

The LDA and GGA energy band structures are qualitatively similar. Indeed, the crossings of bands with the Fermi level are nearly the same in the two approximations, where the values of the Fermi energy in LDA are higher than those in GGA for both dihydrides (as seen in **Tables V-3** and **V-4**). Another significant feature of the band structures in **Figs. V-3** and **V-4** is the different positions of the valence bands (at Γ), where, in the LDA, these shift towards higher energies at the top of the valence band, and towards lower energies at the bottom of the valence band.

Table V-4 Calculated Fermi energy and density of states at the Fermi level for $GdH_{2.25}$ (present work Ref. [14]).

	Fermi energy (Ry)	***$N(E_F)$ (states/Ry)***
GdH_{225} (GGA)	0.42622	38.44
GdH_{225} (LDA)	0.50009	36.85

The total DOS of $LaH_{2.25}$ and $GdH_{2.25}$ has similar features in both GGA and LDA (see **Figs. V-3** and **V-4**) especially at the Fermi level. However, these figures show small but non negligible differences as the peaks in the GGA are fairly sharper and narrower than those in LDA, and the total DOS in LDA moves a little towards lower energies compared to GGA.

From **Figs. V-5** and **V-6**, it is seen that the total DOS of $LaH_{2.25}$ and $GdH_{2.25}$ is almost dominated by the *5d* partial DOS. The partial density of states (PDOS) of $RH_{2.25}$ (R = La, and Gd) in both approximations GGA and LDA are shown in **Figs. V-7** and **V-8**.

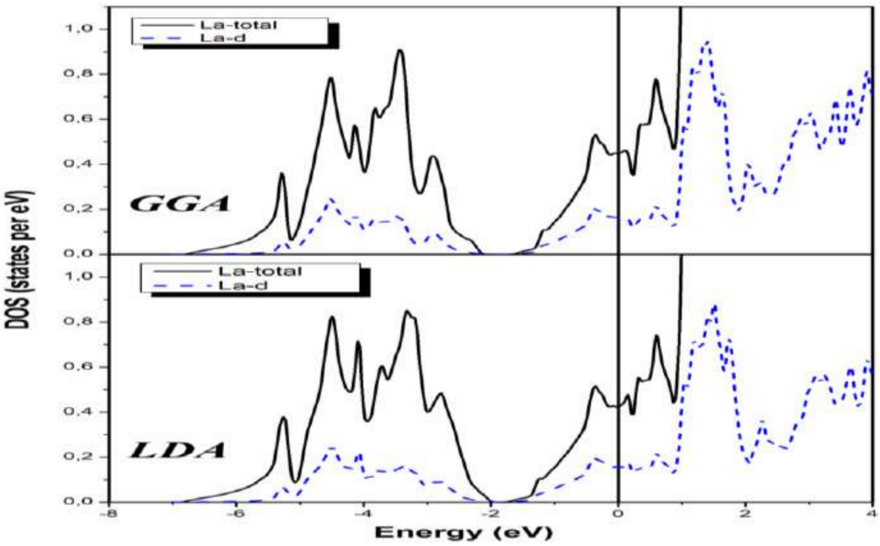

Fig. V-5 The calculated total density of states for La and partial DOS for the La-d in the GGA and in the LDA, the Fermi energy being at 0 eV.

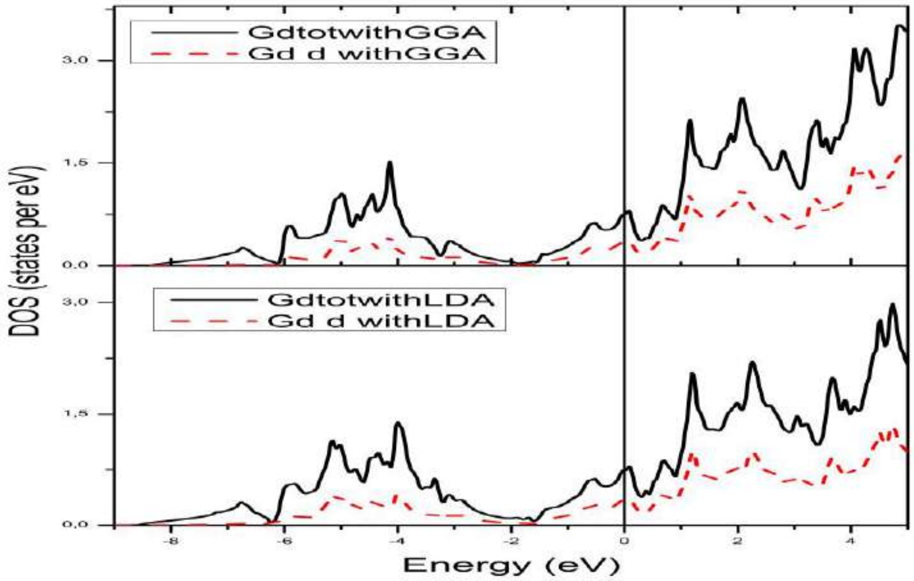

Fig. V-6 The calculated total density of states for Gd and partial DOS for the Gd-d in the GGA and in the LDA, the Fermi energy being at 0 eV.

We can begin this analysis from the situation at the Fermi level. It can be seen clearly that the hydrogen in both interstitial sites (tetrahedral H_{tet} and octahedral H_{oct}), and both R-*s* and R-*p* (R = La, and Gd), do not contribute significantly at the Fermi level, which means that they are essentially not involved in conduction properties. In contrast, the R (R = La, and Gd) *d* electrons represent the majority contribution at E_F.

From the atomic site projected densities of states (PDOS) profiles in **Fig. V-7**, it is shown further that the upper part of the valence band from *-6.86788 eV* to *-2.05147 eV* of GGA and from *-6.91822 eV* to *-1.91133 eV* of LDA contains H *1s* states (in both tetrahedral and octahedral sites), La *5p*, *5d* and *5s* states. While the most prominent unoccupied energy bands in the lowest energy domain of the conduction band are composed of *p* and *d* states from La. The 4*f*-lanthanum unoccupied states manifest themselves with a sharp band structure from *1.21390 eV* of GGA and from *1.29962 eV* of LDA above the Fermi energy.

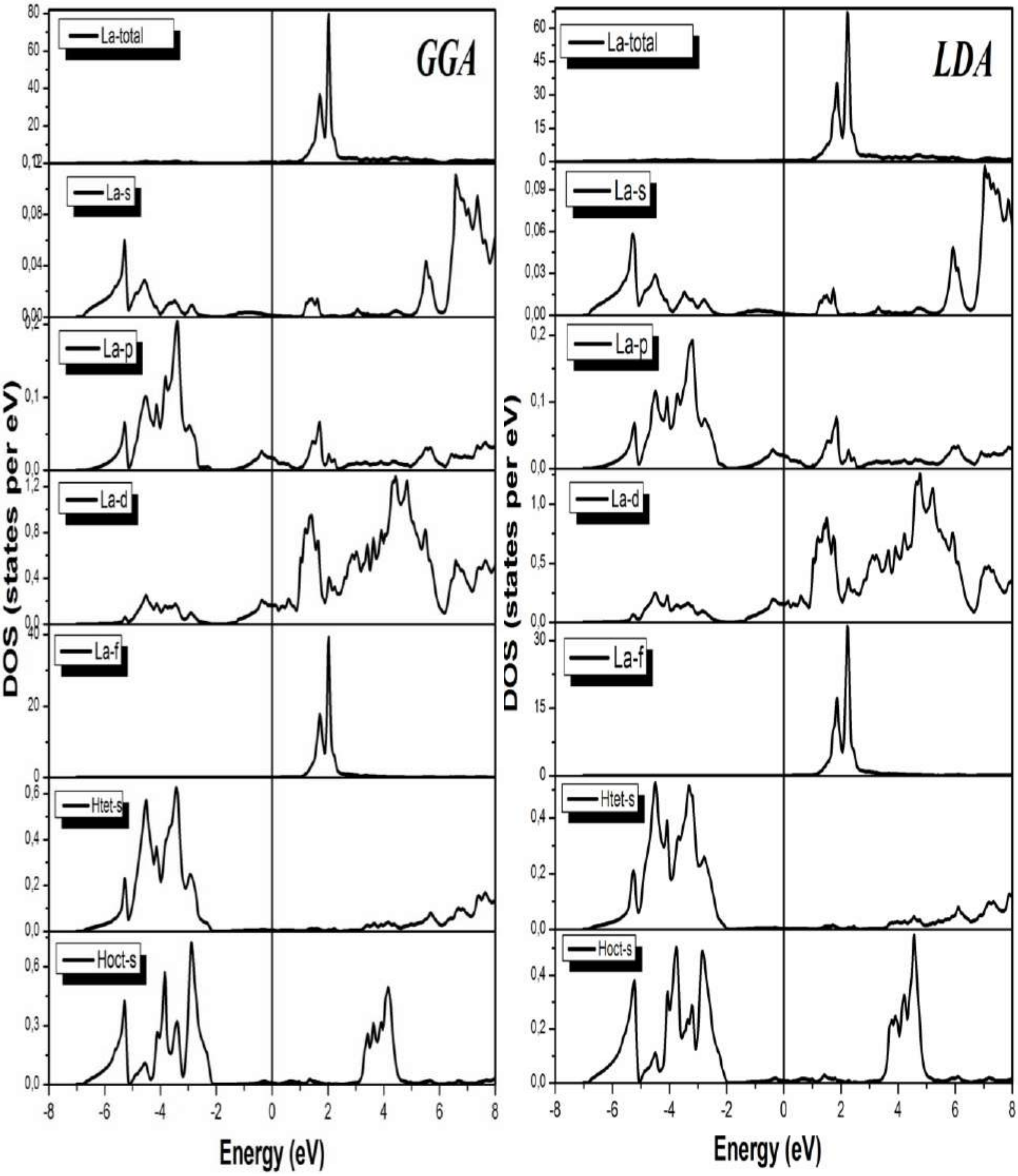

Fig. V-7 The calculated total and partial density of states for LaH$_{2.25}$ in the GGA and in the LDA, the Fermi energy being at 0 eV.

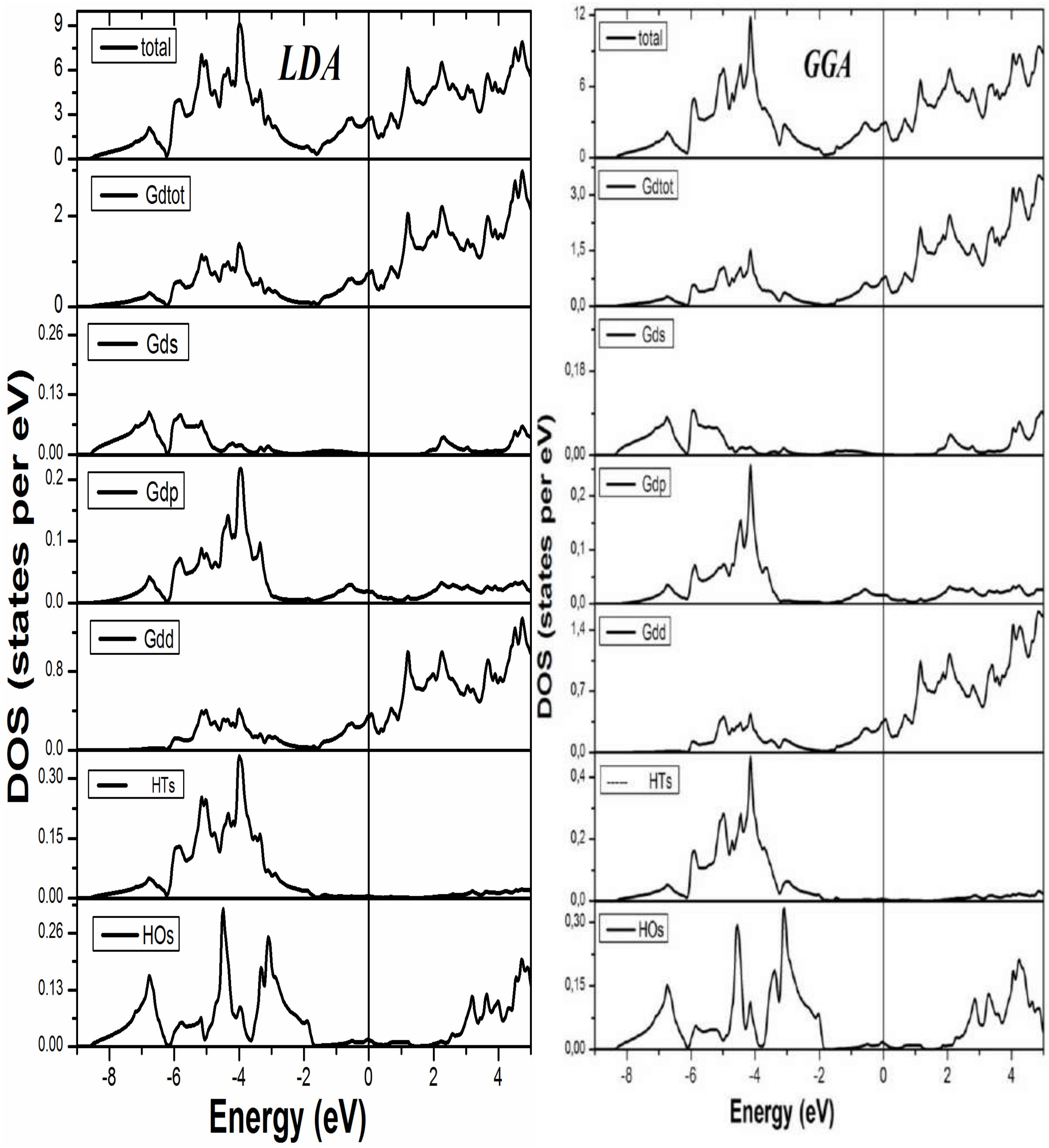

Fig. V-8 The calculated total and partial density of states for $GdH_{2.25}$ in the GGA (right panel) and in the LDA (left panel), the Fermi energy being at 0 eV.

In **Fig. V-8**, it is convenient to divide the DOS into several regions: region I (*-8.44458* to *-1.58725 eV*) of GGA and (*-8.65451* to *-1.60671 eV*) of LDA with a major contribution from Gd *d* states and both H *1s* orbitals and much smaller contributions from Gd *s* and *p* orbitals; region II (*-1.58725 eV* to E_F) of GGA and (*-1.60671 eV* to E_F) of LDA with very few Gd-*p* and Gd-*d* states; region III (above E_F in the lowest energy domain of the conduction band) with unoccupied *s*, *p* and *d* states from Gd and *s* from H in octahedral sites (H_{oct}).

It is interesting to note that a hybridization exists between R (R = La and Gd) and H_{tet} atoms as shown in **Figs. V-7** and **V-8**, which leads to an appreciable covalent component in the R-H bond. On the other hand, hybridization between R (R = La and Gd) and H_{oct} atoms is much weaker, indicating a degree of ionic character in this bond, which is mainly due to the longer R-H_{oct} distance (*2.6516 Å* with GGA and *2.5735 Å* with LDA for R = Gd, *2.8101 Å* with GGA and *2.7565 Å* with LDA for R = La). A minimal atomic bonding distance (*2.2963 Å* with GGA and *2.2287 Å* with LDA of R = Gd, and *2.4417 Å* with GGA and *2.3952 Å* with LDA of R = La) exists between R and H_{tet} atoms. Therefore, the R-H bonds in $LaH_{2.25}$ and $GdH_{2.25}$ have a mixed (covalent-ionic) character as is found in several metal hydrides [21-23].

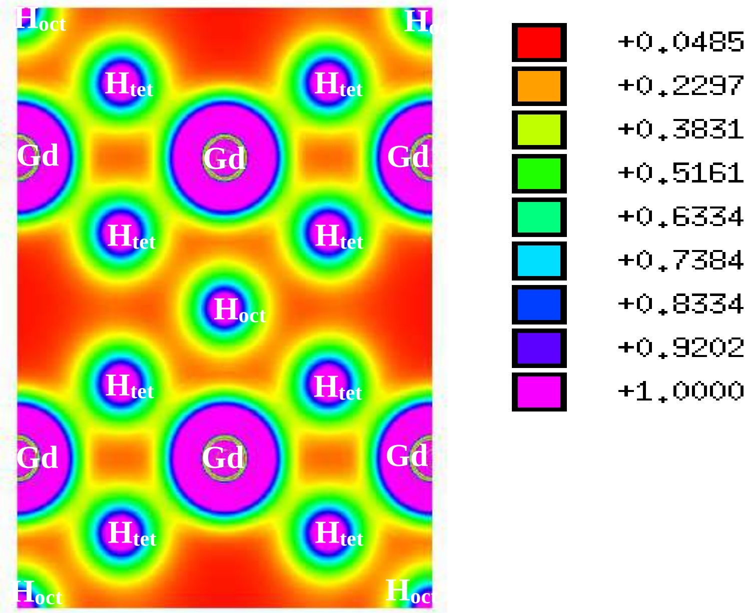

Fig. V-9 Calculated valence-electron-charge density contours (in electrons per $Å^3$) of $GdH_{2.25}$ in the (110) plane.

To gain an insight into the metal–hydrogen bonding of the $RH_{2.25}$ system, we plot the charge-density in the (110) plane of $GdH_{2.25}$ as shown in **Fig. V-9**. The eight H atoms lined out in the map occupy the tetrahedral interstices (H_{tet}). Appreciable charge is distributed in the outer space of Gd and tetrahedral H atoms. To some extent, there is a buildup of charge in the bonding regions between the different atoms. Therefore, their bonding has some covalence, which agrees well with the hybridization analysis.

In addition, as shown in **Fig. V-9**, we have drawn five H atoms occupying octahedral interstices (H_{oct}). The charge density is rather low around Gd and octahedral H atoms in the interstices. Notice that almost little charge accumulates in the bonding regions of Gd and octahedral H atoms, and there is little charge for them to share. Most of the valence electrons of Gd are firmly bound up around their atoms, and the localization reflects the main feature of the ionic chemical bonds. Therefore, the bonding of Gd and octahedral H atoms has ionic character. Apparently, besides the covalent bonds, there are remarkable ionic bonds in the $GdH_{2.25}$ system.

V-III Summary

This work was aimed at establishing a clearer picture of electronic structure and equilibrium properties for rare earth superstoichiometric dihydrides ($LaH_{2.25}$ and $GdH_{2.25}$) with *I4/mmm* space group. Calculations were performed using an *ab initio* FP-LAPW method in the local density approximation (LDA) and generalized gradient approximation (GGA) for exchange correlation as implemented in WIEN2k code. In GGA, the calculated lattice constant is larger and bulk modulus is smaller compared to LDA results. On the other hand, the calculated lattice constant with GGA agrees well with available experimental data. As far as we know, there are no bulk modulus data for the considered crystal structure. Electronic band structure and DOS, which were calculated and presented, clearly show that $LaH_{2.25}$ and $GdH_{2.25}$ exhibit metallic behaviour. The total DOS in GGA and LDA shows important differences in the vicinity of valence band, where GGA presents a tendency for under-binding in this material. In addition, the value of DOS at the Fermi level ($N(E_F)$) in GGA is larger than that in LDA. The DOS analysis shows that the Fermi energy (E_F) falls at a level where most of the electronic states are rare-earth *5d* conduction states, while negligible contribution of both (tetrahedral H_{tet} and octahedral H_{oct}) interstitial H *s* states is observed at E_F.

The *d* states of R (La and Gd) atoms are the main contributors to bonding states in valence bands, whereas *p* and *s* states have a smaller role. It is found that hybridization exists between *s* electronic orbital of both interstitial H atoms and *d* electronic orbitals of R. This hybridization implies that there is a mixture of covalent ($R–H_{tet}$) and ionic ($R–H_{oct}$) bonds.

References

[1] P. Hohenberg, W. Kohn. *Phys. Rev.* **136**, B864 (1964).

[2] W. Kohn and L. J. Sham. *Phys. Rev. A* **140**, A1133 (1965).

[3] P. Blaha, K. Schwarz, G. Madsen, D. Kvasnicka, and J. Luitz. *Wien2k, an Augmented Plane Wave Plus Local Orbitals Program for Calculating Crystal Properties*. Techn. Universität, Vienna, Austria, 2001, ISBN 3-9501031-1-2.

[4] P. Vajeeston, R. Vidya, P. Ravindran, H. Fjellvåg, A. Kjekshus, and A. Skjecltorp. *Phys. Rev. B* **65**, 075101 (2002).

[5] J. P. Perdew, K. Burke, and M. Ernzerhof. *Phys. Rev. Lett.* **77**, 3865 (1996).

[6] J. P. Perdew and Y. Wang. *Phys. Rev.* **45**, 13244 (1992).

[7] F. D. Murnaghan. *Proc. Natl. Acad. Sci.* **30**, 244 (1944).

[8] T. J. Udovic, Q. Huang, J. J. Rush, J. Schefer, and I. S. Anderson. *Phys. Rev. B* **51**, 12116 (1995).

[9] T. C. Kerscher, G. Schöllhammer, P. Herzig, W. Wolf, R. Podloucky, and S. Müller. *Phys. Rev. B* **86**, 014107 (2012).

[10] P. Vajda. *Hydrogen in rare earth metals*. 1995.

[11] T. Palasyuk, M. Tkacz, and P. Vajda. *Solid State Commun.* **135**, 226 (2005).

[12] J. Ai, T. Liu, T. Gao, and B. Ao. *Computat. Mater. Sci.* **51**, 127 (2012).

[13] P. G. Sudha, R. Rajeswarapalanichamy, and K. Iyakutti. *Int. J. Hydrogen Energy* **31**, 415 (2015).

[14] Z. Ayat, A. Boukraa, A. Ouahab, and B. Daoudi. *Rare Met.*, 1 (2017).

[15] M. Chiheb, J. N. Daou, and P. Vajda. *Z. Phys. Chem.* **179**, 271 (1993).

[16] Z. Ayat, B. Daoudi, A. Ouahab, and A. Boukraa. *Metallofiz. Noveishie Tekhnol.* **37**, 593 (2015).

[17] B. Y. Ao, P. Shi, Guo Yong, and T. Gao. *Chin. Phys. B* **3**, 037103 (2013).

[18] G. Schöllhammer, F. Karsai, and P. Herzig. *Fluorite-type rare earth hydrides studied from first principles, in Properties of Fluorite Structure Materials*. 2013.

[19] Y. Wang and M. Y. Chou. *Phys. Rev. B* **49**, 10731 (1994).

[20] B. Y. Ao, X. L. Wang, P. Shi, P. H. Chen, X. Q. Ye, X. C. Lai, J. J. Ai, and T. Gao. *Int. J. Hydrogen Energy* **33**, 5108 (2012).

[21] J. G. Roquefer, S. F. Matar, and J. L. Bobet. *Int. J. Hydrogrn Energy* **35**, 7858 (2010).

[22] P. Vajeeston, P. Ravindran, H. Fjellvåg, and A. Kjekshus. *Phys. Rev. B* **70**, 014107 (2004).

[23] P. Vajeeston, P. Ravindran, R. Vidya, A. Kjekshus, H. Fjellvåg, and V. A .Yartys. *Phys. Rev. B* **67**, 014101 (2003).

CHAPITER VI

Superstoichiometric rare-earth dihydrides $RH_{2.25}$ (R = Gd and Tb) with $Pm\bar{3}m$ space group: structural and electronic properties

In the first section of this chapter, we shall present complete results of a detailed electronic structure calculation of the superstoichiometric $GdH_{2.25}$ $(Pm\bar{3}m)$ without investigating the magnetic properties (caused by the half occupied 4f states), which is based on ab initio calculations at 0K within density functional theory (DFT), using a full-potential linear augmented plane-wave (FP-LAPW) method as implemented in the WIEN2k code.

In the second section, we shall present complete results of a detailed electronic structure calculation of the superstoichiometric compound $TbH_{2.25}$, based on ab initio calculations at 0K within density functional theory (DFT). In addition, we shall look for the role of local atomic relaxation inside the unit cell using both GGA and LDA approximations.

VI-I Gadolinium superstoichiometric dihydride (without relaxation) $GdH_{2.25}$

VI-I-1 Computational methods

Our calculations are based on density functional theory (DFT) [1, 2]. In this work, the full potential linearized augmented plane wave (FP-LAPW) method as implemented in the WIEN2k package [3], which solves the Kohn-Sham equations self-consistently, was used for the calculations. In this method, the electronic wave functions, the charge density and the crystal potential are expanded as spherical harmonics inside the non-overlapping atomic spheres of radius R_{MT}, and as plane waves in the remaining space of the unit cell. The cutoff in the charge density Fourier expansion, G_{MAX}, was taken to be 20 $Ry^{1/2}$.

Rare earths can be problematic for DFT calculations. We note that one can expect the existence of finite localized magnetic moments on the *4f* electrons. This magnetic aspect has not been considered in our calculations. It is known, indeed, that, in rare earths, the *4f* electrons, being very close to the core, are expected to be chemically inert. This leads us to consider *4f* electrons as atomic electrons, i.e. they cannot hybridize with the other valence *s*, *p*, and *d* electrons anymore and are perfectly localized [4]. For these reasons, the contribution of the *4f* electrons is removed from the valence bands, and is treated as that of core electrons. It is known that in WIEN2k the core states feel only a spherical potential, are not split by crystal fields and do not contribute to it.

We used an energy of -8 Ry to separate core and valence states, and the Gd ($5s^2 5p^6 5d^1 6s^2$) and H ($1s^1$) orbitals were treated as valence states. Exchange and correlation effects were treated within the density functional with the generalized-gradient approximation of Perdew, Burke and Ernzerhof (GGA 96) [5] and the local density approximation (LDA) [6]. The calculations were based on an optimized number of k-points of 1000, without considering the spin polarization. The self-consistent calculations are considered to be converged only when the calculated energy changes by less than 0.1 mRy.

VI-I-2 Results and discussion

VI-I-2-1 Equilibrium properties

The space group of $GdH_{2.25}$ is chosen to be $Pm\bar{3}m$ (*No. 221*), whose structure is plotted in **Fig. IV-1** (by using Xcrysden [7]).

The ground-state structural parameters have been obtained by fitting the total energy E versus volume V data to the non-linear Murnagham equation of state [8].

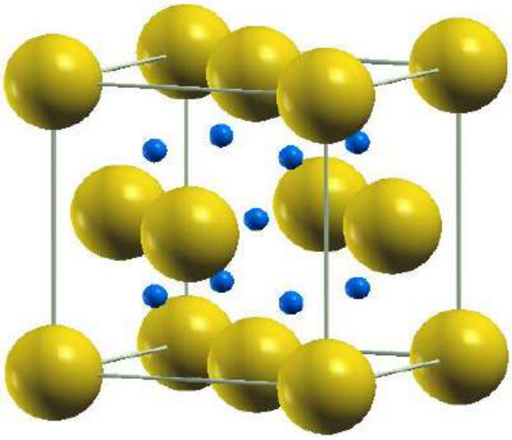

Fig. VI-1 The compound crystallises in the CaF_2 fluorite type structure: the large spheres represent rare earth atoms (×4) and small spheres hydrogen atoms occupying tetrahedral sites (×8) and the central octahedral site (×1).

We present the E(V) relationship of the $GdH_{2.25}$ for both LDA and GGA approximations in **Figs. VI-2 (*a*)** and **(*b*)** respectively.

We extracted the lattice parameter, the value of the bulk modulus, and its first order pressure derivative. The results data are listed in **Table VI-1** together with previous findings on GdH_{2+x} and on another rare-earth hydride. There are no experimental data for the bulk modulus available for this material and there is no direct *ab initio* theoretical information available for $GdH_{2.25}$ related to the effects of interstitial H atoms on their local atomic environment.

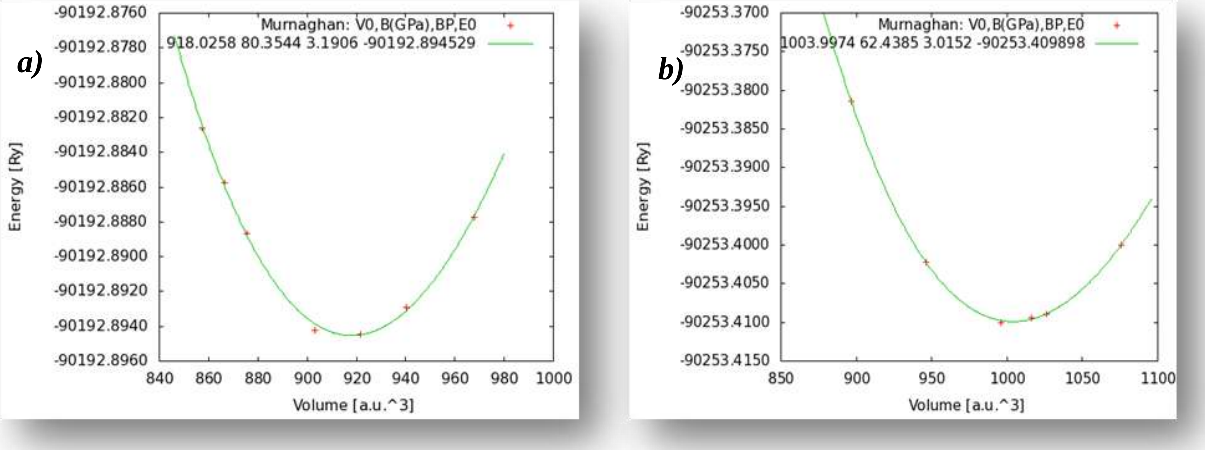

Fig. VI-2 Calculated total energy curves for $GdH_{2.25}$ as a function of cell volume in the (a) LDA and (b) GGA approximations.

Table VI-1 Calculated equilibrium lattice constant a_0 (in Å), bulk modulus B_0 (in GPa), its first order pressure derivative B_0', of $GdH_{2.25}$ for GGA and LDA compared to other available data.

	Method	*a_0*	*B_0*	*B_0'*	*Total energy*	*Reference*
$GdH_{2.25}$	GGA	5.299	62.4385	3.0152	-90253.409898	Present work [9]
	LDA	5.143	80.3544	3.1906	-90192.894529	
$GdH_{2.26\,(6)}$	Exp.	5.284				[10]
GdH_2	GGA	5.326	53.1873	4.0861		[11]
$ErH_{1.95}$	Exp.		67±3	9 fixed		[12]
$ErH_{2.091}$	Exp.		73±4	8 fixed		[12]

The GGA equilibrium lattice parameter (a_0), from **Table VI-1**, slightly overestimates the experimental value by 0.28%, while the LDA value is clearly smaller than the experimental one by 2.6%. Conversely, for the bulk modulus, it is the GGA value which is lower than that of the LDA by 22.2% as a result of the over-binding characteristic of LDA. Hence, GGA overestimates the lattice parameter whereas it underestimates bulk modulus (B_0) in comparison with LDA, a feature also observed in several similar systems in other simulation works [13]. Moreover, our calculated lattice parameter of $GdH_{2.25}$ in GGA is smaller than that of GdH_2 in both GGA and GGA+*U* methods reported by Sudha Priyanga et al. [14], which is in agreement with the experimental observation reported by Ref. [15].

In addition, one can see a difference in the magnitude of the total energy (see **Table VI-1**), which means that it is sensitive to the approximations used in the calculation. Furthermore, in GGA, bulk modulus value of $GdH_{2.25}$ is larger than that of GdH_2. This behaviour is similar to that found experimentally in the ErH_x system [12] (as shown in **Table VI-1**) and theoretically by using GGA+*U*+SO (SO stands for spin-orbit coupling) calculations in the PuH_x system [16] and by using GGA method in the ScH_x, YH_x, LaH_x and LuH_x systems [17]. In contrast, we found that the value of the lattice parameter decreases with increasing excess hydrogen (x) in the GdH_x system as found by a pseudopotential method and the local-density-functional approximation with a plane-wave basis in the YH_x system (1994) [18], by LDA+*U* calculations in the CeH_x system (2012) [19], and by GGA+*U*+SO calculations in the PuH_x system (2013) [16], where x=2, 2.25.

VI-I-2-2 Electronic properties

The calculated electronic band structures at the equilibrium lattice constant for different high-symmetry points in the Brillouin zone and the total density of states DOS (measured in one state per unit cell per electron-Volt) of $GdH_{2.25}$ in GGA and LDA at 0K are shown in **Fig. VI-3**, where the dashed line at zero eV indicates the Fermi energy.

Clearly, in both figures, several bands cross the Fermi level (E_F), confirming that $GdH_{2.25}$ possesses a metallic ground-state (the density of states on the Fermi level N (E_F) is not negligible as seen in **Table VI-2**), in agreement with electrical resistivity measurement interpretations [5]. The LDA and GGA energy band structures are qualitatively similar.

Table VI-2 Fermi energy (in Ry) and density of states at the Fermi level (in states/Ry) for $GdH_{2.25}$ (Ref. [9]).

	Fermi energy	$N(E_F)$	$N_s(E_F)$	$N_p(E_F)$	$N_d(E_F)$	$N_{d\text{-}eg}(E_F)$	$N_{d\text{-}t2g}(E_F)$	$N_{Htet\text{-}s}(E_F)$	$N_{Hoct\text{-}s}(E_F)$
GGA	0.46639	40.30	0.00	0.29	2.97	2.69	0.28	0.06	0.12
LDA	0.50542	37.82	0.00	0.33	3.02	2.71	0.31	0.05	0.10

Indeed, the crossings of bands with the Fermi level are nearly the same in the two approximations, where the values of the Fermi energy is *0.46639 Ry* in GGA and a higher *0.50542 Ry* in LDA (as seen in **Table VI-2**). Another significant feature of the band structures in **Fig. VI-3** is the different positions of the valence bands (at Γ), where, in the LDA, these shift towards the higher-energy region in the valence band top, and towards the lower energy region in the valence band bottom, and a clearer splitting between the valence bands, which indicates increase in the bandwidth. This is a consequence of the reduction in lattice parameter (a) [14].

The total DOS of $GdH_{2.25}$ has similar features in both GGA and LDA (see **Fig. VI-4**) especially at the Fermi level. However, these figures show small but non negligible differences as the peaks in the GGA are fairly sharper and narrower than those of LDA, and the total DOS in LDA moves a little towards the lower energy region compared to GGA.

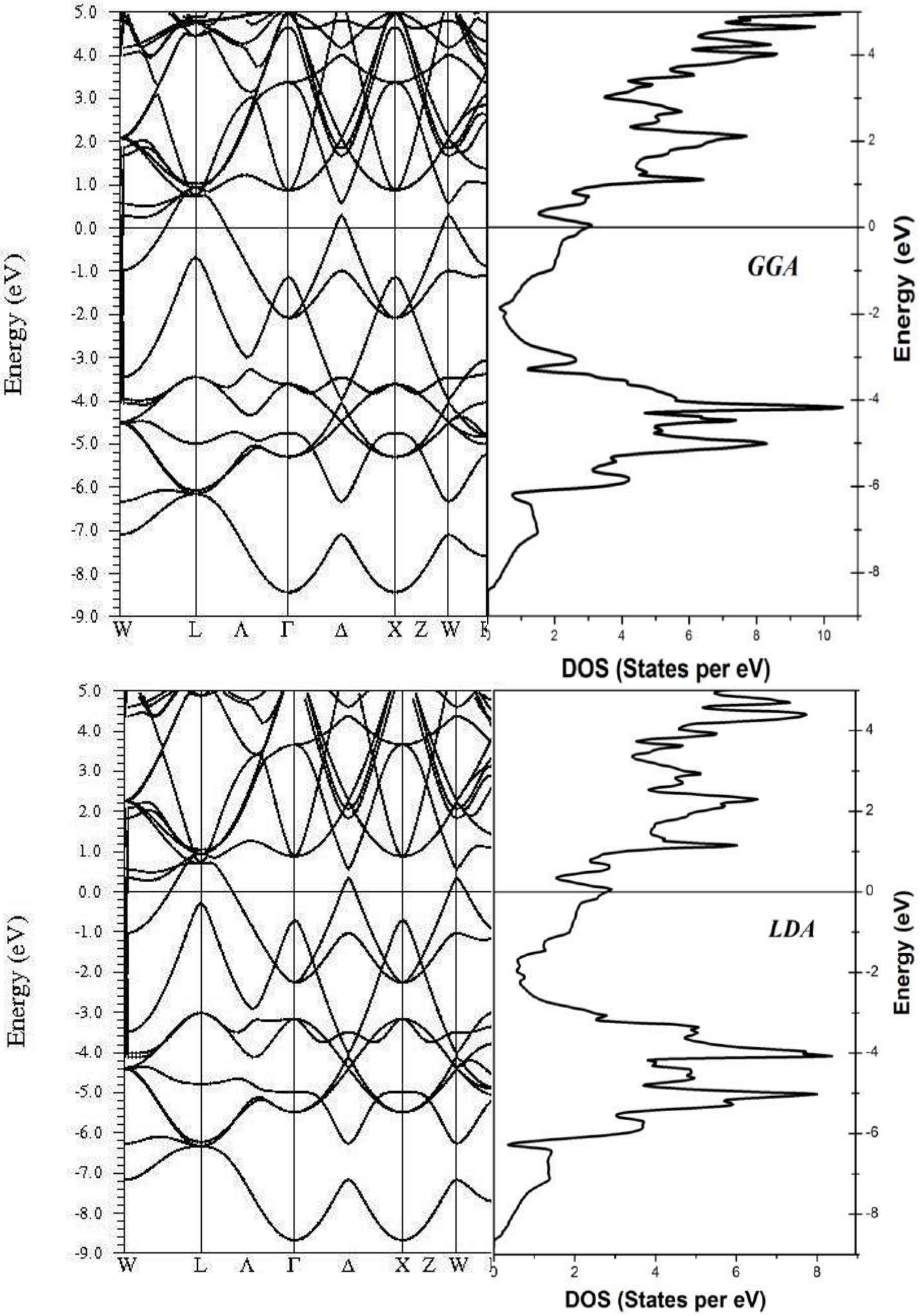

Fig. VI-3 Total density of states (right panel) and electronic band structure along high-symmetry directions (left panel) of $GdH_{2.25}$ in the GGA and LDA, the Fermi energy being at 0 eV.

In order to analyze the atomic interaction between a hydrogen atom and its different neighboring atoms, the total DOS has been decomposed into its partial-wave (*s*, *p*, and *d*) components around the H.

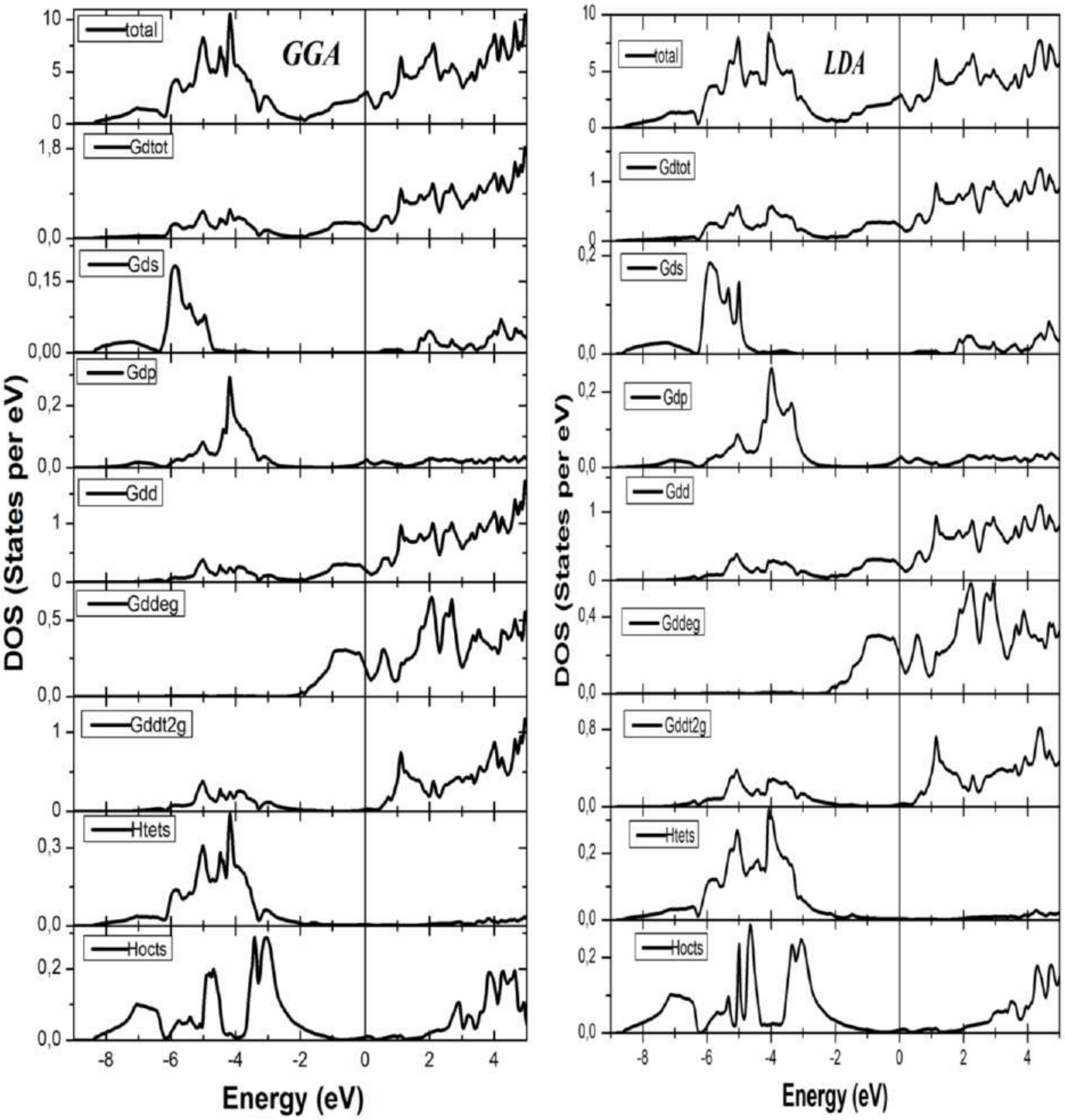

Fig. VI-4 The calculated total and partial density of states for $GdH_{2.25}$ in the LDA (right panel) and in the GGA (left panel), the Fermi energy being at 0 eV.

The total DOS decomposition into components according to the value of the angular momentum (*s*: L=0; *p*: L=1; *d*: L=2) inside the MT spheres of the metal and of the hydrogen as shown in **Fig VI-4**, where the left and the right columns correspond respectively to the GGA and LDA computations. It may be seen that the total DOS of $GdH_{2.25}$ is almost composed by that of Gd atoms, which is itself dominated by the *5d* partial DOS.

We can actually begin this analysis from the position at the Fermi level. It can be seen clearly in **Table VI-2** that the hydrogen in both interstitial sites (tetrahedral H_{tet} and octahedral H_{oct}), and both *d-t2g* and *p* from Gd, do not contribute significantly at the Fermi level, which means that they are essentially not involved in conduction properties. In contrast, the Gd *d-eg* electrons represent the majority contribution at E_F.

It is convenient to divide the DOS into regions:

- region I (*-8.495 to -1.475 eV*) of GGA and (*-8.727 to -1.5432 eV*) of LDA with a major contribution of Gd *d-t2g* states and both H *1s* orbitals and much smaller contributions of Gd *s* and *p*;
- region II (*-1.475 eV to* E_F) of GGA and (*-1.543 eV to* E_F) of LDA with Gd *d-eg* states and very few Gd *p* states;
- region III (above E_F in the lowest energy domain of the conduction band) with unoccupied *s*, *p* and *d* states from Gd and *s* from H in octahedral sites (H_{oct}).

It is interesting to note that a strong hybridization exists between Gd *d-t2g* and H_{tet} atoms (in region I) as shown in **Fig. VI-4**, which leads to an appreciable covalent component in the Gd-H bond (in the direction [111]). On the other hand, hybridization between Gd and H_{oct} atoms is much weaker, indicating a degree of ionic character in this bond, which is mainly due to the longer Gd-H_{oct} distance (*2.6495 Å* of GGA and *2.5710 Å* of LDA). The minimal atomic bonding distance (*2.2945* Å of GGA and *2.2266* Å of LDA) exists between Gd and H_{tet} atoms. Therefore, the Gd-H bonds in $GdH_{2.25}$ have a mixed (covalent-ionic) character as is found in several metal hydrides [18, 20, and 21].

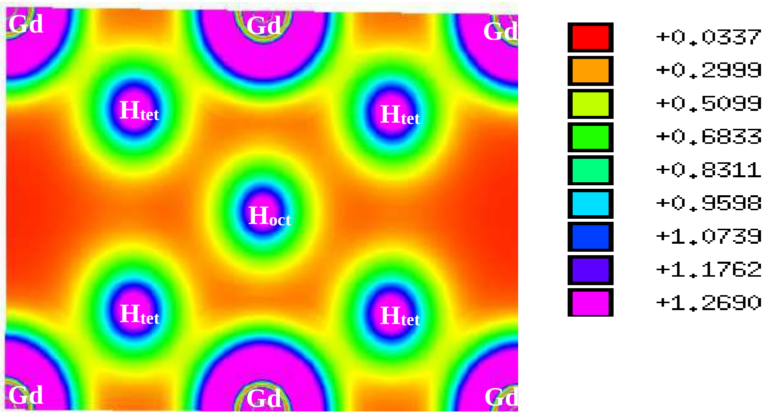

Fig. VI-5 Calculated valence-electron-charge density contour (in electrons per Å^3) of $GdH_{2.25}$ in the (110) plane.

We now turn our attention to the analysis of valence electron-charge density. The charge density in the (110) plane is displayed in **Fig.VI-5** which is similar for that found by Ao et al. (2012) [19] and by Ao et al. (2013) [16] for $CeH_{2.25}$ and $PuH_{2.25}$ respectively. It is observed that appreciable charge density exists in the outer regions of Gd and H_{tet} atoms with a slight deformation in the direction of these nearst-neighboring atoms. This feature indicates that the bonding between Gd and H_{tet} atoms is certainly covalent, a fact confirmed by the hybridization analysis. At the same time, it is clear that very little electronic charge is shared between Gd and H_{oct}, where most of the valence electrons of H_{oct} are tightly bound around their atoms and this implies that the bond has some ionic character (is much weaker). Another point of interest is the existence of a little charge in the interstitial regions away from the bonds, which gives a metallic character to this compound, confirming therefore our DOS analysis.

VI-II Terbium superstoichiometric dihydride (with relaxation) $TbH_{2.25}$

VI-II-1 Computational method

Density functional theory calculations were performed using the WIEN2k package [3] with the full potential linearized augmented plane wave (FP-LAPW) method. The generalized-gradient approximation of Perdew, Burke, and Ernzerhof (GGA 96) [5] and the local density approximation (LDA) [6] were adopted to describe the exchange and correlation effects. The cut-off energy, which defines the separation energy between core and valence states, was taken to be -8 Ry, while the Tb ($5s^2 5p^6 5d^1 6s^2$) and H ($1s^1$) orbitals were treated as valence states. We did not treat the *f* orbitals of Tb as valence electrons but as core electrons because, in rare earths, the *4f* electrons, being very close to the core, are expected to be chemically inert, i.e. they cannot hybridize with the other *s*, *p*, and *d* valence electrons anymore and are perfectly localized [4]. Self-consistency is obtained using an optimized value of 1000 k-points in the irreducible Brillouin zone (IBZ), without considering the spin polarization. All atoms were fully relaxed until the forces were less than 0.01 eV/Å. The self-consistent calculations are considered to be converged only when the total energy of the system changes by less than 10^{-4} Ry.

VI-II-2 Results and discussion

VI-II-2-1 Equilibrium properties

The conventional unit cell for the superstoichiometric dihydride $TbH_{2.25}$ with $Pm\bar{3}m$ space group (*No. 221*) is shown in **Fig. VI-6** (by using Xcrysden [7]).

Table VI-3 summarizes the results for $TbH_{2.25}$ obtained before (unrelaxed state) and after (relaxed state) the geometrical optimization of the internal variables with both GGA and LDA approximations. We can see that the atomic positions after relaxation calculated with GGA are closer to the ideal atomic positions than those calculated with LDA.

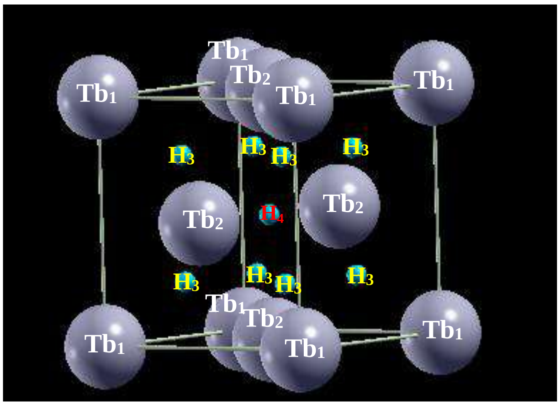

Fig. VI-6 The compound crystallizes in the CaF_2 fluorite type structure: the large spheres represent rare earth atoms and small spheres hydrogen atoms occupying tetrahedral sites (H_3) and the central octahedral site (H_4).

Table VI-3 Unrelaxed and relaxed positions of equivalent atoms for the $TbH_{2.25}$ structure ($Pm\overline{3}m$ space group) in units of lattice parameters (*a*, *b*, *c*) for (*x*, *y*, *z*) coordinates, respectively (present work in Ref. [28]).

		Tb_1		*Tb_2*		*H_3*		*H_4*	
		LDA	*GGA*	*LDA*	*GGA*	*LDA*	*GGA*	*LDA*	*GGA*
Unrelaxed	x	0.00	0.00	0.50	0.50	0.25	0.25	0.50	0.50
				0.50	0.50	0.75	0.75		
				0.00	0.00	0.75	0.75		
						0.25	0.25		
						0.25	0.25		
						0.75	0.75		
						0.25	0.25		
						0.75	0.75		
	y	0.00	0.00	0.50	0.50	0.25	0.25	0.50	0.50
				0.00	0.00	0.25	0.25		
				0.50	0.50	0.75	0.75		
						0.75	0.75		
						0.75	0.75		
						0.75	0.75		
						0.25	0.25		
						0.25	0.25		
	z	0.00	0.00	0.00	0.00	0.25	0.25	0.50	0.50
				0.50	0.50	0.25	0.25		
				0.50	0.50	0.25	0.25		
						0.25	0.25		

						0.75	0.75		
						0.75	0.75		
						0.75	0.75		
						0.75	0.75		
Relaxed	x	0.00	0.00	0.50	0.50	0.24445753	0.24925265	0.50	0.50
				0.50	0.50	0.75554247	0.7507435		
				0.00	0.00	0.75554247	0.7507435		
						0.24445769	0.24925265		
						0.24445769	0.24925265		
						0.75554247	0.7507435		
						0.24445769	0.24925265		
						0.75554247	0.7507435		
	y	0.00	0.00	0.50	0.50	0.24445769	0.24925265	0.50	0.50
				0.00	0.00	0.24445769	0.24925265		
				0.50	0.50	0.75554231	0.7507435		
						0.75554247	0.7507435		
						0.75554247	0.7507435		
						0.75523367	0.7507435		
						0.24445769	0.24925265		
						0.24445769	0.24925265		
	z	0.00	0.00	0.00	0.00	0.24445769	0.24925265	0.50	0.50
				0.50	0.50	0.24445769	0.24925265		
				0.50	0.50	0.24445769	0.24925265		
						0.24445769	0.24925265		
						0.75554231	0.7507435		
						0.75554231	0.7507435		
						0.75554247	0.7507435		
						0.75554231	0.7507435		

The total energy versus volume is fitted by the non-linear Murnaghan equation of state [8]. Under relaxation, the energy vs. volume curves of $TbH_{2.25}$ for both LDA and GGA approximations are shown in **Figs. VI-7 (*a*)** and **(*b*)** respectively, whereas those for the unrelaxed states are plotted in **Figs. VI-7 (*c*)** and **(*d*)**. From this fit, we can obtain the equilibrium lattice parameter (a_0), the bulk modulus (B_0), its first order pressure derivative (B_0'), and the total energy (E_0). The calculated structural parameters of $TbH_{2.25}$ before and after the relaxation are reported in **Table VI-4** together with other available data. It can be seen that this relaxation lowers the total energy as expected. To the best of our knowledge, the experimental or theoretical bulk moduli of this material have not been reported and there is no direct *ab initio* theoretical information available for $TbH_{2.25}$ related to the effects of interstitial

H atoms on their local atomic environment. Our calculated values can thereby be considered as a prediction for future investigations.

We find that the structure of $TbH_{2.25}$ is stabilized by local atomic relaxations in both approximations, in agreement with previous first-principles computational work in other hydrides [22-24]. Thus, the energy gain (the absolute value of relaxed minus unrelaxed minimum energy) after internal coordinate relaxation is *0.0131 eV/cell* (*0.964 mRy*) within GGA and *0.0364 eV/cell* (*2.673m*Ry) within LDA approximation.

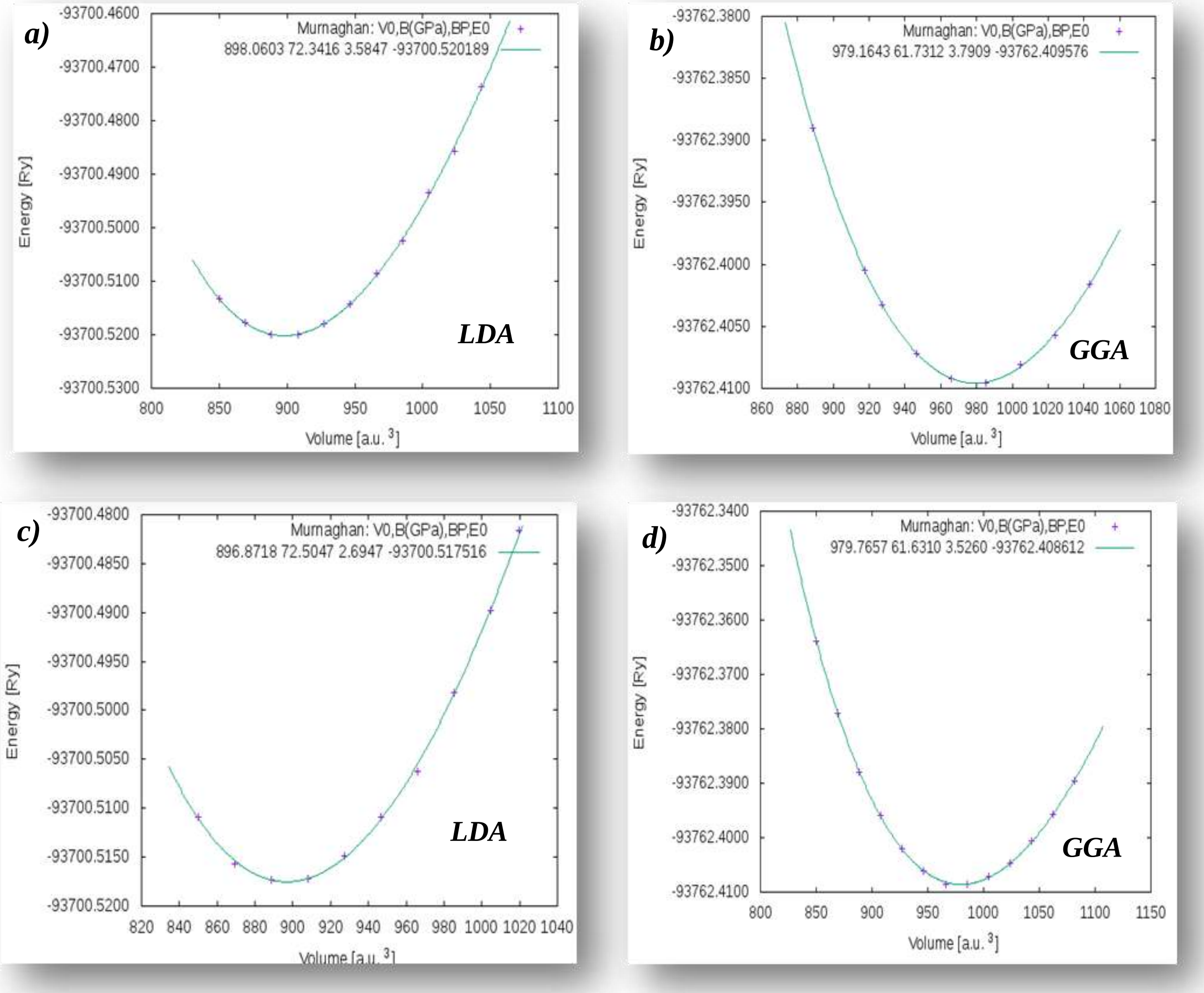

Fig. VI-7 Calculated total energy curves for $TbH_{2.25}$ as a function of cell volume in the LDA approximation: (a) relaxed state, (c) unrelaxed state, and in the GGA approximation: (b) relaxed state, (d) unrelaxed state.

It is easily seen from **Table VI-4** that the equilibrium lattice parameter after relaxation is in better agreement with the experimental value in both approximations, but the GGA equilibrium lattice parameter (a_0) value is closest to the experimental value and is smaller than that for the calculated lattice parameters of TbH_2 and $GdH_{2.25}$. This concords with experimental observations reported by Ref. [15], as it is know that a_0 decreases with increasing octahedral hydrogen content *x* [13, 25-27] and also with increasing rare earth atomic number. As a general rule, H_{oct} atom addition leads to lattice contraction whereas H_{tet} atoms lead to lattice expansion [17]. The LDA value is clearly smaller than the experimental one, indicating the occurrence of over-binding in this latter method. This shows that GGA is the most reliable for optimized lattice constants.

Table VI-4 Calculated equilibrium lattice constant a_0 (in Å), bulk modulus B_0 (in GPa), its first order pressure derivative B_0', and total energy (Ry), of $TbH_{2.25}$ for GGA and LDA compared to other available data.

	Method		***a_0***	***B_0***	***B_0'***	***Total energy***	***Reference***
$TbH_{2.25}$	GGA	Unrelaxed	5.2558	61.631	3.526	-93762.408612	Present work [28]
		Relaxed	5.2548	61.7312	4.8942	-93762.409576	
	LDA	Unrelaxed	5.1032	72.5047	2.6947	-93700.517516	
		Relaxed	5.1056	72.3416	3.5847	-93700.520189	
$TbH_{2.24}$	Exp.		5.2308				[15]
TbH_2	GGA		5.2993	59.9989	1.9613	-23440.304180	Present work [28]
	LDA		5.1360	67.2194	4.0944	-23424.830688	Present work
$GdH_{2.25}$	GGA	Unrelaxed	5.299	62.4385	3.0152	-90253.409898	Present work [9]
	LDA	Unrelaxed	5.143	80.3544	3.1906	-90192.894529	
$GdH_{2.26\,(6)}$	Exp.		5.284				[10]
GdH_2	GGA		5.326	53.1873	4.0861	-22563.057167	Present work [11]
$ErH_{1.95}$	Exp.			67±3	9 fixed		[12]
$ErH_{2.091}$	Exp.			73±4	8 fixed		[12]

Conversely, for the bulk modulus in both relaxed and unrelaxed states, it is the GGA value which is lower than that of the LDA as a result of the over-binding characteristic of LDA. Furthermore, in both GGA and LDA approximations, the bulk modulus value of $TbH_{2.25}$ is larger than that of TbH_2; this behaviour is similar to that found experimentally in the ErH_x system (as shown in **Table VI-4**) [12] and theoretically by Refs. [9, 16, 17].

Hence, in both relaxed and unrelaxed states, GGA overestimates the lattice parameter whereas it underestimates bulk modulus (B_0) in comparison with LDA, a feature also observed in several similar systems in other simulation works [13]. It may be concluded that the GGA, with or without relaxation, compares favorably with LDA.

VI-II-2-2 Electronic properties

From the last section, we find that with both approximations the relaxed structure of $TbH_{2.25}$ is more stable and the relaxed equilibrium lattice parameter agrees better with the experimental value. For this reason, all figures presented in this section are for the relaxed state.

The calculated electronic band structures at the equilibrium lattice constant for different high-symmetry points in the Brillouin zone and the total density of states DOS (measured in states per electron-Volt) of $TbH_{2.25}$ in GGA and LDA at 0K are shown in **Fig. VI-8**, where the line at zero eV indicates the Fermi energy.

In **Fig. VI-8**, it is clear that $TbH_{2.25}$ possesses a metallic ground state because several bands cross the Fermi level (E_F), in agreement with electrical resistivity measurement interpretations [15]. In both approximations, the energy band structures are qualitatively similar. Indeed, the crossings of bands with the Fermi level are nearly the same, where in the relaxed state the values of the Fermi energy are *0.56402 Ry* in GGA and a higher *0.59989 Ry* in LDA (as seen in **Table VI-5**). Another significant feature of the band structures in the two approximations is the different positions of the valence bands (at Γ), where, in the LDA, these shift towards higher energies at the top of the valence band, and towards lower energies at the bottom of the valence band. All of these indicate a slight increase in the bandwidth, as a consequence of the reduced lattice parameter.

We now turn our attention to the calculated total density of states of $TbH_{2.25}$, which has similar features in both GGA and LDA (see **Fig. VI-8**) especially at the Fermi level. However, these figures show small but non negligible differences as the peaks in the GGA are

Table VI-5 Fermi energy (Ry) and density of states at the Fermi level (in states/Ry) for $TbH_{2.25}$ in the two approaches GGA and LDA (present work Ref. [28]).

		Fermi energy	$N(E_F)$	$N_{Tb1\text{-}tot}(E_F)$	$N_{Tb1\text{-}d}(E_F)$	$N_{Tb2\text{-}tot}(E_F)$	$N_{Tb2\text{-}d}(E_F)$	$N_{Htet\text{-}s}(E_F)$	$N_{Hoct\text{-}s}(E_F)$
GGA	Unrelaxed	0.56297	39.69	0.00	0.17	2.14	1.93	0.08	0.16
	Relaxed	0.56402	39.80	0.00	0.17	2.13	1.92	0.08	0.16
LDA	Unrelaxed	0.60011	37.21	0.00	0.20	2.18	1.95	0.07	0.14
	Relaxed	0.59989	37.87	0.00	0.19	2.13	1.91	0.07	0.13

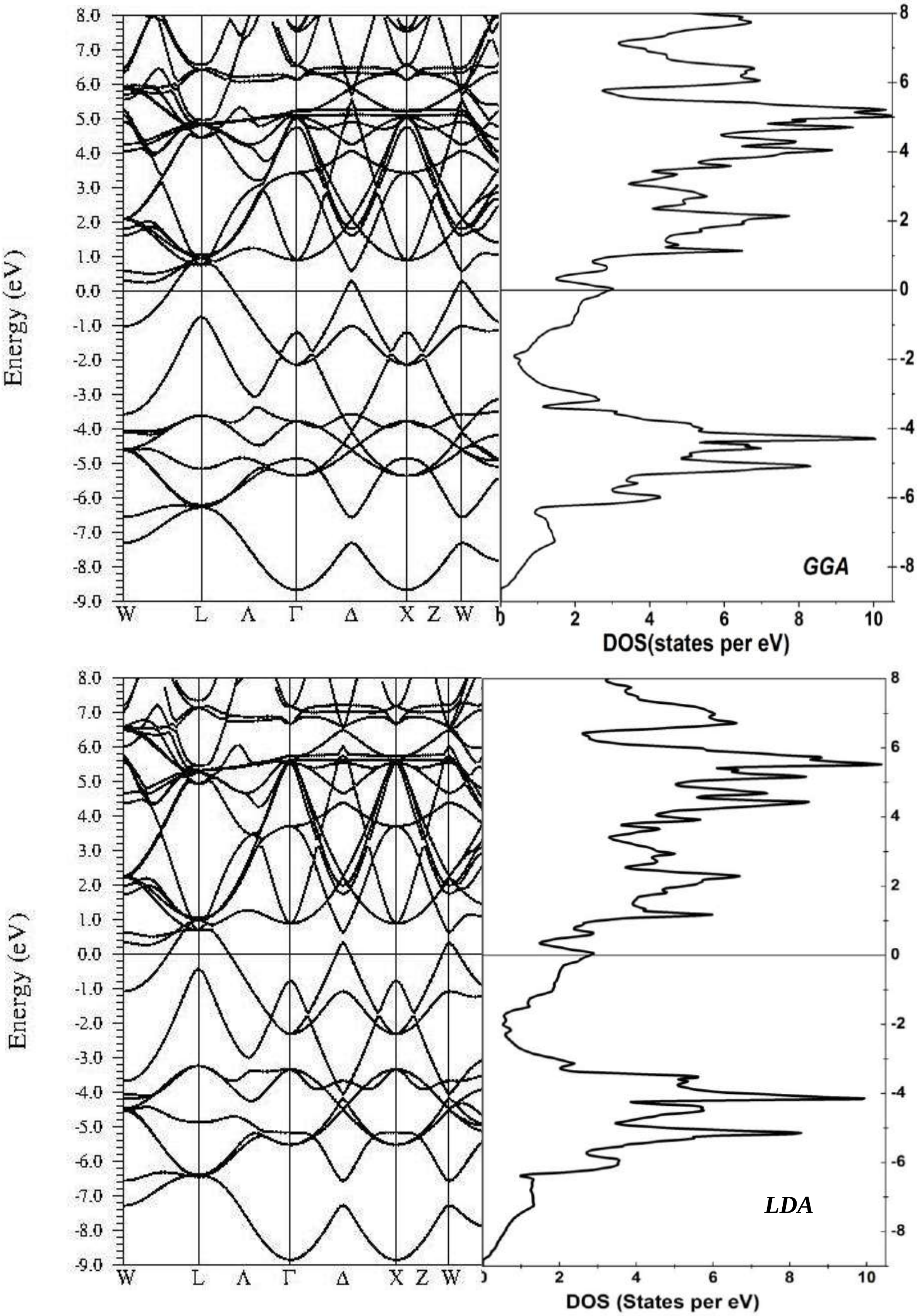

Fig. VI-8 total density of states (right panel) and electronic band structure along high-symmetry directions (left panel) of $TbH_{2.25}$ in the GGA and LDA, the Fermi energy being at 0 eV.

fairly sharper and narrower than those of LDA, and the total DOS in LDA moves a little towards lower energies compared to GGA. Therefore, it is concluded that the width of the valence states in LDA is increased due to the lattice contraction.

The present study shows that the density of states on the Fermi level $N(E_F)$ in both relaxed and unrelaxed states is not negligible as seen in **Table VI-5** and is smaller in LDA than in GGA because the latter causes an under-binding effect of the crystal, thus the crystal structure is more compact in LDA.

Also from **Table VI-5**, it can be remarked that when the equilibrium lattice parameter decreases, the Fermi energy increases in both approximations.

In order to explain the chemical bonding in $TbH_{2.25}$, we have calculated total and partial density of states (PDOS) as shown in **Fig. VI-9**.

From **Fig. VI-9**, the conduction band is mainly dominated by unoccupied *s*, *p* and *d* states from terbium and *s* from hydrogen in octahedral sites (H_{oct}). The Fermi level is completely dominated by the d-e_g states of terbium. The upper valence states situated between *-1.96 eV* and E_F in GGA and *-1.93 eV* and E_F in LDA are dominated by the Tb d-e_g states. Whilst it can be seen that in low energy levels ranging between *-8.71 eV* and *-1.96 eV* in GGA and between *-8.90* and *-1.93 eV* in LDA, $TbH_{2.25}$ dihydride exhibits hybridization mainly between Tb d-t_{2g} states and both H *1s* orbitals, implying directional (covalent) bonding in Tb d-t_{2g}-H_{tet} (bonding distance is *2.2672 Å* in GGA and *2.1653 Å* in LDA) and a degree of ionic character in Tb d-t_{2g}- H_{oct} (bonding distance is *2.6258 Å* in GGA and *2.5537 Å* in LDA).

This can be clearly understood from the electronic charge density contours along a (110) plane as shown in **Fig. VI-10**. The charge density was presented only for the GGA method because it is similar to that of the LDA method with an insignificant difference. In **Fig. VI-10**, it is clear that appreciable charge density exists in the outer regions of Tb and H_{tet} atoms with a slight deformation in the direction of these nearest-neighbouring atoms. This feature confirms that the bonding between Tb and H_{tet} atoms is certainly covalent, a fact confirmed by the hybridization analysis. At the same time, it is clear that very little electronic charge is shared between Tb and H_{oct}, where most of the valence electrons of H_{oct} are tightly bound around their atoms and this implies that the bond has some ionic character (the electron density is much weaker in the middle of the bond). Therefore, the Tb-H bonds in $TbH_{2.25}$ have a mixed (covalent-ionic) character as is found in several metal hydrides [9, 16, 19-21, 29]. Another point of interest is the existence of little charges in the interstitial regions away from the bonds, which gives a metallic character to this compound.

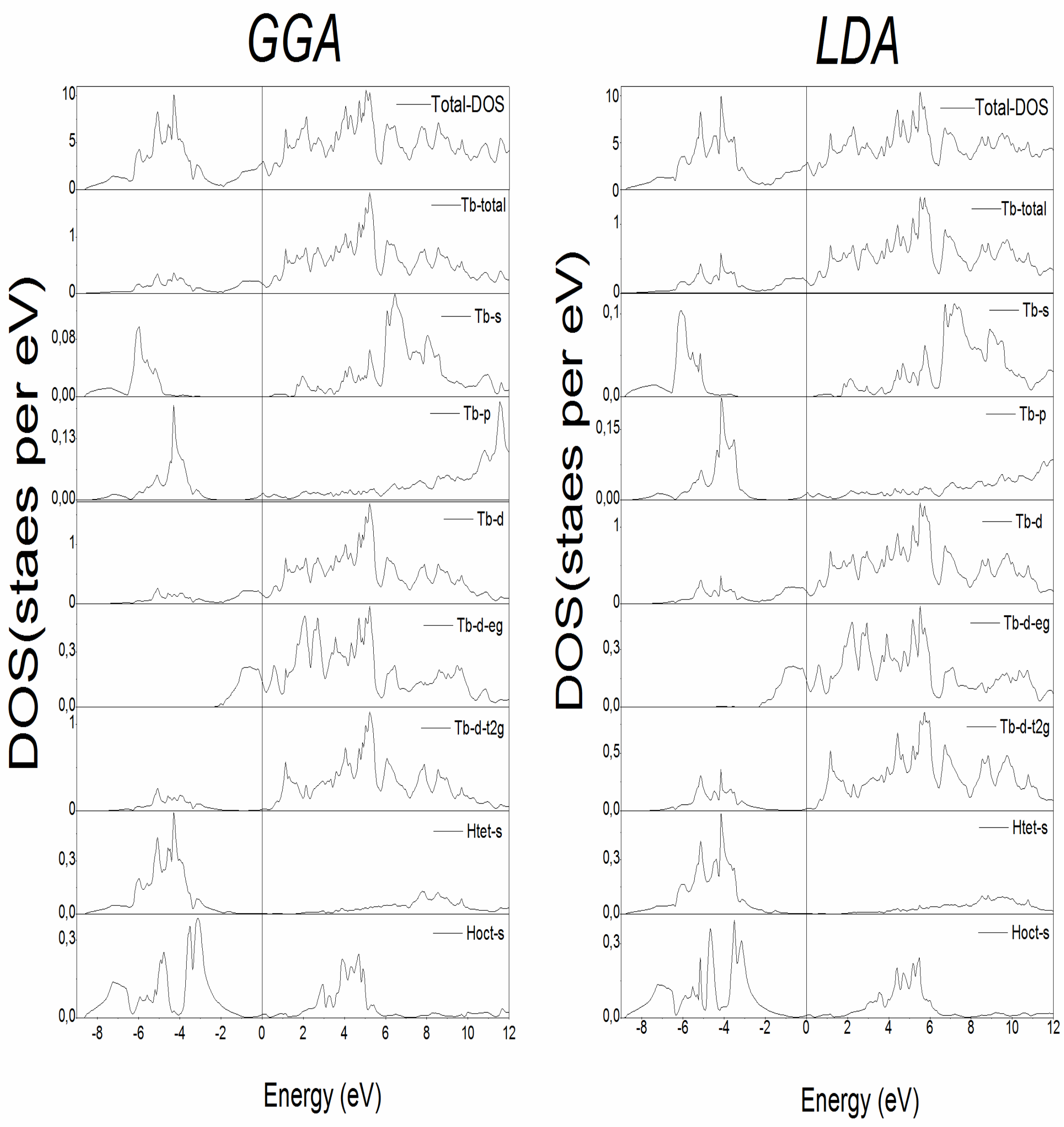

Fig. VI-9 The calculated total and partial density of states for $TbH_{2.25}$ in the LDA (right panel) and in the GGA (left panel), the Fermi energy being at 0 eV.

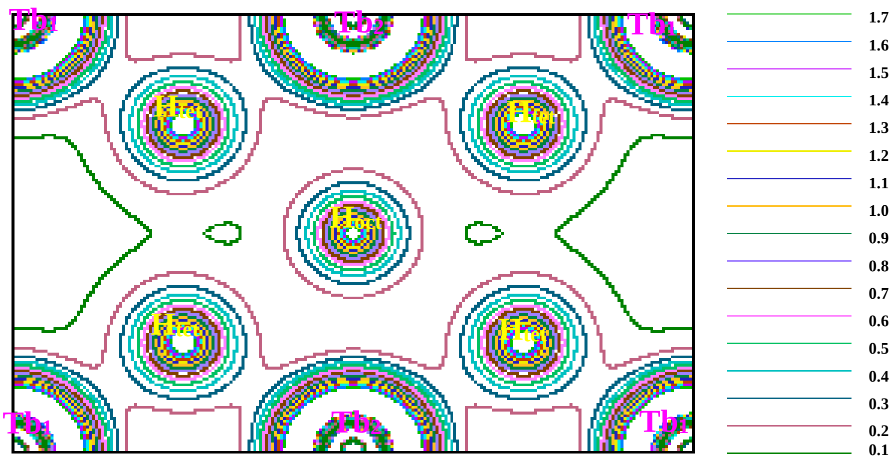

Fig. VI-10 Calculated valence-electron-charge density contour (in electrons per Å^3) of $TbH_{2.25}$ in the (110) plane.

VI-III Summary

To summarize, we have shown that in the generalized gradient approximation (GGA) the lattice constant is larger and the bulk modulus is smaller as compared to the local density approximation (LDA) results. On the other hand, the calculated lattice constant with the GGA agrees well with available experimental data. For $TbH_{2.25}$, the atomic positions under relaxation calculated with the GGA are closer to the center of the ideal atomic positions than those calculated with the LDA. The equilibrium lattice parameter under relaxation is in better agreement with the experimental values in both approximations, the GGA value being the best. There were no bulk modulus data, to our best knowledge, for the considered materials.

We also calculated and presented the electronic band structure and density of states, which clearly showed that the superstoichiometric rare earth dihydrides $RH_{2.25}$ (R = Gd and Tb) with $Pm\bar{3}m$ space group exhibited metallic behaviour. The GGA presented a tendency for underbinding in this material. The DOS analysis showed that the Fermi energy (E_F) fell at a level where most of the electronic states were rare-earth *5d-eg* conduction states, while negligible contribution from both interstitial H *s*-states was observed at E_F. The *d* states of the R (R=Gd and Tb) atoms were the main contributors to bonding states in the valence bands, whereas *p* and *s* states had a smaller role. It was found that hybridization existed between the s electronic orbital of both interstitial H atoms and the *d-t2g* electronic orbitals of R (R=Gd and Tb). This hybridization implies that there is a mixture of covalent ($R–H_{tet}$) and ionic ($R–H_{oct}$) bonds, a fact confirmed by the charge density analysis.

References

[1] P. Hohenberg and W. Kohn. *Phys. Rev. B* **136**, 864 (1964).

[2] W. Kohn and L. J. Sham. *Phys. Rev. A* **140**, A1133 (1965).

[3] P. Blaha, K. Schwarz, G. Madsen, D. Kvasnicka, and J. Luitz. *Wien2k, an Augmented Plane Wave Plus Local Orbitals Program for Calculating Crystal Properties*. Techn. Universität, Vienna, Austria, 2001, ISBN 3-9501031-1-2.

[4] P. Vajeeston, R. Vidya, P. Ravindran, H. Fjellvåg, A. Kjekshus, and A. Skjecltorp. *Phys. Rev. B* **65**, 075101 (2002).

[5] J. P. Perdew, K. Burke, and M. Ernzerhof. *Phys. Rev. Lett.* **77**, 3865 (1996).

[6] J. P. Perdew and Y. Wang. *Phys. Rev.* **45**, 13244 (1992).

[7] A. Kokalj. *XCrysDen - a new program for displaying crystalline structures and electron densities*. *Comp. Mater. Sci.* **28**, 155 (2003). Code available from http://www.xcrysden.org.

[8] F. D. Murnaghan. *Proc. Natl. Acad. Sci.* **30**, 244 (1944).

[9] Z. Ayat, A. Boukraa, and B. Daoudi. *J. Rare Earths* **34**, 66 (2016).

[10] M. Ellner, H. Reule, and E. J. Mittemeijer. *J. Alloys and Compd.* **279**, 179 (1998).

[11] Z. Ayat, B. Daoudi, A. Ouahab, and A. Boukraa. *Metallofiz. Noveishie Tekhnol.* **37**, 593 (2015).

[12] T. Palasyuk, M. Tkacz, and P. Vajda. *Solid State Commun.* **135**, 226 (2005).

[13] J. Ai, T. Liu, T. Gao, and B. Ao. *Computat. Mater. Sci.* **51**, 127 (2012).

[14] P. G. Sudha, R. Rajeswarapalanichamy, and K. Iyakutti. *Int. J. Hydrogen Energy* **31**, 415 (2015).

[15] P. Vajda. *Hydrogen in rare earth metals*. 1995.

[16] B. Y. Ao, P. Shi, Guo Yong, and T. Gao. *Chin. Phys. B* **3**, 037103 (2013).

[17] G. Schöllhammer, F. Karsai, and P. Herzig. *Fluorite-type rare earth hydrides studied from first principles, in Properties of Fluorite Structure Materials*. 2013.

[18] Y. Wang and M. Y. Chou. *Phys. Rev. B* **49**, 10731 (1994).

[19] B. Y. Ao, X. L. Wang, P. Shi, P. H. Chen, X. Q. Ye, X. C. Lai, J. J. Ai, and T. Gao. *Int. J. Hydrogen Energy* **33**, 5108 (2012).

[20] P. Vajeeston, P. Ravindran, H. Fjellvåg, and A. Kjekshus. *Phys. Rev. B* **70**, 014107 (2004).

[21] P. Vajeeston, P. Ravindran, R. Vidya, A. Kjekshus, H. Fjellvåg, and V. A. Yartys. *Phys. Rev. B* **67**, 014101 (2003).

[22] J. Garcés, J. L. Gervasoni, and P. Vajda. *J. Alloys Compd.* **404-406**, 126 (2005).

[23] J. Garcés, R. González, and P. Vajda. *Phys. Rev. B* **79**, 054113 (2009).

[24] J. Garcés and P. Vajda. *Int. J. Hydrogen Energy* **35**, 6025 (2010).

[25] C. E. Holley, R. N. R. Mulford, F. H. Ellinger, W. C. Koehler, and W. H. Zachariasen. *J. Phys. Chem.* **59**, 1226 (1955).

[26] H. Müller, P. Knappe, and O. Greis. *Z. Phys. Chem. Neue Fol.* **114**, 45 (1979).

[27] P. Knappe P and H. Müller. *Z. Anorg. Allg. Chem.* **487**, 63 (1982).

[28] Z. Ayat, A. Boukraa, B. Daoudi, and A. Ouahab. *Chin. J. Phys.* **55**, 2157 (2017).

[29] J. G. Roquefer, S. F. Matar, and J. L. Bobet. *Int. J. Hydrogen Energy* **35**, 7858 (2010).

Summary and Outlook

In this thesis, *ab-initio* calculations were performed with the WIEN2k code (at 0 K) to investigate structural and electronic properties for R (R = Gd and Tb), RH_2 (R = Gd and Tb), and $RH_{2.25}$ (R = La, Gd and Tb) using the FP-LAPW method in the local density approximation (LDA) and the generalized gradient approximation (GGA) for the exchange correlation of the non spin-polarized study. LSDA/LSDA+U and GGA/GGA+U for the exchange correlation of a spin-polarized study was also used for the pure R (R = Gd and Tb). In addition, the magnetic properties of R and thermodynamic properties of RH_2 are also investigated.

The results of the calculations presented in this thesis illustrate that in the pure rare earths R, rare earth dihydrides and superstoichiometric dihydrides, the LDA leads to an overbinding— smaller lattice constants and larger cohesive energies and bulk moduli — while the GGA results show a significant underbinding in both spin polarized and non-spin polarized study. On the other hand, the GGA calculated lattice constants agree well with available experimental data. The absolute values of cohesive energy of the R (R = Gd, and Tb) calculated by LDA (LSDA/LSDA+U in the spin polarization calculation) are higher than those calculated by GGA (GGA/GGA+U in the spin polarization calculation) due to the overbinding effect.

The calculations of band structures and densities of states clearly show that the pure R (R = Gd, Tb) in both spin polarized and non-spin polarized study, dihydrides RH_2 and superstoichiometric dihydrides $RH_{2.25}$ in both the tetragonal structure (R = La and Gd) and in the cubic structure (R = Gd and Tb) exhibit metallic behavior. In addition the calculated magnetic moment of the R (R = Gd, and Tb) show reasonable agreement with previous results in the literature.

❖ For rare-earth dihydrides RH_2 (R = Gd, Tb):

- The nature of bonding in the rare-earth dihydrides RH_2 (R = Gd, Tb) must be discussed in terms of interaction between metal *d* states and hydrogen 1*s*-states. The position and width of the low-lying bands depend quite sensitively on the type of rare earth considered.
- The low-lying bands found in these dihydrides are not composed uniquely of hydrogen *s* states but rather show a strong hybridization with metal *d*- and also metal *s*- and *p*-states.

- LDA leads to an overestimation of cohesion and formation energy.
- It is found that the GdH_2 and TbH_2 have negative heats of formation, which suggests that these dihydrides can be easily synthesized at ambient condition.
- The values of cohesive energy and average binding energy per H atom decrease with increasing cell parameter.
- The Fermi energy E_F falls at a level where most of the electronic states are rare-earth *5d* conduction states.
- The H*s*-state has no contribution near the Fermi level.

- For rare earth superstoichiometric dihydrides ($LaH_{2.25}$ and $GdH_{2.25}$) with *I4/mmm* space group:

The total DOS in GGA and LDA shows important differences in the vicinity of valence band, where GGA presents a tendency for underbinding in this material. In addition, the value of DOS at the Fermi level (N(E_F)) in GGA is larger than that in LDA. The DOS analysis shows that the Fermi energy (E_F) falls at a level where most of the electronic states are rare-earth *5d* conduction states, while negligible contributions from both (tetrahedral H_{tet} and octahedral H_{oct}) interstitial H*s* states are observed at E_F.

The *d* states of R (La and Gd) atoms are the main contributors to bonding states in valence bands, whereas *p* and *s* states have a smaller role. It is found that hybridization exists between *s* electronic orbitals of both interstitial H atoms and *d* electronic orbitals of R. This hybridization implies that there is a mixture of covalent (R–H_{tet}) and ionic (R–H_{oct}) bonds.

- For rare earth superstoichiometric dihydrides ($GdH_{2.25}$ and $TbH_{2.25}$) with $Pm\overline{3}m$ space group:

a) $GdH_{2.25}$:

The DOS analysis shows that the Fermi energy (E_F) falls at a level where most of the electronic states were rare earth *5d-eg* conduction states, while negligible contribution of both interstitial H *s*-states was observed at E_F.

The *d* states of the Gd *d-t2g* atoms were the main contributors to bonding states in the valence bands, whereas *p* and *s* states had a smaller role. It was found that hybridization existed between the *s* electronic orbital of both interstitial H atoms and the *d-t2g* electronic orbitals of Gd. This hybridization implies that there was a mixture of covalent (Gd–H_{tet}) and ionic (Gd–H_{oct}) bonds, which was confirmed by the charge density analysis.

b) $TbH_{2.25}$:

The atomic positions under relaxation calculated with the GGA are closer to the center of the ideal atomic positions than those calculated with the LDA. The structure of $TbH_{2.25}$ is stabilized by local atomic relaxations. The equilibrium lattice parameter under relaxation is in better agreement with the experimental value in both approximations, the GGA value being the best. The bulk modulus is determined by fitting the energy vs. cell volume curve to the Murnaghan equation of state. Under relaxation, the GGA value is smaller by 14.67% than that of the LDA. In addition, we propose new results concerning the not yet measured bulk modulus of this system. The electronic band structure, the density of states and electronic charge density confirm the metallic character of $TbH_{2.25}$. The total density of states in both approximations shows important differences in the vicinity of the valence band, where, in both the relaxed and unrelaxed states, the GGA presents a tendency for underbinding in this material. Atomic relaxation shows that the Fermi energy changes in all cases are inversely proportional to those of the equilibrium lattice parameter. The electronic charge density has been plotted and shows a covalent character for the Tb-H_{tet} bonds and an ionic character for the Tb-H_{oct} bonds.

For future work, we would like to carry on more research on the rare earth hydrides and calculate their other physical properties such as lattice dynamics (phonon), magnetism, optics, thermodynamics and mechanics.

ملخص

في هذه الأطروحة، استعملنا برنامج المحاكاة WIEN2k لدراسة الخصائص البنيوية و الالكترونية للعناصر الترابية النادرة R (R=Gd, Tb)، لثنائيات هيدريدات العناصر الترابية النادرة RH_2 (R=Gd et Tb) و ثنائيات هيدريدات العناصر الترابية النادرة $RH_{2.25}$ فوق القياسية ذي زمرة التناظر *I4/mmm* (R=La, Gd) و ذي زمرة التناظر $Pm\bar{3}m$ (R=Gd, Tb) في حالة عدم استقطاب السبين، باستعمال نظرية دالية الكثافة في قاعدة أمواج مستوية مزادة و خطية مع كمون كامل في تقريب التدرج المعمم (GGA) وتقريب الكثافة المحلية (LDA). بهذه الطريقة قمنا بتحديد الثوابت البلورية، معاملات الإنضغاطية، كثافات الحالات و بنى عصابات الطاقة في هذه المركبات. بالإضافة إلى دراسة الخصائص المغناطيسية لـ R و الخصائص الترموديناميكية لثنائيات الهيدريدات لعناصر ترابية نادرة. في حالة استقطاب السبين و باستعمال تقريبات LSDA، GGA، LSDA+U و GGA+U، قمنا بدراسة الخصائص البنيوية، الالكترونية و المغناطيسية للعناصر الترابية النادرة (R=Gd, Tb). النتائج المتحصل عليها كانت متوافقة مع النتائج التجريبية و النظرية المتوفرة حول هذه المركبات.

كلمات مفتاحية : *هيدريدات الترابيات النادرة، نظرية دالية الكثافة (DFT)، الخصائص الالكترونية، WIEN2k.*

Résumé

Dans cette thèse, nous avons utilisé le code de simulation WIEN2k pour étudier les propriétés structurales et électroniques de terres rares R (R=Gd et Tb), des dihydrures de terres rares RH_2 (R=Gd et Tb) et des dihydrures superstoechiométriques de terres rares $RH_{2.25}$ avec un groupe d'espace *I4/mmm* (R=La et Gd) et avec un groupe d'espace $Pm\bar{3}m$ (R=Gd et Tb) dans le cas d'un spin non polarisé, en utilisant la théorie de la fonctionnelle de densité (DFT) dans une base d'ondes planes augmentées et linéarisées, avec un potentiel (FP-LAPW) dans l'approximation de gradient généralisé (GGA) et dans l'approximation de densité locale (LDA). Les paramètres de maille, les modules de compressibilité, les densités d'états et les structures de bande d'énergie dans ces composés ont ainsi été déterminés. En outre, les propriétés magnétiques de R et les propriétés thermodynamiques de RH_2 sont étudiées. Dans le cas du spin polarisé, nous étudions les propriétés structurelles, électroniques et magnétiques de la terre rare pure R (R=Gd et Tb) en utilisant les approximations LSDA, GGA, LSDA+U et GGA+U. Les résultats obtenus sont en accord avec la littérature et les résultats expérimentaux disponibles.

Mots-clés : *hydrures de terres rares, théorie de la fonctionnelle de densité, propriétés électroniques, WIEN2k.*

Abstract

In this thesis, we used the WIEN2k code to study the structural and electronic properties for pure rare earths R (R=Gd and Tb), rare earth dihydrides RH_2 (R=Gd and Tb) and superstoichiometric rare earth dihydrides $RH_{2.25}$ with *I4/mmm* space group (R=La and Gd) and with $Pm\bar{3}m$ space group (R=Gd and Tb) in the case of non-polarized spins, using the density functional theory (DFT) in the full-potential linearized augmented plane wave (FP-LAPW) basis in the generalized gradient approximation (GGA) and in the local density approximation (LDA). Lattice parameters, bulk moduli, density of states and energy band structures in these compounds have been determined. Besides, the magnetic properties of R and thermodynamic properties of RH_2 are studied. In the case of spin polarization and using LSDA, GGA, LSDA+U and GGA+U approximations, we investigate the structural, electronic and magnetic properties of pure rare earths R (R=Gd and Tb). The results are found to agree with the literature and available experimental data.

Keywords: *rare-earth hydrides, density functional theory, electronic properties, WIEN2k.*